Incorporation of Pyramidal Heteroanions in Mixed-Metal Polyoxometalate Based Cages

Maria de las Nieves Corella Ochoa

A thesis submitted to the University of Glasgow for the degree of Doctor of Philosophy

School of Chemistry

October 2011

A mi padre, mi madre y mi hermano.
Por los valores que me han inculcado.
Por su incondicional apoyo y fuerza.

"One has to have persistence, but above all else belief in oneself."

E. Curie

Acknowledgements

This project was carried out between October 2008 and September 2011 in the School of Chemistry at the University of Glasgow, during which time I received the help and advice of many people. In particular, I owe a great deal of gratitude to the following:

Professor Lee Cronin, for giving me the opportunity to do research in his group, for sharing the motivation and endless enthusiasm in his unique way to think and do chemistry, and for his constant support, patience and understanding.

Dr De-Liang Long, the crystallography master, for his time and continuous help in understanding the complicated world of single crystals.

Dr Haralampos N. Miras, for his infinite patience and unconditional support during these three years, for being such an amazing mentor from day one, for sharing his huge chemistry knowledge and experience, and for all the good laughs!

Dr Craig J. Richmond, what could I say that you already don't know eh? Thank you for all the moments, thank you for being you.

Dr Graham N. Newton, Dr Scott G. Mitchell, Dr Philip J. Kitson, Dr Jennifer S. Mathieson, Dr Johannes Thiel, Dr Thomas McGlone, Dr Liz Wilson and **Dr Carsten Streb**, for introducing me to the Cronin group, for taking good care of me and making research such a wonderful experience over so many cups of coffee.

Mali Husby Rosnes for being a great friend, for sharing the lab, the office and even the flat with me!, for all the many moments we had together since we met almost four years ago! A big thank you for everything!

Roslyn Eadie, Feng Xu, Claire Lydon and David Gabb for sharing the PhD adventure, for being such a good bunch of mates, and for all the fun times.

Nuria Tapia Ruiz, for the little big moments, for her enthusiasm, for her smile and big friendship.

Dr Geoffrey J. T. Cooper, for all his help with computers and software, **Dr Christoph Busche, Dr Yun Yan, Tommy Boyd** and **Jamie Cameron**, for the scientific discussions and help over the past years; and special thanks to **Ross Winter** for proof reading this thesis.

Prof. Jun Kawamata from Yamaguchi University in Japan for running the NLO studies.

Jim McIver, for being the most versatile person in the group and for sharing the Jelly Bellys!.

The technical staff of the University of Glasgow; **Michael Beglan** for FAAS, **Kim Wilson** for EA and **Andy Monaghan** for the TGA.

Finally, I would like to thank **The Whole Cronin Group**, a fascinating, amusing and talented bunch of people to work with.

Table of Contents

Publications

The following articles and communications were published as a result of work undertaken over the course of this PhD programme.

"Pyramidal Heteroanions Take Control: Self-Assembly of Mixed-Metal Polyoxometalates", M. N. Corella-Ochoa, H. N. Miras, D.-L. Long, and L. Cronin; *Chem. Eur. J*., **2010**, *in preparation.*

"Assembly of a family of mixed metal {Mo : V} polyoxometalates templated by TeO_3^{2-}: $\{Mo_{12}V_{12}Te_3\}$, $\{Mo_{12}V_{12}Te_2\}$ and $\{Mo_{17}V_8Te\}$", M. N. Corella-Ochoa, H. N. Miras, A. Kidd, D.-L. Long and L. Cronin, *Chem. Commun.*, **2011**, *47*, 8799-8801 .

"Controlling transformations in the assembly of polyoxometalate clusters: $\{Mo_{11}V_7\}$, $\{Mo_{17}V_8\}$ and $\{Mo_{72}V_{30}\}$" H.N. Miras, M.N.C. Ochoa, D.L. Long and L. Cronin, *Chem. Commun.*, **2010**, *46*, 8148-8150.

"Modular Inorganic Polyoxometalate Frameworks Showing Emergent Properties: Redox Alloys", J. Thiel, C. Ritchie, H. N. Miras, C. Streb, S. G. Mitchell, T. Boyd, M. N. C. Ochoa, M. H. Rosnes, J. McIver, D. L. Long and L. Cronin. *Angew. Chemie Int. Ed.*, **2010**, *49*, 6984-6988.

Abbreviations

BVS_{av}	Bond valence sum average
CSI-MS	Cryospray ionization mass spectroscopy
ESI-MS	Electrospray ionization mass spectroscopy
FT-IR	Fourier-transformation infra-red
HPOM	Heteropolyoxometalate
Ln	Lanthanide
NLO	Non-linear optical
NMR	Nuclear magnetic resonance
POM	Polyoxometalate
Pr_4NBr	Tetrapropylammonium bromide
PXRD	Powder X-ray diffractometry
SBU	Secondary building unit
SHG	Second harmonic generation
TBA	Tetra-*n*-butyl ammonium
TGA	Thermogravimetric analysis
TEA	Triethanol amine
UV-VIS	Ultraviolet-visible
XRD	X-ray diffractometry

Notation

In line with standard notation, the full formulae of anionic cluster compounds will be noted in square brackets, such as $[\gamma\text{-}SiW_{10}O_{36}]^{8-}$ and $[(P_2W_{16}Co_2O_{60})_3]^{24-}$. However, this example illustrates that such notation can result in rather long and awkward formulae which do not necessarily add to the clarity of the text. As a result, an abbreviated notation will be introduced where the number and type of addenda and substituted metal centres and heteroatoms of the cluster are indicated by curly brackets, thereby representing the complete cluster unit. For example, the formula of the cluster units above, $[\gamma\text{-}SiW_{10}O_{36}]^{8-}$ and $[(P_2W_{16}Co_2O_{60})_3]^{24-}$ may be reduced to $\{SiW_{10}\}$ and $\{P_2W_{16}Co_2\}_3$ respectively.

In addition, the presence of geometric coordination motifs within one cluster will be indicated using a MO_x notation. For example, an octahedral building unit where six oxygen ligands (O) coordinate to a central transition metal (M) will be noted as MO_6. In this case, no charge will be assigned since this description illustrates a purely formal structural building unit.

The compounds containing mixed-metal molybdenum-vanadium fragments with disordered atom positions where crystallographically treated by refining each position by assigning the occupancy of x% and (100-x)% for molybdenum and vanadium respectively. For example, the $\{Mo_5V_4\}$ motif will be refined as 5/9 for molybdenum and 4/9 for vanadium.

Abstract

The incorporation of pyramidal heteroanions from Group XVI (SO_3^{2-}, SeO_3^{2-} and TeO_3^{2-}) within molybdovanadate mixed-metal inorganic cages has led to the isolation of a new family of materials with unprecedented archetypes and structural motifs. During the course of this study, it has been demonstrated that there is an important correlation between the geometry and the size of the anionic templates, which is reflected in the plethora of structures that have been isolated in the different scenarios as well as the wide variety of coordination modes that the heteroanion displays.

The reaction of molybdate with vanadium in the presence of sulfite anions is explored, showing how *via* cation control it is possible to direct the self-assembly process to the formation of three different archetypes namely: $\{Mo_{11}V_7S\}$, $\{Mo_{17}V_8S\}$ and $\{Mo_{72}V_{30}(SO_4)_{12}\}$. Further investigations revealed that the sulfite heteroanion not only templates the isolated archetypes but also triggers the stepwise assembly through the $\{Mo_{11}V_7S\}$ cluster, which yields the formation of the $\{Mo_{17}V_8S\}$ anion, first discovered using mass spectroscopy.

When the bigger selenite heteroanion was incorporated within the mixed-metal systems, the self-assembly process led to the isolation of a larger family of polyoxometalates composed of the novel archetypes $\{Mo_{12}V_{10}Se_8\}$ and $\{Mo_{20}V_{16}Se_{10}\}$ along with the $\{Mo_{11}V_7Se\}$ and $\{Mo_{17}V_8Se\}$ Dawson-like cages that are isostructural to the sulfite-based cluster. The contribution of the larger anion is not only observed in the wide variety of structural motifs that the above mentioned structures unveil but on the diversity of coordination modes that the selenites themselves display when acting as a templating agent and a ligand.

Finally, when the even larger tellurite heteroanions are used as a template, the steric restrictions introduced by the heteroanion in the mixed-metal system are increased, as is reflected in the formation of the tellurite-based cages $\{Mo_{12}V_{12}Te_3\}$ and $\{Mo_{12}V_{12}Te_2\}$ and the $\{Mo_{17}V_8Te\}$ Dawson-like anion. The latter of the three is isostructural to the

sulfite- and selenite-based clusters, whereas the two former anions are isostructural to each other with the exception of an additional tellurite centre exhibiting a novel bridging mode, previously unseen in pyramidal-based mixed-metal polyoxometalates.

During the course of this study, ESI and CSI mass spectrometry along with X-ray crystallography has allowed us to analyse the isolated materials in the solid state and in solution, and also helped us to correlate the self-assembly process with experimental variables, such as counter-cation and heteroatom size. ESI and CSI mass spectrometry techniques have been used to understand the structural evolution process along with the chemical information transfer from the parent molecule $\{Mo_{11}V_7S\}$ to the daughter molecule $\{Mo_{17}V_8S\}$; as well as to confirm the novel coordination motifs of the TeO_3^{2-} heteroanion in the $\{Mo_{12}V_{12}Te_3\}$ and $\{Mo_{12}V_{12}Te_2\}$ cages. Furthermore, FT-IR analyses were done to identify and distinguish the different coordination modes of the corresponding heteroanion; unveiling that the bigger the heteroanion is the larger the separation between the stretching X-O (X = S, Se and Te) of the heteroanion becomes.

1 INTRODUCTION

Polyoxometalate chemistry has undergone an exponential growth over the last few decades due to the vast range of properties and applications that this diverse family of inorganic materials present.[1-4] This resurge in interest has principally been promoted by the development of analytical instrumentation and novel synthetic approaches. The use of X-ray diffraction has proven to be one of the most powerful tools for the characterization of such materials, providing precious information on the relationship between structure, bonding and reactivity of these compounds.[5] Since the special issue on polyoxometalate systems was published in *Chemical Reviews* in 1998,[6] which provided an up to date overview of the most recent developments on the polyoxometalate field, many groups all over the world have focused on the isolation, characterization and application of these novel materials. This fact is not surprising since polyoxometalates (POMs) have proved to be a valuable subset of metal oxide materials, with an unmatched range of dynamic structures and physical properties that lend themselves to interdisciplinary research, encompassing areas such as catalysis, medicine, geochemistry, biology, materials and nanotechnology.[7-11]

1.1 Polyoxometalates

1.1.1 Historical Background / Perspective

The first account of a polyoxometalate dates from 1826 when J. J. Berzelius observed the formation of a yellow precipitate upon addition of ammonium molybdate, $(NH_4)_2MoO_4$, to an excess of a phosphoric acid solution.[12] Later on, Marignac isolated and characterized the first heteropolytungstates in 1864;[13] and A. Werner and L. Pauling proposed structures for such species, anticipating the edge- and face-sharing of the polyhedra.[14, 15] It was not until 1933, when J. F. Keggin solved the powder X-ray diffraction pattern of 12-phosphotungstic acid, today known as the phosphotungstate "Keggin" structure, of formula

$H_3PW_{12}O_{40}\cdot 5H_2O$,[16, 17] that definitive evidence for the structural composition of these heteropolyacids existed.

Since then, advances in X-ray diffraction instrumentation, coupled with cheap and powerful computing power for structure solution and refinement,[5] has allowed the rapid growth of POM chemistry, as is reflected by the trend in the number of POM-based compounds reported (Figure 1). Over the last decade, this upsurge in concern with the field has mainly been attributed to the use of POMs in other multidisciplinary areas such as: surface science,[18] catalysis,[19] supramolecular and molecular materials,[20, 21] electronic materials including electro/photo-chromic systems,[22, 23] and molecular materials and magnets.[24] Furthermore, with the use of novel techniques such as Raman, NMR and mass spectrometry, which have enabled the important link between the solid and solution structures to be established, it is not surprising that the polyoxometalate field keeps expanding rapidly, unveiling novel materials with unexpected reactivity and unique properties and applications.

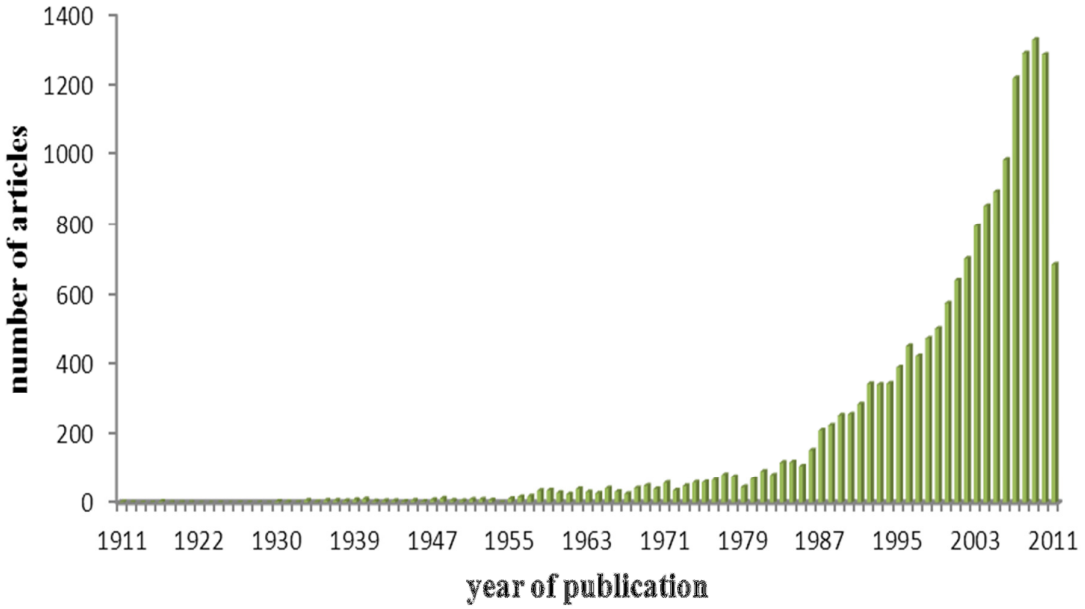

Figure 1: Illustration of the exponential increase in the number of publications containing "polyoxometalate" as a keyword over the last century. Data taken from SciFinder Scholar.

1.1.2 Features of Polyoxometalates

Polyoxometalates are inorganic metal oxide clusters unique in topology and electronic versatility. This class of polyanions is composed of early transition metals (also called *addenda*), mainly of molybdenum (V/IV), vanadium (IV/V), tungsten (V/VI) and niobium (V), in their highest oxidation state (d^0, d^1 configurations). Their mechanism of formation consists of the condensation of different $\{MO_x\}$ (x = 4 – 7) units under acidic aqueous conditions and can be controlled by several synthetic parameters (e.g. the counterion, pH, temperature, solvent, ionic strength, type of acid, concentration of the metal oxide units, time of reaction, etc.), forming clusters of nuclearities ranging from 2 to 368 metal centres (Figure 2).[14]

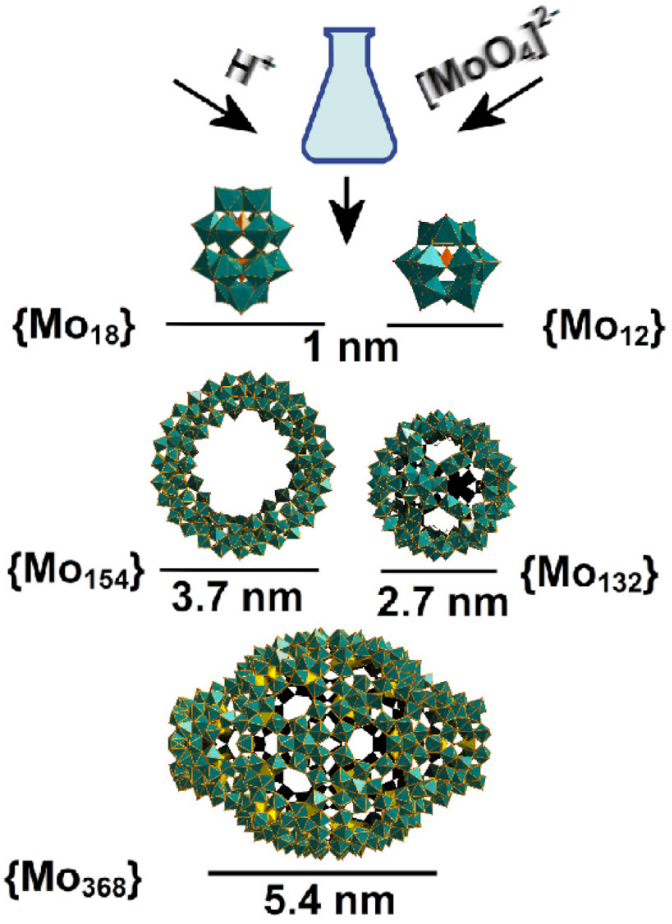

Figure 2: Self-assembly of polyoxometalate clusters, from $\{Mo_{12}\}$ to the protein-sized $\{Mo_{368}\}$. The molybdenum centres are shown as green polyhedra.[25]

POMs are predominantly composed of MO_6 octahedra, although tetragonal and square pyramidal geometries are also common, so it is easier to describe the structure of the different $\{MO_x\}$ units as polyhedrons where the metal ion is at the centre and the oxygen ligands at the vertices. Upon reaction, the different $\{MO_x\}$ building blocks aggregate with one another *via* corner-, edge- or face-sharing binding modes (Figure 3). Corner-sharing offers flexibility; whereas edge-sharing confers a degree of rigidity to the forming cluster.

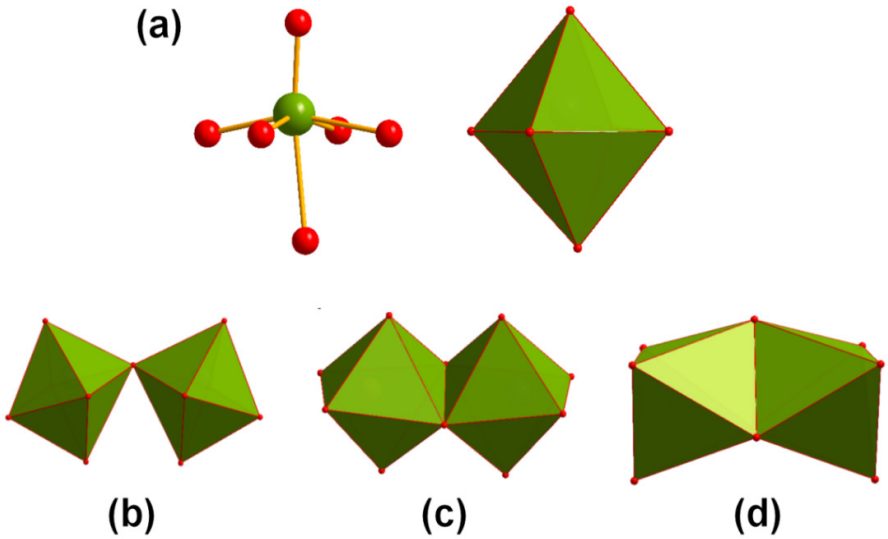

Figure 3: (a) Ball-and-stick and polyhedral representation of the principle MO_6 octahedral building unit. Polyhedral representation of the principle modes of oxygen sharing atoms between two octahedra MO_6 units: (b) corner-sharing, (c) edge-sharing and (d) face-sharing.

Molybdenum and tungsten based POMs have been by far the most explored classes of polyanions to date. This fact is due to their favourable combination of ionic radius and charge and the accessibility of their empty *d* – orbitals which allow the formation of the metal-oxygen π – bonding.[4] The ability of these atoms to form double bonds with the unshared oxygens of their MO_6 octahedra (pπ-dπ interactions) results in *closed* discrete structures with the M=O pointing outwards. The formation of such double bonds causes the displacement of the metal centre towards the outer vertices of the polyhedron as a consequence of the large polarization of the unshared oxygens towards the metal. Simultaneously, the highly charged metal centre produces a strong ion-induced dipole

attraction towards the adjacent unshared oxygen resulting in the M=O bond shortening and distortion of the MO_6 octahedra. This combination forms a "shell" where the exterior layer of the POM is strongly polarized towards the interior of the cluster and the interior layer, formed by the metal centres, is strongly attracted towards the outer layer, creating a free space in the interior of the cluster which can be occupied by a variety of heteroatoms.[4, 14, 26]

1.1.3 Synthetic methodologies

The commonest synthetic methodology used to synthesise polyoxometalate clusters is based on the acidification of an aqueous solution which contains the different metal oxide building units and heteroanions (Figure 4b). In many cases, the equilibrium constants and rates of formation are large enough that the polyoxoanions can be crystallised as salts from stereochemically acidified mixtures of the components at room temperature. Acidification is generally achieved by addition of a common mineral acid. Isolation of the polyanion from solution is mainly achieved by the addition of an appropriate counter-cation, such as alkali metals, ammonium or tetraalkylammonium. Lithium and sodium salts tend to be more water-soluble than those of the larger cations, whereas salts of the larger alkylammonium are usually insoluble in water but recrystallizable from solvents such as acetonitrile and acetone. The accurate control of the pH and temperature of the reaction mixture, as well as the sequence of reagent addition, is also important.[14]

Over the last decade, the use of hydrothermal techniques for the isolation of this class of metal oxide materials has increased considerably since it has proved to give numerous unusual polyoxometalates.[27] Hydrothermal reactions are typically carried out between 120 and 260 ºC under autogenous pressure, where the viscosity of water is reduced, enhancing diffusion processes so that crystal growth from solution is favoured (Figure 4a). By using this technique, solubility problems are minimized and a variety of simple precursors may be introduced, as well as organic and/or inorganic structure-directing agents from which those of appropriate size and shape may be selected for efficient crystal packing during the crystallization process. Under such non-equilibrium crystallization conditions, metastable

kinetic phases are most likely to be isolated rather than the thermodynamic phase, resulting in the formation of structurally unexpected materials.[28-31]

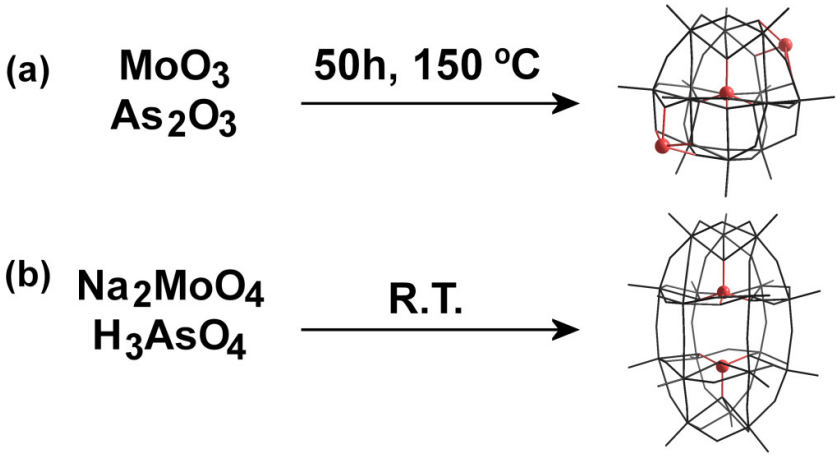

Figure 4: Comparison of two synthetic procedures: (a) the hydrothermal reaction between MoO_3 and As_2O_3 leads to the isolation of the bicapped Keggin-like structure[27] $[As_3Mo_{12}O_{40}]^{5-}$; whereas in (b) the reaction mixture of Na_2MoO_4 and H_3AsO_4 leads to the Wells-Dawson $[As_2Mo_{18}O_{62}]^{6-}$ anion.[32] The inorganic molybdenum-oxide cages are in dark grey and the As metal centres are in light pink.

1.1.3.1 Flow Reactors for the Discovery of New POM Clusters

Even though it is well-accepted that the formation mechanism of polyoxometalates involves the condensation of metal oxide units under aqueous acidic conditions, the complete understanding of how this self-assembly process works remains a big challenge. In an effort to gain control and direct the assembly process, different techniques have been employed such as the structure directing properties of "shrink-wrapping" organic cations,[33, 34] control of ionic strength,[35] the direct observation of new clusters as they are formed using electrospray and cryospray mass spectrometry,[36] and the reaction and crystallisation under flow conditions.[37]

Figure 5: Scheme of the flow reactor system with the mixing chambers, showing the blue reduction gradient formed within the vessel during the assembly of $\{Mo_{186}\}$.[37]

The use of a flow reactor to study the formation mechanism of previously characterized molybdenum blues wheels (see *Section 1.4*) has proven to be a powerful tool in unveiling the nucleation process of the $\{Mo_{154-x}\}$ nanowheel family. Cronin *et al.* demonstrated how by using a flow system that enabled real-time control of the input variables (pH, concentration of molybdate and reducing agent) it was possible to control the synthesis of the molybdenum blue molecular nanosized-wheels. By reduction of an acidic aqueous solution containing $Na_2MoO_4{\cdot}2H_2O$ with $Na_2S_2O_4$ under continuous addition of HNO_3 (Figure 5), crystals of the host guest complex $Na_{22}[Mo^{VI}_{36}O_{112}(H_2O)_{16}]\subset[Mo^{VI}_{130}Mo^{V}_{20}O_{442}(OH)_{10}(H_2O)_{61}]{\cdot}180H_2O$ were obtained. The ellipsoidal structure appears to be a consequence of the central host $\{Mo_{36}\}$ cluster which is templating the hollow $\{Mo_{150}\}$ wheel.

During this process the use of nitric acid as a proton source and oxidant reagent was shown to be crucial, leading to the incomplete reduction of the wheel and therefore to the isolation of the $\{Mo_{186}\}$ cluster. If hydrochloric acid was used instead, no formation of the intermediate cluster was observed but instead a mixed batch of $\{Mo_{36}\}$ and $\{Mo_{150}\}$ crystals was obtained. From this data, they postulated that the whole mechanism behind the formation of the $\{Mo_{154-x}\}$ family involves the $\{Mo_{36}\}$ cluster as a structure-directing template (Figure 6).[37]

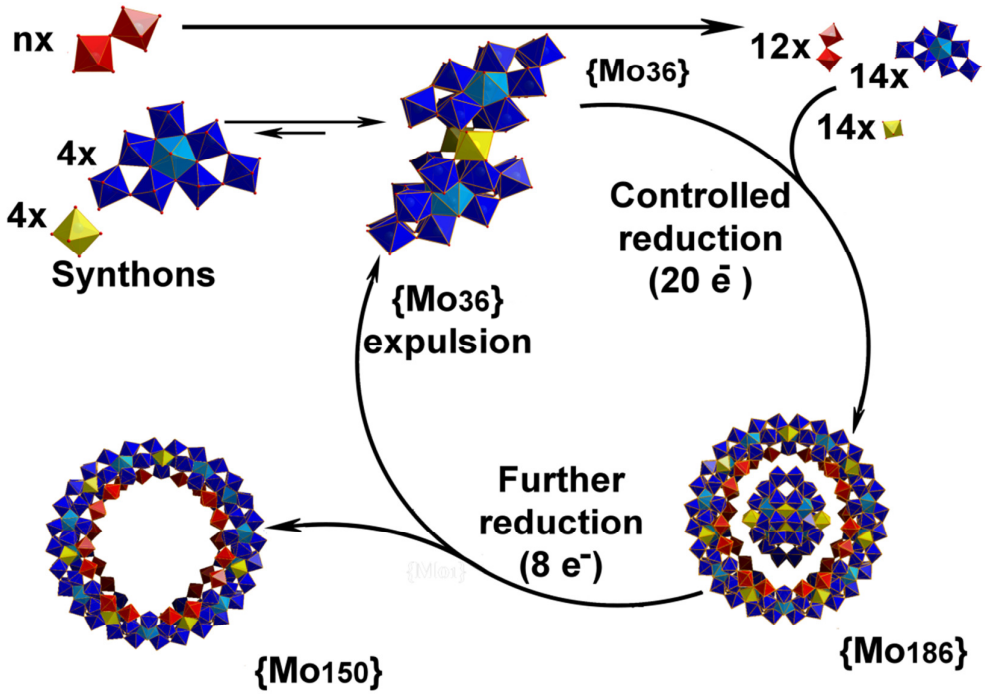

Figure 6: Conceptual representation of the *Molybdenum Blues* assembly showing the building block "synthons" (which are assigned on the basis of structural considerations) that form the complex. Continuous flow-reaction conditions, along with a finely tuned reducing environment, are required to trap the template complex. The polyhedral building blocks are coloured as follows: $\{Mo_1\}$ yellow, $\{Mo_2\}$ red, $\{Mo_8\}$ blue with a blue pentagonal central group.[37]

1.1.4 Polyoxometalates Classification

Polyoxometalates can be classified into three main subclasses: Isopolyoxometalates, Heteropolyoxometalates and Molybdenum Blues and Browns (Figure 7):

- *Isopolyoxometalates* which consist of an inorganic framework built up from the condensation of only metal oxide building blocks, with no internal heteroatom or supporting ligand. Examples of such clusters include the Linqvist ion $[M_6O_{19}]^{2-}$.[38, 39]

- *Heteropolyoxometalates* where an additional templating or stabilizing heterogroup (X) has been incorporated in the centre of the inorganic cage. Examples of such clusters include the Keggin anion $[XM_{12}O_{40}]^{n-}$ and the Wells - Dawson anion $[X_2M_{18}O_{62}]^{n-}$.[16, 17, 40]

- *Molybdenum Blues and Browns* which were first observed by Scheele in 1783 as a class of polyoxoanions composed of Mo^{VI} and Mo^{V} metal centres. Later on Müller and co-workers expanded the studies of this class of compounds, leading to nanoscale dimension clusters.[41]

Each of these subclasses of polyoxoanions will be discussed in more detail in the following sections.

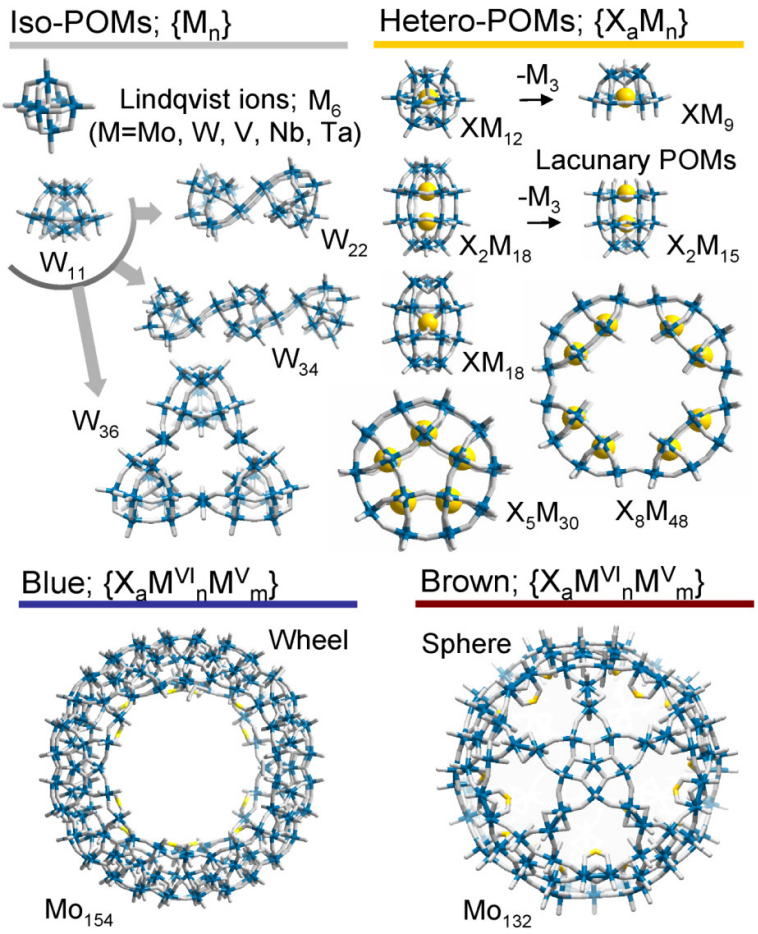

Figure 7: Polyoxometalates classification. The metal-oxygen framework is represented by sticks.[2] M: blue, O: grey, X: heteroatom.

1.2 Iso-Polyoxometalates

1.2.1 Vanadates

Over the last 20 years, research in isopolyvanadate chemistry has been expanded quickly as a consequence of their intriguing topological structures and their interesting electronic and magnetic properties.[42, 43] Their ability to adopt different oxidation states (III, IV, and V) along with different coordination modes (VO_4 tetrahedral, VO_5 square based pyramidal and VO_6 octahedral) leads to the formation of a wide range of structures (Figure 8) with different nuclearities, reduced/oxidized metal centres and shapes: $[V_4O_{12}]^{4-}$,[44] $[V_5O_{14}]^{3-}$,[45] $[V_{10}O_{28}]^{6-}$,[46] $[V_{12}O_{32}]^{4-}$,[47] $[V_{13}O_{34}]^{3-}$,[48] $[V_{16}O_{38}]^{7-}$,[49] $[V_{17}O_{42}]^{4-}$,[50] and $[V_{19}O_{49}]^{9-}$.[51]

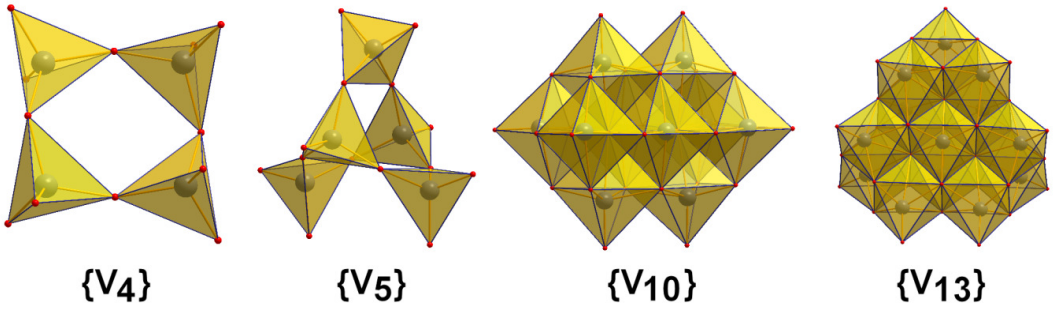

Figure 8: Polyhedral representation of different isopolyoxovanadates: $\{V_4\}$ and $\{V_5\}$ built up from $\{VO_4\}$ tetrahedral, $\{V_{10}\}$ and $\{V_{13}\}$ built up from $\{VO_6\}$ octahedral. V: grey spheres, O: red spheres.

An important feature of this class of POMs is their ability to act as cryptands. The condensation of VO_5 units ($O{=}VO_4$), which confer flexibility to the cluster, results in the formation of highly symmetrical archetypes which can act as hosts and encapsulate negatively charged ions that influence the shape and size of the cluster shell (e.g. $[V_{15}O_{36}(Cl)]^{6-}$, $[V_{18}O_{42}(SO_4)]^{11-}$ and $[V_{22}O_{54}(ClO_4)]^{5-}$).[52-54] On the other hand, the isolation of the vanadates can also act as a template as in the case of the cubane type $\{(V_4O_4)O_4\}$ which leads to the formation of $[\{(V^{IV}{}_4O_4)O_4\}V^{V}{}_{18}V^{IV}{}_{12}O_{74}]^{10-}$ (Figure 9).[55] The formation of these hollow spheres is only observable in the case of vanadates because molybdates

and tungstates prefer the MO_6 octahedral linking rather than the linking of tetragonal pyramids. Additional to their interesting structural properties, isopolyoxovanadates are an attractive subclass of POMs due to their applications in catalysis, anti-HIV chemotherapy, sol-gel chemistry, lithium batteries and sensor technology.[56-58]

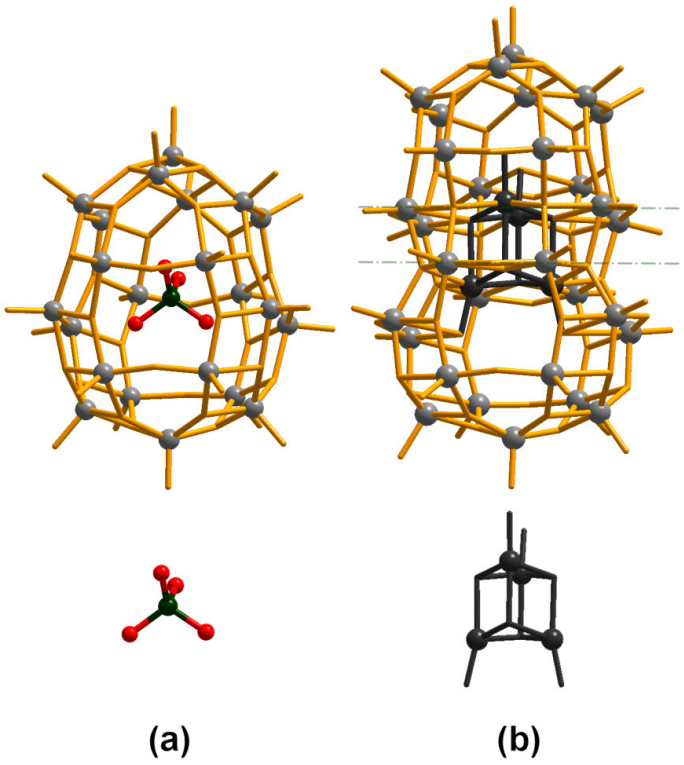

Figure 9: Ball-and-stick representation of (a) $[V_{22}O_{54}(ClO_4)]^{5-}$ and (b) $[\{(V^{IV}{}_4O_4)O_4\}V^{V}{}_{18}V^{IV}{}_{12}O_{74}]^{10-}$ with their central units. The cluster shell from (a) is formally formed from (b) by removal of the two middle layers (green lines). The oxygen atoms from the metal oxide cages have been removed for clarity. V: grey, $[\{(V^{IV}{}_4O_4)O_4\}]$ core: dark grey, Cl: dark green, O: red.[53]

1.2.2 Molybdates

The polymerization of the tetrahedral $[MoO_4]^{2-}$ anion under acidic conditions leads to the isolation of several isopolyoxomolybdates with diverse nuclearities and shapes. $[Mo_6O_{19}]^{2-}$, $[Mo_7O_{24}]^{6-}$, $[Mo_8O_{26}]^{4-}$, $[Mo_{10}O_{34}]^{8-}$ and $[Mo_{36}O_{112}(H_2O)_{16}]^{8-}$ are the predominant species

in such reaction systems.[59-63] In almost all the cases the molybdenum centres adopt MoO_6 octahedra although exceptions do exist, such as the $[Mo_8O_{26}]^{4-}$ and $[Mo_{10}O_{34}]^{8-}$ clusters which contain one or more MoO_4 tetrahedra, and the largest isopolyoxomolybdate known to date, $[Mo_{36}O_{112}(H_2O)_{16}]^{8-}$, with two seven coordinated molybdenum atoms (Figure 10).

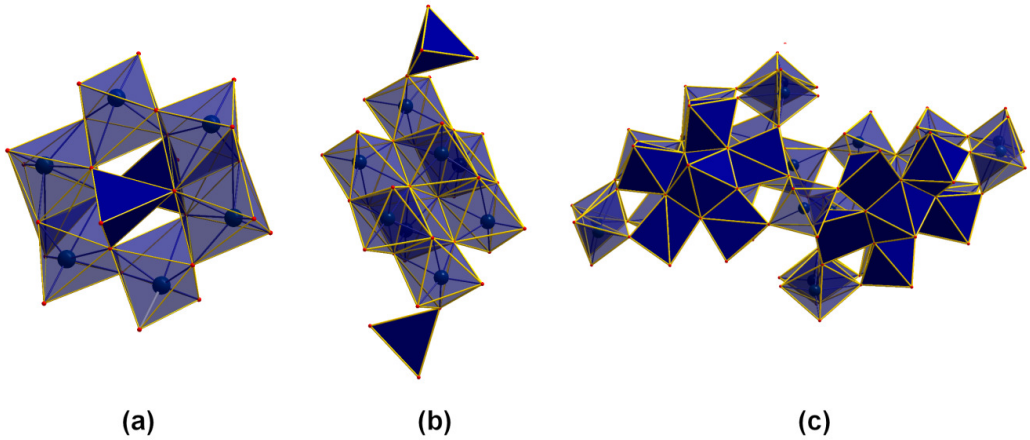

Figure 10: Polyhedral representation of (a) the $[Mo_8O_{26}]^{4-}$ anion which consists of a ring made up of six MoO_6 octahedra linked to one MoO_4 tetrahedron above, and another below its octahedral cavity; (b) the $[Mo_{10}O_{34}]^{8-}$ anion, equivalent to $[Mo_8O_{26}(MoO_4)_2]^{8-}$, which consists of an arrangement of eight edge-sharing distorted MoO_6 octahedra linked by a pair of distorted MoO_4 tetrahedra; and (c) the $[Mo_{36}O_{112}(H_2O)_{16}]^{8-}$ anion which consists of two 18-molybdate subunits related to each other by a centre of inversion, with two MoO_7 polyhedra in each subunit. Tetrahedra in (a) and (b), and the heptacoordinated molybdenum atoms and the five MoO_6 octahedra in (c), are shown in dark blue. Mo: blue spheres, O: red spheres.

Another interesting feature of isopolyoxomolybdates is the incorporation of mixed-valence metal centres within the same inorganic cage. This fact leads to the isolation of novel archetypes such as the $[(Mo^{VI}O_3)_4Mo^{V}_{12}O_{28}(OH)_{12}]^{8-}$ anion reported by Zubieta *et. al.* (Figure 11a) which is a rare example of an oxomolybdate cage capable of accommodating cations,[64] and the $[H_2Mo^{V}_4Mo^{IV}_{12}O_{52}]^{10-}$ cluster (Figure 11b) reported by Cronin *et. al.* which was isolated by using the "shrink-wrapping" approach that employs bulky water soluble tertiary amines.[65]

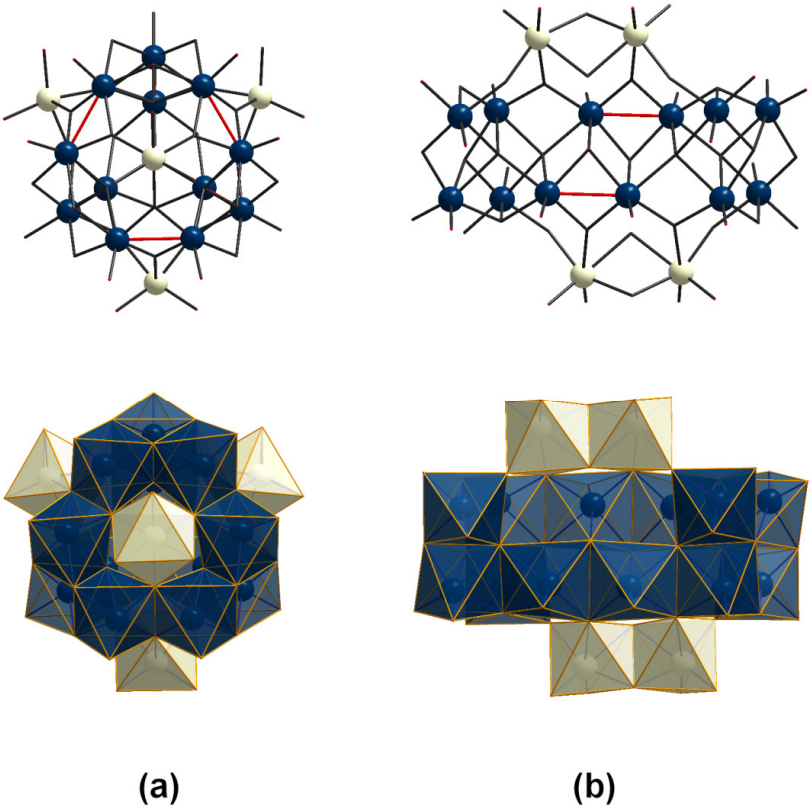

Figure 11: Ball-and-stick (top) and polyhedral (bottom) representation of the crystal structures of (a) $[(Mo^{VI}O_3)_4Mo^{V}_{12}O_{28}(OH)_{12}]^{8-}$ and (b) $[H_2Mo^{V}_4Mo^{IV}_{12}O_{52}]^{10-}$. The discrete anion in (a) exhibits a central Keggin unit built up from twelve reduced Mo^{V} centres (blue spheres) which form six binuclear units with Mo-Mo distance of 2.62(1) Å (red bonds) and four facial $Mo^{VI}O_3$ "anti-Lipscomb" units (cream spheres).[66] The cluster framework in (b) displays an unusual flat shape with a central unit of twelve molybdenum atoms (blue spheres) and two peripheral molybdenum centres on each side (cream spheres). The four Mo^{V} centres are located in the central part of the cluster core and reveal a short Mo-Mo contact of 2.64(4) Å (red bonds).

Further studies in this subclass of isopolyoxoanions have revealed that such materials are involved in more complex reaction systems leading to gigantic archetypes which will be discussed in *Section 1.4. Molybdenum Blues and Browns*.

1.2.3 Tungstates

Upon acidification of an aqueous solution containing $[WO_4]^{2-}$, addition and condensation reactions occur, leading to the formation of isopolyoxotungstate anions with different nuclearities. Depending on the pH, the total concentration of the solution and the crystallization times, different structure types can be isolated: e.g. $[HW_5O_{19}]^{7-}$, $[W_6O_{19}]^{2-}$, $[H_3W_6O_{22}]^{5-}$, $[W_7O_{24}]^{6-}$, $[W_{10}O_{32}]^{4-}$, $[H_4W_{11}O_{38}]^{6-}$, $[H_2W_{12}O_{40}]^{6-}$, $[H_2W_{12}O_{42}]^{10-}$ and $[W_{24}O_{84}]^{24-}$.[67-75]

In comparison with isopolyoxoanions based on vanadium and molybdenum, which exhibit a variety of coordination modes and oxidation states, isopolyoxotungstates have a more limited number of structural motifs but larger crystallization times. For these reasons, this subclass of isopolyoxoanions has not attracted as much attention in current years. In 1992, Howarth *et. al.* reported a study on isopolyoxotungstate chemistry whereby using NMR spectroscopy different intermediates and confirmed known isopolytungstate structural types were identified.[70] Afterwards different synthetic techniques have been used in the attempt to further expand this subclass of isopolyanions. By applying the "shrink-wrapping" strategy, Cronin *et. al.* isolated two novel archetypes: the largest isopolyoxotungstate to date $[H_{12}W_{36}O_{120}]^{12-}$, which comprises three $\{W_{11}\}$ clusters subunits linked together by three $\{W_1\}$ bridges and can be considered as an inorganic crown,[76] and the $[H_4W_{19}O_{62}]^{6-}$ anion which is isostructural to the $\{M_{18}\}$ Dawson archetype and encapsulates a WO_6 moiety.[77]

One of the most intriguing properties of isopolyoxoanions is the use of small known building units to generate larger archetypes. The control of such reaction pathways remains a challenge although after the isolation of $[H_4W_{22}O_{74}]^{12-}$ and $[H_{10}W_{34}O_{116}]^{18-}$ (Figure 12) from the same reaction mixture under pH and anion control, it was revealed that a new building block principle can be generated using pure isopolyoxotungstate-based $\{W_{11}\}$ units. Both the $\{W_{22}\}$- and the $\{W_{34}\}$-based clusters have related architectures based upon

the linkage of $\{W_{11}\}$ building units, a feature that was already observed in the $\{W_{36}\}$ cluster.[35]

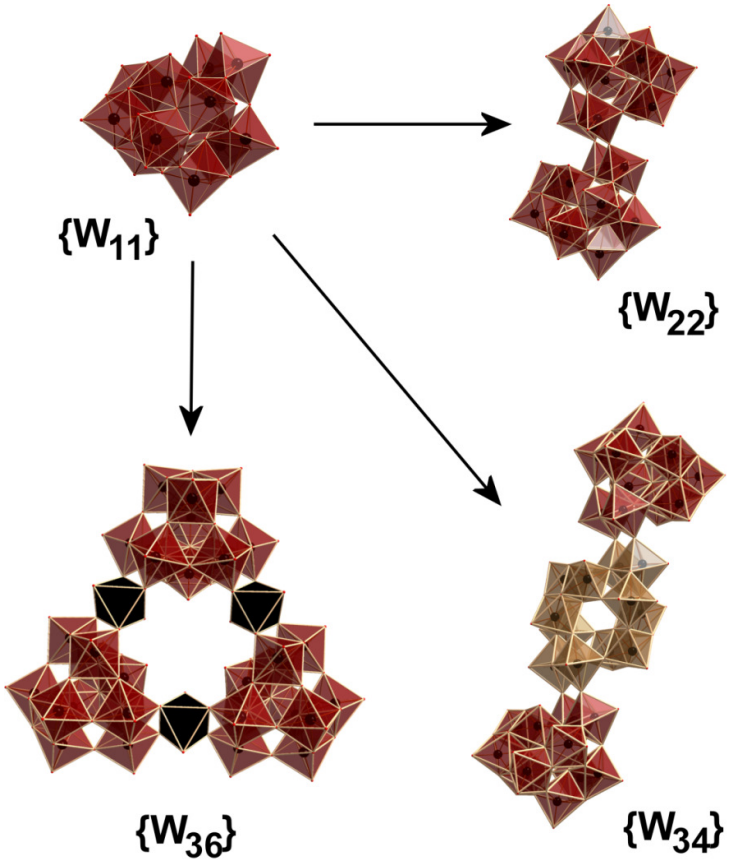

Figure 12: Polyhedral representation of the self-assembly of the $\{W_{22}\}$ cluster built up from two $\{W_{11}\}$ subunits linked by μ_2-oxo bridges in *trans*-fashion, the $\{W_{34}\}$ cluster which consists of two identical $\{W_{11}\}$ subunits which are linked in a *trans*-fashion by a $\{W_{12}\}$ (beige polyhedral) unit through μ_2-oxo bridges, and the trimeric $\{W_{36}\}$ cluster which consists of three *cis* edge-shared $\{W_{11}\}$ units linked by three $\{W_1\}$ groups (black polyhedral).[35]

1.2.4 Mixed-Metal Isopolyanions

Although all the isopolyoxoanions described so far are composed only of one type of metal centre and the corresponding oxygen ligands, isopolyanions containing two or more of the

elements vanadium, molybdenum and tungsten do exist. The most explored mixed-metal isopolyanions are those built up from molybdenum and vanadium, followed by tungsten and vanadium; mixed-metal molybdenum and tungsten isopolyanions have not yet been reported.

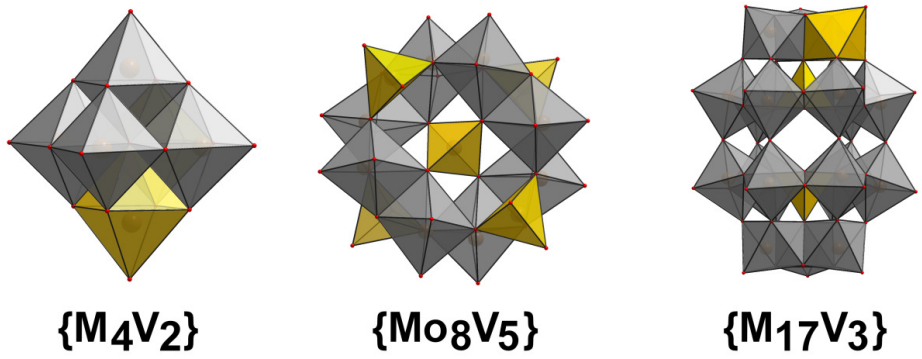

Figure 13: Polyhedral representation of three different mixed metal isopolyoxometalates. The Linqvist $\{M_4V_2\}$, the ring $\{Mo_8V_5\}$ and the Wells-Dawson $\{M_{17}V_3\}$ where M = Mo or W. V: Yellow polyhedra, Mo or W: grey polyhedra, O: red spheres.

The first report of a molybdovanadate dates from 1891 when Liebert isolated salts with a Mo/V ratio of 6:2; but it was not until Björnberg refined the crystal structure that the compound was characterized as the $[Mo_6V_2O_{26}]^{6-}$ anion,[78] which is isostructural to the $[Mo_8O_{26}]^{4-}$ anion. Further investigations within this area revealed the existence of more molybdovanadates with a wide variety of Mo/V ratios such as the $[H_2MoV_9O_{28}]^{3-}$ anion which displays the structure of a decavanadate with the Mo atom substituted at one "capping" vanadium site;[79] the $[Mo_8V^{IV}V^{V}{}_4O_{40}]^{8-}$ ($\{Mo_8V_5\}$ in Figure 13) with a central VO_4 tetrahedron surrounded by a double-ring of eight alternated edge-sharing MoO_6 octahedra and four VO_4 tetrahedra;[80] the $[V^{V}Mo_{12}O_{40}]^{3-}$ Keggin-type polyanion with a $V^{V}O_4$ tetrahedron at the centre of the twelve surrounding MO_6 octahedra;[81] and the $[V_2Mo_{18}O_{62}]^{6-}$ anion isostructural to the conventional Dawson structure with two $V^{V}O_4$ tetrahedron at the centre of the $\{Mo_{18}\}$ cage.[82] In the case of the tungstovanadates, the anions either adopt the $[M_6O_{19}]^{n-}$ Linqvist anion or the Keggin structure with V/W ratios $\leq$ 1:2 (e.g. $[V_2W_4O_{19}]^{4-}$ ($\{M_4V_2\}$ in Figure 13), $[VW_5O_{19}]^{3-}$ and $[V^{IV}V^{V}{}_2W_{10}O_{40}]^{6-}$).[83, 84]

Extension of the previously mentioned "shrink-wrapping" approach by Cronin *et. al.* revealed two unprecedented isopolyanions with formula $[H_2VM_{17}O_{54}(VO_4)_2]^{6-}$ with M = Mo or W, where each $\{M_{17}V_3\}$ cluster anion contains two $\{V^{IV}O_4\}$ vanadate templates with one $\{V^{IV}O\}^{2+}$ vanadyl group integrated into the $\{M_{18}\}$ cluster framework (Figure 13).[85]

1.3 Hetero-Polyoxometalates

As was mentioned in *Section 1.1.3* heteropolyoxometalates are polyanions which contain the $[MO_x]$ building units and one or more *p* block elements as "heteroatoms" (Table 1). The presence of a primary heteroatom is crucial for the stabilization and completion of the polyanion structure and it is normally (but not necessarily) located in the centre of the cluster. Secondary heteroatoms may be excised from the heteropolyanion structure to leave an independently stable cluster. In heteropolyoxometalate chemistry, the concentration, charge and geometry of the heteroanions are fundamental variables that control and direct the self-assembly process of desired archetypes. For that reason, and due to the huge amount of literature containing heteropolyoxometalates, this section will be split into four main groups based on the geometry of the heteroanion involved in the formation mechanism.

Table 1: Currently known heteroatoms in heteropolyoxometalates.

B				
Al	Si	P	S	Cl
Ga	Ge	As	Se	
In	Sn	Sb	Te	I
		Bi		

1.3.1 Tetrahedral Heteroatoms

Generally, most of the polyanions templated by tetrahedral heteroanions adopt the Keggin based structure $[(XO_4)M_{12}O_{36}]^{n-}$ or a structure derived from fragments of it.[17] The quasi-spherical archetype is formed from one XO_4 tetrahedral heteroatom surrounded by twelve MO_6 octahedra. These octahedra are arranged in four $[M_3O_{13}]$ triads connected together *via* corner sharing oxygen atoms. The successive 60º rotations of each of the $[M_3O_{13}]$ triads leads to five possible isomers of the Keggin anion (Figure 14).[86]

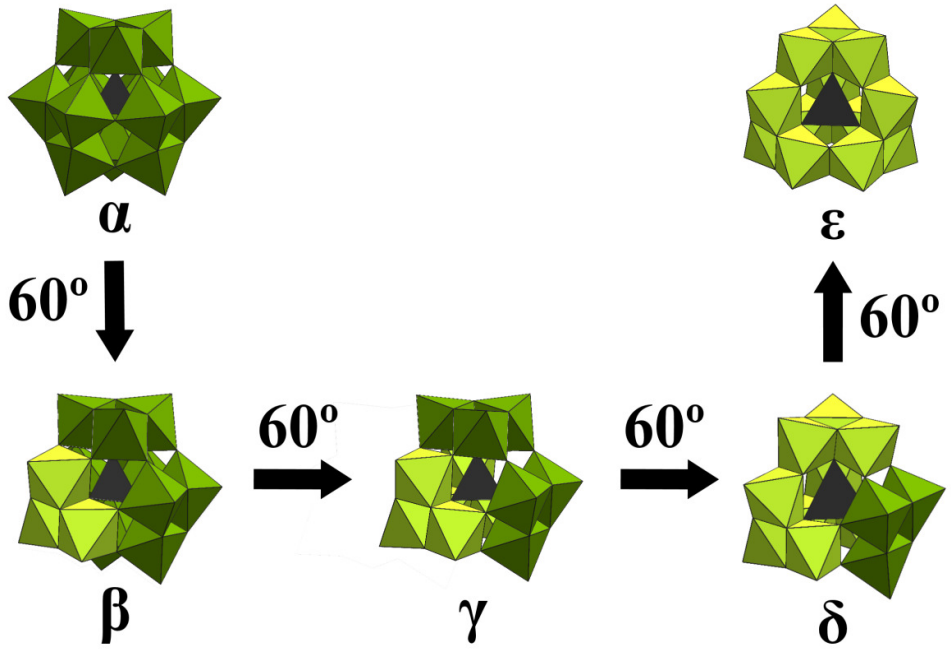

Figure 14: Isomers of the Keggin anion. The central tetrahedral heteroatom (black) is surrounded by four M_3O_{13} triads, each consisting of three edge-shared MO_6 octahedra. The five isomers are related to each other by successive 60º rotations of each of the four triads (rotated triads are represented by light green polyhedra).

The variation of the transition metal (M = W and Mo), the diversity on the heteroatom (X = B, Al, Si, Ge, P, As and S, etc.) and the five possible isomers leads to the isolation of a large number of heteropolyoxometalates with specific properties and applications.[87-91]

Furthermore, this subset of clusters has the ability to form "lacunary" derivatives by removal of one or more MO_6 octahedra from the Keggin cage when treated with base (Figure 15).[92] These lacunary polyanions can then undergo further condensation reactions and produce larger novel POMs (see *Section 1.5.1*).

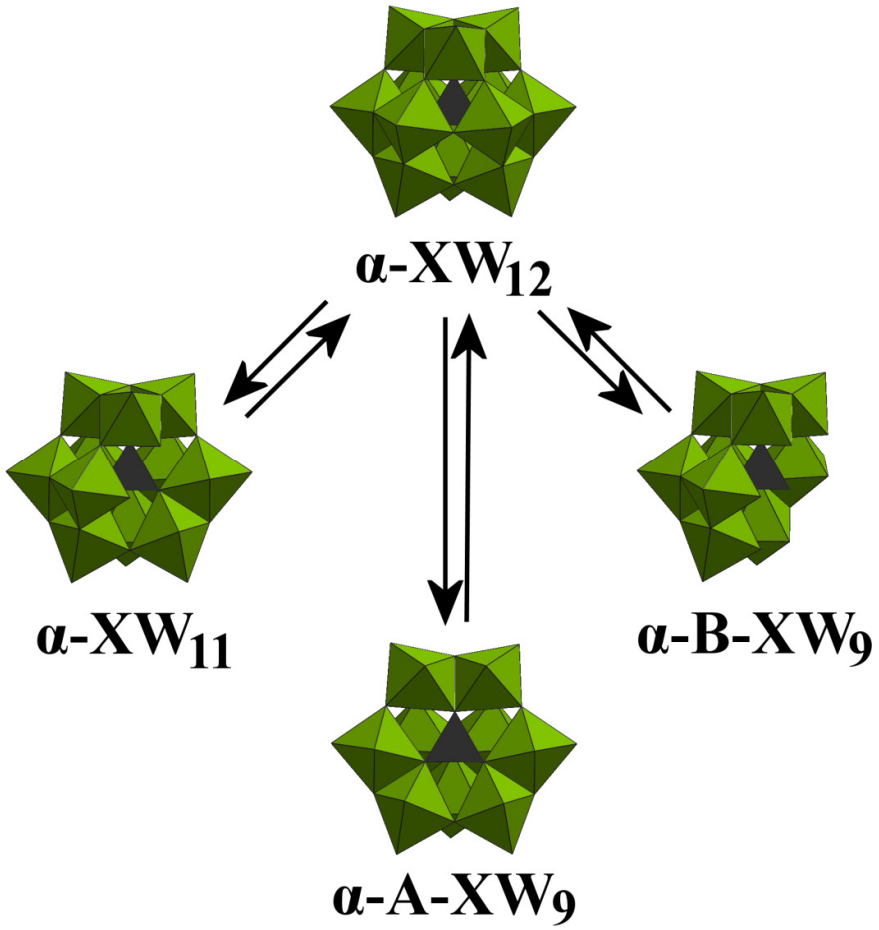

Figure 15: Lacunary structures derived from the α-$XW_{12}O_{40}$ Keggin anion by removal of on WO_6 octahedron or a trigonal group of three adjacent WO_6 octahedra. The A-type XW_9 structure derives from the loss of a corner-shared group whereas the B-type XW_9 derives from the loss of an edge-shared group. In the B-type XW_9 anion the heteroatom has an unshared terminal oxygen atom.

Besides the Keggin anion, a significant number of heteropolyoxometalates adopt the classic Wells-Dawson structure which incorporates two tetrahedral heteroanions,

$[(XO_4)_2M_{18}O_{62}]^{n-}$ (M = Mo and W, X = Cl, S, P, As, etc.).[40, 93] The anion can be described as the fusion of two identical { α-A-XM_9O_{34}} units, lacunary derivatives from the Keggin anion, joined together *via* six common oxygen atoms.[94] Each subunit consists of a central XO_4 tetrahedra surrounded by nine MO_6 octahedra linked together *via* corner- and edge-sharing binding modes. As in the case of the Keggin anion, isomers and lacunary derivatives for the Wells Dawson structure are also known (see Figure 16).[95, 96]

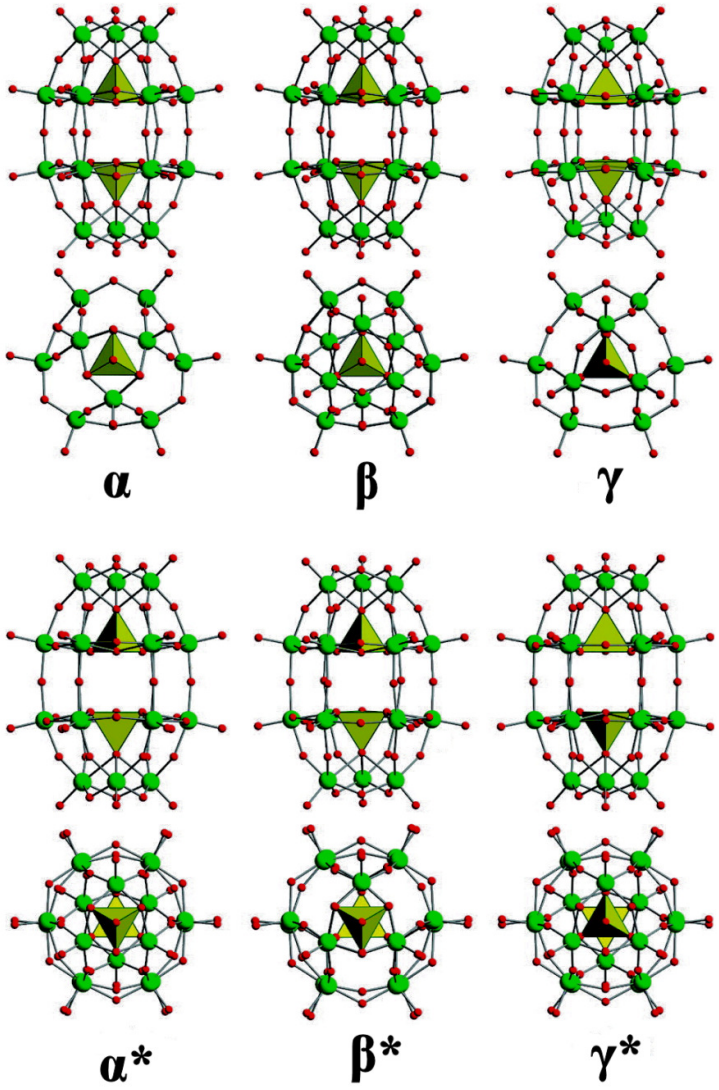

Figure 16: Schematic ball-and-stick representation of the six isomers of the Wells-Dawson $[(XO_4)_2M_{18}O_{62}]^{n-}$ anion. Rotation of one or both M_3O_{13} cap groups of the α-isomer leads to

the formation of the β- and γ-isomers respectively. α, β and γ structures encapsulate two eclipsed tetrahedral heteroanions whereas in the α*, β* and γ* structures the heteroanions are staggered (reproduced without permission).[96]

To date, there is no evidence of the existence of a pure heteropolyoxovanadate $\{XV_{12}\}$ Keggin or $\{X_2V_{18}\}$ Dawson anion; although heteropolyoxovanadates templated by tetrahedral heteroanions do exist. The first example dates from 1969 when Averbuch-Pouchot *et. al.* reported the $[As_6V_4O_{30}]^{10-}$ anion built up from a double pair of edge-sharing VO_6 octahedra linked by AsO_4 tetrahedra.[97] Further studies within heteropolyoxovanadate chemistry revealed the existence of the $[XV_{14}O_{42}]^{9-}$ (X = P and As) anion which consists of a bicapped Keggin anion (Figure 17).[98, 99] The central XO_4 tetrahedron shares its oxygen atoms with four $[V_3O_{13}]$ triads, which are joined to each other by corner-sharing. This assembly creates a slightly distorted Keggin framework, capped by two VO^{3+} subunits. This Keggin structure with the bicapped [VO] units has not been observed in molybdenum- and tungsten- cages. This might be justified by the need for the two capping VO^{3+} units to stabilize the highly charged $PV_{12}O_{40}^{15-}$ normal Keggin anion and to the ability of only vanadium to adopt square pyramidal geometry.

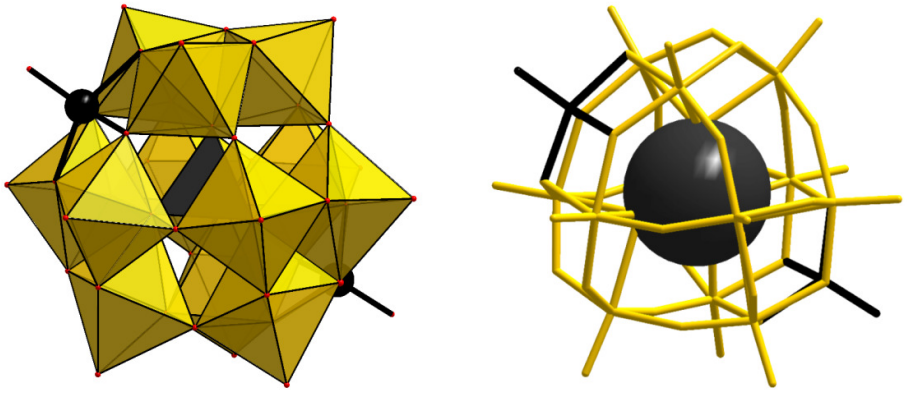

Figure 17: Polyhedral (left) and stick (right) representation of the $[XV_{14}O_{42}]^{9-}$ anion (X = P and As). The two capping VO^{3+} units are shown as black spheres and black wires whereas the twelve VO_6 octahedra which comprise the Keggin cage are shown as yellow polyhedra.

Partially substituted Keggin and Dawson anions have also been isolated and characterized, although these clusters are not easily identified crystallographically because the individual metal substitutions do not normally occupy specific positions in the cluster framework. However, the overall composition of the cluster can be calculated by the average electron density of each metal site in the X-ray structure along with elemental analysis and spectroscopy techniques.

1.3.2 Octahedral Heteroatoms

Most of the POMs templated by octahedral heteroanions adopt the well know Anderson – structure $[H_y(XO_6)M_6O_{18}]^{n-}$ where M = Mo or W.[100] The archetype is built up from a central XO_6 octahedral heteroatom surrounded by a ring of six edge-sharing MO_6 octahedra and the overall structure displays a planar arrangement as shown in Figure 18.

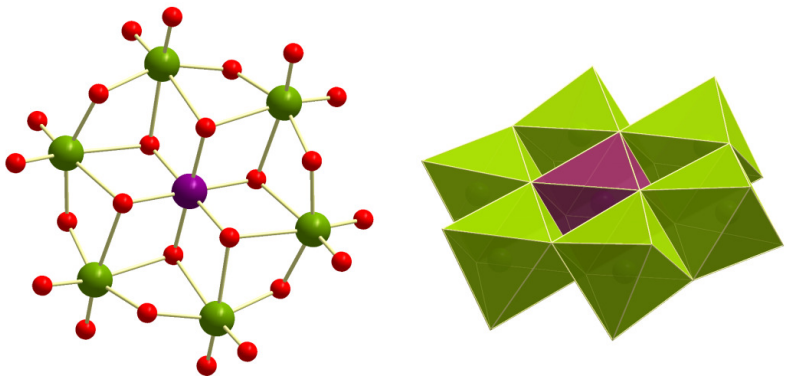

Figure 18: Ball-and-stick (left) and polyhedral (right) representations of the Anderson anion $[H_y(XO_6)M_6O_{18}]^{n-}$ where y = 0-6, n = 2-6 and 8, X = Ni, Cr, Mn, Te, I. M: green, X: purple and O: red.

Numerous examples are found in the literature of the Anderson archetype templated by octahedral heteroatoms and octahedral metal addenda in a wide range of oxidation states, for example: $[Ni^{II}(OH)_6W_6O_{18}]^{4-}$,[101] $[Cr^{III}(OH)_6Mo_6O_{18}]^{3-}$,[102] $[Mn^{IV}O_6W_6O_{18}]^{8-}$,[103] $[Te^{VI}O_6W_6O_{18}]^{6-}$[104] and $[I^{VII}O_6Mo_6O_{18}]^{5-}$.[105] The majority of Anderson species are form by

molybdenum, whereas tungsten seems to more readily adopt Keggin structures.[100, 106-112] This is perhaps a consequence of the shown prevalence molybdenum has for forming *cis* terminal dioxo groups. No vanadium-based Anderson clusters have been reported, however polyoxovanadates templated by octahedral addenda do exist. For example, the $[Ni_4V_{10}O_{30}(OH)_2(H_2O)_6]^{4-}$ anion which comprises a central Ni^{2+} tetramer, formed from four NiO_6 octahedral units, surrounded by ten VO_4 tetrahedral connected to each other *via* corner-sharing;[113] and the recently reported cyclic "sandwich" polyoxovanadates $[Mn_2V_{10}O_{30}]^{6-}$ and $[Co_2(H_2O)_2V_{10}O_{30}]^{6-}$ (Figure 19).[114] The former is built up from two V_5 rings connected together *via* bridging oxygen atoms from two MnO_6 octahedral units; whereas the latter forms one cyclic decavanadate with two CoO_6 octahedral units occupying the centre of the ring connected *via* edge sharing. In both cases all the vanadates adopt VO_4 tetrahedral geometries and are linked to each other *via* corner-sharing.

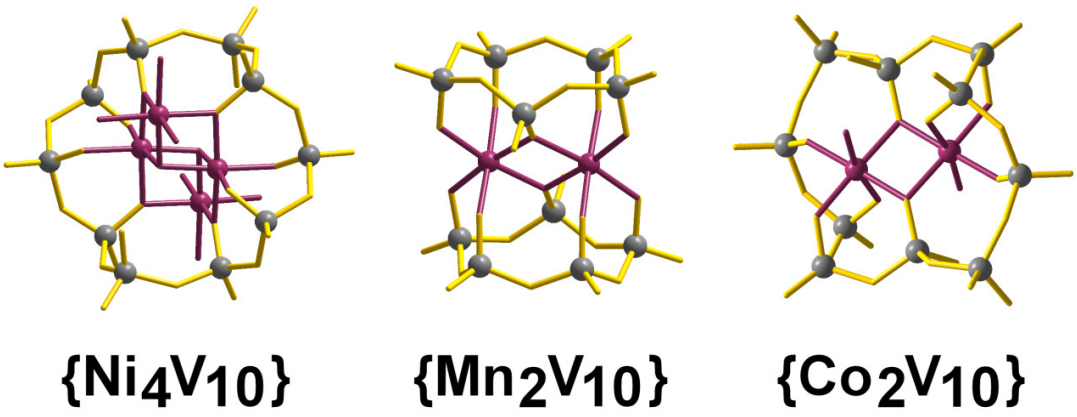

Figure 19: Ball-and-stick representation of three cyclic polyoxovanadates templated by octahedral addendas: $[Ni_4V_{10}O_{30}(OH)_2(H_2O)_6]^{4-}$ (left), $[Mn_2V_{10}O_{30}]^{6-}$ (middle) and $[Co_2(H_2O)_2V_{10}O_{30}]^{6-}$ (right). The XO_6 octahedra are represented by purple spheres and the VO_4 tetrahedral by grey spheres. Oxygen atoms have been omitted for clarity.

Over the last couple of years, the need to gain control and better understand the self-assembly process of the different metal oxide units has led to the development of new synthetic routes to isolate novel materials. The use of high-resolution mass spectrometry techniques has proven to be crucial for the isolation of two novel Dawson-type shells templated by one heteroatom: $[H_3W_{18}O_{56}(Te^{VI}O_6)]^{7-}$ and $[H_3W_{18}O_{56}(I^{VII}O_6)]^{6-}$ (Figure

20).[36, 115] Both clusters differ from the conventional Dawson archetype due to the encapsulation of one XO_6 octahedral heteroatom, which occupies the centre of the cage and the two additional interior oxygen positions each bridge one of the capping $\{W_3\}$ groups of the clusters. These features affect the overall structure of the clusters, leading to two different conformations: for the tellurate based cage the anion adopts a γ*-configuration whereas for the iodate based cage it has a β*-configuration.

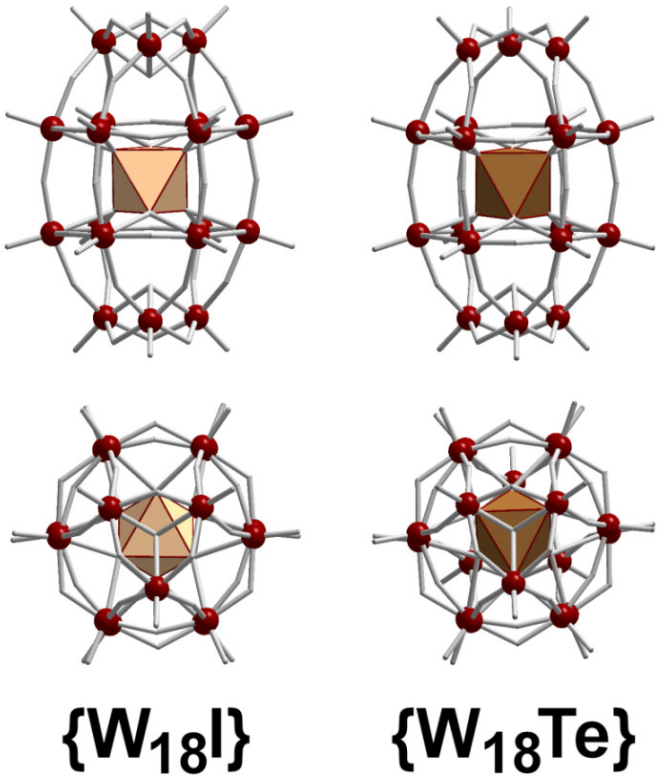

Figure 20: Polyhedral representations of the two Dawson-like $\{W_{18}O_{54}\}$ cages templated by XO_6 moieties: $I^{VII}O_6$ (left) and $Te^{VI}O_6$ (right) viewed from the side (top) and above (bottom). The heteroatoms are represented by octahedral polyhedra occupying the centre of the shells, the W atoms are shown as dark brown spheres and O atoms have been omitted for clarity.

1.3.3 Higher Coordinated Heteroatoms

Although this sub-class of POMs remains unexplored, in comparison with their tetrahedral and octahedral analogues, interest into this area has grown rapidly over recent years. Lanthanide ions and their complexes exhibit unique spectroscopic, electrochemical, and magnetic properties, and have wide potential applications.[116, 117] It is therefore expected that POM containing lanthanides as the central heteroatom will display interesting properties and have potential applications as, for example, catalysts for alcohol and alkene oxidations with H_2O_2 as a co-oxidant.[118]

A series of heteropolyoxomolybdates with general formula $[XMo_{12}O_{42}]^{8-}$ ($X = Ce^{4+}$, Th^{4+}, U^{4+})[119, 120] and $[XMo_{12}O_{42}]^{9-}$ ($X = Gd^{3+}$)[121] has been reported and fully characterized (Figure 21b). The respective anions are built up from six Mo_2O_9 units formed by two face-sharing octahedra. The Mo_2O_9 units share corners with each of the four adjacent Mo_2O_9 units and the 12 – coordinated heteroatom is at the centre of the two, six Mo_2O_9 units. Equally, the first heteropolyoxotungstate containing lanthanides as the heteroatom was the $[Ce^{IV}W_{10}O_{36}]^{8-}$ anion where the 8 – coordinated Ce^{4+} atom is at the centre of two pentatungstate ligands W_5O_{18}, each of which is derived from the $W_6O_{19}^{2-}$ anion (Figure 21a).[122]

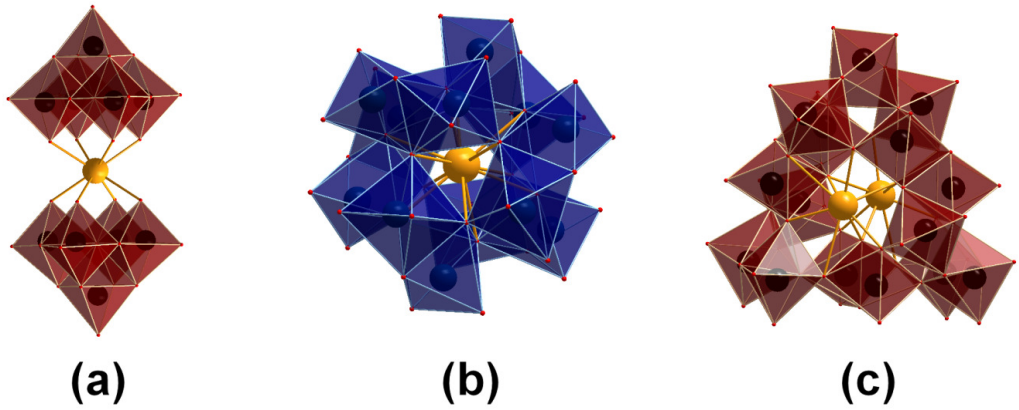

Figure 21: Polyhedral representation of polyoxoanions containing high coordinated heteroatoms. (a) $[Ce^{IV}W_{10}O_{36}]^{8-}$ with an eight coordinated Ce^{4+} atom, (b) $[CeMo_{12}O_{42}]^{8-}$

with a twelve coordinated Ce^{4+} atom and (c) $[H_6Ce_2(H_2O)Cl(W_5O_{18})_3]^{7-}$ with two nine coordinated Ce^{3+} atom. W: black spheres, Mo: blue spheres, X: orange sphere and O: red sphere.

Although most of the examples of POMs templated by lanthanides consist of two heteropolyanions acting as a penta- or hexa- ligands connected through a central lanthanide in 8- or 12- coordination mode, other examples exhibiting different bridging modes are found in the literature: The dinuclear 9-coordinated Ce^{3+} heteropolytungstate $[H_6Ce_2(H_2O)Cl(W_5O_{18})_3]^{7-}$ which is a novel Ln-POM cluster where the two Ce^{3+} cations are located at the centre of the cluster (Figure 21c);[123] and the dimer formed from condensation of two ZrW_5 monomers linked through two hydroxo bridges (Zr – OH – Zr) with the Zr atoms in sevenfold coordination, $[\{W_5O_{18}Zr(\mu\text{-}OH)\}_2]^{6-}$.[124]

1.3.4 Pyramidal Heteroatoms

The first crystal structure of a POM templated by a pyramidal heteroatom dates from 1976 when Sasaki and co-workers reported the ammonium salt of the pentamolybdodisulfate anion $[S^{IV}_2Mo_5O_{21}]^{4-}$, which was built up from a pentagonal Mo_5O_{21} ring capped by two SO_3^{2-} heteroanions.[125] Since then, some other examples of cyclic heteropolyanions with XO_3^{2-} heteroanions can be found in the literature such as the selenite analogue $[Mo_5O_{15}(SeO_3)_2]^{4-}$,[126] the $[Mo_4O_{13}(XO_3)]^{4-}$ anion with one capping XO_3 heteroanion (X = S^{IV} and Se^{IV});[126, 127] or the $[Se^{IV}S^{VI}_3Mo_6O_{33}]^{8-}$ with a pyramidal SeO_3 group in the centre of a six MoO_6 ring.[128]

Pyramidal heteroanions (XO_3) consist of a central atom connected to three oxygen atoms which define the base of the trigonal pyramid. The fourth vertex of the pyramid, which would be occupied by a fourth oxygen atom in the tetragonal analogue, is now occupied by a lone pair of electrons (Figure 22 top). Heteroatoms that can adopt such geometry are mainly the elements from group 15 in oxidation state +3 (As, Sb and Bi) and from group 16 in oxidation state +4 (S, Se and Te). It is to be expected that POMs templated by

heteroatoms with lone pair of electrons adopt unprecedented architectures to accommodate the unpaired electrons. Although this subclass of heteropolyoxometalates remains unexplored in contrast with the tetrahedral analogues, the interest in these materials has increased considerably over the last decades, not only due to the particular archetypes they exhibit, but the interesting properties that they display.

The most studied example so far is the well-known anion $[Mo_{18}O_{54}(SO_3)_2]^{4-}$ which exhibits the distinctive peanut-like shape of the $\{Mo_{18}O_{54}\}$ framework (Figure 22),[127, 129, 130] also found for the $\{W_{18}O_{54}\}$ cages in the Dawson – type compounds $[W_{18}O_{54}(O)(OH)_2(XO_3)]^{7-}$ ($X = As^{III}$ and Sb^{III}),[131, 132] $[W_{18}O_{54}(OH)_3(BiO_3)]^{6-}$,[133] $[H_3Sn^{II}W_{18}O_{60}]^{7-}$[134] and $[H_3W_{18}O_{57}(TeO_3)]^{5-}$.[36] This subset of compounds is built up from two equivalent M_9O_{33} half units linked together by six shared oxygen atoms. Whereas in the case of the tungstate-based Dawson-type compounds the cage is templated by one pyramidal heteroatom which is disordered over the two M_9O_{33} half units; the molybdenum-based Dawson archetype is templated by two sulfite heteroanions, one in each of the M_9O_{33} half units. This fact can be attributed to size restrictions as the SO_3^{2-} anion is smaller than the AsO_3^{3-}, SbO_3^{3-} and BiO_3^{3-}.

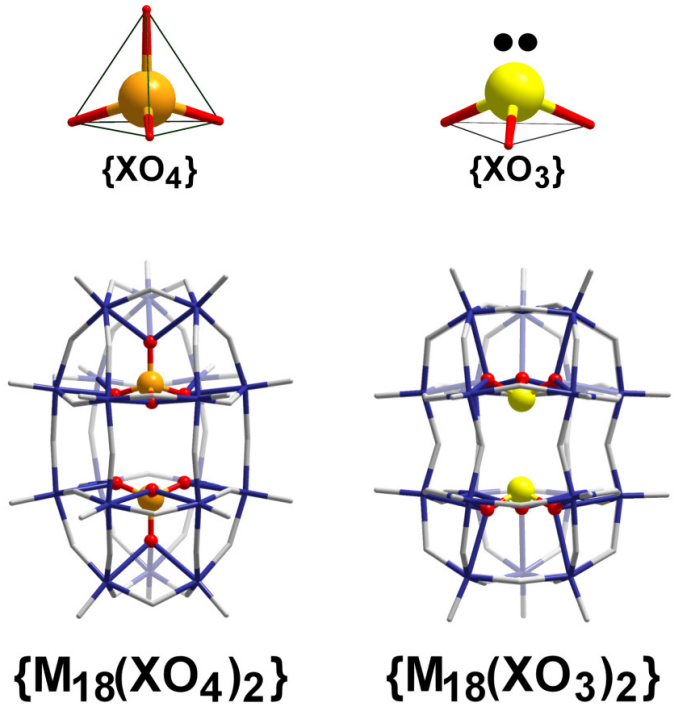

Figure 22: Comparison between the Wells-Dawson $\{M_{18}(XO_4)_2\}$ templated by two tetrahedral heteroanions and the peanut-like Dawson $\{M_{18}(XO_3)_2\}$. In the case of the XO_4 heteroanion, one oxygen coordinates to the three capping metal centres and the remaining three μ_3-oxo ligands each coordinate to two metal centres from the belt; whereas each oxygen atom from the XO_3 heteroanion bridges three metal centres. M: blue sticks, O from the cage: grey sticks.

An interesting feature of the $[Mo_{18}O_{54}(SO_3)_2]^{4-}$ anion is its thermochromic behaviour, the tetrabutylammonium salts change colour from pale green at 77 K to dark red at 500 K. The short non-bonding intramolecular S···S interaction between the two sulfite anions suggests the possibility to form a dithionate $S_2O_6^{2-}$ anion which could supply electrons to reduce the $\{Mo_{18}\}$ cage.[135] This feature was revealed in the tungstate analogue $[W_{18}O_{56}(SO_3)_2(H_2O)_2]^{8-}$ anion "*Trojan Horse*" when upon heating the cluster undergoes a structural re-arrangement where the two sulfite anions release up to four electrons to the surface of the cluster generating the sulfate-based, deep blue, mixed-valence cluster $[W_{18}O_{54}(SO_4)_2]^{8-}$.[136]

Equally, these heteroanions can be incorporated into the inorganic framework where they act as a ligand. The incorporation of the sulfite anion in $[(Mo^{V}_{2}O_4)_6(\mu_2\text{-}SO_3)_{12}(\mu_3\text{-}SO_3)_4]^{20-}$ results in an unprecedented archetype where the six binuclear units $[Mo^{V}_{2}O_4]^{2+}$ are connected to each other by sixteen sulfite heteroanions with different coordination modes (Figure 23 left).[137] In the case of polyoxotungstates it has been observed that by employing XO_3^{2-} as a heteroatom and linker, high nuclearity POMs can be isolated such as $[H_2W_{43}Se_3O_{148}]^{24-}$, $[W_{28}Te_8O_{112}]^{24-}$ (Figure 23 middle) or the gigantic nanosize cluster $[(H_8W_{100}Se_{16}O_{364})WO(H_2O)_2]^{52-}$.[138, 139]

Polyoxovanadates incorporating pyramidal heteroanions are limited. In 1987 Sasaki *et. al.* reported the $[Se_4V_{10}O_{37}]^{8-}$ anion which consists of a *B*-SeV_9 type derivative form of the Keggin structure to which three suspended SeO_3 trigonal pyramids and one capping trigonal bipyramid are attached.[140] Although this is so far the only example where a heteropolyvandate anion is templated by a central pyramidal heteroanion, other examples of polyoxovanadates incorporating heteroatoms with unshared pair of electrons do exist. For example the $[As^{III}_{8}V^{IV}_{14}O_{42}(H_2O)]^{4-}$ anion with four handle-like As_2O_5 moieties stabilizing the ball-like structure of condensed VO_5 square pyramids;[141] or the vanadium – sulfite $[(V^{IV}O)_6(\mu_4\text{-}O)_2(\mu_2\text{-}OH)_2(\mu_3\text{-}SO_3)_4(H_2O)_2]^{2-}$ anion where the μ_3-SO_3 moieties are coordinated to the $\{V^{IV}_{4}O_2(OH)_2\}$ core along with two square pyramid VO_5 units (Figure 23 right).[142]

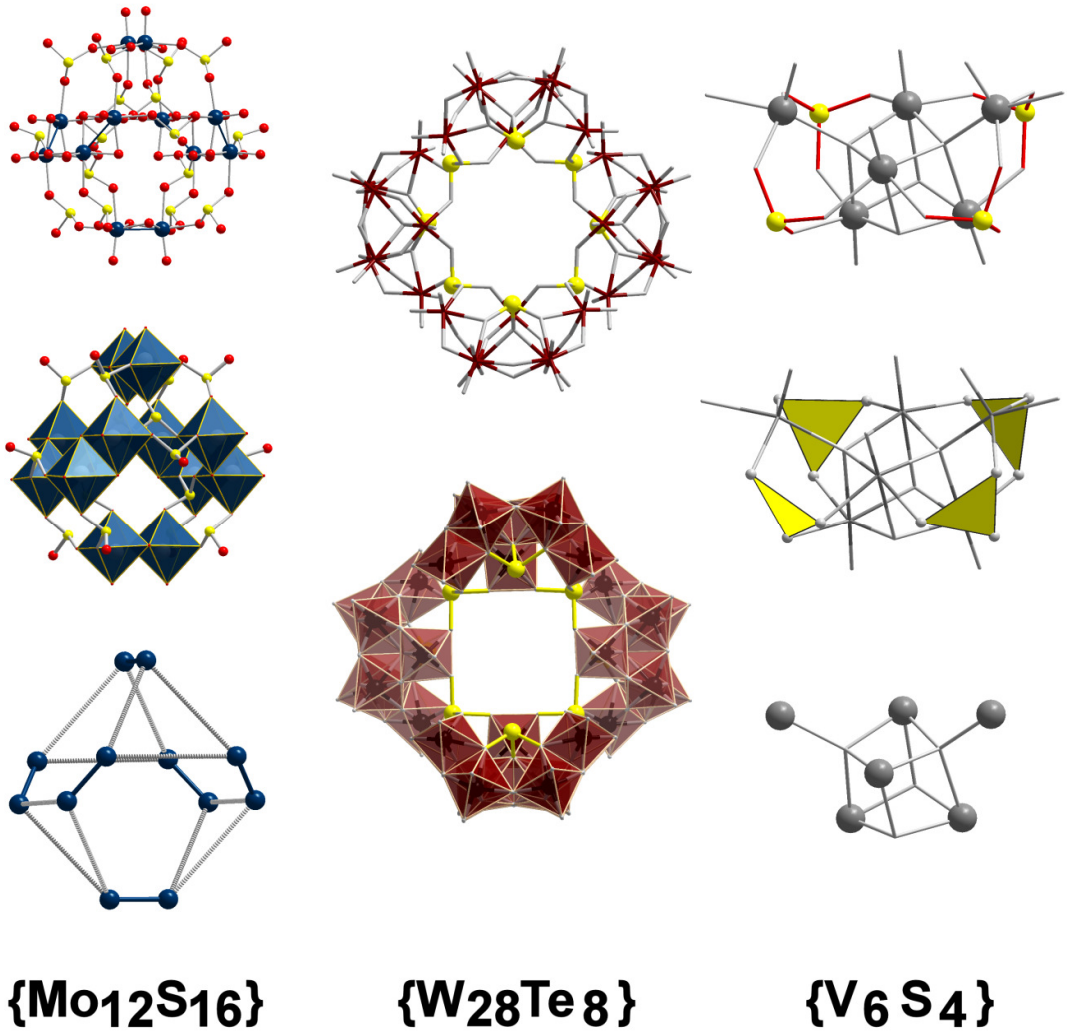

Figure 23: Ball-and-stick and polyhedral representations of three different polyoxometalates templated by pyramidal heteroanions: the $\{Mo_{12}S_{16}\} = [(Mo^{V}{}_2O_4)_6(\mu_2\text{-}SO_3)_{12}(\mu_3\text{-}SO_3)_4]^{20-}$ (left), where the arrangement of the twelve molybdenum atoms is similar to the ε-Keggin isomer except that in this case the anion contains six separated $\{Mo_2O_{10}\}$ moieties (blue bonds), connected to each other *via* $\mu_2\text{-}SO_3^{2-}$ and $\mu_3\text{-}SO_3^{2-}$ anions; the $\{W_{28}Te_8\} = [W_{28}Te_8O_{112}]^{24-}$ (middle), where the macrocyclic polyoxotungstate anion, built up from four $\{W_7(TeO_3)\}$ fragments connected to one another *via* $\{TeO_4\}$ linkers, displays a square saddle-like archetype; and the $\{V_6S_4\} = [(V^{IV}O)_6(\mu_4\text{-}O)_2(\mu_2\text{-}OH)_2(\mu_3\text{-}SO_3)_4(H_2O)_2]^{2-}$ (right), which exhibits a unique structural motif with a central cubic $\{V^{IV}{}_4O_2(OH)_2\}$ fragment connected to two $V^{IV}O_5$ square pyramid ions *via* $\mu_3\text{-}SO_3^{2-}$ anions. Mo: blue, W: brown, V: dark grey, S/Te: yellow, O: red.

1.4 Molybdenum Blues and Browns

Upon reduction of an acidified aqueous solution of molybdates a plethora of well-defined linkable building blocks exists, which can be connected under suitable conditions to form a wide variety of sophisticated nanostructures. This subclass of POMs, which precipitate from characteristic blue or brown solutions due to the amount of reduced molybdenum metal centres, was first reported by Scheele in 1778 as an amorphous blue material. It was not until 1995 when Müller *et.al.* synthesised and structurally characterized the high nuclearity wheel – shaped cluster $\{Mo_{154}\}$ (Figure 24) that the mystery of the molybdenum blue solutions was solved.[41, 143] Further studies within this area revealed that by slightly changing the reaction conditions a "giant-wheel" cluster could also be isolated $\{Mo_{176}\}$.[144]

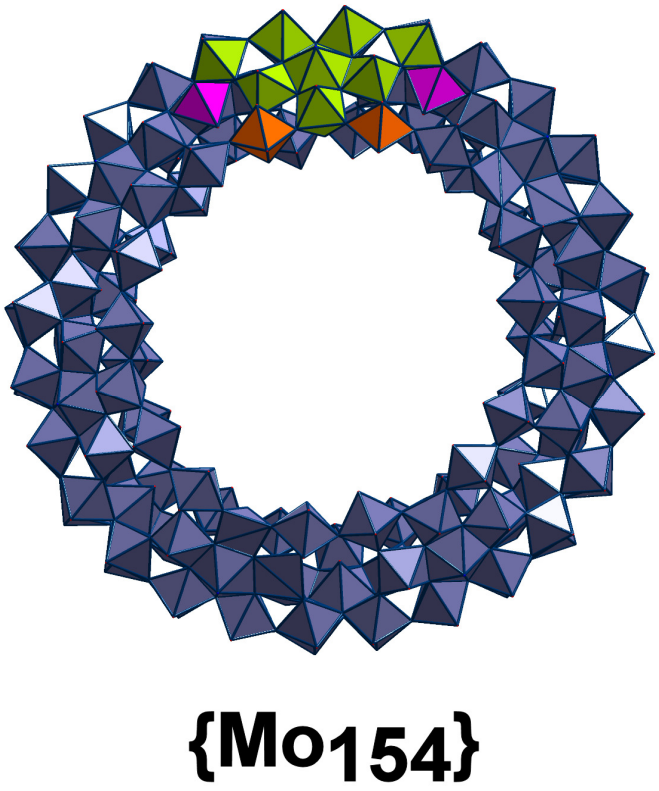

Figure 24: Polyhedral representation of the "giant-wheel" type $\{Mo_{154}\}$ with its structural building blocks: the $\{Mo_8\}$ units (green polyhedra) which are connected *via* the $\{Mo_2\}$

units (orange polyhedra) on the inner side of the wheel, and the {Mo_1} units (pink polyhedra) which link together the {Mo_8} moieties above and below the equatorial plane.

Both mixed-valence polyoxomolybdates, {Mo_{154}} and {Mo_{176}}, are built up from {Mo_{11}}$_n$ ≡ {(Mo)Mo_5Mo_5}$_n$ fragments (n = 14 and 16 respectively) which consists of three types of building units: (1) the {Mo_8}-type group, which contains a central pentagonal-bipyramidal Mo(NO)O_6 or MoO_7 around which five MoO_6 octahedral are grouped by equatorial edge-sharing, creating an {(Mo)Mo_5} fragment onto which two extra MoO_6 octahedra are attached through shared vertices; (2) the {Mo_2} group formed by two corner-sharing MoO_6 octahedra and (3) the {Mo_1} unit.[145]

By controlling pH and reduction, these new clusters with nanometre-sized cavities can be transformed into different ring-shaped clusters by generating defects and can also be derivatized to larger archetypes. By using elemental iron instead of $NH_2OH{\cdot}HCl$ as a reducing agent, five {Mo_2} units from the {Mo_{154}} cluster are missing giving rise to the formation of the ellipsoidal {Mo_{144}} cluster.[146] On the other hand, by using stronger reducing conditions, the {Mo_{176}} cluster undergoes a molecular growth process where two {Mo_{36}} clusters cover the cavity of the wheel-shaped cluster like "hubcaps", leading to the formation of the {Mo_{248}} cluster (Figure 25).[147]

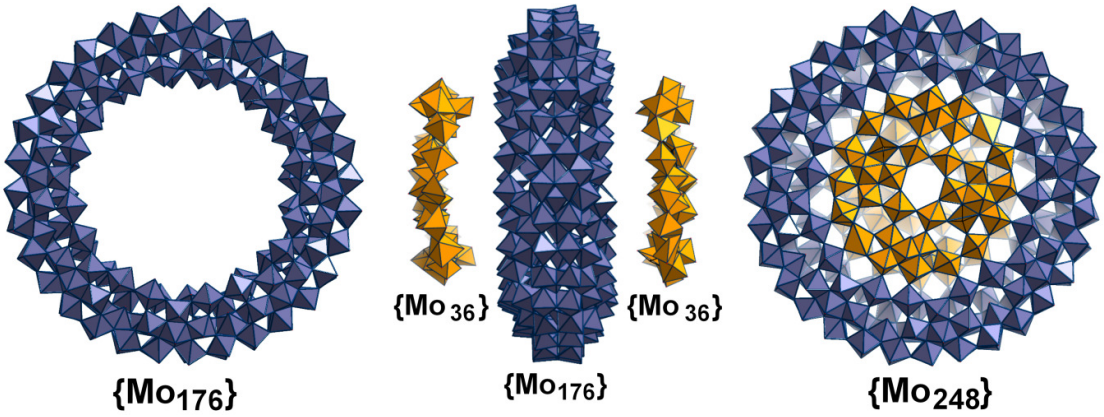

Figure 25: Representation of the addition of the two {Mo_{36}} "hubcaps" to the inner surface of the {Mo_{176}} "giant wheel" leading to the formation of the {Mo_{248}} cluster. The {Mo_{176}} acts as a compartment for the aggregation of the two additional {Mo_{36}} building

units, which are not stable on their own, to form the {Mo_{248}} cluster (reproduced without permission).

Another representative feature of the *Molybdenum – Blues* is the formation of Keplerate balls, giant molecular spheres with an integrated icosahedron. The first reported Keplerate was the {Mo_{132}} ball which is built up from 12 {Mo_{11}} fragments (Figure 26).[148] Each of the 12 {(Mo)Mo_5} groups is linked by 30 {Mo_2^{V}} units. The substitution of the {Mo_2^{V}} spacers by other linker groups such as the aqua-ligand-Fe^{III} polyhedra or VO^{2+} groups results in the formation of Keplerate spheres with different sizes and properties.[149]

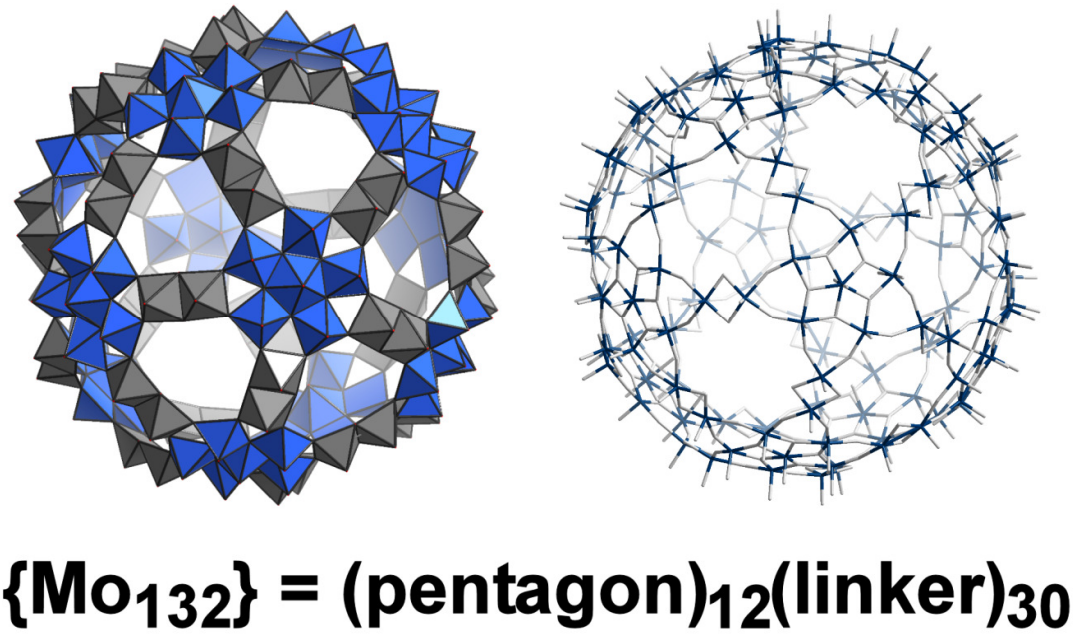

Figure 26: Polyhedral (left) and wire frame (right) representation of the highly symmetric Keplerate ball {Mo_{132}}. The inorganic cage comprises 12 pentagonal {(Mo)Mo_5} groups (blue polyhedra) connected by 30 {Mo^{V}_2} groups (dark grey polyhedra) acting as a linkers.

Along these investigation lines, Müller and co-workers reported the largest purely inorganic cluster known to date, built up from a {Mo_{288}} ball capped by two {Mo_{40}} units.

The lemon-shaped cluster {Mo_{368}} is obtained from a special type of molybdenum blue solution where only H_2SO_4 is used to control the pH of the reaction. This fact is related to the stability that the SO_4^{2-} ligands provide to the intermediates and the final cluster; whereas the presence of weaker coordinating ligands such as Cl^- or ClO_4^- ions leads to the formation of the wheel-shaped {Mo_{154}} or {Mo_{176}} instead.[150]

1.5 Synthetic Strategies

1.5.1 Metal Complexes of Lacunary Clusters

A widely used approach used to synthesise novel polyoxoanions has been the interaction of lacunary heteropolyanion precursors with transition metal and/or lanthanide ions. This synthetic approach involves the production of highly negatively charged (and therefore soluble) intermediate units, which can then be stabilised by electrophilic groups or joined together in polycondensation reactions (Figure 27).[151-154]

Of particular interest are the polyoxoanions containing heteroatoms with a lone pair of electrons such as As^{III}, Sb^{III}, Bi^{III}, Se^{IV} and Te^{IV}. The unshared pair of electrons prevents the formation of the closed Keggin heteroanion leading to the formation of polymeric polyoxoanions. For example, the reaction of Na_2WO_4 and Sb_2O_3 in aqueous solution at pH 7.5 leads to the formation of the trivacant Keggin anion $[SbW_9O_{33}]^{9-}$. Due to its charge, the $[SbW_9O_{33}]^{9-}$ can either be stabilised by cations or undergo further condensation processes upon protonation to give larger inorganic clusters such as the $[Na_2Sb_8W_{36}O_{132}(H_2O)_4]^{22-}$ anion which combines four $[SbW_9O_{33}]^{9-}$ subunits with Na^+ and Sb^{3+} cations between them. Furthermore, the addition of extra electrophilic groups into the reaction mixture of WO_4^{2-} and/or M^{n+} (M = Fe^{3+}, Co^{2+}, Mn^{2+}, Ni^{2+}), leads to novel heteroanions with general formula $[Sb_2W_{20}M_2O_{70}(H_2O)_6]^{(14-2n)-}$ where two $[SbW_9O_{33}]^{9-}$ subunits are connected to each other by two $M^{n+}(H_2O)$ and two WO_2OH groups.[155] Further examples of dimeric polyanions

built up from two $\{XMo_9O_{33}\}^{n-}$ (X = As^{III}, Sb^{III}, Bi^{III}, Se^{IV} and Te^{IV}) lacunary building units can be found in the literature with analogous archetypes.[156-158]

Alternatively, POMs containing high nuclearity lanthanide atoms have also been investigated. Due to their multiple coordination requirements and oxophilicity, lanthanide cations are suitable for linking POMs together to form new materials with extended metal-oxygen frameworks. For example, the addition of stoichiometric quantities of tungstate, arsenite and cerium in acidified aqueous solution leads to the isolation of the largest heteropolytungstate anion, containing a cyclic $[As_{12}Ce_{16}(H_2O)_{36}W_{148}O_{524}]^{76-}$ anion,[159] whereas the addition of Gd^{3+} and Yb^{3+} yield the $[Gd_6As_6W_{65}O_{229}(OH)_4(H_2O)_{12}(OAc)_2]^{38-}$ and $[Yb_{10}As_{10}W_{88}O_{308}(OH)_8(H_2O)_{28}(OAc)_4]^{40-}$ polyoxoanions respectively.[160]

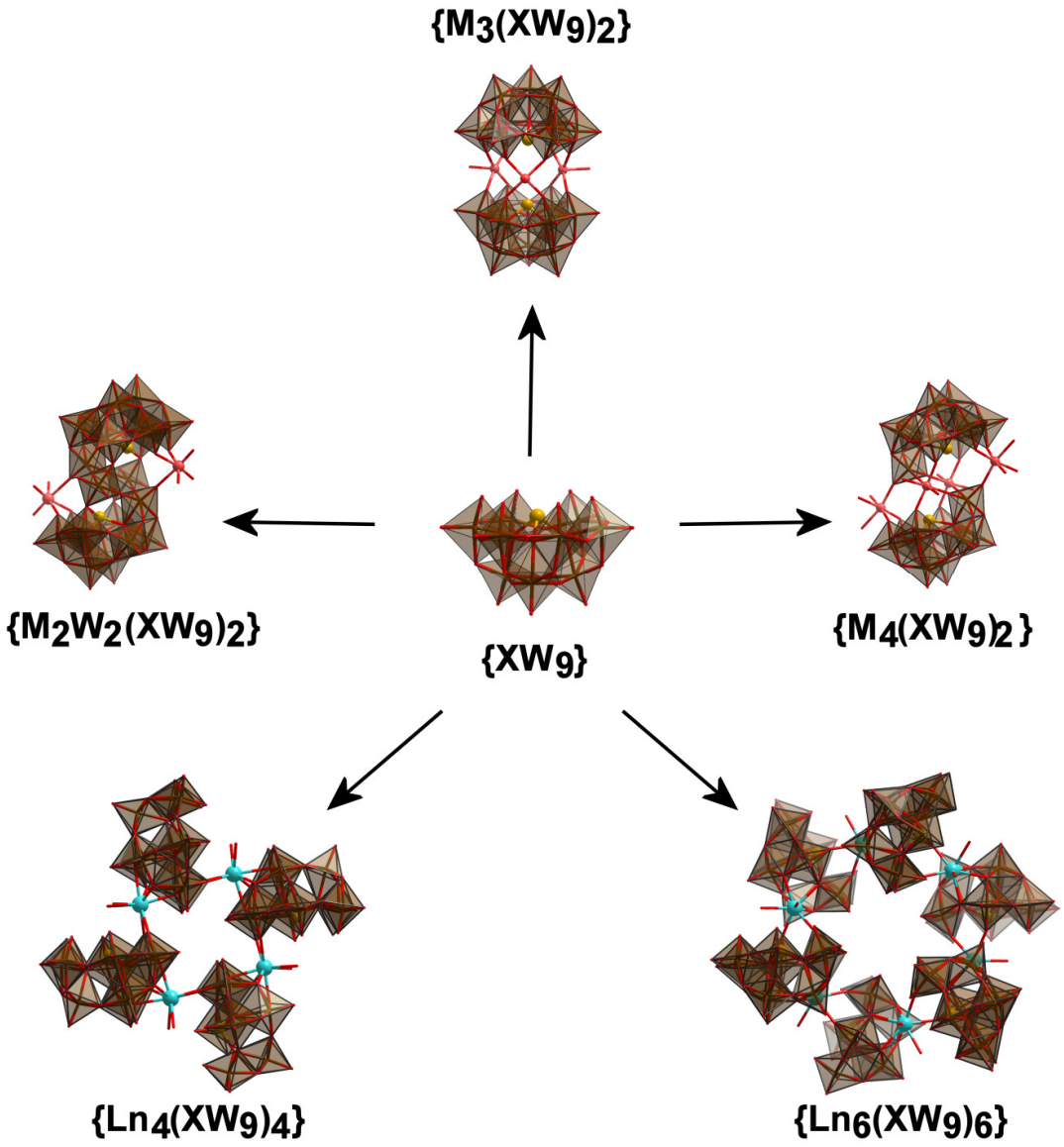

Figure 27: Summary of the different heteropolyanions obtained upon reaction of the trivacant lacunary precursor $\{XW_9\}$ with different transition metal ions and lanthanides. The interaction of the lacunary $\{XW_9\}$ Keggin anion with transition metals leads to the formation of sandwich type polyanions such as $\{M_2W_2(XW_9)_2\}$, $\{M_3(XW_9)_2\}$ and $\{M_4(XW_9)_2\}$ where the two $\{XW_9\}$ fragments are linked together *via* two, three or four metal atoms.[155-157] Whereas the incorporation of lanthanide (Ln) ions into the system leads to larger polyoxoanions such as the crown-shaped ring structures $\{Ln_4(XW_9)_4\}$ and $\{Ln_6(XW_9)_6\}$.[161] W: brown, M: pink, X: light brown, Ln: cyan and O: red.

1.5.2 Thiometalates

The incorporation of sulphur into the polyoxoanionic frameworks results in the isolation of unusual POM archetypes, called thiometalates, which display unique electronic and chemical properties. Although the first thiometalate was isolated by sulfurization of a preformed Keggin unit, nowadays the synthetic strategies for the production of such materials are based on the self-condensation of $[M_2S_2O_2]^{2+}$ units with or without the presence of guest species.[162]

The acid-base self-condensation of the $[M_2S_2O_2]^{2+}$ building units leads to the formation of cyclic molecules such as $[Mo_{10}S_{10}O_{10}(OH)_{10}(H_2O)_{10}]$ and $[Mo_{12}S_{12}O_{12}(OH)_{12}(H_2O)_6]$ (Figure 28 left).[163] These clusters have a cationic cavity which can be filled with anionic molecules such as phosphates or carboxylates (Figure 28 right). It has been demonstrated that these species can be used as templates to control the nuclearity of the inorganic host.[164] For example, the use of different dicarboxylate anions leads to compounds with the same type of topology derived from the neutral $\{Mo_{2n}S_{2n}O_{2n}(OH)_{2n}\}$ backbone but with different nuclearities.[165] Additionally, the use of tetrahedral templates as in the case of conventional POMs has also an effect on the final archetype. The condensation of $[M_2S_2O_2]^{2+}$ units in solution with high phosphate concentrations leads to the formation of $[(HPO_4)_4Mo_6S_6O_6(OH)_3]^{5-}$ anions, whereas if the concentration is lower the diphosphato $[(HPO_4)_2Mo_{12}S_{12}O_{12}(OH)_{12}(H_2O)_2]^{4-}$ ion is formed.[166, 167]

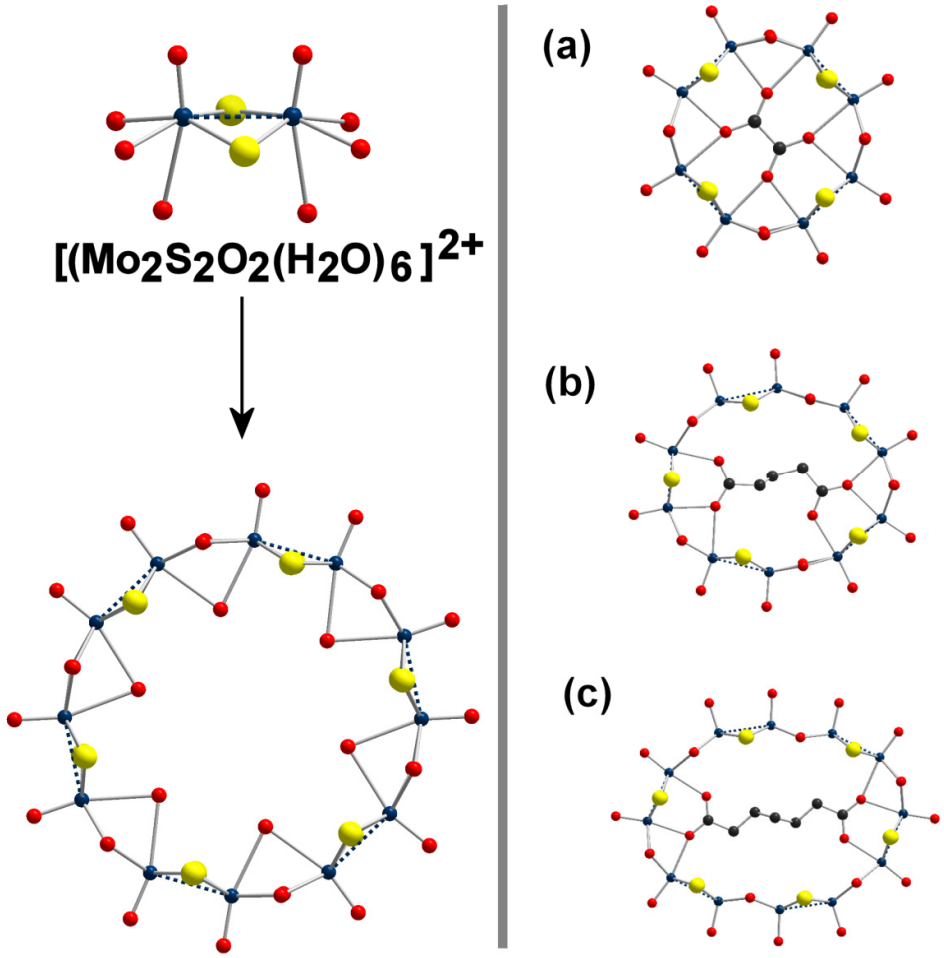

Figure 28: Ball-and-stick representation for the self-assembly of the $[Mo_{12}S_{12}O_{12}(OH)_{12}(H_2O)_6]$ wheel (left) from the $[(Mo_2S_2O_2(H_2O)_6]^{2+}$ building unit.[163] Polycarboxylate-containing rings (right): (a) $[Mo_8S_8O_8(OH)_8(C_2O_4)]^{2-}$, (b) $[Mo_{10}S_{10}O_{10}(OH)_{10}(H_6C_5O_4)]^{2-}$ and (c) $[Mo_{12}S_{12}O_{12}(OH)_{12}(H_{10}C_7O_4)]^{2-}$.[165] Mo: blue, S: yellow, O; red and C: dark grey.

Alternatively, the reaction of the $[M_2S_2O_2]^{2+}$ units with mono- or trivacant polyoxoanions leads to sandwich clusters where the lacunary polyanions are bridged by different thiocation fragments. Such as the $[(PW_{11}O_{39})_2(H_4Mo_4S_4O_6)]^{10-}$ anion with two $[PW_{11}O_{39}]^{7-}$ subunits and a central $\{H_4Mo_4S_4O_6\}$ core;[168] or the $[(H_2P_2W_{15}O_{56})_4\{Mo_2O_2S_2(H_2O)\}_4\{Mo_4S_4O_4(OH)_2(H_2O)\}_2]^{28-}$ anion with two formal dimers formed from two $[P_2W_{15}O_{56}]^{12-}$ units connected to two $\{Mo_2S_2O_2(H_2O)_2\}^{2+}$ ions, connected all together by two tetranuclear $\{Mo_4S_4O_4(OH)_2(H_2O)\}^{2+}$ moieties (Figure 29).[169]

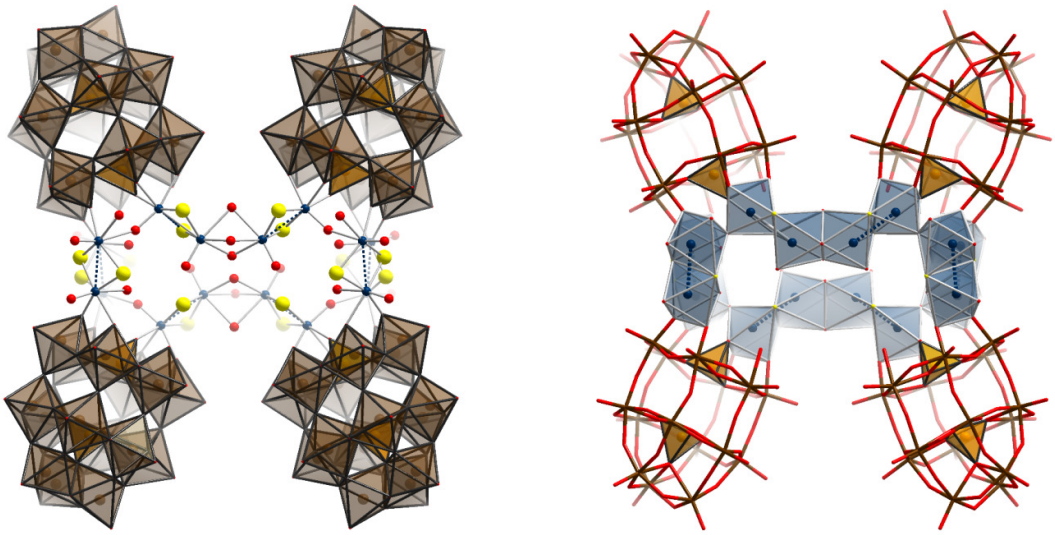

Figure 29: Polyhedral and ball-and-stick representations of the Dawson thio derivative $[(H_2P_2W_{15}O_{56})_4\{Mo_2O_2S_2(H_2O)\}_4\{Mo_4S_4O_4(OH)_2(H_2O)\}_2]^{28-}$ anion. W: brown, P: orange, Mo: blue, S: yellow and O: red.

1.5.3 Hybrid Organic - Inorganic Polyoxometalate Architectures

The functionalization of polyoxometalate cages by formal replacement of either terminal or bridging oxo groups by other ligands like nitride-, imido- and alkoxo groups yields the formation of POM-based inorganic/organic hybrids.[170-172] Such materials are of great importance not only from a structural point of view but for the interesting redox, magnetic and electrical properties that they exhibit.[173-175]

Several strategies have been considered to modify POMs, although originally they were mainly focused on the ionic or non-covalent interaction between the inorganic cluster and the organic ligands; covalent POM-based hybrids have been developed readily over the last decade.[176, 177] The covalent interaction between the POM and the organic moiety improves the stability of the hybrid, allows tuning of the redox and acid properties, and solubility of the primary POM, and in some cases the organic component may direct the formation of frameworks and networks.[178-180]

One well-known example is the functionalization of the Mn-Anderson anion (Figure 30). The cluster can be derivatized by using three pendant hydroxyl groups that can replace the hydroxide groups on both sides of cluster leading to symmetrical and/or asymmetrical architectures, e.g. the reaction of tris(hydroxylmethyl)aminomethane ($C_4H_6O_3H_3NH_2$ = H_3L1) and tris(hydroxylmethyl)nitromethane ($C_4H_6O_3H_3$-NO_2 = H_3L2) with $[TBA]_4[Mo_8O_{26}]$ and $Mn(CH_3COO)_3$ in MeCN leads to the isolation of $[MnMo_6O_{18}(L1)_2]^{3-}$, $[MnMo_6O_{18}(L1)(L2)]^{3-}$ and $[MnMo_6O_{18}(L2)_2]^{3-}$ with TBA as the cation.[181]

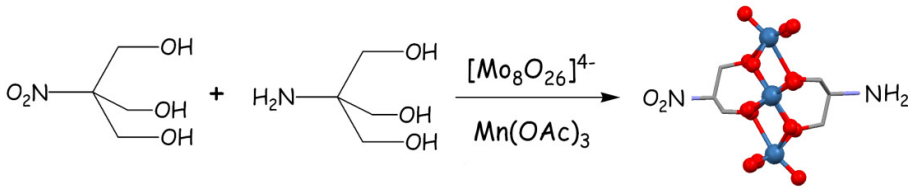

Figure 30: Synthetic scheme for the formation of the functionalized Mn-Anderson anion. The Mn Anderson cluster is shown in ball-and-stick representation (Mo: blue, O: red).[181]

1.6 Applications of Polyoxometalates

Owing to their unique versatility in terms of size, lability, thermal stability, photochemical response, ionic charge, conductivity, redox and magnetic properties, polyoxometalates have attracted significant attention in interdisciplinary areas such as biology, catalysis, nanotechnology or medicine.[182] Their predominant applications are found in the area of catalysis where hundreds of papers and patents are published every year.[183] Examples include: oxidation of aromatic hydrocarbons, olefin polymerization, development of green H_2O_2-based epoxidation systems and catalytic oxidation of organic substrates by molecular oxygen and hydrogen peroxide (Figure 31). [171, 184-187] In recent years, a number of studies have also been carried out employing POMs as anti-viral and anti-cancer agents as their ability to produce organic-inorganic hybrids means that they have great potential to interact with biomolecules.[188-194] A number of POMs have been tested for the anti-RNA viral activity and have been proved to be broad spectrum and nontoxic anti-RNA virus agents that are promising candidates for first line-therapeutics in acute respiratory diseases.[195]

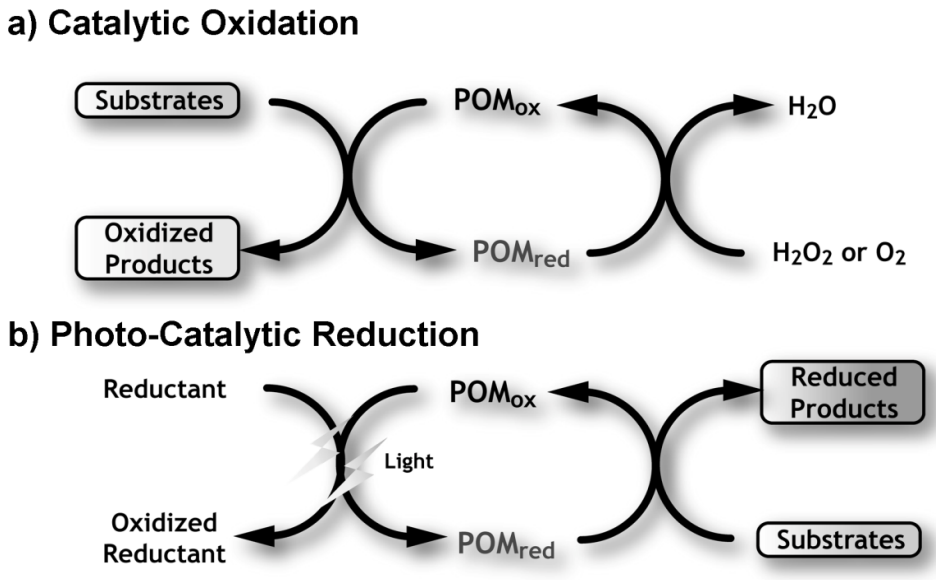

Figure 31: POM-catalyzed reaction systems: (a) catalytic oxidation reaction and (b) photocatalytic reduction.

Polyoxometalates' ability to act as multidentate ligands for the formation of polynuclear complexes with other transition metals leads to the stabilization of novel cores which display interesting and potential applications. For example, the formation of POM-based single molecular magnet clusters (SMM) $\{[Mn^{III}_4Mn^{II}_2O_4(H_2O)_4][XW_9O_{34}]_2\}^{12-}$ (X = Ge and Si) with mixed-valence $\{Mn_6\}$ cores that reveal ferro- and antiferromagnetic exchange interactions (Figure 32a);[196] or the redox active tetraruthenium $[\{Ru_4O_4(OH)_2(H_2O)_4\}(SiW_{10}O_{36})_2]^{10-}$ anion (Figure 32b) that when combined with Ce^{IV} or $[Ru(bpy)_3]^{3+}$ catalysts was found to catalyse the rapid oxidation of H_2O to O_2 in water at room temperature.[197] This last example has supposed a novel and fascinating discovery since water splitting is one promising approach to convert and store energy. Groups all over the globe are developing novel methodologies for the production of cheap and renewable energy using polyoxometalates as a main catalyst source.

(a)

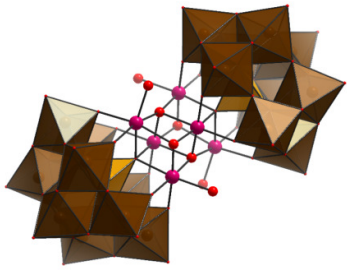

$\{[XW_9O_{34}]_2[Mn^{III}_4\,Mn^{II}_2O_4(H_2O)_4]\}^{12-}$

(b)

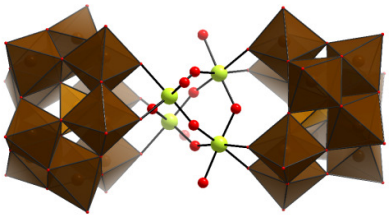

$[\{Ru_4O_4(OH)_2(H_2O)_4\}(SiW_{10}O_{36})_2]^{10-}$

$$4[Ru(bpy)_3]^{3+} + 2H_2O \longrightarrow 4[Ru(bpy)_3]^{2+} + O_2 + 4H^+$$

Figure 32: (a) Representation of the $[\{X^{IV}W_9\}\{Mn_6\}]^{12-}$ polyanions (X = Si, Ge) which can be described as $[XW_9O_{34}]^{10-}$ polyanion that sandwich a mixed-valence double cubane cationic hexamer $\{Mn_6\}$. Each cubane comprises three Mn^{III} and one Mn^{II} centre, with two of the Mn^{III} centres shared between cubanes.[196] (b) Structure of the polyanion $[\{Ru_4O_4(OH)_2(H_2O)_4\}(SiW_{10}O_{36})_2]^{10-}$ with a central $\{Ru_4O_4(OH)_2(H_2O)_4\}$ core.[197] W: brown, X: orange, Mn: pink, Ru: lima, O: red.

2 AIMS

Polyoxometalates are a vast class of transition metal oxide clusters that display a wide range of structural properties and applications. The total understanding of their formation mechanism remains one of the biggest challenges within this sub-class of inorganic materials; even though it is well-establish that it involves the self-assembly process of the different building blocks involved in the reaction mixture. The incorporation of tetrahedral heteroanions such as phosphates or sulfates has been widely studied, whereas the integration of non-conventional (non-tetrahedral) heteroanions has not attracted that much attention.

The isolation of materials templated by pyramidal heteroanions has been reported and has demonstrated that the incorporation of non-conventional heteroanions within the inorganic metal-oxide cages can lead to the formation of novel materials with interesting redox properties and different structural motifs than the tetrahedral analogues.[127, 130, 135, 136, 198, 199] On the other hand, tungstate-based polyoxometalates have been broadly studied in comparison with the vanadium- and molybdenum-based materials. Due to considerable differences with regards to lability, molybdenum and vanadium metal oxide units exhibit different geometries and the combination of the Mo- and V-based building block libraries might have a dramatic effect on the isolated archetypes.

The reported Dawson-like $[Mo_{11}V_7O_{52}(SO_3)]^{7-}$ archetype, which displays a plethora of coordination modes and oxidation states, is templated by the pyramidal sulfite heteroanions, demonstrates that the permutation between the molybdenum-vanadium oxides and the pyramidal heteroanion has an important effect on the final archetype. Following this approach, we decided to study the effect of pyramidal heteroanions in the presence of molybdovanadate mixed-metal species. In order to do so we decided to explore the influence of the pyramidal heteroanions from Group XVI (SO_3^{2-}, SeO_3^{2-} and TeO_3^{2-}) because since they belong to the same group of the periodic table they present similar properties while exhibiting different atomic radius. We believed that the latter feature

would have an important effect on the self-assembly process which would influence the final archetype because, as the atomic radius gets bigger, more steric restrictions are introduced. Additionally, the presence of the stereochemically active lone pair of electrons of the pyramidal heteroanions, could make the resulting materials excellent candidates for non-linear optical (NLO)-based applications.

Moreover, the introduction of paramagnetic metal centres into the inorganic cages, such as vanadium, which is rapidly reduced to V^{IV} (d^1) in the presence of a reducing agent, could result in the isolation of novel materials with interesting magnetic properties. For that reason, we planned to study the effect of different synthetic variables, such as the ratio between the starting materials and the pH, and study how these parameters in the presence of the pyramidal heteroanion can influence the formation of the final archetype.

3 RESULTS AND DISCUSSION

Polyoxometalates are anionic metal oxide clusters with a vast range of structural properties and applications.[2, 4, 6, 193] The 'one-pot' reaction approach to the formation of this class of clusters can be extremely frustrating since very small changes in the reaction conditions can yield totally different results. This is because, in general, the mechanism of POM self-assembly, which consists of the condensation of $\{MO_x\}$ units (M = W, Mo and V) under acidic aqueous conditions, is complex and depends on many parameters such as pH, temperature, redox agents, templates and cations.[65, 76, 135] In an effort to gain control and direct the assembly process, different techniques have recently been employed such as the structure directing properties of "shrink-wrapping" organic cations,[65, 76, 135] control of the ionic strength,[35] reaction and crystallisation under continuous flow conditions[37] and the direct observation of new clusters as they are formed using electrospray and cryospray mass spectrometry.[25]

When a heteroatom $\{XO_y\}$ (X = S, P, Si, Ge) is present in the one-pot reaction system, the self-assembly process of the different building units leads to the isolation of inorganic archetypes called Heteropolyoxometalates (HPOMs). It has been shown, that the heteroatom plays a crucial role in the self-assembly process, templating the condensation of the $\{MO_x\}$ moieties, stabilizing reactive intermediates and consequently influencing the final architecture of the cluster.[125, 127, 128, 198] Previously described in *Section 1.3.*, depending on the geometry and concentration of the heteroatom, different structures can be isolated: the Anderson $\{XM_6O_{24}\}$ with an octahedrally coordinated heteroatom $\{XO_6\}$ in the centre of a six-membered cyclic polyanion,[100, 200] the Keggin $\{XM_{12}O_{40}\}$ with one $\{XO_4\}$ tetrahedral heteroanion within the central cavity[201, 202] and the Wells-Dawson $\{X_2M_{18}O_{62}\}$ with two $\{XO_4\}$ tetrahedrally coordinated heteroanions inside the inorganic metal cage,[203] are examples of the different architectures commonly displayed by HPOMs.

In HPOM chemistry, many reactions have been done utilising tetrahedral main group anions such as sulfate and phosphate.[204] However, it has been shown that the use of non-

conventional (non-tetrahedral) heteroanions such as the pyramidal sulfite anion has a profound effect on the structure and functionality of the resulting compound.[125, 127, 130, 136, 199, 205, 206] This is because the C_{3v} symmetric sulfite anion contains a non-bonding, but stereochemically active lone pair of electrons which can help impart additional redox and photophysical properties.[115, 130, 207, 208] HPOMs templated by non-conventional heteroanions are less common and are limited to mainly tungstate-based materials, which are less labile and therefore impart stability on the lacunary species (see *Section 1.5.1*.).[130, 133, 138] In contrast, only a few molybdate,[126, 209] vanadate[199, 210] and palladate[211, 212] examples exist in the literature. The majority of HPOMs templated by tetrahedral heteroanions adopt Keggin and Wells-Dawson architectures and are mainly molybdenum and tungsten based inorganic frameworks. Replacing some of these metal atoms with other transition metal centres can yield novel clusters with related structures which exhibit different properties, as in the case of the Dawson-like capsules $\{V^{IV}M^{VI}_{17}(VO_4)_2\}$ (M = Mo, W).[85] The incorporation of the sulfite heteroanion, or any non-conventional heteroatom, into mixed-metal polyoxometalate cages could then lead to the isolation of new materials with unprecedented archetypes and redox properties.

Herein, we present and discuss a complete study on the incorporation of pyramidal heteroanions from Group XVI (SO_3^{2-}, SeO_3^{2-} and TeO_3^{2-}) within molybdo-vanadate mixed-metal and mixed-valence systems, and how the atomic radius of the heteroanion (Table 2) along with its geometry has an important effect on the self-assembly process of the different building units involved in the reaction mixture, and the archetype of the final products. This correlation between structure and heteroanion for these systems has never been observed before and consequently opens the door for new discoveries and further exploration in the diverse field of POM chemistry.

Table 2: Some properties of the Group XVI elements.[213]

Element	Covalent radius –x– Å	Electronegativity
S	1.03	2.44
Se	1.17	2.48
Te	1.37	2.01

3.1 Sulfite-based Mixed-Metal Polyoxometalates

3.1.1 The ancestor {$Mo_{11}V_7S$}: $[Mo^{VI}_{11}V^{V}_{5}V^{IV}_{2}O_{52}(\mu_9\text{-}SO_3)]^{7-}$ 1

The sequential addition of $NH_4V^{V}O_3$ and $(NH_4)_2SO_3$ to an acidified aqueous (37% HCl in water, 1:4 v/v) solution of $(NH_4)_6Mo^{VI}_{7}O_{24}$ resulted in the formation of deep green crystals of **1** after 3 days.[206] The cluster was first characterized using mass spectrometry techniques, where *via* cation exchange with tetrapropylammonium bromide it was possible to roughly identify the anion as a mixed Mo/V cluster with ratio 11/7. Further characterization of the solid state revealed that **1** can be formulated as $(NH_4)_7[Mo^{VI}_{11}V^{V}_{5}V^{IV}_{2}O_{52}(\mu_9\text{-}SO_3)]\cdot 12H_2O$ and adopts a Dawson-like structure where seven of the molybdenum metal centres have been replaced by vanadium atoms (two reduced V^{IV} and five oxidized V^{V}) (Figure 33 right). The egg-shaped cage is built up from two hemispheres: a well-defined upper hemisphere where three $Mo^{VI}O_6$ octahedra form the cap, which is connected to an alternating corner-sharing $Mo^{VI}O_6$ octahedra and $V^{V}O_4$ tetrahedra belt; and a lower hemisphere where five $Mo^{VI}O_6$ and four $V^{IV/V}O_6$ octahedra are disordered over nine positions.

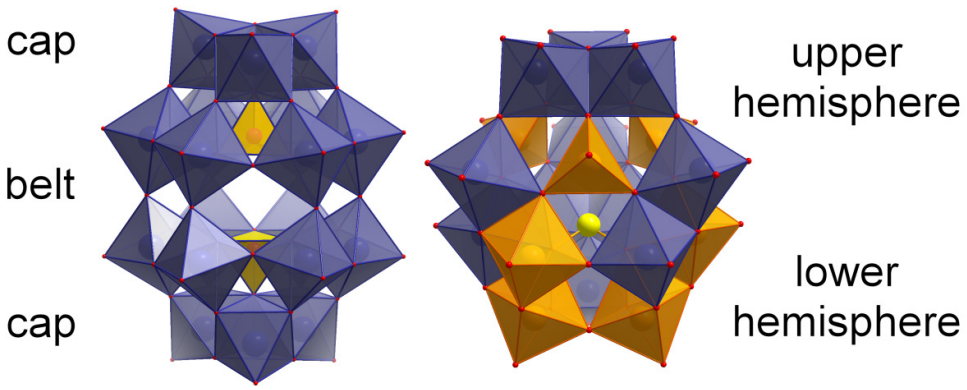

Figure 33: Polyhedral representation of the anion for the classical Dawson $[Mo_{18}O_{54}(XO_4)]^{n-}$ (left) and the egg-shaped Dawson $[Mo^{VI}_{11}V^{V}_{5}V^{IV}_{2}O_{52}(\mu_9\text{-}SO_3)]^{7-}$ moiety (right). Mo: purple polyhedra, V: orange polyhedra, XO_4: orange polyhedra, S: yellow spheres and O: red spheres.

The unique archetype adopted by the Dawson-like cluster revealed that the combination of both pyramidal heteroanions and mixed metal centres is suitable for the formation of novel inorganic frameworks. Firstly, the inclusion of the pyramidal heteroanion with the lone pair of electrons directs the assembly towards the formation of a Dawson type compound instead of the stable Keggin anion, leading to a higher nuclearity cluster. Secondly, the incorporation of the three tetrahedral V^{V} atoms in the upper belt prevents the incorporation of a second SO_3^{2-} heteroanion due to steric limitations. The interatomic distance between the tetrahedral V centres of the upper hemispheres is 4.751(2) Å whereas the equivalent Mo centres in the conventional Dawson lie 6.134(1) Å apart (Figure 33). As a result, there is a larger internal volume in the classical Dawson archetype which allows the incorporation of a second tetrahedral heteroanion. In addition, the observation *in situ* of the formation of the $[Mo^{VI}_{11}V^{V}_{5}V^{IV}_{2}O_{52}(\mu_9\text{-}SO_3)]^{7-}$ anion using mass spectrometry (Figure 34) proved to be crucial for the isolation of novel materials and at the same time to better understand the self-assembly process of such clusters, where the template effect of the sulfite anion triggers the formation of the mixed-metal cage $\{Mo_{11}V_7S\}$.

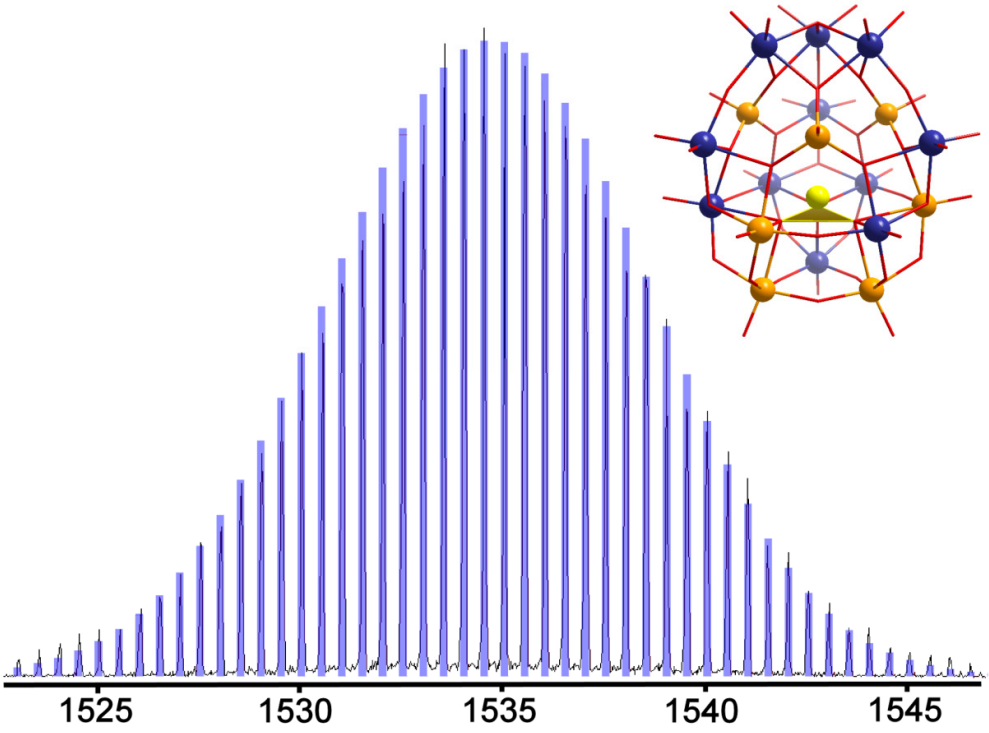

Figure 34: Negative ion mass spectrum of an acetonitrile solution of $\{(Pr_4N)_4[H_{1\text{-}n}Mo_{11}V^{V}_{5+n}V^{IV}_{2\text{-}n}O_{52}(SO_3)]\}^{2-}$. Envelopes can be seen where n = 1 (with one V^{IV}) giving an

envelope centred at *m/z ca.* 1534.5, and where n = 0 (with two V^{IV}, requiring one proton) giving an envelope centred at *m/z ca.* 1535.0. Black line: experimental data, blue bars: simulation of isotope pattern.

At this point it is important to note that: (i) even though V^{V} is rapidly reduced to V^{IV} in the presence of $(NH_4)_2SO_3$ it is present in its oxidized form in the cluster cage; (ii) the different metal centres exhibit diverse geometries within the same structure; (iii) the cluster is only templated by one pyramidal sulfite heteroanion, which occupies the central part of the lower hemisphere; (iv) each of the three oxygens of the SO_3^{2-} anion is connected to one metal centre from the cap and two from the belt in a μ_9- coordination mode, whereas in the classical Dawson three oxygens from the tetrahedral XO_4 heteroatom are ligated to two metal centres from the belt, and the fourth oxygen is coordinated to the three capping metal atoms; and (v) the coordination sphere of the Mo^{VI} located at the upper hemisphere exhibit two terminal oxo groups, while in the conventional Dawson they only support one.

3.1.2 Isolation of the larger sulfite-based anion {$Mo_{17}V_8S$}: $[Mo^{VI}_{11}V^{V}_{5}V^{IV}_{2}O_{52}(\mu_9\text{-}SO_3)(Mo^{VI}_{6}V^{V}O_{22})]^{10-}$ **2**

Generally, the design of new cluster systems which exhibit novel archetypes that potentially give rise to unprecedented properties is a major goal in inorganic cluster chemistry, since this could potentially lead to the discovery and development of functional nanoscale materials built using a 'bottom-up' self-assembly approach.[150] The sequential addition of solid $NH_4V^{V}O_3$ and $(NH_4)_2SO_3$ to an acidified aqueous (37% HCl in water, 1:4 v/v) solution of $(NH_4)_6Mo^{VI}_{7}O_{24}$, resulted in the formation of deep green crystals of **2**, after fine adjustment of the experimental conditions such as metal to metal ratio and acidity (Figure 35). We then dissolved some crystals of **2** in water, added an excess of tetrapropylammonium bromide (Pr_4NBr) and stirred the solution for five minutes. After this time, a green precipitate formed which was collected by centrifuging the suspension and decanting the supernatant, and was finally dissolved in acetonitrile. We studied the solution system with mass spectrometry, which confirmed that **2** is a mixed-metal mixed-valence sulfite-based polyoxometalate cluster with Mo/V ratio 17/8. These results were

confirmed by matching the experimental data with the simulated isotopic pattern (see *Section 2.1.3*).

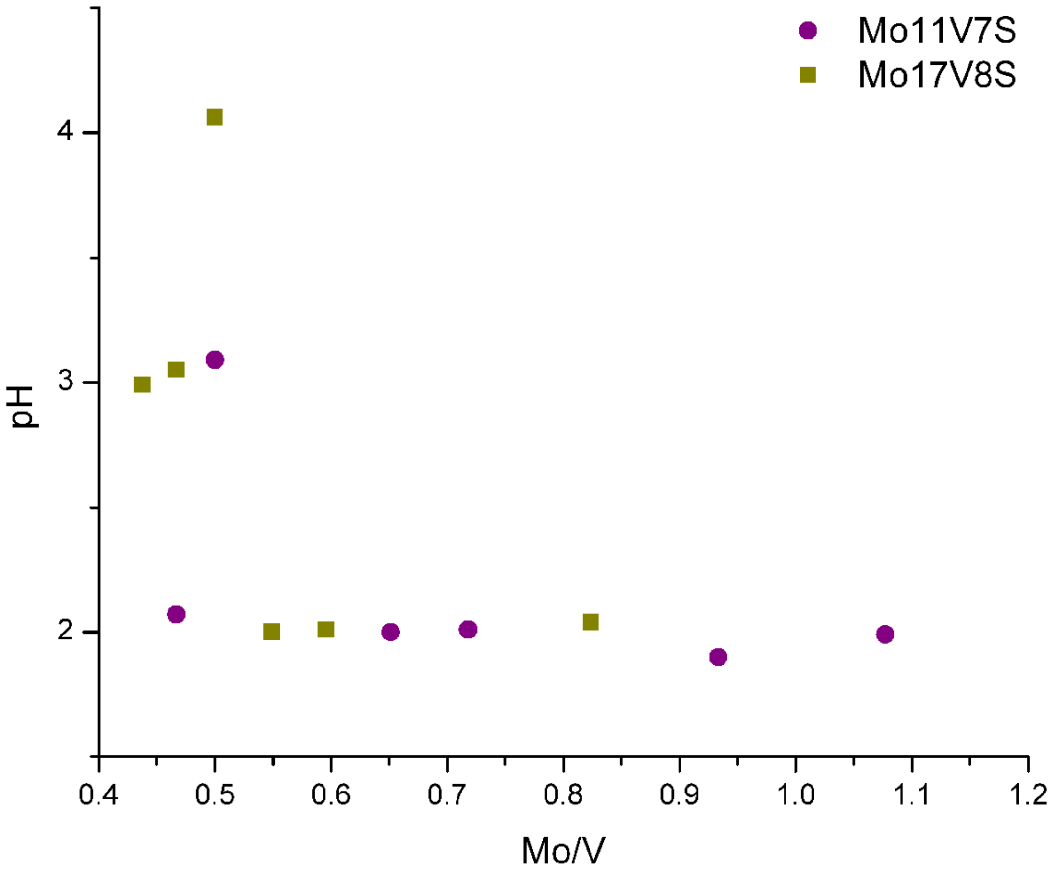

Figure 35: Reaction map of the isolation of $\{Mo_{11}V_7S\}$ **1** *versus* $\{Mo_{17}V_8S\}$ **2** between pH 2 – 4 and Mo/V between 0.4 - 1.2. Higher concentration of molybdate leads to the isolation of only compound **1**.

Subsequent characterisation of the material in the solid state, *via* crystallographic studies and complementary analytical techniques, revealed that **2** can be formulated as $(NH_4)_{10}[Mo^{VI}_{11}V^{V}_{5}V^{IV}_{2}O_{52}(\mu_9\text{-}SO_3)(Mo^{VI}_{6}V^{V}O_{22})]\cdot 14H_2O$ whereby the anion **2a** adopts a "crowned"-Dawson-like structure and consists of 3 parts (Figure 36). The distorted egg-shaped capsule of the molybdovanadate-sulfite anion is built up from two different hemispheres, being related to the parent cluster $[Mo^{VI}_{11}V^{V}_{5}V^{IV}_{2}O_{52}(\mu_9\text{-}SO_3)]^{7-}$ **1**. As shown before, the lower part of **2a** consists of two hemispheres where three edge-sharing MoO_6 octahedra from the cap are connected to the belt *via* vertices of alternating $V^{V}O_4$ tetrahedra

and MoO_6 octahedra. The remaining four V positions (two V^V and two V^{IV}) are crystallographically disordered in the lower part of the cluster over nine potential positions. The cavity is occupied by one sulfite anion since the tetrahedral geometry of the V metal centres cause the upper hemisphere to contract and diminish the available space. In this case a "crown"-like fragment is attached to the 3 MoO_6 centres located at the top of the 'Dawson' cap through 6 oxo-bridges and consists of 3 pairs of corner sharing MoO_6 units comprising two terminal oxo groups. The centre of the "crown" is occupied by a tetrahedral vanadium (V) centre.

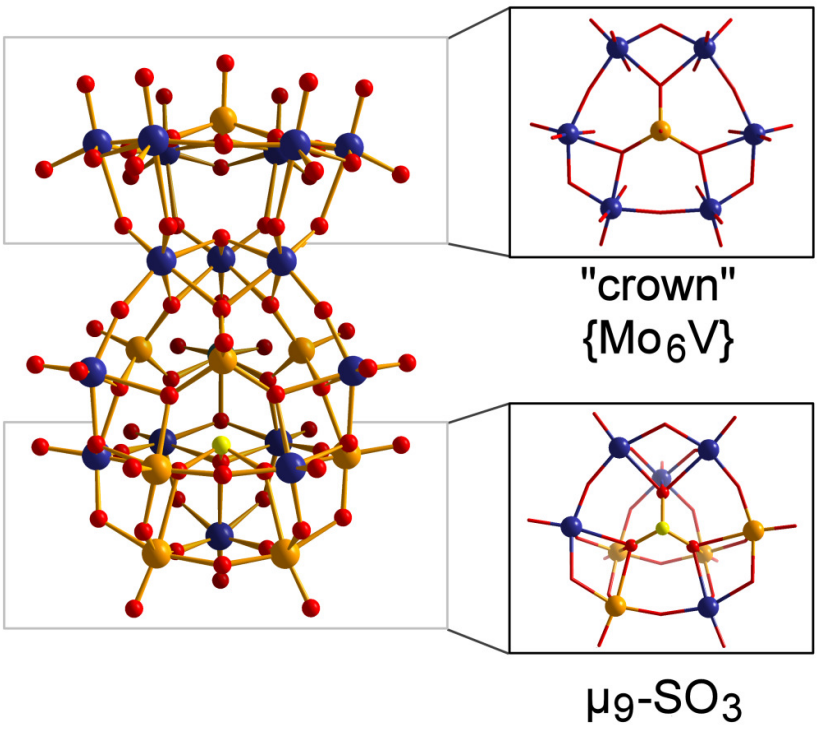

Figure 36: Ball-and-stick representation of $[Mo^{VI}_{11}V^{V}_{5}V^{IV}_{2}O_{52}(\mu_9\text{-}SO_3)(Mo^{VI}_{6}V^{V}O_{22})]^{10-}$ **2a** (left); the sulfite heteroanion coordination mode in the lower hemisphere (bottom right), where all the molybdenum and vanadium metal centres are disordered over the nine positions and the S atom has the formal oxidation state IV (BVS_{av} = 3.86); and the crown $\{Mo_6V\}$ (top right), which is attached on top of the $\{Mo_{11}V_7S\}$ capsule. Mo: purple spheres, V: orange spheres, S: yellow spheres and O: red spheres.

Whilst the Mo and V atoms in **2** are crystallographically distinguishable in the upper hemisphere and in the "crown" moiety, the metal sites in the bottom hemisphere are

disordered. Therefore, the assignment of formal charges on the metals was made on the basis of charge balance considerations for the entire compound, combined with BVS calculations,[214] redox titrations, and elemental analysis, as well as high resolution cryospray mass spectrometry. All the Mo atoms have the formal oxidation state VI (BVS_{av} = 5.99), the V atoms in the VO_4 tetrahedra are in the oxidation state V (BVS_{av}=5.05), whilst two out of the four V atoms in the bottom hemisphere are in the oxidation state IV (BVS_{av} = 4.25) and the remaining two are in the oxidation state V (BVS_{av}= 4.60). The V atoms in the VO_4 tetrahedra are coordinated by three μ_3-O^{2-} moieties, with V–O bonds spanning the range 1.728(6)–1.774(6) Å, and one terminal oxo group with V=O bonds of 1.627(9) and 1.634(7) Å respectively. The Mo atoms in the MoO_6 octahedra belonging to the upper hemisphere are coordinated by two terminal oxo groups in *cis*-positions, with Mo=O bonds spanning 1.686(7)–1.732(7) Å, one μ-O^{2-}, with Mo–O bonds spanning 1.882(8)–1.914(7) Å, and three μ_3-O^{2-} moieties, with Mo–O bonds spanning 1.935(8)–2.429(8) Å. A direct comparison between the bond distances from compound **1** and **2** are summarized in Table 3. To the best of our knowledge compound **2** is the largest sulfite-based polyoxometalate reported so far. It crystallizes in the space group of *Pnma* and the clusters are connected to each other *via* ammonium cations. Each crown is connected to the belt of two adjacent clusters by sharing two cations with each anion (Figure 37).

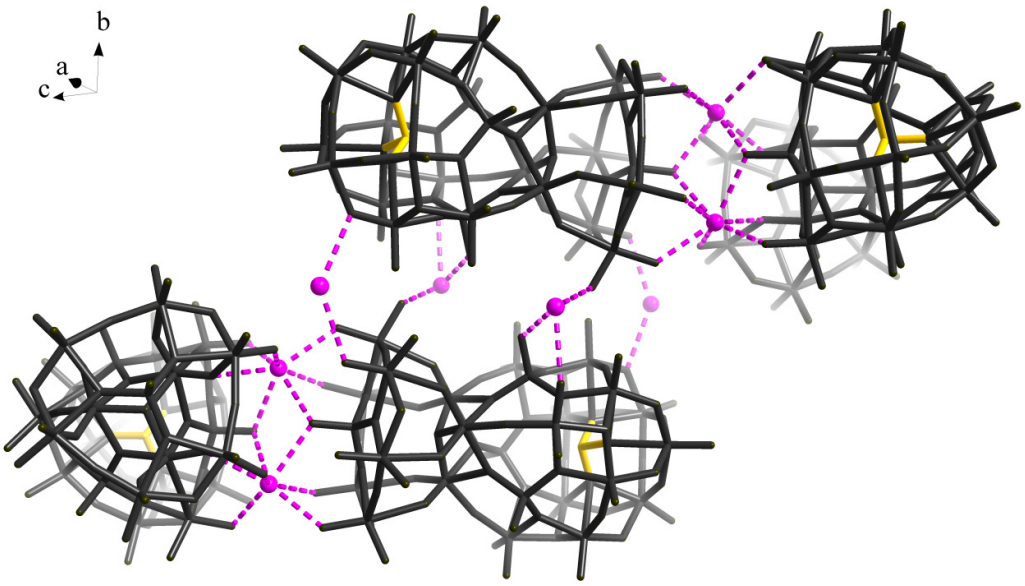

Figure 37: Wire representation showing the packing of the discrete cluster **2**. The network of the hydrogen bonds between the ammonium cations (N: pink balls) and the clusters are

display in pink. The inorganic framework is represented by the dark grey wires and the sulfite anion is shown in yellow.

Table 3 Comparison of the bond distances from the upper hemisphere of the egg-shaped Dawson-like cage in **1** and **2** (see Appendix Section 7.1 and 7.2)**.**

Bond distances (Å)								
Upper cap **1**			Upper belt **1**					
Mo2	O22	1.698(4)	Mo1	O23	1.705(4)	V10	O6	1.642(5)
Mo2	O4	1.715(4)	Mo1	O27	1.715(3)	V10	O1	1.711(5)
Mo2	O21	1.896(3)	Mo1	O21	1.867(3)	V10	O28	1.760(3)
Mo2	O11	2.033(3)	Mo1	O24	2.010(3)	V11	O34	1.636(4)
Mo2	O17	2.247(3)	Mo1	O28	2.245(3)	V11	O17	1.724(3)
Mo2	O1	2.290(3)	Mo1	O26	2.263(3)	V11	O29	1.754(3)
Mo3	O3	1.706(4)	Mo4	O2	1.705(4)	V11	O26	1.764(3)
Mo3	O13	1.883(5)	Mo4	O13	1.893(5)			
Mo3	O11	2.063(5)	Mo4	O32	2.018(5)			
Mo3	O17	2.256(3)	Mo4	O29	2.271(3)			
Upper cap **2**			Upper belt **2**					
Mo5	O14	1.696(6)	Mo4	O12	1.683(8)	V12	O13	1.642(1)
Mo5	O15	1.707(8)	Mo4	O34	1.722(7)	V12	O9	1.738(1)
Mo5	O10	1.861(8)	Mo4	O10	1.880(8)	V12	O11	1.750(7)
Mo5	O8	2.025(7)	Mo4	O3	2.000(8)	V13	O33	1.639(8)
Mo5	O9	2.207(8)	Mo4	O11	2.235(7)	V13	O32	1.729(7)
Mo5	O32	2.232(6)	Mo4	O2	2.270(7)	V13	O2	1.753(9)
Mo6	O17	1.693(8)	Mo7	O45	1.701(8)	V13	O31	1.773(7)
Mo6	O7	1.882(9)	Mo7	O7	1.899(1)			
Mo6	O8	2.030(9)	Mo7	O6	2.000(1)			
Mo6	O32	2.239(8)	Mo7	O31	2.255(8)			

Upon adjusting the pH by addition of $(NH_4)_2SO_3$ the reaction mixtures acquire a deep purple colour which turns green after 24 hours. After collection of the first yield of crystals, the mother liquor of the reaction becomes oxidized in contact with the air. This

process is easily observed by eye as the reaction mixture turns noticeably lighter, then crystallization of the well-known orange crystals of $[V_{10}O_{28}]^{6-}$ occurs.[46] Sometimes, during this oxidative process, other species co-crystallized from solution. For example, when the Mo/V ratio of the starting material was 1.08, yellow crystals of $[Mo^{VI}_4O_{13}(SO_3)]^{4-}$ (first reported by Kabanos *et.al.*)[127] co-crystallized with the hexagonal dark green crystals of **1**; whereas if the ratio was 1.65 yellow crystals of the isopolyoxomolybdate $[Mo_7O_{24}]^{6-}$ were formed instead[215] (Figure 38).

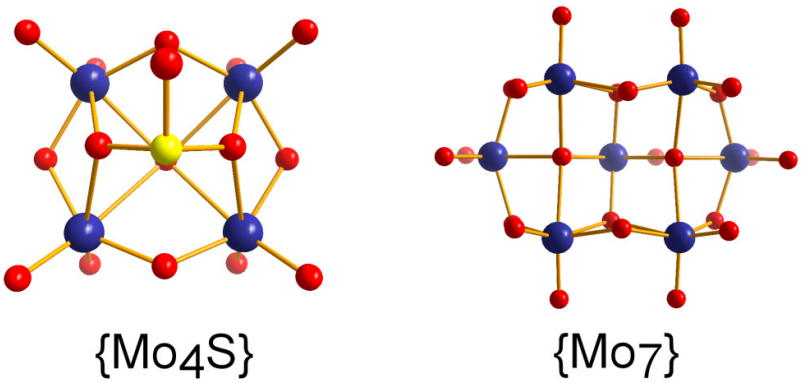

Figure 38: Ball-and-stick representation of the side-products of the mixed-metal Mo/V sulfite-based systems upon oxidation of the reaction mixture. Mo: blue spheres, S: yellow spheres and O: red spheres.

At this point it is worth noting the interesting chemical information which has been transferred from the parent molecule **1** to the daughter product **2** (Figure 39): (i) the existence of the oxidized form of six vanadium centres in the presence of a reducing agent, even though the vanadium(V) at the beginning is reduced rapidly to vanadium(IV) by the sulfite anion;[127, 136, 199, 205, 206] (ii) a plethora of geometries are adopted by the metal centres in the same structure as shown by the structural analysis (dioxo-/oxo-Mo^{VI} and octahedral/tetrahedral $V^{V/IV}$ centres); and (iii) the presence of the μ_9-SO_3 bridging anion, which occupies the central part of the lower hemisphere; that is only the third reported example of the bridging mode found in the literature.[37, 206]

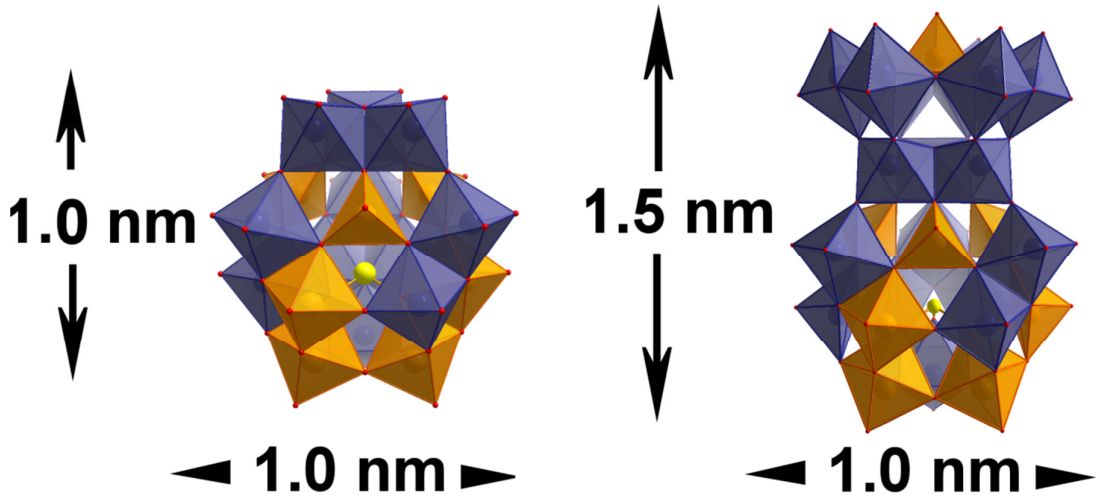

Figure 39: Polyhedral representation of **1** (left) and **2** (right) and their dimensions. Mo: blue polyhedra, V: grey polyhedra, S: yellow spheres and O: red spheres.

IR spectroscopy studies where performed to identify the vibrational modes of the sulfite-based polyoxoanions **1** and **2**. Assignment of some diagnostic bands for the mixed-metal cages **1** and **2** is given in Table 4 as well as for some known metal-sulfite compounds.[199] The vibrational frequencies of the pyramidal (C_{3v}) free sulfite anion are well-known[216] and are found within the region of 1000 – 450 cm^{-1}: $\nu_1(A_1)$ = 967 cm^{-1}, $\nu_2(A_1)$ = 620 cm^{-1}, $\nu_3(E)$ = 933 cm^{-1} and $\nu_4(E)$ = 469 cm^{-1}; where ν_1 and ν_3 are stretching vibrations and ν_2 and ν_4 correspond to bending vibrations. However, the coordination of the sulfite anion with other building units is expected to lower its symmetry and splits its degenerate bands (ν_3 and ν_4) into two. Such an effect is reflected in the shift of the four fundamental bands; even though in the case of compounds **1** and **2** the sulfite anion is in an equivalent environment where each of the three oxygen ligands is coordinated to three metal centres. An overlap between the M=O (M = Mo and V) and SO stretches is expected for compounds **1** and **2**. From Table 4, it is observed that the difference between the highest and the lowest SO stretching vibrations, $\Delta|\nu_3 - \nu_1|$, is proportional to the coordination of the sulfite anion: the lower μ-SO_3 and μ_3-SO_3 coordination modes have a difference of 193 cm^{-1} and 176 cm^{-1} respectively, whereas the μ_9-SO_3 coordination mode is *ca.* 150 cm^{-1}. Thus, it is easy to distinguish the different coordination modes of the sulfite anion.

Table 4: Diagnostic IR bands [cm^{-1}] of the molybdovanadate sulfite compounds **1** and **2** and some known metal sulfite compounds. Intensity codes: vs = very strong; s = strong; sh = sharp; m = medium

Compound	Bonding modes of SO_3^{2-}	ν_3(E)	ν_1(A_1)	$\Delta\lvert \nu_3 - \nu_1 \rvert$ [cm^{-1}]	ν_2 (A_1)	ν_4 (E)	ν(V=O) ν(Mo=O)	Ref
1	μ_9- SO_3^{2-}	944s, 817vs	970sh, 866s, 861 s,	153			970 sh, 944 s	206
2	μ_9- SO_3^{2-}	944s, 812 vs	962 sh, 895 s, 872 s	150			962 sh, 944s	This work
$\{(V^{IV}O)_6(\mu_3\text{-}SO_3)_4\}$	μ_3- SO_3^{2-}	839 m	1014 s	175			967 vs 960 vs	199
$[V^{IV}(OH)_2(\mu\text{-}SO_3)_2]^{2-}$	μ- SO_3^{2-}	835 vs	1028 vs	193			952 vs	199

3.1.3 Solution identification of $\{Mo_{11}V_7S\}$ 1 and $\{Mo_{17}V_8S\}$ 2

During the course of this study, CSI-MS studies have proven to be a powerful tool[25, 77] in our effort to unveil the novel "Crowned" Dawson type cluster in solution, allowing **2a** to be identified in solution prior to structural analysis, and to examine its structural evolution. In these studies, the Pr_4N salts of the $\{Mo_{17}V_8S\}$ cluster **2a**, dissolved in acetonitrile confirmed that the sulfite-capsule retains its integrity in solution, see Figure 40, and peaks are seen in the spectrum which are assigned to $\{(Pr_4N)_7[H_nMo_{11}V^{V}_{4-n}V^{IV}_{3+n}O_{52}(SO_3)(Mo^{VI}_6V^{V}O_{22})](NH_4)_2(CH_3CN)\}^{2-}$ where n = 0 (with three vanadium ion in oxidation state IV) giving an envelope centred at *m/z ca.* 2342.1, and where n = 1 (with four vanadium ions in oxidation state IV, requiring one proton) giving an envelope centred at *m/z ca.* 2342.6. The presence of the ammonium cations in the detected species is due to the network of hydrogen bonds between the ammonium cations and the clusters (see Figure 37). Despite our efforts, we did not manage to achieve 100% cation exchange in this case.

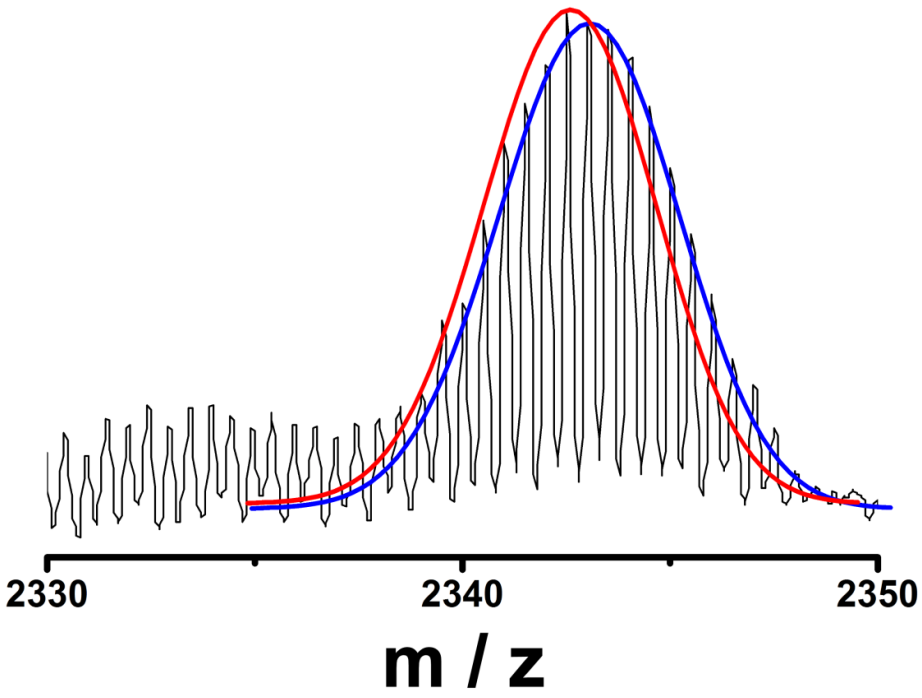

Figure 40: Negative ion mass spectrum in acetonitrile solution of $\{(Pr_4N)_7[H_nMo_{11}V^V_{4-n}V^{IV}_{3+n}O_{52}(\mu_9\text{-}SO_3)(Mo^{VI}_6V^VO_{22})](NH_4)_2(CH_3CN)\}^{2-}$. Two envelopes can be seen where n = 0 (with three vanadium ions in oxidation state IV) giving an envelope centred at *m/z ca.* 2342.1, and where n = 1 (with four vanadium ions in oxidation state IV, requiring one proton) giving an envelope centred at *m/z ca.* 2342.6. Black line: experimental data, Red/blue lines: profile lines of the simulated isotope patterns.

MS-spectrometry was also used to unveil the Mo/V ratios of **1**. The Pr_4N salts of the egg-shaped Dawson-like cluster confirmed that the mixed-metal sulfite-based archetypes have the same ratio as the already reported $\{Mo_{11}V_7S\}$ anion.[206] As it was previously observed, the egg-shaped Dawson-like structure retains its integrity in solution, see Figure 41, and the observed peaks centred at *m/z ca.* 2076.1 and 2077.6 can be formulated as $\{(Pr_4N)_8[HMo^{VI}_{11}V^VV^{IV}_6O_{52}(\mu_9\text{-}SO_3)](CH_3CN)_6(H_2O)_5\}^{2-}$ (with 6 reduced V) and $\{(Pr_4N)_8[Mo^{VI}_{11}V^V_2V^{IV}_5O_{52}(\mu_9\text{-}SO_3)](CH_3CN)_7(H_2O)\}^{2-}$ (with 5 reduced V) respectively (green box) are seen. Peaks which can be assigned to traces of compound **2** have also been observed as $\{(Pr_4N)_7(Mo^{VI}_{11}V^V_6V^{IV}O_{52}(\mu_9\text{-}SO_3)(Mo^{VI}_6V^VO_{22}))(CH_3CN)_2\}^{2-}$ (with 1 reduced V) and $\{(Pr_4N)_7(H_5Mo^{VI}_{11}V^VV^{IV}_6O_{52}(\mu_9\text{-}SO_3)(Mo^{VI}_6V^VO_{22}))(CH_3CN)_7(H_2O)_3\}^{2-}$

(with 6 reduced V) giving envelopes centred at *m/z ca.* 2344.0 and 2476.6 respectively (purple and yellow boxes).

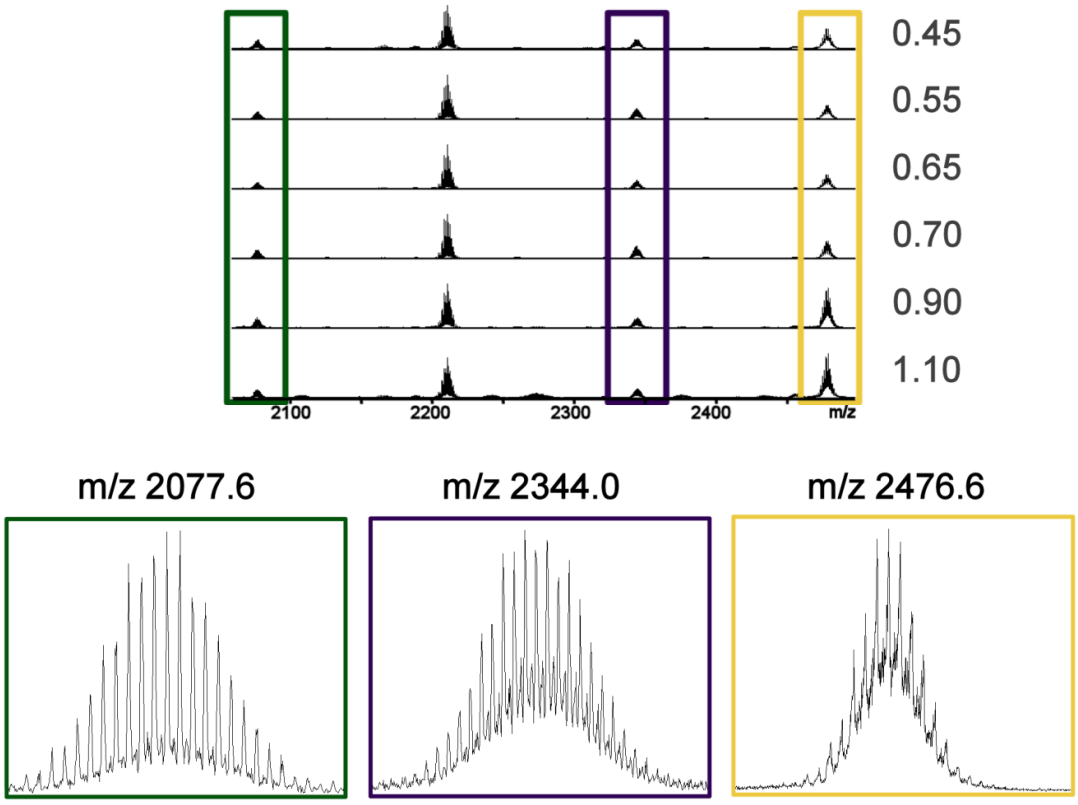

Figure 41: Negative ion mass spectra of acetonitrile solutions of the different $\{Mo_{11}V_7S\}$ clusters (top) isolated at pH 2 in Figure 35, with relevant starting materials ratios presented on the right hand side. Expanded MS spectrum (bottom) of **1** (green box) and the traces found of **2** (purple and yellow boxes).

3.1.4 Controlling transformations in the assembly of $\{Mo_{11}V_7S\}$ 1 and $\{Mo_{17}V_8S\}$ 2

It is interesting to note that the existence of the di-oxo Mo units on the cap of the distorted $\{Mo_{11}V_7S\}$ Dawson structure was previously considered inert because the site on the cap is electronically saturated, and as a consequence non-reactive. In this case, and in contrast to this preliminary hypothesis, we proved that this site of the molecule is able to react

efficiently in the presence of appropriate building units under controlled experimental conditions to give bigger architectures while at the same time retaining the structural and chemical information from the parent molecule. Indeed, our structural analysis showed that compound **2** incorporates 6 dioxo-Mo units in the "crown" formation. This makes compound **2** an excellent candidate for use in the assembly of even larger nanoscale clusters since it can potentially be used as a 'third generation' synthon, building on the previous assembly steps.

In an effort to extend our studies, as well as to observe experimentally the "information transfer" from the parent molecule to the daughter product, we used the $[Mo^{VI}_{11}V^{V}_{5}V^{IV}_{2}O_{52}(\mu_9\text{-}SO_3)]^{7-}$ **1** as secondary building unit (SBU) in an effort to *directly* construct compound **2,** to see if the observed structural evolution process takes place. Upon addition of 0.15 g of $(NH)_6Mo_7O_{24}$ and 0.1 g NH_4VO_3 followed by adjustment of the pH at the value of 3.5 with small amounts of $(NH_4)_2SO_3$ in a stirred solution of $\{Mo_{11}V_7S\}$ led to the isolation of X-ray quality single crystals of the $(NH_4)_{10}[Mo^{VI}_{11}V^{V}_{5}V^{IV}_{2}O_{52}(\mu_9\text{-}SO_3)(Mo^{VI}_{6}V^{V}O_{22})]\cdot 14H_2O$ **2** in 52 % yield (Figure 42). The role of the sulfite anion for this transformation is very important as has been proven in previously reported studies.[130, 199, 205] In this case the reduction of the V^{V} metal centres, as well as the adjustment of the pH value offered by the sulfite anions, triggers the aggregation and finally the structural evolution of the parent molecule towards the formation of compound **2**.

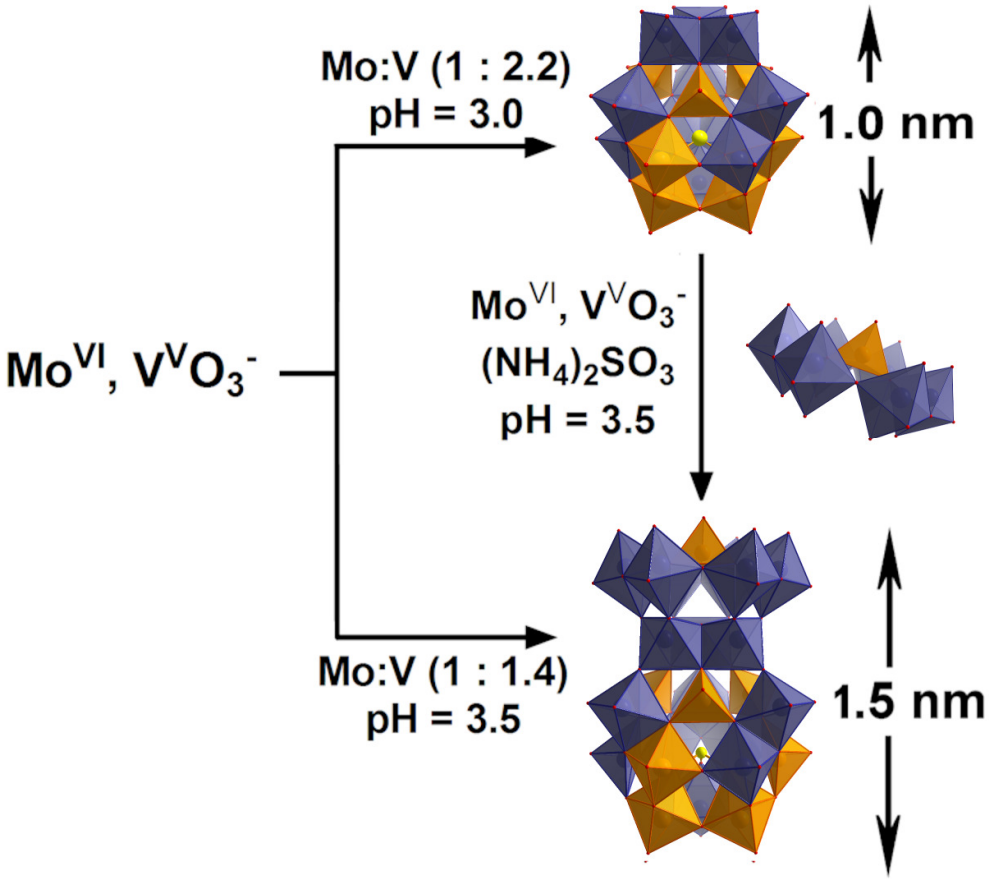

Figure 42: Schematic representation of the synthetic procedure for the isolation of compounds $\{Mo_{11}V_7S\}$ **1** and $\{Mo_{17}V_8S\}$ **2** separately; and how it is possible to produce **2** (bottom) by using **1** (top) as a building unit. Such processes confirm the chemical and structural information transferred from the parent molecule **1** to the daughter **2**. Mo: purple polyhedra, V: orange polyhedra, S: yellow spheres and O: red spheres.

Interestingly, the use of ammonium cations proved to be crucial for the synthesis of compound **2**. In the presence of Na^+ or K^+, instead of NH_4^+ cations, combined with TEA molecules for the "shrink-wrapping" effect, gave us the opportunity to direct the self-assembly process and control the size of the isolated nanosized species. In the latter case the assembly process promoted the synthesis of the gigantic Keplerate ball (a class of molecule first discovered by Achim Müller,[148] see *Section 1.4*) with the formula $\{Mo_{72}V_{30}(SO_4)_{12}\}$,[217, 218] architecture of 2.5 nm (Figure 43). The demonstration of the cation directed self-assembly process is extremely intriguing, not only because of the given

opportunity to control the Mo/V-sulfite system but also for the potential offered towards the sizing of nanoparticles. Indeed, Keplerate-POM clusters are proving to define a whole new class of nanomaterial with unique functionalities, and it is possible that the approach used here could be employed to expand the mechanistic investigations into the assembly process of the Keplerates, and perhaps even allow the direct assembly of new families of Keplerates.

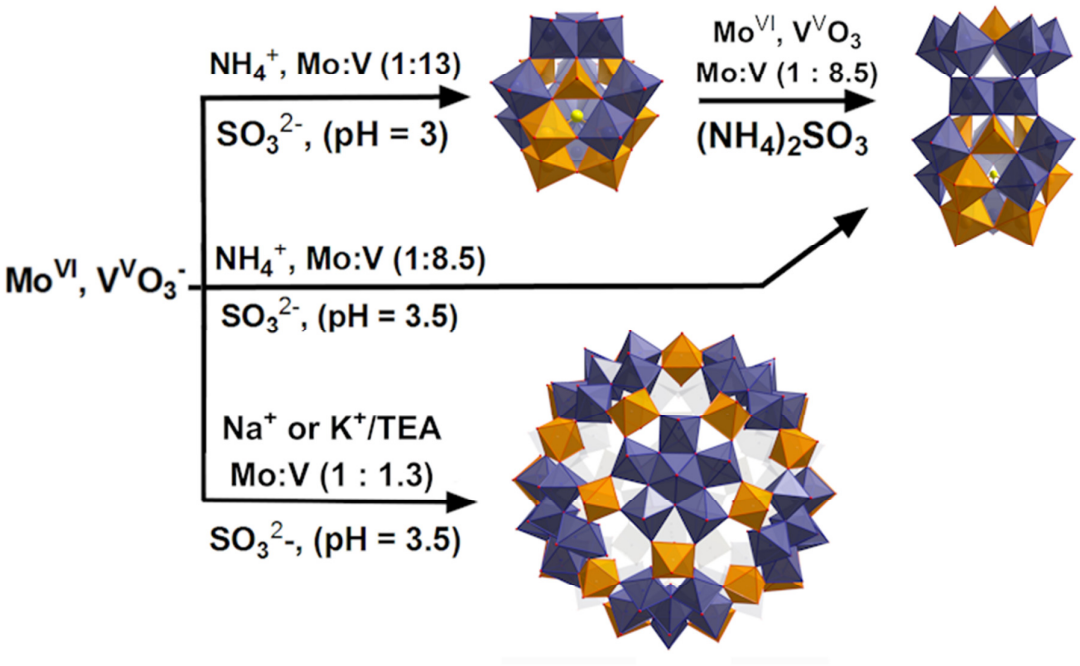

Figure 43: Polyhedral representations of $\{Mo_{11}V_7S\}$ **1** (top- left), $\{Mo_{17}V_8S\}$ **2** (top-right) and the $\{Mo_{72}V_{30}\}$ **3** (bottom). The scheme represents the conditions which lead to control of the assembly process and the structural transformations between the POM species. Mo: purple polyhedra, V: orange polyhedra, S: yellow spheres and O: red spheres.

3.1.5 Summary

We have reported the synthesis and structural studies of an unprecedented mixed metal sulfite Dawson-based structure $(NH_4)_{10}[Mo^{VI}_{11}V^{V}_{5}V^{IV}_{2}O_{52}(\mu_9\text{-}SO_3)(Mo^{VI}_{6}V^{V}O_{22})]\cdot 14\ H_2O$ **2**, and a ligand triggered structural evolution process of the parent cluster $\{Mo_{11}V_7S\}$ to $\{Mo_{17}V_8S\}$ which consists the largest sulfite-based POM reported so far. The accurate control of the reaction parameters allowed us to selectively isolate compounds **1** and **2**. In

this respect we used mass spectrometry to 'scan' the reaction parameters of **1** to help identify potentially novel and interesting cluster architectures in solution before 'discovery' by crystallisation. The use of the sulfite anion is crucial for the successful isolation of both products since it acts as a pH controller and heteroanion template. In addition we have shown that it is possible to utilise reactive non-lacunary polyoxometalate-based species as synthons to trigger the formation of new cluster types, as well as demonstrating a parent-to-child 'crowning' of the precursor $\{Mo_{11}V_7S\}$ (Figure 44). The further development of this synthetic approach will allow the isolation of novel and larger structures as well as to better understand the mechanistic details of the assembly of the $\{Mo_{72}V_{30}\}$ Keplerate cluster.

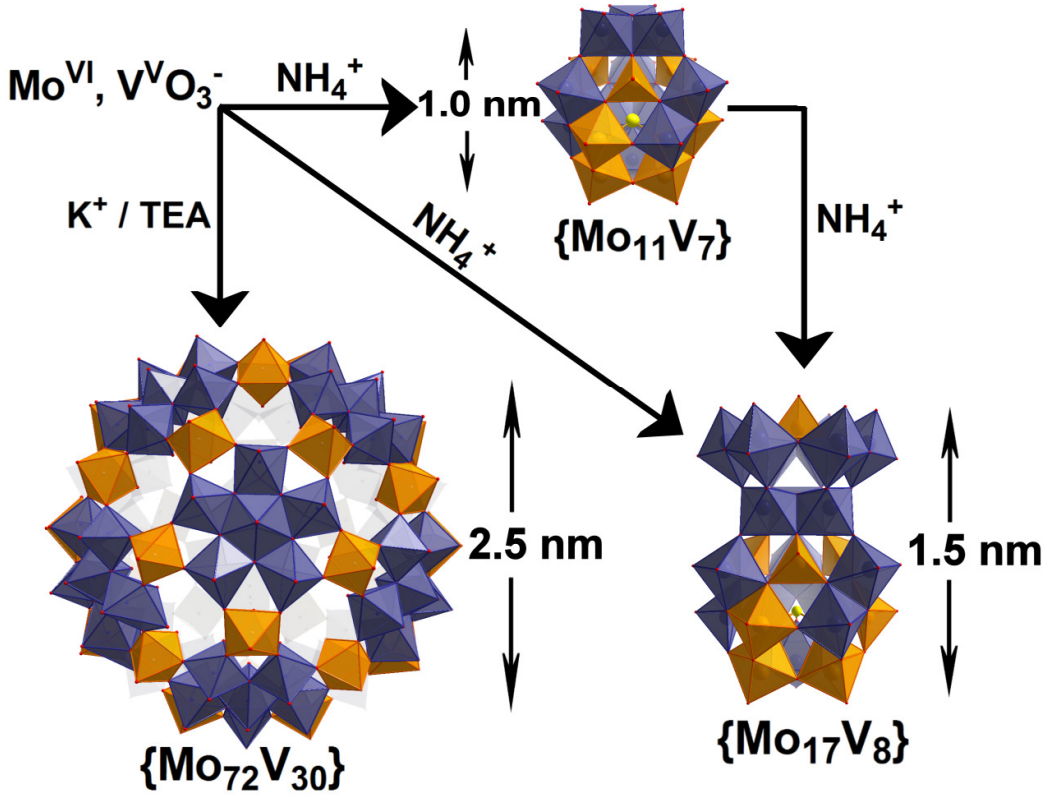

Figure 44: Summary of the different mixed-metal POMs isolated by using sulfite as a heteroanion. The different synthetic routes are shown to demonstrate how the self-assembly process can be controlled by accurate selection of the parameters of the reaction, especially the cation involved in solution. Mo: purple polyhedra, V: orange polyhedra, S: yellow spheres and O: red spheres.

3.2 Selenite-based Mixed-Metal Polyoxometalates

In the previous chapter (*Section 3.1.*) we have reported the characterization of two novel sulfite-based polyoxometalates with unprecedented mixed-metal/valence archetypes, $[Mo^{VI}_{11}V^{V}_{5}V^{IV}_{2}O_{52}(\mu_9\text{-}SO_3)]^{7-}$ $\{Mo_{11}V_7S\}$ and $[Mo^{VI}_{11}V^{V}_{5}V^{IV}_{2}O_{52}(\mu_9\text{-}SO_3)(Mo^{VI}_{6}V^{V}O_{22})]^{10-}$ $\{Mo_{17}V_8S\}$, and we showed the use of reactive POM-based species as secondary building units towards the design of higher nuclearity architectures. In an effort to further investigate the effect of the geometry and size of the incorporated heteroanions from Group XVI, we studied the implication of the pyramidal selenite heteroanion within the molybdenum and vanadium mixed-metal systems. Herein we report the synthesis, solid state and solution characterization of a new family of selenite-based mixed-metal and mixed-valence polyoxometalates namely: **{**$Mo_{12}V_{10}Se_8$} = $K_{10}[Mo^{VI}_{12}V^{V}_{10}O_{58}(SeO_3)_8]\cdot 18H_2O$ **4** and $(NH_4)_6K_4[Mo^{VI}_{12}V^{V}_{10}O_{58}(SeO_3)_8]\cdot 18H_2O$ **5**; $\{Mo_{11}V_7Se\}$ = $K_7[Mo^{VI}_{11}V^{V}_{5}V^{IV}_{2}O_{52}(\mu_9\text{-}SeO_3)]\cdot 31H_2O$ **6** and $(NH_4)_4K_3[Mo^{VI}_{11}V^{V}_{5}V^{IV}_{2}O_{52}(\mu_9\text{-}SeO_3)]\cdot 29H_2O$ **7**; $\{Mo_{17}V_8Se\}$ = $(NH_4)_7K_3[Mo^{VI}_{11}V^{V}_{5}V^{IV}_{2}O_{52}(\mu_9\text{-}SeO_3)(Mo_6VO_{22})]\cdot 40H_2O$ **8**; and $\{Mo_{30}V_{16}Se_{10}\}$ = $(NH_4)_{19}K_3[Mo^{VI}_{20}V^{V}_{12}V^{IV}_{4}O_{99}(SeO_3)_{10}]\cdot 36H_2O$ **9**.

3.2.1 Isolation of a new family of HPOMs *via* pH and cation control

The addition of $KV^{V}O_3$ to a hot aqueous solution containing $K_2Mo^{VI}O_4$ leads to a deep yellow solution which turned dark brown after the sequential addition of K_2SeO_3 and $NH_2NH_2\cdot 2HCl$. The reaction mixture was then cooled down to room temperature and the pH was adjusted to 1.5 by drop-wise addition of a 3M HCl solution. Dark orange rhomboid crystals of $K_{10}[Mo^{VI}_{12}V^{V}_{10}O_{58}(SeO_3)_8]\cdot 18H_2O$ **4** appeared after two days. Crystals of **4** were collected from the solution and the mother liquor was left to evaporate at room temperature. After three days dark hexagonal crystals of $K_7[Mo^{VI}_{11}V^{V}_{5}V^{IV}_{2}O_{52}(\mu_9\text{-}SeO_3)]\cdot 29H_2O$ **6** were formed alongside further crystals of **4**. In an attempt to obtain pure crystals of **6**, we mapped this K^+-{Mo:V} system over a wide range of pH values and observed that when the pH was adjusted to 3.0 after the addition of the reducing agent

$NH_2NH_2{\cdot}2HCl$, crystals of **6** formed within a week (Figure 45). This systematic process was analysed using IR spectroscopy (Figure 46) and single crystal X-ray diffraction.

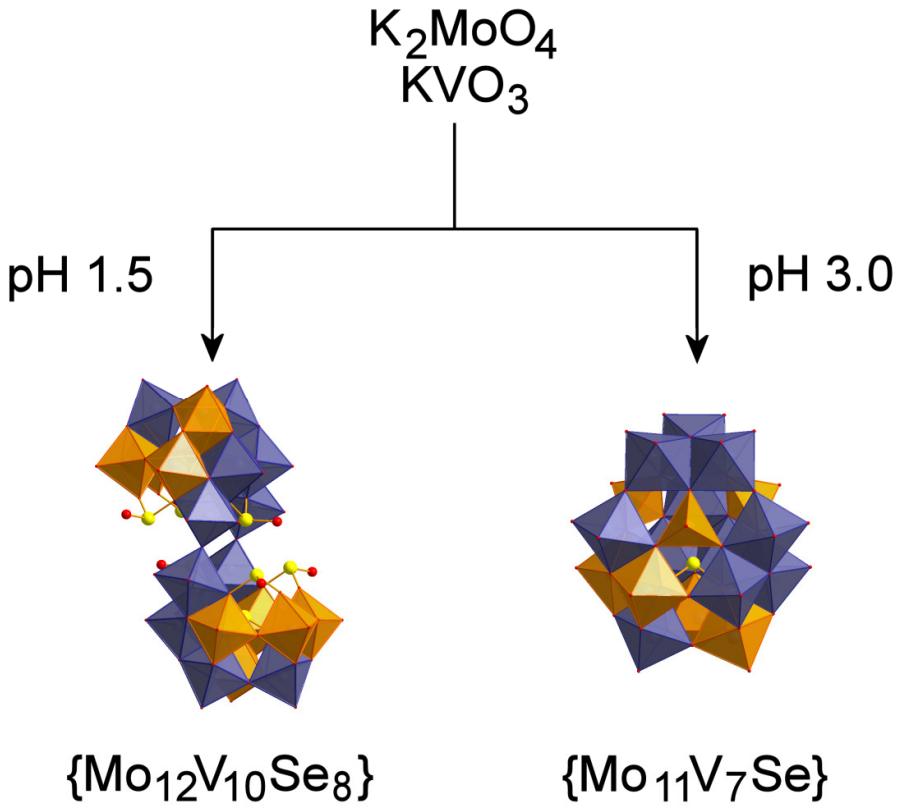

Figure 45: Summary of the reaction between K_2MoO_4 and KVO_3 upon addition of K_2SeO_3 and the reducing agent $NH_2NH_2{\cdot}2HCl$. At pH 1.5 crystals of $\{Mo_{12}V_{10}Se_8\}$ **4** (left) are isolated, whereas if the pH is increased to 3.0, crystals of $\{Mo_{11}V_7Se\}$ **6** (right) are obtained instead. Mo: purple polyhedra, V: orange polyhedra, Se: yellow spheres and O: red spheres.

The first batch of crystals (1st yield, blue spectrum in Figure 46) corresponded to the isolation of compound **4**, which was later confirmed by X-ray diffraction (Figure 47). The spectrum shows three characteristic bands between 1000 – 600 cm^{-1} which correspond to the stretching bands of the M=O groups (M = Mo and V) and to the SeO_3^{2-} anion. After collecting the crystals of **4**, the mother liquor was left to evaporate. Three days later, we collected a second batch of crystals (2nd yield, brown spectrum in Figure 46) and as

observed in the IR spectrum, it does look like compound **4** but the shape of the IR bands within the region of 1000 – 600 cm^{-1} are not as intense and sharp as in the case of **4**. This fact was explained later on, when after further evaporation of the mother liquor, a third batch of crystals was obtained (3rd yield, green spectrum Figure 46) which corresponded to compound **6**, also confirmed by X-ray diffraction (Figure 48). The IR spectrum of **6** revealed two significant bands within the 1000 – 600 cm^{-1} region instead of three as in the case of **4**. By comparing the three different spectra it seems reasonable to assign the brown spectrum as a mixture of both compounds **4** and **6**, since it looks like a mixture of both spectra.

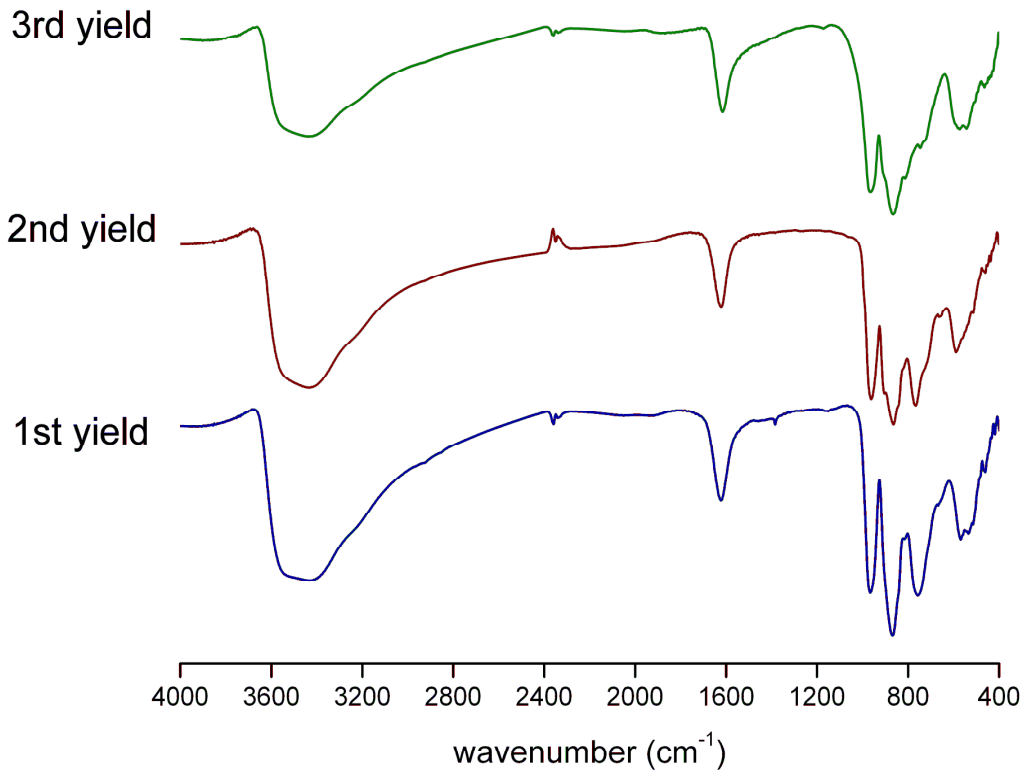

Figure 46: IR spectroscopic study of the crystallization times of **4** and **6**.

To prove that we obtained pure material of **4** and **6** we ran powder X-ray diffraction (PXRD) of both compounds (Figures 47 and 48). The experimental PXRD data was compared with the simulated XRD pattern from the single crystal structure. The PXRD were collected at room temperature, whereas single crystal data were collected at 150 K.

Due to temperature difference, the corresponding peaks in the two diffraction patterns have different shifts at different index space.

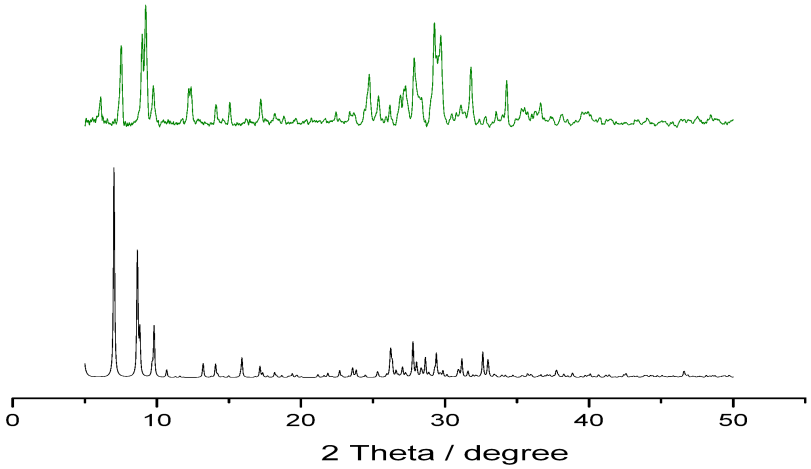

Figure 47: Comparison of the experimental (green line) and simulated (black line) X-ray diffraction powder patterns for compound **4**.

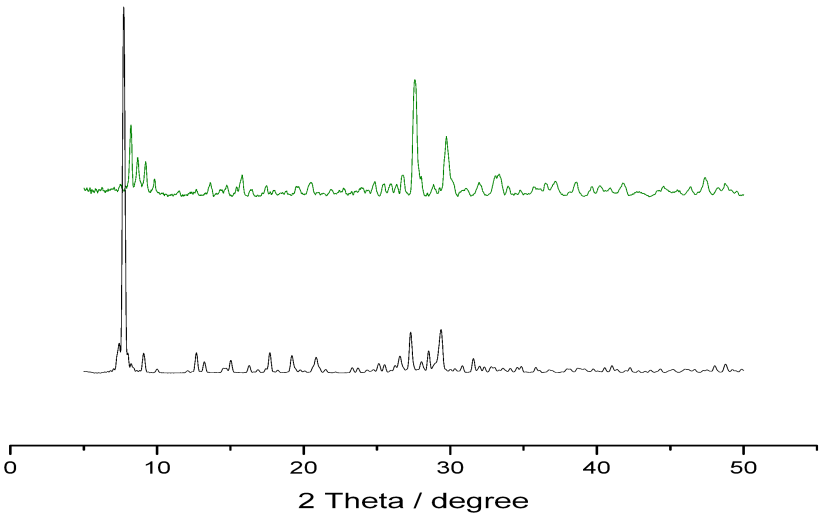

Figure 48: Comparison of the experimental (green line) and simulated (black line) X-ray diffraction powder patterns for compound **6**.

In our previous studies of sulfite-based mixed-metal polyoxometalates we demonstrated how the cation involved in the self-assembly process of the different building units had a profound effect on the isolation of the final product. In the present case, the successive

addition of $NH_4V^VO_3$, K_2SeO_3 and $NH_2NH_2{\cdot}2HCl$ into an acidic aqueous (37% HCl in water, 1:4 v/v) solution of $(NH_4)_6Mo^{VI}_7O_{24}$ (pH ~ 0) led to the formation of four new compounds after adjusting the pH by addition of a 7.5 M NH_3 aqueous solution. At a pH value of 1.5, crystals of $(NH_4)_6K_4[Mo^{VI}_{12}V^V_{10}O_{58}(SeO_3)_8]\cdot 18H_2O$ **5** formed within a week. Whereas when the pH was increased to 2.8, crystals of $(NH_4)_4K_3[Mo^{VI}_{11}V^V_5V^{IV}_2O_{52}(\mu_9\text{-}SeO_3)]\cdot 29H_2O$ **7** were isolated along with crystals of $(NH_4)_7K_3[Mo^{VI}_{11}V^V_5V^{IV}_2O_{52}(\mu_9\text{-}SeO_3)(Mo^{IV}_6V^VO_{22})]\cdot 29H_2O$ **8** after two weeks. To try to avoid the co-crystallization of compounds **7** and **8** we increased the pH of the solution to 4.5. Between pH 2.8 and 4.0 both species co-crystallised but between pH 4 and 4.5 only crystals of **7** were isolated. When the pH was increased to 5.0, crystals of $(NH_4)_{19}K_3[Mo^{VI}_{20}V^V_{12}V^{IV}_4O_{99}(SeO_3)_{10}]\cdot 36H_2O$ **9** were formed within ten days; whereas if the pH was increased to 6.0 yellow crystals of the already known $K_7[Mo^{VI}_8V^V_5O_{40}]\cdot 9H_2O$[219] were formed instead (see Figure 49). Above this pH the reaction mixture was oxidized rapidly by air and only crystals of $[V_{10}O_{28}]^{6-}$ were obtained.[46]

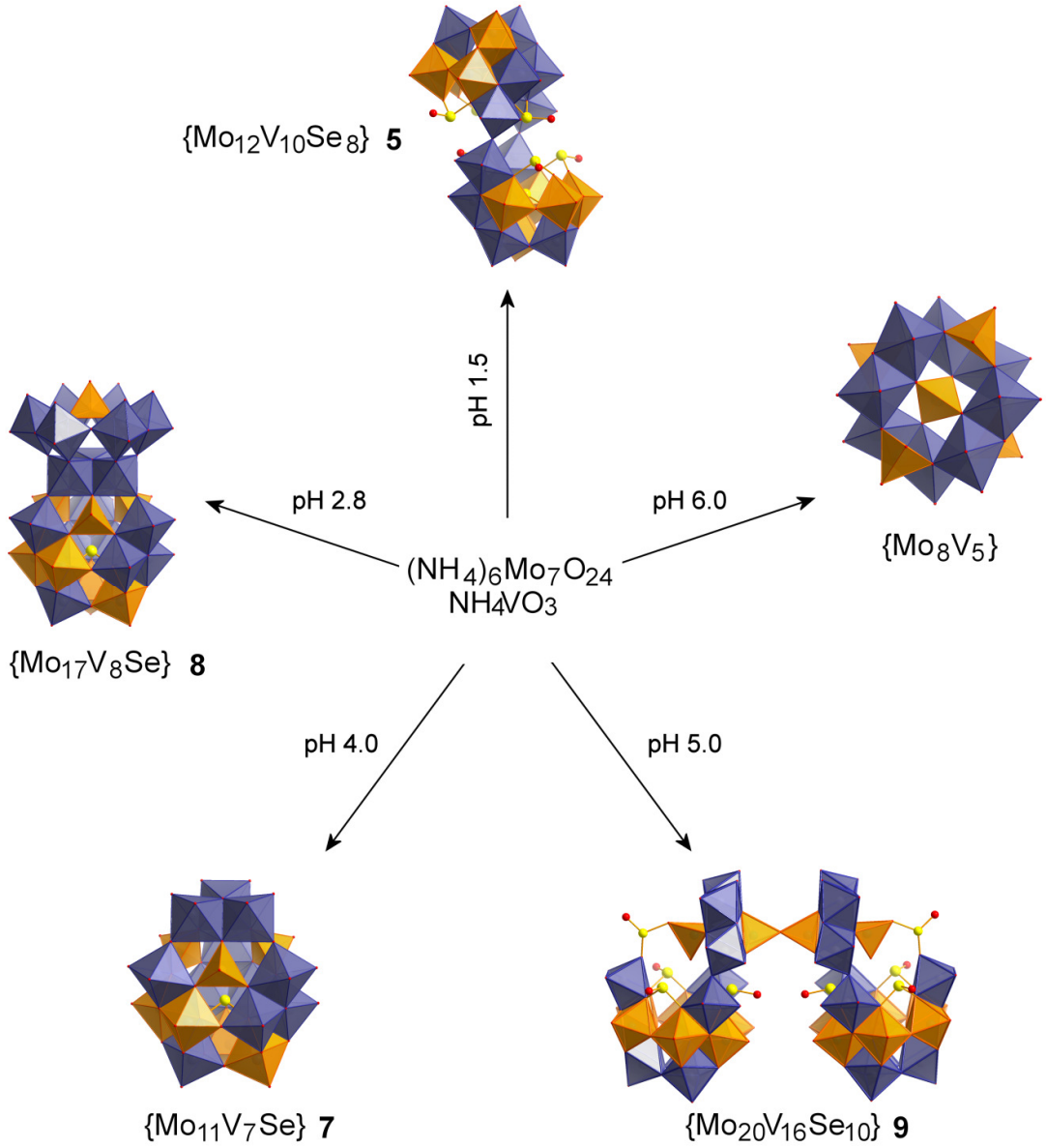

Figure 49: Summary of the reactions between ammonium metavanadate and ammonium molybdate upon addition of the selenite heteroanion and the reducing agent. As a function of the final pH five different materials were obtained: $\{Mo_{12}V_{10}Se_8\}$ = $(NH_4)_6K_4[Mo^{VI}_{12}V^{V}_{10}O_{58}(SeO_3)_8]\cdot 18H_2O$ **5**; $\{Mo_{11}V_7Se\}$ = $(NH_4)_4K_3[Mo^{VI}_{11}V^{V}_{5}V^{IV}_{2}O_{52}(\mu_9\text{-}SeO_3)]\cdot 29H_2O$ **7**; $\{Mo_{17}V_8Se\}$ = $(NH_4)_7K_3[Mo^{VI}_{11}V^{V}_{5}V^{IV}_{2}O_{52}(\mu_9\text{-}SeO_3)(Mo_6VO_{22})]\cdot 40H_2O$ **8**; $\{Mo_{30}V_{16}Se_{10}\}$ = $(NH_4)_{19}K_3[Mo^{VI}_{20}V^{V}_{12}V^{IV}_{4}O_{99}(SeO_3)_{10}]\cdot 36H_2O$ **9**, and $\{Mo_8V_5\}$ =

$K_7[Mo^{VI}_8V^{V}_5O_{40}]\cdot 9H_2O$. Mo: purple polyhedra, V: orange polyhedra, Se: yellow spheres and O: red spheres.

Further studies into the effect of the cation revealed that when K_2SeO_3 was replaced by Na_2SeO_3 within the ammonium mixed metal system and in the pH range 2.5 to 4.0, crystals of $(NH_4)_{15}[Na_3(H_2O)_5(Mo_{11}V_7O_{52})(\mu_9\text{-}SeO_3))(Mo_5V_4O_{24}(SeO_3)_4)]\cdot 10H_2O$ **10** were formed after two weeks (Figure 50). Under these synthetic conditions, where there is a Na^+/NH_4^+ cation mixture, compound **10** always co-crystallised with $[V_{10}O_{28}]^{6-}$ and crystals of $\{Mo_{11}V_7Se\}$, with compound **10** being the minority product. For that reason the amount of data for compound **10** presented here is limited.

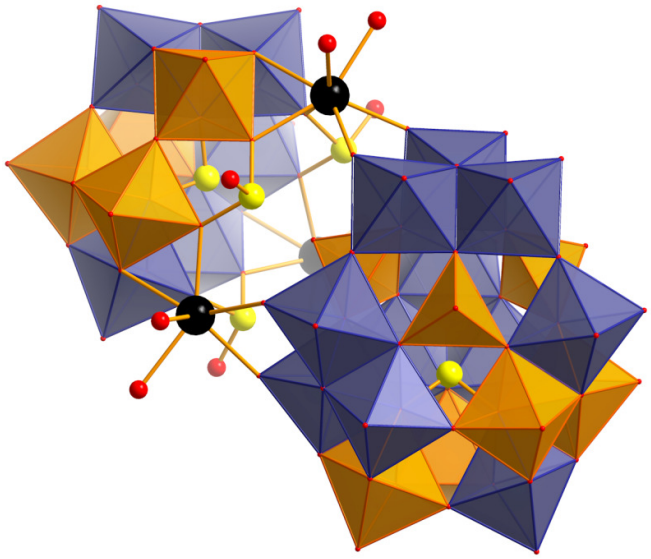

$\{Na_3(Mo_{11}V_7Se)(Mo_5V_4Se_4)\}$

Figure 50: Polyhedral representation of compound **10**. The $\{Mo_{11}V_7Se\}$ unit, analogous to compounds **6** and **7**, is linked to the $\{Mo_5V_4Se_4\}$ building unit *via* three sodium cations. Mo: purple polyhedra, V: orange polyhedra, Se: yellow spheres, Na: black spheres and O: red spheres.

At this point it is interesting to notice that: (i) the accurate selectivity of the experimental parameters was crucial for the isolation of the new archetypes; (ii) the ionic radius of the heteroanion involved (r_{at} = 1.17 Å), along with its pyramidal geometry, affected the final

archetype and led to unique unsaturated cages such as **{**$Mo_{12}V_{10}Se_8$} and {$Mo_{20}V_{16}Se_{10}$} and (iii) we have been able to unveil a number of new coordination modes of the selenite anion, within the same inorganic framework. The different coordination modes have an impact on the self-assembly process of the different building units involved in the reaction mixtures, leading to a wide range of novel structural motifs. Further discussion on these points will be addressed over the next sections.

3.2.2 Structural description of the selenite-molybdovanadate clusters

3.2.2.1 The novel {$Mo_{12}V_{10}Se_8$} archetype in 4 and 5

Crystallographic studies revealed that **4** and **5** could be formulated as $K_{10}[Mo^{VI}_{12}V^{V}_{10}O_{58}(SeO_3)_8]\cdot 18H_2O$ and $(NH_4)_6K_4[Mo^{VI}_{12}V^{V}_{10}O_{58}(SeO_3)_8]\cdot 18H_2O$ respectively. The anion $[Mo^{VI}_{12}V^{V}_{10}O_{58}(SeO_3)_8]^{10-}$, common in both compounds, adopts an S-shaped topology analogous to the 22-isopolytungstate cluster $[H_4W_{22}O_{74}]^{12-}$, previously reported by Cronin *et al.*.[35] A direct comparison between these two clusters reveals a similar framework, although the hetero-POM {$Mo_{12}V_{10}Se_8$} cluster (1.668(1) nm in length and 1.022(4) nm wide) is slightly smaller and wider than the iso-POM {W_{22}} analogue (1.808(2) nm in length and 0.994(1) nm in wide) (see Figure 51). This difference in size between the two compounds can be attributed to (i) the distance between the bridging WO_6 octahedra 3.794(1) Å with an angle of 171.0(8)º, which is larger than in the case of **4** and **5** with an Mo-O-Mo angle of 133.6(3)º; and (ii) to the existence of the W-O-W bridge between the two WO_6 bridges that connect the two {W_{11}} subunits 3.341(1) Å, whereas the is the case of **4** and **5** there is no Mo-O-Mo bridge leading to a longer distance between the two MoO_6 centres, 7.077(4) Å. The absence of the latter mentioned bridge in the case of **4** and **5** is caused by the fact that the four MoO_6 octahedra belonging to the bridge have two *cis* terminal Mo=O groups each, a structural feature that we have previously seen in compounds **1** and **2**. On the other hand, the rearrangement of the different MO_6 octahedra which form the {$Mo_6V_5Se_4$} subunit in **4** and **5** is completely different to the {W_{11}} subunit observed in {W_{22}}. This could be as a consequence of the incorporation of the four

SeO_3^{2-} heteroanions, one in the middle of the $\{Mo_6V_5\}$ cage and the other three alternating vertices with the MO_6 moieties from the top layer of the $\{Mo_6V_5\}$ cage.

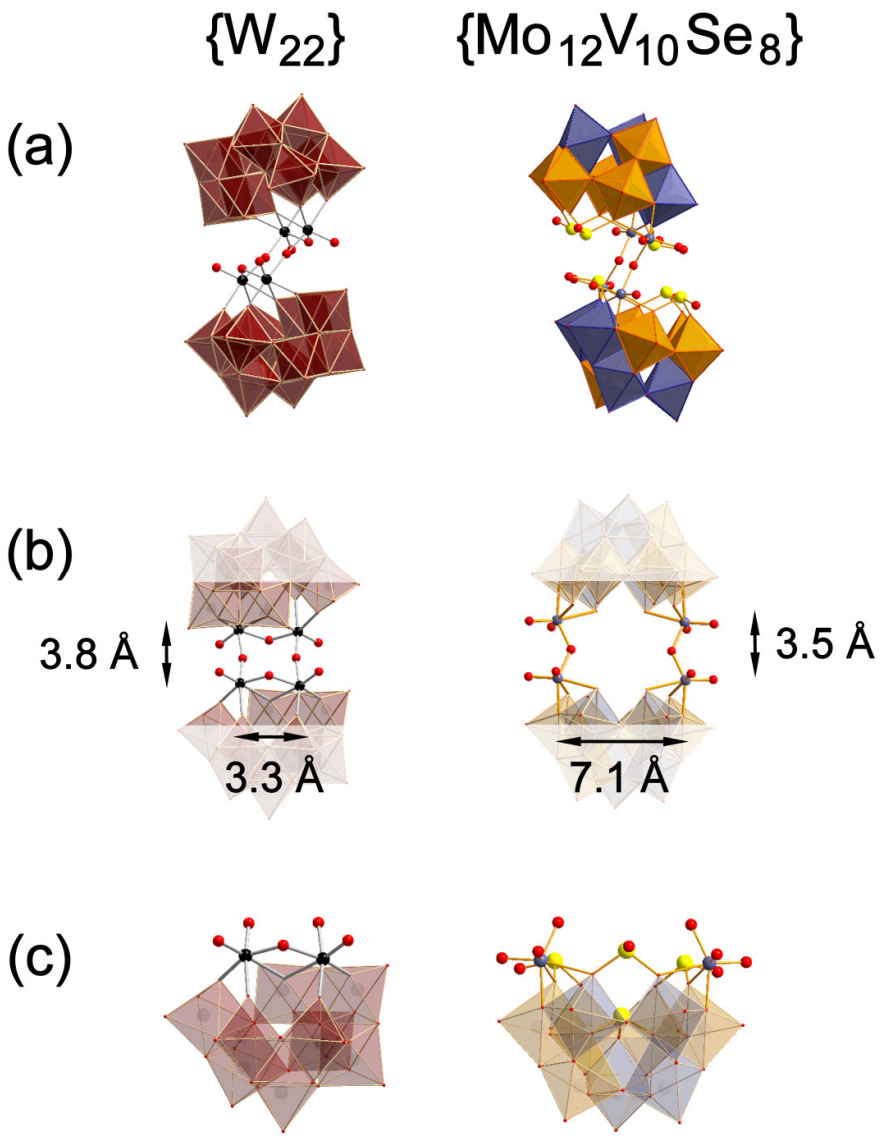

Figure 51: Combination of ball-and-stick and polyhedral representation of (a) $\{W_{22}\}$ *versus* $\{Mo_{12}V_{10}Se_8\}$; (b) μ-O^{2-} bridge distances between the MO_6 octahedra; and (c) representation of the $\{W_{11}\}$ and $\{Mo_6V_5Se_4\}$ subunits corresponding to each cluster. Mo: purple polyhedra/spheres, V: orange polyhedra, W: black spheres; Se: yellow spheres and O: red spheres.

As was previously discussed, the $\{Mo_{12}V_{10}Se_8\}$ cluster is built up from two $\{Mo_6V_5Se_4\}$ subunits linked by two μ_2-oxo bridges in *trans* fashion. Each subunit can be described as a basket where the $[Mo^{VI}_4V^{V}_5O_{24}(\mu_9\text{-}SeO_3)]^{-1}$ cap is connected to the $[Mo^{VI}_2Se^{IV}_3O_{14}]^{4-}$ belt *via* vertices of alternating SeO_3^{2-} pyramids and MoO_6 octahedra. Whilst the Mo atoms are crystallographically distinguishable in the belt, the metal sites in the cap are disordered. The assignment of formal charges on the metal ions was made on the basis of charge balance considerations for the entire compound, combined with bond valance sum (BVS) calculations,[214] redox titrations, and elemental analysis as well as high resolution electrospray mass spectroscopy. The Mo atoms in the MoO_6 octahedra belonging to the belt have the formal oxidation state VI (BVS_{av} = 5.82) and are coordinated by two terminal oxo groups in *cis*-position, with Mo = O bonds of 1.70(1) Å, one μ-O^{2-}, with Mo – O bond of 1.90(8) Å, and three μ_3-O^{2-} moieties, with Mo – O bonds spanning 1.98(1) – 2.28(1) Å.

An important feature of the $\{Mo_{12}V_{10}Se_8\}$ cluster is the incorporation of eight SeO_3^{2-} heteroanions with three distinct bridging coordination modes (Figure 52): (a) one μ_9-SeO_3 bridging anion occupying the central part of each cap; (b) one (μ,μ)-SeO_3 bridging anion in each belt; and (c) two (η,μ)-SeO_3 bridging anions in each belt. All the Se atoms have the formal oxidation state IV (BVS_{av} = 3.94). Bond distances for the Se atoms in the SeO_3^{2-} pyramids are described in Table 5.

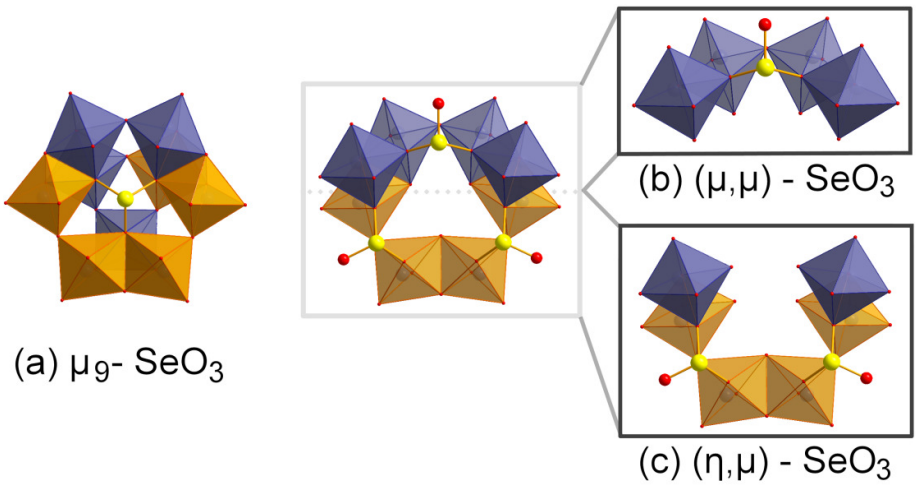

Figure 52: Combination of ball-and-stick and polyhedral representations of the coordination modes that the SeO_3^{2-} heteroanion exhibits in $\{Mo_{12}V_{10}Se_8\}$. (a) bird-eye-view of the $[Mo^{VI}_4V^{V}_5O_{24}(\mu_9\text{-}Se(1)O_3)]^{-1}$ cap; (b) and (c) bird-eye-view of the

$[Mo^{VI}_2Se^{IV}_3O_{14}]^{5-}$ belt built up *via* vertices of alternating (μ,μ)-$Se(3)O_3^{2-}$ and (η,μ)-$Se(2)O_3^{2-}$ pyramids and MoO_6 octahedra. Mo: purple polyhedra, V: orange polyhedra, Se: yellow spheres and O: red spheres.

Table 5: Selected interatomic distances and angles relevant to the coordination sphere of the SeO_3^{2-} groups in $\{Mo_{12}V_{10}Se_4\}$ (see Appendix Section 7.3).

bond length [Å]		angles [°]	
Se(1)-O(16)	1.69(1)	O(16)-Se(1)-O(16A)	98.1(9)
Se(1)-O(17)	1.69(1)	O(16)-Se(1)-O(17)	99.3(6)
Se(2)-O(5)	1.62(1)	O(16A)-Se(1)-O(17)	99.3(6)
Se(2)-O(20)	1.72(1)	O(5)-Se(2)-O(20)	106.3(7)
Se(2)-O(21)	1.77(1)	O(5)-Se(2)-O(21)	103.0(7)
Se(3)-O(30)	1.70(1)	O(20)-Se(2)-O(21)	98.6(6)
Se(3)-O(9)	1.76(1)	O(30)-Se(3)-O(9)	117.2(1)
		O(30)-Se(3)-O(9A)	117.2(1)
		O(9)-Se(3)-O(9A)	102.8(9)

As was mentioned before, $\{Mo_{12}V_{10}Se_8\}$ could be synthesized at different pH values and by using different cations in solution. This fact led to the crystallization of $\{Mo_{12}V_{10}Se_8\}$ in different crystal systems, with different packing modes, as a function of the pH and cation used. When we used potassium as a cation, compound **4** crystallized in the space group *C2/m* and every $\{Mo_{12}V_{10}Se_8\}$ unit is connected to each other *via* potassium cations in a *trans*-fashion (Figure 53a). When ammonium and potassium cations were used, compound **5** crystallized in the *C2/c* space group and every $\{Mo_{12}V_{10}Se_8\}$ subunit is connected through potassium cations to the neighbour $\{Mo_{12}V_{10}Se_8\}$ subunit in a *zigzag* fashion (Figure 53b).

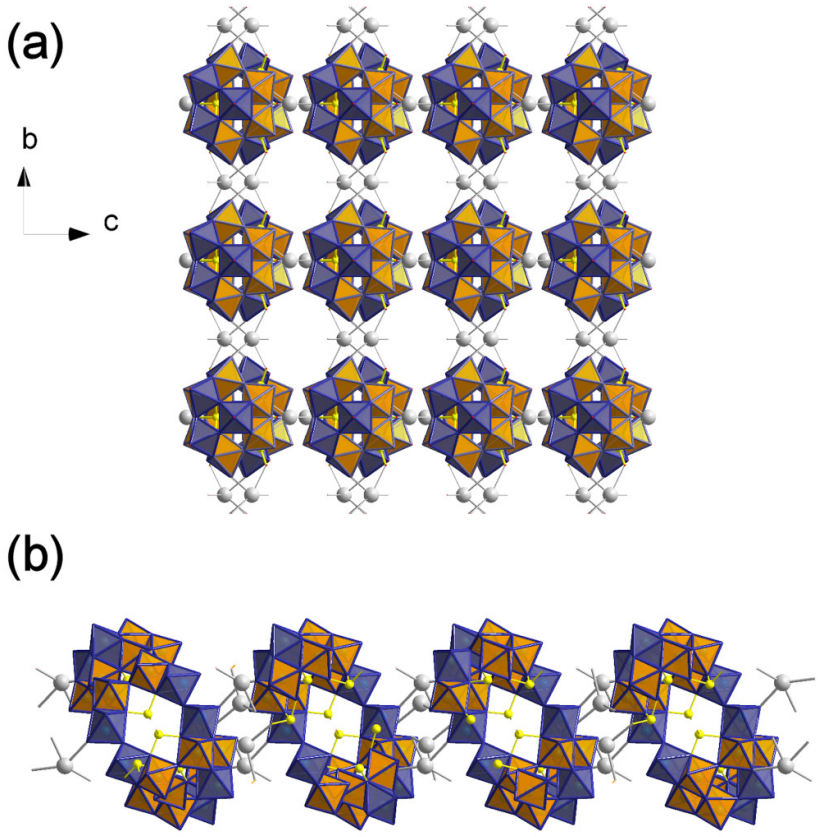

Figure 53: Packing modes for $\{Mo_{12}V_{10}Se_8\}$: (a) in *C2/m* for **4** (view from the *a* axis) and (b) in *C2/c* for **5** (view from the *a* axis). Mo: purple polyhedra, V: orange polyhedra, Se: yellow spheres; K: grey spheres and O: red spheres.

3.2.2.2 The $\{Mo_{11}V_7Se\}$ archetype in 6 and 7

Compounds **6** and **7** contain $[Mo^{VI}_{11}V^{V}_{5}V^{IV}_{2}O_{52}(\mu_9\text{-}SeO_3)]^{7-}$ anions (Figure 54), which are isostructural to the sulfite-based Dawson-like structure $[Mo^{VI}_{11}V^{V}_{5}V^{IV}_{2}O_{52}(\mu_9\text{-}SO_3)]^{7-}$ discussed in *Section 3.1.1*. The disordered egg-shaped cage can be split in two hemispheres. As before, the upper hemisphere consists of three edge-sharing MoO_6 octahedra connected to the upper belt *via* vertices of alternating $V^{V}O_4$ tetrahedra and MoO_6 octahedra. The remaining four V positions (two V^{V} and two V^{IV}) are crystallographically refined as being disordered over the nine MO_6 octahedra positions in the lower hemisphere

of the cluster, where its cavity is occupied by the μ_9-SeO_3 bridging anion. Whilst the Mo and V atoms are crystallographically distinguishable in the upper hemisphere, the metal sites in the lower hemisphere are disordered. Therefore, the assignment of formal charges on the metal ions was made on the basis of charge balance considerations for the entire compound, combined with bond valance sum (BVS) calculations,[214] redox titrations, and elemental analysis as well as high resolution cryospray mass spectroscopy.

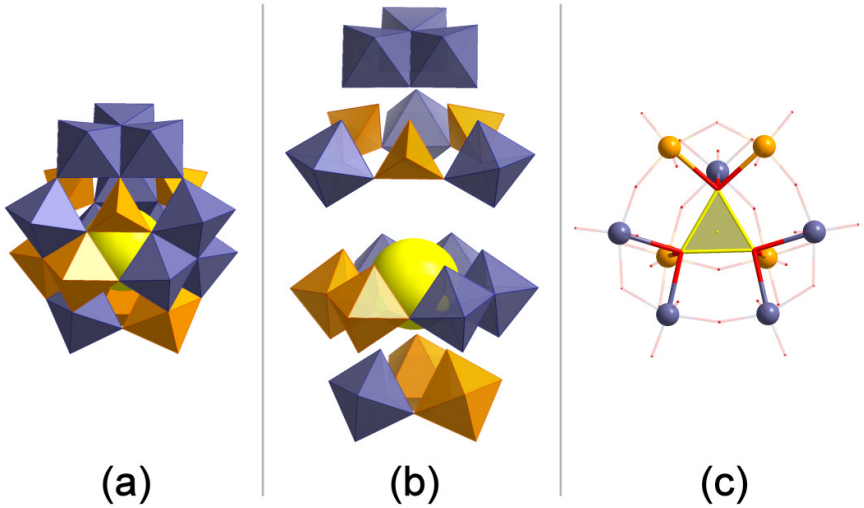

Figure 54: (a) Polyhedral representation of $\{Mo_{11}V_7Se\}$ and (b) its two hemispheres with the corresponding belt and cap. (c) Ball-and-stick representation of the lower hemisphere where it is shown the coordination mode of the μ_9-SeO_3 heteroanion (yellow pyramid). Mo: purple polyhedra, V: orange polyhedra, Se: yellow spheres and O: red spheres.

All the Mo atoms have the formal oxidation state VI (BVS_{av} = 5.89), the V atoms in the VO_4 tetrahedra are in the oxidation state V (BVS_{av} = 5.14) and the Se atom in the μ_9-SeO_3 in the oxidation state IV (BVS = 4.01). The V atoms in the VO_4 tetrahedra are coordinated by three μ_3-O^{2-} moieties, with V-O bonds spanning the range 1.722(4) – 1.755(4) Å, and one terminal oxo group with V=O bonds of 1.626(5) Å. The Mo atoms in the MoO_6 octahedra belonging to the upper hemisphere are coordinated by two terminal oxo groups in *cis*-positions, with Mo=O distances between 1.693(4) – 1.718(4) Å, one μ-O^{2-} moieties, with Mo-O bonds between 1.873(4) – 1.888(4) Å, and three μ_3-O^{2-} moieties, with Mo-O bonds in the range of 2.000(4) – 2.264(4) Å.

When only potassium is used as a cation, $\{Mo_{11}V_7Se\}$ crystallizes in the space group $P\bar{4}b2$ (Figure 55a), whereas if ammonium is also present in solution it crystallised in $R\bar{3}c$ (Figure 55b). The clusters in $P\bar{4}b2$ space group pack in herring bone patterns exhibiting rectangular cavities, while the clusters in $R\bar{3}c$ space group pack in trigonal patterns. Such arrangement leaves a triangular cavity between the $\{Mo_{11}V_7Se\}$ motifs with an interatomic K^+---K^+ distance of *ca.* 7.281(5)Å.

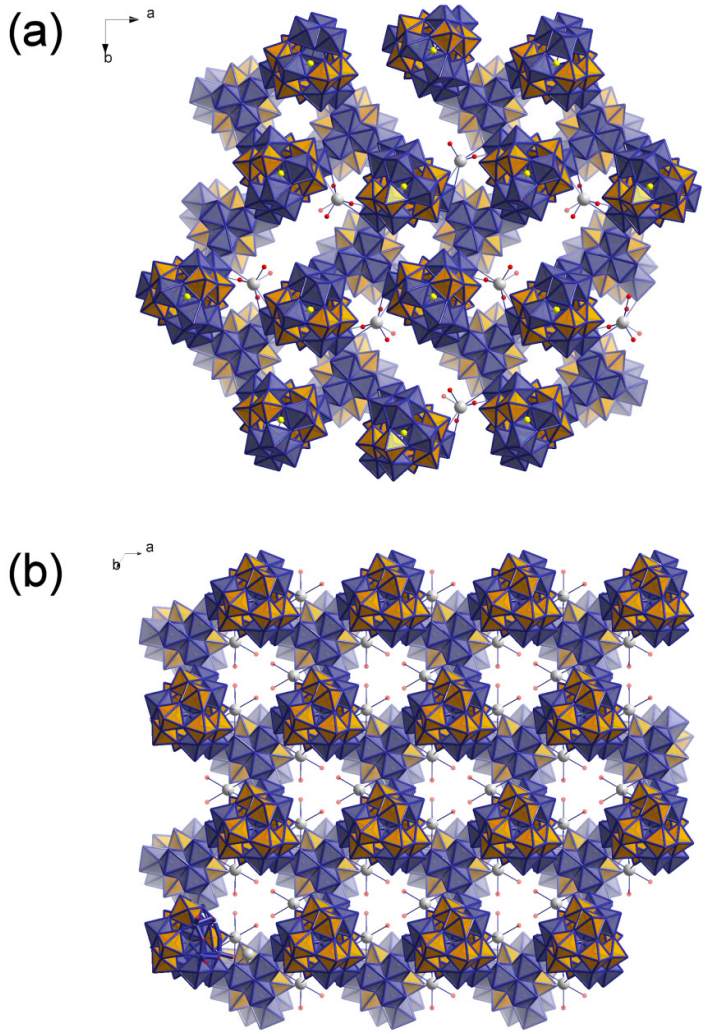

Figure 55: Packing modes for $\{Mo_{11}V_7Se\}$: (a) in $P\bar{4}b2$ for **6** (view from the *c* axis) and (b) in $R\bar{3}c$ for **7** (view from the *c* axis). Mo: purple polyhedra, V: orange polyhedra, Se: yellow spheres and O: red spheres.

3.2.2.3 The {$Mo_{17}V_8Se$} archetype in 8

$(NH_4)_7K_3[Mo^{VI}_{11}V^{V}_5V^{IV}_2O_{52}(\mu_9\text{-}SeO_3)(Mo^{VI}_6V^{V}O_{22})]\cdot 40H_2O$ **8** adopts the "Crowned"-Dawson-like structure, isostructural to the sulfite HPOMs previously discussed in *Section 3.1.2.*, and can be formulated as $[Mo^{VI}_{11}V^{V}_5V^{IV}_2O_{52}(\mu_9\text{-}SeO_3)(Mo^{VI}_6V^{V}O_{22})]^{10-}$ **8a**. It is built up from two parts: a disordered egg-shaped capsule $\{Mo^{VI}_{11}V^{V}_5V^{IV}_2O_{52}(\mu_9\text{-}SeO_3)\}$ identical to the $\{Mo_{11}V_7Se\}$ cage in **6** and **7**; and a $\{Mo^{VI}_6V^{V}O_{22}\}$ crown attached to the top of the Dawson-like capsule *via* six oxo bridges (Figure 56).

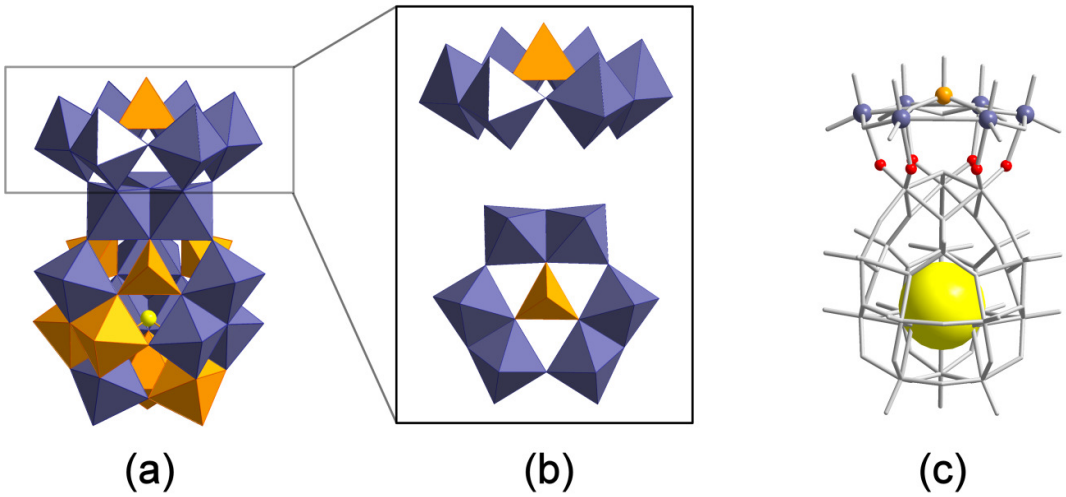

Figure 56: (a) Polyhedral representation of compound **8a**; (b) Polyhedral representation of the $\{Mo^{VI}_6V^{V}O_{22}\}$ crown which is formed from three pairs of corner-shared MoO_6 octahedral units comprising two terminal oxo groups and one VO_4 tetrahedron occupying the centre of the crown; and (c) combination of ball-and-stick and wire representation of **8a** highlighting the six oxo bridges through which the crown is attached to the $\{Mo^{VI}_{11}V^{V}_5V^{IV}_2O_{52}(\mu_9\text{-}SeO_3)\}$ body. Mo: purple polyhedra, V: orange polyhedra, Se: yellow spheres and O: red spheres.

While the Mo and V atoms are crystallographically distinguishable in the crown and in the upper hemisphere of the Dawson-like capsule, the metal sites in the lower hemisphere are disordered. Therefore, the assignment of formal charges on the metal ions was made on the basis of charge balance considerations for the entire compound, combined with bond

valance sum (BVS) calculations,[214] redox titrations, and elemental analysis as well as high resolution electrospray mass spectroscopy. All the Mo atoms have the formal oxidation state VI (BVS_{av} = 6.12), the V atoms in the VO_4 tetrahedra are in the oxidation state V (BVS_{av} = 5.14) and the Se atom in the μ_9-SeO_3 in the oxidation state IV (BVS = 3.94). The V atoms in the VO_4 tetrahedra are coordinated by three μ_3-O^{2-} moieties, with V-O bonds spanning the range 1.71(1) – 1.78(1) Å, and one terminal oxo group with V=O lengths between 1.61(1) – 1.62(1) Å. Whilst the Mo atoms in the MoO_6 octahedra belonging to the upper hemisphere exhibit two terminal oxo groups in *cis*-positions, with Mo=O bonds in the range of 1.67(1) – 1.69(1) Å, one μ-O^{2-} moieties, with Mo-O bonds between 1.870(9) – 1.88(1) Å, and three μ_3-O^{2-} moieties, with Mo-O bonds between 1.99(1) and 2.286(9) Å; the Mo atoms in the MoO_6 octahedra belonging to the crown exhibit two terminal oxo groups in *cis*-positions, with Mo=O bonds spanning the range 1.68(1) – 1.73(1) Å, three μ-O^{2-} moieties, with Mo-O lengths between 1.89(1) and 2.453(9) Å, and one μ_3-O^{2-} moieties, with Mo-O bonds between 2.21(1) and 2.23(1) Å.

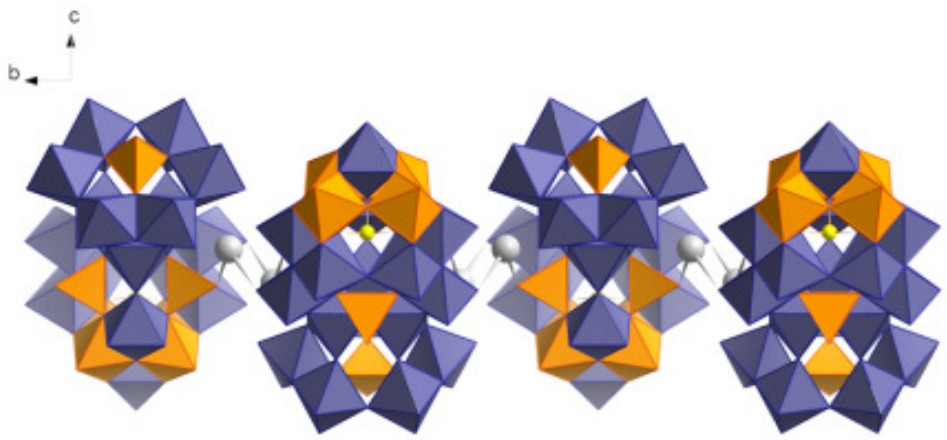

Figure 57: Polyhedra representation of the packing mode of **8a**, which crystallizes in the space group *Pnma*. Each $\{Mo_{17}V_8Se\}$ unit is linked to the next one *via* K^+ cations from the well-defined upper belt in an antiparallel arrangement. Mo: purple polyhedra, V: orange polyhedra, Se: yellow spheres and O: red spheres.

3.2.2.4 The $\{Mo_{20}V_{16}Se_{10}\}$ archetype in 9

$(NH_4)_{19}K_3[Mo^{VI}_{20}V^{V}_{12}V^{IV}_{4}O_{99}(SeO_3)_{10}]\cdot 36H_2O$ **9** is a new lacunary molybdovanadate cluster, templated by ten pyramidal heteroanions and can be formulated as $[Mo^{VI}_{20}V^{V}_{12}V^{IV}_{4}O_{99}(SeO_3)_{10}]^{22-}$ **9a**. It can be seen as a dimer of two $[Mo^{VI}_{10}V^{V}_{6}V^{IV}_{2}O_{50}(SeO_3)_5]^{11-}$ ($\{Mo_{10}V_8Se_5\}$) units which display a "δ"-shape morphology (Figure 58a). Each $\{Mo_{10}V_8Se_5\}$ unit can be split in two hemispheres in a similar fashion to the case of the egg-shaped Dawson archetype. The lower hemisphere is isostructural to the one we observed in $\{Mo_{11}V_7Se\}$, where the nine MO_6 octahedra positions are disordered Mo and V metal centres. In the upper hemisphere, however, the three VO_4 tetrahedra from $\{Mo_{11}V_7Se\}$ have been replaced by three (μ,μ)-SeO_3 anions and the three edge-sharing MoO_6 octahedra from the cap have been replaced by the $\{Mo_4V_2Se\}$ unit (Figure 58b). The upper cap is linked to the upper belt *via* three μ-O^{2-} bridges, one from the (μ,μ)-SeO_3 and the other two from the MoO_6 units.

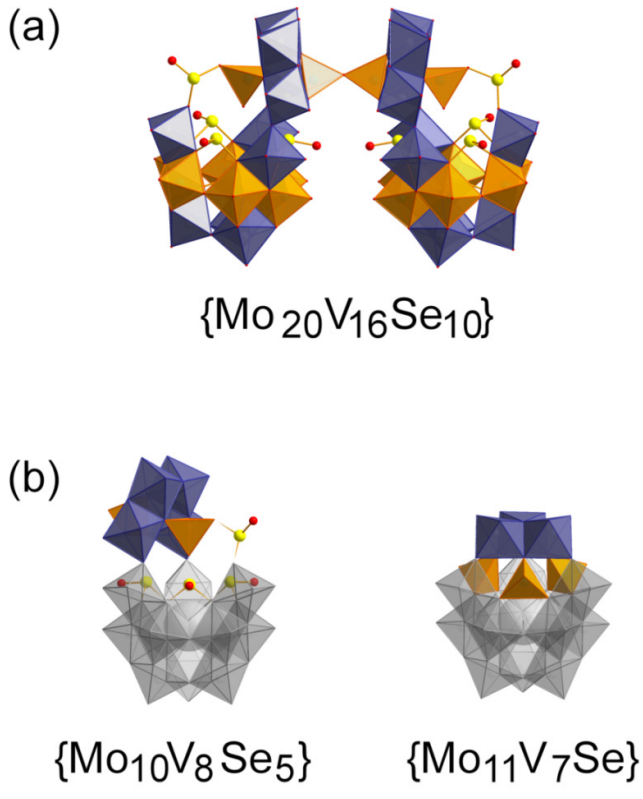

Figure 58: Combination of ball-and-stick and polyhedral representations of (a) compound **9a**; and (b) structural comparison between the monomer unit from compound **9a** and the

{$Mo_{11}V_7Se$}archetype found in **6a** and **7a**. Coloured polyhedra represent the substituted moieties. Mo: purple polyhedra, V: orange polyhedra, Se: yellow spheres and O: red spheres.

The Mo and V atoms are crystallographically distinguishable in the upper hemisphere of the cluster whereas as in the case of {$Mo_{11}V_7Se$} and {$Mo_{17}V_8Se$}, the metal sites in the lower hemisphere are disordered over the nine positions. Hence, the assignment of formal charges on the metal ions was made on the basis of charge balance considerations for the entire compound, combined with bond valance sum (BVS) calculations,[214] redox titrations, and elemental analysis. All the Mo atoms have the formal oxidation state VI (BVS_{av} = 5.92), the V atoms in the VO_4 tetrahedra are in the oxidation state V (BVS_{av} = 5.15) and the Se atoms in SeO_3 pyramids are in the oxidation state IV (BVS_{av} = 3.92). The Mo atoms in the MoO_6 octahedra belonging to the upper hemisphere are coordinated by two terminal oxo groups in *cis*-positions, with Mo=O bonds spanning the range 1.696(8) – 1.717(9) Å. Bond distance for the V atoms in the VO_4 tetrahedra and the Se atoms in the SeO_3^{2-} pyramids are described in Table 6 and 7 respectively. As in the case of {$Mo_{12}V_{10}Se_8$} (**4a** and **5a**) it is really fascinating to see such a variety of bridging coordination modes that the selenite heteroanions adopt within the same archetype (Figure 59): (a) one μ_9-$Se(1)O_3$ bridging anion occupying the central part of the lower hemisphere; (b) three (μ,μ)-SeO_3 bridging anion in the upper belt; and (c) one (η,η)-$Se(5)O_3$ bridging anion in the upper cap which adopts a more planar geometry in comparison with the pyramidal selenite from the upper belt.

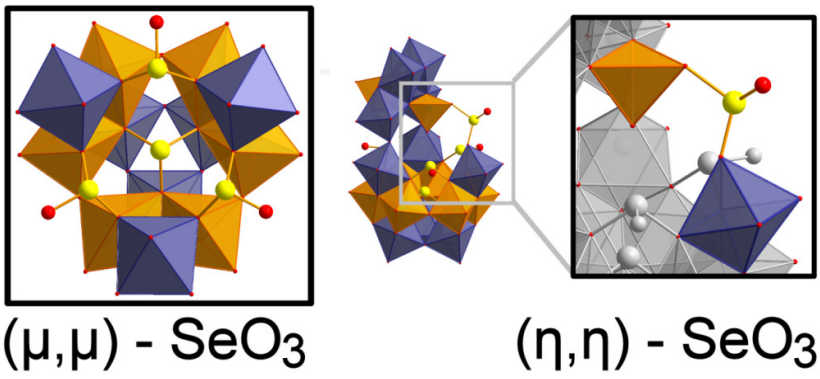

Figure 59: Coordination modes from the SeO_3^{2-} bridging anions found in **9a**. Mo: purple polyhedra, V: orange polyhedra, Se: yellow spheres and O: red spheres.

Table 6: Selected interatomic distances relevant for the coordination sphere of the vanadate atoms in compound **9** (see Appendix Section 7.8)**.**

Bond length [Å]			
V(10)-O(62)	1.666(9)	V(11)-O(41)	1.590(8)
V(10)-O(42)	1.666(8)	V(11)-O(44)	1.758(8)
V(10)-O(48)	1.714(8)	V(11)-O(43)	1.760(8)
V(10)-O(63)	1.763(4)	V(11)-O(78)	1.788(9)

Table 7: Selected interatomic distances and angles relevant to the coordination sphere for selenite atoms in compound **9**(see Appendix Section 7.8)**.**

Bond length [Å]			
Se(1)-O(18)	1.700(7)	Se(3)-O(16)	1.748(7)
Se(1)-O(4)	1.702(7)	Se(4)-O(38)	1.648(7)
Se(1)-O(9)	1.707(7)	Se(4)-O(25)	1.726(7)
Se(2)-O(13)	1.646(8)	Se(4)-O(17)	1.738(7)
Se(2)-O(10)	1.727(7)	Se(5)-O(51)	1.57(1)
Se(2)-O(39)	1.730(7)	Se(5)-O(68)	1.67(1)
Se(3)-O(15)	1.642(7)	Se(5)-O(78)	1.843(9)
Se(3)-O(14)	1.746(7)		
Angles [°]			
O(18)-Se(1)-O(4)	99.8(3)	O(14)-Se(3)-O(16)	98.0(3)
O(18)-Se(1)-O(9)	100.1(3)	O(38)-Se(4)-O(25)	103.6(4)
O(4)-Se(1)-O(9)	99.7(3)	O(38)-Se(4)-O(17)	103.4(4)
O(13)-Se(2)-O(10)	104.1(4)	O(25)-Se(4)-O(17)	99.0(4)
O(13)-Se(2)-O(39)	103.5(4)	O(51)-Se(5)-O(68)	120.0(10)
O(10)-Se(2)-O(39)	100.1(3)	O(51)-Se(5)-O(78)	107.6(7)
O(15)-Se(3)-O(14)	103.2(3)	O(68)-Se(5)-O(78)	111.8(5)
O(15)-Se(3)-O(1)	102.6(4)		

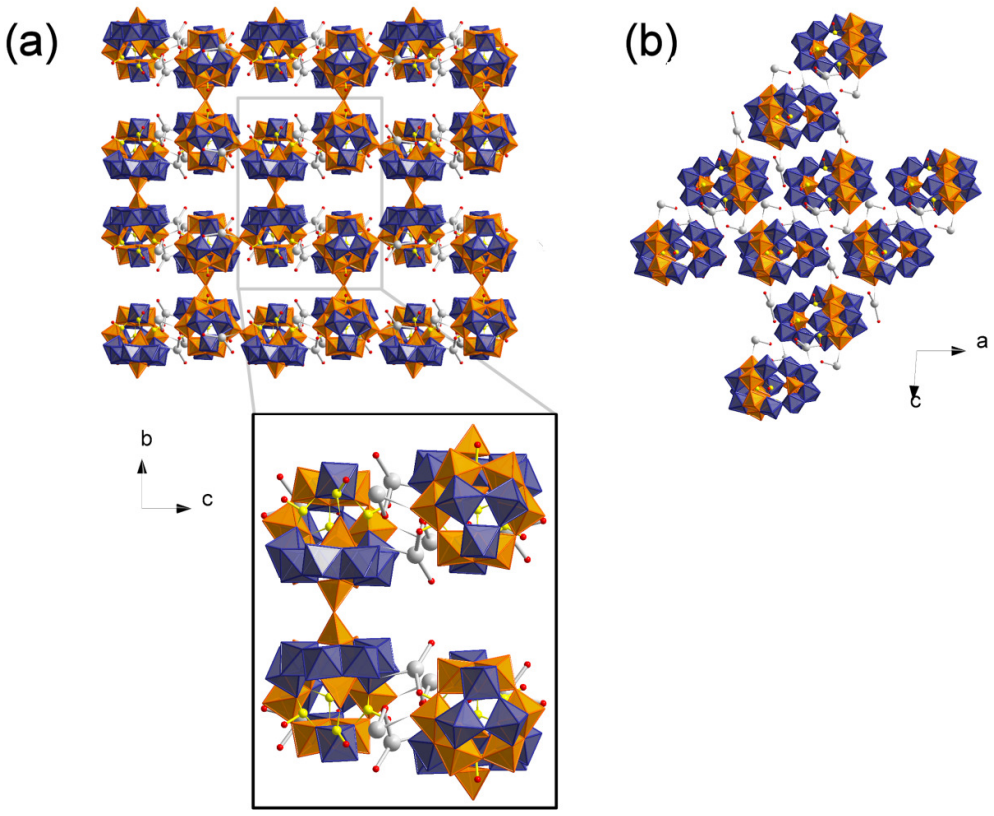

Figure 60: Polyhedra representation of the packing mode from **9a** in the space group $P2_1/m$ where a mirror plane pass across *b* axis and parallel to crystallographic *ac* plane. View from (a) the *a* axis and (b) the *b* axis. Each monomer unit from the $\{Mo_{20}V_{16}Se_{10}\}$ cluster is linked *via* K^+ cations to the monomer of the next $\{Mo_{20}V_{16}Se_{10}\}$ moiety in an antiparallel arrangement, leading to an overall *zigzag* layout between the different $\{Mo_{20}V_{16}Se_{10}\}$ units. From the *a* axis (a) it is visible how the arrangement of the different $\{Mo_{20}V_{16}Se_{10}\}$ units leads to the formation of a rectangular cavity of *ca.* 25.430(2) Å lengthways and *ca.* 8.505(2) Å widthways hosting potassium cations. Mo: purple polyhedra, V: orange polyhedra, Se: yellow spheres and O: red spheres.

3.2.2.5 The $\{Na_3(Mo_{11}V_7Se)(Mo_5V_4Se_4)\}$ archetype in 10

Crystallographic studies of **10** reveal that the discrete anion can be formulated as $[Na_3(H_2O)_5(Mo_{11}V_7O_{52}(\mu_9\text{-}SeO_3))(Mo_5V_4O_{24}(SeO_3)_4)]^{15-}$ **10a** (Figure 61a). Due to the co-crystallization of **10** with $\{Mo_{11}V_7Se\}$ and $[V_{10}O_{28}]^{6-}$ it was not possible to accurately

characterize and determinate the molecular formula of the titled compound. However, based on the crystallographic data combined with the bond valence sum calculations and elemental analysis, we can describe **10a** as being composed of one $[Mo_{11}V_7O_{52}(\mu_9\text{-}SeO_3)]^{n-}$ unit, isostructural to **5a** and **6a**, which is connected *via* three sodium cations to a $[Mo_5V_4O_{24}(SeO_3)_4]^{m-}$ unit. The $[Mo_5V_4O_{24}(SeO_3)_4]^{m-}$ moiety is isostructural to the lacunary Keggin $[XM_9O_{34}]^{x-}$,[92] where three (μ,μ)-SeO_3 bridging anions have been assembled on top of the trivacant cage (Figure 61b). Although all the Mo an V atoms are crystallographically undistinguishable in the $[Mo_5V_4O_{24}(SeO_3)_4]^{m-}$ cage and the lower hemisphere of the $[Mo_{11}V_7O_{52}(\mu_9\text{-}SeO_3)]^{n-}$ Dawson-like cluster, the upper hemisphere of the latter is well resolved with six Mo atoms in the MoO_6 octahedra with formal oxidation state VI (BVS_{av} = 5.95) and three V atoms in the VO_4 tetrahedra with oxidation state V (BVS_{av} = 5.09). The Mo atoms are coordinated by two terminal oxo groups in *cis*-positions, with Mo=O distances in the range of 1.687(7) and 1.711(7) Å, one μ-O^{2-} moiety, with Mo-O bonds between 1.875(7) – 1.902(8) Å, and three μ_3-O^{2-} moieties with Mo-O bonds spanning the range of 1.994(7) – 2.278(7) Å. The V atoms in the VO_4 tetrahedra are coordinated by three μ_3-O^{2-} units and one terminal oxo group V=O with distances between 1.723(8)-1.773(7) Å and 1.611(8) – 1.615(8) Å, respectively.

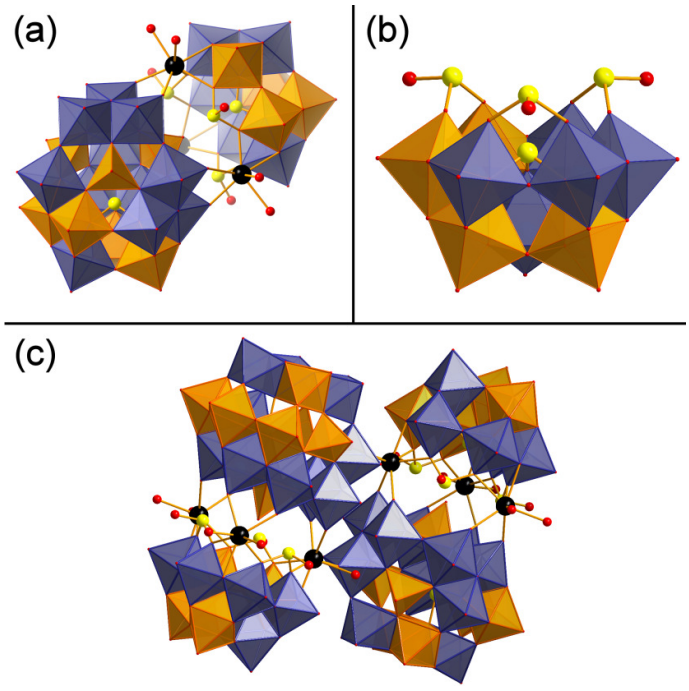

Figure 61: Ball-and-stick and polyhedral representations of (a) compound **10a**; (b) the $[Mo_5V_4O_{24}(SeO_3)_4]^{m-}$ cage templated by four selenite heteroanions (sodium cations have

been omitted for clarity); and (c) packing mode of **10a** in the space group $P\bar{1}$ where the clusters are linked together *via* the sodium cation in an antiparallel way. Mo: purple polyhedra, V: orange polyhedra, Se: yellow spheres and O: red spheres.

Once more it is interesting to notice the variety of coordination modes that the selenite anions exhibit within the same archetype (Figure 62): (a) the predominant μ_9-SeO_3 heteroatoms, previously observed in compounds **4 – 9**, which templates the central part of the $[Mo_{11}V_7O_{52}(\mu_9\text{-}SeO_3)]^{n-}$ and $[Mo_5V_4O_{24}(SeO_3)_4]^{m-}$ cages; and (b) the three (μ,μ)-SeO_3 bridging anions on top of the $[Mo_5V_4O_{24}(SeO_3)_4]^{m-}$ unit which were also observed in the assembly of compound **9**. All the Se atoms are SeO_3 pyramidal with oxidation state IV (BVS_{av} = 3.97) and selected interatomic distances and angles are shown in Table 8.

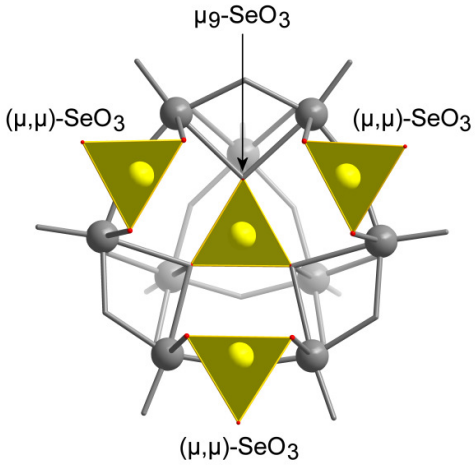

Figure 62: Representation of the $[Mo_5V_4O_{24}(SeO_3)_4]^{m-}$ cage highlighting its SeO_3 heteroanion coordination modes (yellow polyhedra). The cage is represented by grey ball-and-stick framework.

Table 8: Selected interatomic distances and angles relevant to the coordination sphere for the selenite atoms in **10**. Se(8) and Se(2) correspond to μ_9-SeO_3 in $[Mo_{11}V_7O_{52}(\mu_9\text{-}SeO_3)]^{n-}$ and $[Mo_5V_4O_{24}(SeO_3)_4]^{m-}$ respectively, whereas Se(1), Se(3) and Se(4) correspond to (μ,μ)-SeO_3^{2-} (see Appendix Section 7.9)**.**

Bond length [Å]			
Se(1)-O(13)	1.666(7)	Se(3)-O(23)	1.737(7)
Se(1)-O(5)	1.721(7)	Se(4)-O(17)	1.669(7)
Se(1)-O(12)	1.725(7)	Se(4)-O(18)	1.718(7)
Se(2)-O(10)	1.687(7)	Se(4)-O(16)	1.727(7)
Se(2)-O(11)	1.700(6)	Se(8)-O(76)	1.694(7)
Se(2)-O(9)	1.704(7)	Se(8)-O(53)	1.695(7)
Se(3)-O(62)	1.655(7)	Se(8)-O(72)	1.705(8)
Se(3)-O(27)	1.729(8)		
Angles [°]			
O(13)-Se(1)-O(5)	103.0(4)	O(27)-Se(3)-O(23)	100.0(4)
O(13)-Se(1)-O(12)	103.0(4)	O(17)-Se(4)-O(18)	103.7(4)
O(5)-Se(1)-O(12)	101.4(3)	O(17)-Se(4)-O(16)	103.2(4)
O(10)-Se(2)-O(11)	99.1(3)	O(18)-Se(4)-O(16)	101.6(4)
O(10)-Se(2)-O(9)	99.2(3)	O(76)-Se(8)-O(53)	100.6(3)
O(11)-Se(2)-O(9)	98.6(3)	O(76)-Se(8)-O(72)	100.1(4)
O(62)-Se(3)-O(27)	104.3(4)	O(53)-Se(8)-O(72)	100.2(4)
O(62)-Se(3)-O(23)	103.4(4)		

3.2.3 Study of the different coordination modes of the SeO_3^{2-} anion by using IR spectroscopy

Assignments of some diagnostic bands for the mixed-metal (Mo:V) selenite-based polyoxometalates **4 - 10** are given in Table 9. The bands for the free selenite anion (C_{3v} symmetry) are found in the region of 900 – 250 cm^{-1}, where four vibrational modes are observed: $\nu_1(A_1)$ = 807 cm^{-1}, $\nu_2(A_1)$ = 432 cm^{-1}, $\nu_3(E)$ = 737 cm^{-1} and $\nu_4(E)$ = 326 cm^{-1} (Figure 63).[216] We expected the SeO_3^{2-} bands of compounds **4 - 10** near the four fundamental (ν_1 – ν_4) vibrational modes of the pyramidal heteroanion. However, the symmetry of the free anion is lowered to C_s due to the coordination through the oxygen atoms, the doubly degenerate vibration (E) is split into two bands (A′+A″) and therefore six vibrational modes are expected to be observed. Instead, we only observed five bands due to overlapping signals.

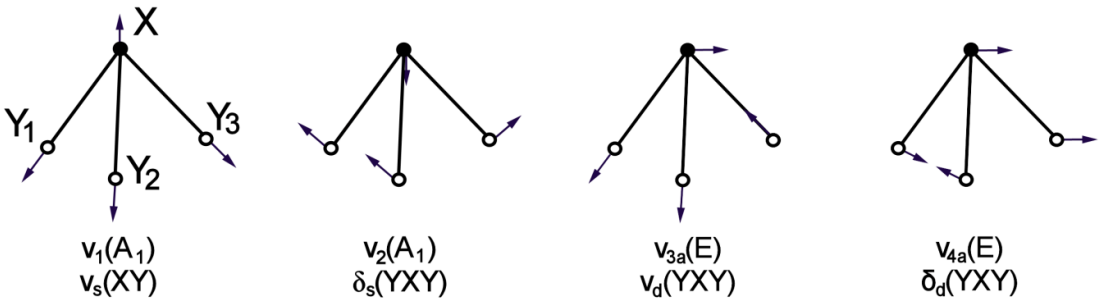

Figure 63: Normal modes of vibration of pyramidal XY_3 molecules (ν, stretching; δ, in-plane bending or deformation. Subscripts, *a*, *s*, and *d* denote antisymmetric, symmetric, and degenerate mode, respectively.[216]

The ν(M=O) bands appear between 1000 – 800 cm^{-1} leading to an overlapping with the SeO stretching bands as for compounds $\{Mo_{12}V_{10}Se_8\}$, $\{Mo_{20}V_{16}Se_{10}\}$ and $\{Na_3(Mo_{11}V_7Se)(Mo_5V_4Se_4)\}$ where there is an overlap between the Mo=O and SeO stretches at 863, 852 and 841 respectively. From Table 9, it is observed that $\Delta|\nu_3 - \nu_1|$, the difference between the highest and the lowest SeO stretching vibrations in metal selenite species, is significantly larger for the μ_3-SeO_3 coordination mode of the SeO_3^{2-} anion,[212] where this difference is ≈ 180 cm^{-1} (very similar as for the μ_3-(O,O,O) coordination mode

of the SO_3^{2-} anion[199]), compared to either the μ_6-SeO ($\Delta|\nu_3 - \nu_1| \approx 160$ cm^{-1}) and μ_9-SeO_3 ($\Delta|\nu_3 - \nu_1| \approx 148$ cm^{-1}) coordination modes. Thus, utilization of FT-IR spectroscopy offers an easy way to distinguish the μ_3-SeO_3 from the μ_6- and μ_9-SeO_3 coordination modes. It is important to take into consideration that different types of coordination modes cause different splitting of the vibration modes. However, when the coordination environment of a specific selenite anion is not equivalent or there is a combination of coordination modes within the same structure it is hard to predict unambiguously the way those selenite anions are coordinated in a specific material since there is a tendency to give an average splitting between the maximum (μ_3-) and the minimum (μ_9-) observed values. In the case of the (μ,μ)-SeO_3 and (η,μ)-SeO_3 coordination modes for example, the peak splitting gives a value of $\Delta| \nu_3 - \nu_1 | \approx 120$ cm^{-1} for both bridging anions and consequently is not possible to determine the type of coordination without having structural data. Furthermore, the determination of the respective coordination modes in compounds $\{Mo_{12}V_{10}Se_8\}$, $\{Mo_{20}V_{16}Se_{10}\}$ and $\{Na_3(Mo_{11}V_7Se)(Mo_5V_4Se_4)\}$ is not possible due to the presence of more than one bridging mode within the same inorganic framework.

Table 9: (shown overleaf) Diagnostic IR bands [cm^{-1}] of compound **4-9** and some known metal selenite compounds. ([a] See figures 52, 59 and 62; [b] Intensity codes: vs = very strong; s = strong; m = medium; w = weak; sh = shoulder)

Compound	Bonding modes of SeO_3^{2-} [a]	$\nu_1(A_1)$ [b]	$\nu_3(E)$	$\Delta\lvert\nu_3 - \nu_1\rvert$ [cm^{-1}]	$\nu_2(A_1)$	ν(V=O) ν(Mo=O)	ref
$\{Mo_{12}V_{10}Se_8\}$ (**4-5**)	μ_9 - SeO_3^{2-} (μ,μ) - SeO_3^{2-} (η,μ) - SeO_3^{2-}	863 vs	754 s 665 s	198	569 m 533 m	971 s 863 s	this work
$\{Mo_{11}V_7Se\}$ (**6-7**)	μ_9 - SeO_3^{2-}	898 m	747 m	151	580 m 546 m	952 s 945 s	this work
$\{Mo_{17}V_8Se\}$ (**8**)	μ_9 - SeO_3^{2-}	899 sh	754 s	145	589 vs	966 sh 905 s	this work
$\{Mo_{20}V_{16}Se_{10}\}$ (**9**)	μ_9 - SeO_3^{2-} (μ,μ) - SeO_3^{2-} (η,η) - SeO_3^{2-}	852 s	727 sh	125	579 w 537 m	954 sh 852 s	this work
$\{Na_3(Mo_{11}V_7Se)\ (Mo_5V_4Se_4)\}$ (**10**)	μ_9 - SeO_3^{2-} (μ,μ) - SeO_3^{2-}	841 s	744 s	97	596 vs	954 s 841 s	this work
$K_8[SeS_3Mo_6O_{33}]\cdot 5.5H_2O$	μ_6-SeO_3^{2-}	780 vs; 740 vs	904	164	551 m		128
$\{Hbipy\}_3\{KMo_4O_{13}(SeO_3)\}$	μ,μ -SeO_3^{2-}	723 s; 685 s	807	122	539 m		126
$\{H_2bipy\}_2\{Mo_5O_{15}(SeO_3)_2\}.H_2O$	η, μ-SeO_3^{2-}	723 s; 684 s	803	119	553 s		126
$Na_6[Pd_{13}Se_8O_{32}]\cdot 10H_2O$	μ_3-SeO_3^{2-}	712 s; 615 s	797	182	549 s		212

3.2.4 Solution identification (MS spectroscopy and UV-Vis stability over the time)

During the course of this study, ESI-MS studies have proved to be a valuable tool in our effort to discover and to identify the composition of the different isolated archetypes. The ESI-MS studies were performed by precipitating solids from the various reaction mixtures (**4 - 10**), which were then transferred into the organic phase by ion exchange with tetrabutylammonium (TBA), and analysed by using mass spectroscopy in acetonitrile. The studies showed that the TBA salts of the $\{Mo_{12}V_{10}Se_8\}$ (**4** and **5**) and the $\{Mo_{11}V_7Se\}$ (**6** and **7**) clusters retain their integrity in solution; whereas for compounds **8**, **9** and **10** it was not possible to establish the presence of the respective clusters. This fact could be a consequence of the multiple fragmentation processes that labile POM clusters undergo at relatively high temperatures during the ESI process. Moreover, to prove that compounds **8**, **9** and **10** are labile species and therefore decompose in solution, we ran UV-Vis experiments where we studied the different reaction mixtures in aqueous solution during a certain period of time, through which we were able to observe what the ESI-MS had previously revealed, that such compounds are not stable in solution.

ESI-MS studies showed that the TBA salts of the $\{Mo_{12}V_{10}Se_8\}$ (in **4** and **5**) cluster dissolve in acetonitrile and are stable in solution in a range of charge and protonation states. The main species observed in the case of compound **4** gives two envelopes centred at *m/z ca.* 2088.3 for $\{(C_{16}H_{36}N)H_7[Mo^{VI}_{12}V^{V}_{10}O_{58}(SeO_3)_8](H_2O)_{18}\}^{2-}$ with all the V centres oxidized and seven protons and at *m/z ca.* 2097.3 for $\{(C_{16}H_{36}N)_2K_3H_{14}[Mo^{VI}_{12}V^{V}_{1}V^{IV}_{9}O_{58}(SeO_3)_8](H_2O)_{12}\}^{2-}$ with one V centre oxidized and fourteen protons (Figure 64a); and at *m/z ca.* 2380.9 for $\{(C_{16}H_{36}N)_3K_9H_5[Mo^{VI}_{12}V^{V}_{1}V^{IV}_{9}O_{58}(SeO_3)_8](H_2O)_4\}^{2-}$ with nine V^{4+} and five protons (Figure 64b). ESI-MS analysis for compound **5** give envelopes at *m/z ca.* 2110.9, 2180.0 and 2251.7 which can be formulated as $\{(C_{16}H_{36}N)_{10}K_5[Mo^{VI}_{12}V^{V}_{2}V^{IV}_{8}O_{58}(SeO_3)_8](H_2O)_6\}^{3-}$ (Figure 65a), $\{(C_{16}H_{36}N)_{11}K_6[Mo_{12}V^{IV}_{10}O_{58}(SeO_3)_8](H_2O)_2\}^{3-}$ (Figure 65b) and $\{(C_{16}H_{36}N)_{11}K_5[Mo_{12}V^{V}_{1}V^{IV}_{9}O_{58}(SeO_3)_8](H_2O)_{16}\}^{3-}$ (Figure 65c) with eight, ten and nine vanadium centres reduced respectively and no protons.

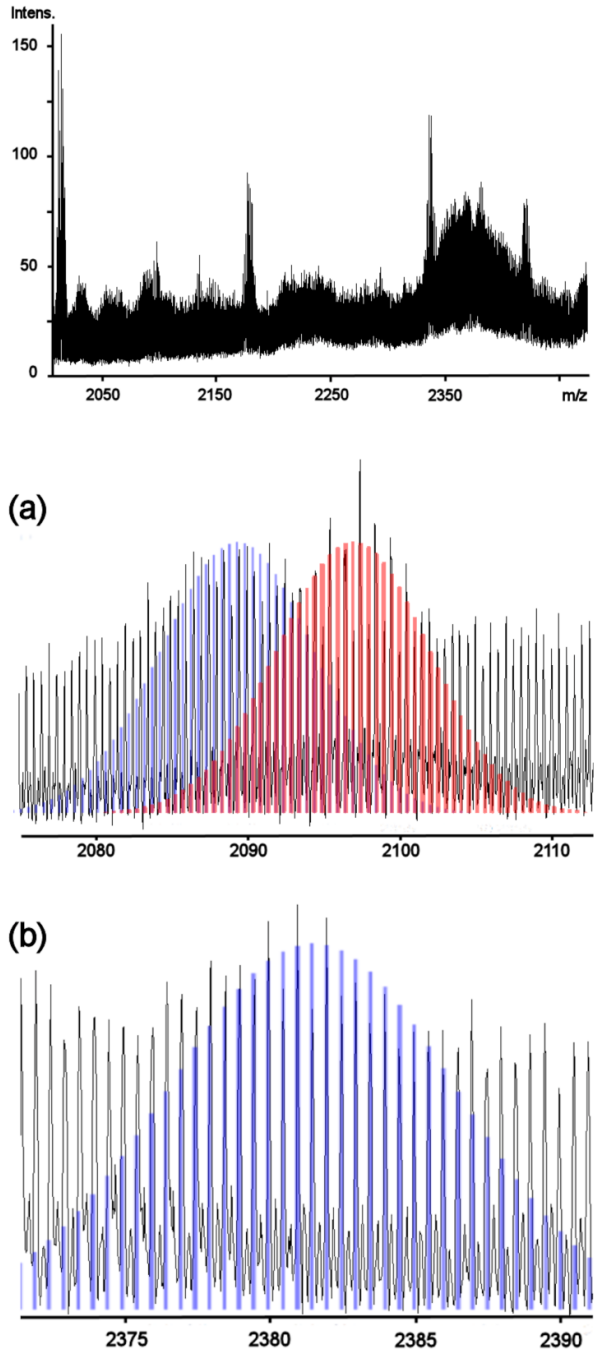

Figure 64: Negative ion mass spectrum for **4a** in acetonitrile solution; (a) two expanded envelopes centred at *m/z ca.* 2088.3 (blue line) and at *m/z ca.* 2097.3 (red line) with zero and nine V^{IV} respectively; and (b) expanded envelope centred at *m/z ca.* 2380.9 with nine reduced vanadium centres. Black line: experimental data, red/blue lines: profile lines of the simulated isotope patterns.

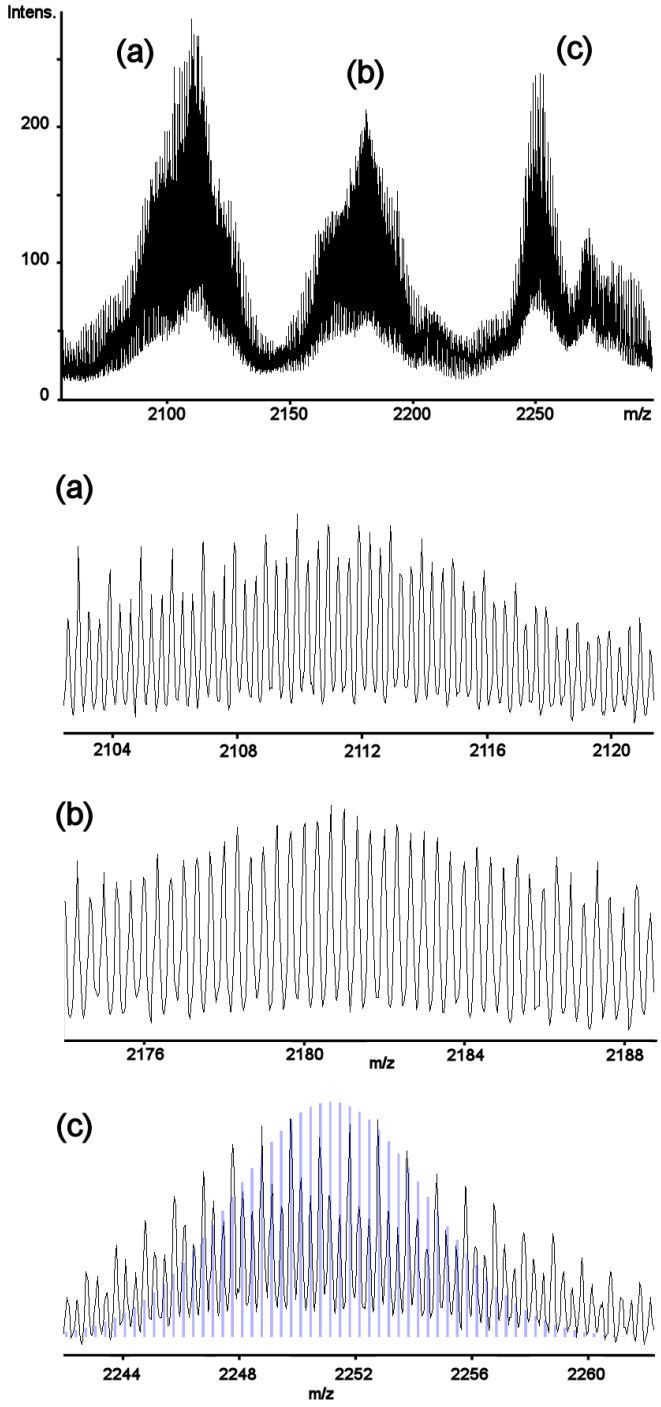

Figure 65: Negative ion mass spectrum for **5a** in acetonitrile solution and three expanded envelopes centred at (a) *m/z ca.* 2110.9 (with eight reduced vanadium centres); (b) *m/z ca.* 2180.0 (with ten reduced vanadium centres); and (c) *m/z ca.* 2251.7 (with nine reduced vanadium centres). Black line: experimental data, blue lines: profile lines of the simulated isotope patterns.

The TBA salts of the egg-shaped Dawson-like archetype (**6a** and **7a**) dissolved in acetonitrile confirmed that the selenite capsule retains its integrity in solution and peaks for both compounds (**6** and **7**) were also identified by using ESI-MS. For both compounds a plethora of different envelopes is seen in the respective spectra. This fact is a consequence of the different protonation and oxidation states that the polyoxoanions adopt. Moreover, peaks which are assigned to monomers, dimers and trimers have also been identified. For that reason we show the overall spectra for **6** and **7** with their highest peak expanded, which correspond to the $\{Mo_{11}V_7Se\}$ cage. We also compare the simulated isotope pattern (blue and red line) and the experimental data (black line). We should point out that the experimental data fits with the Gaussian pattern but, due to the overlapping of the different envelopes in the experimental data, the assumption is not definite. Tables 10 and 11 show selected peaks from the overall spectra for **6** and **7** respectively, which are assigned to the main species in solution, the $\{Mo_{11}V_7Se\}$ cage, with different oxidation and protonation states, and an overall charge between -1 and -4. Both ESI-MS spectra confirm that both clusters are stable in solution: for compound **6** the highest intensity envelope can be assigned to $\{(C_{16}H_{36}N)K_7H[Mo^{VI}_{11}V^{V}_{1}V^{IV}_{6}O_{52}(\mu_9\text{-}SeO_3)](H_2O)_{20}\}^{2-}$ at *m/z ca.* 1624.7 with six reduced vanadium centres and one proton (Figure 66); and for compound **7** the highest intensity envelope is centred at *m/z ca.* 2830.2 and can be assigned to $\{(C_{16}H_{36}N)_2K_{11}H_3[Mo^{VI}_{11}V^{V}_{3}V^{IV}_{4}O_{52}(\mu_9\text{-}SeO_3)]_2\}^{2-}$ with four reduced vanadium centres and three protons (Figure 67).

Table 10: Selected *m/z* range of the ESI-MS of **6a**

Label	*m/z*	Formula
1	1534.8	$\{(C_{16}H_{36}N)_3K_7[Mo^{VI}_{11}V^{V}_{6}V^{IV}O_{52}(\mu_9\text{-}SeO_3)]_2(H_2O)_{22}\}^{4-}$
2	1624.7	$\{(C_{16}H_{36}N)K_7H[Mo^{VI}_{11}V^{V}_{1}V^{IV}_{6}O_{52}(\mu_9\text{-}SeO_3)](H_2O)_{20}\}^{2-}$
3	2047.4	$\{(C_{16}H_{36}N)_5H_{10}[Mo^{VI}_{11}V^{V}_{3}V^{IV}_{4}O_{52}(\mu_9\text{-}SeO_3)]_2(H_2O)_{10}\}^{3-}$
4	2125.8	$\{(C_{16}H_{36}N)_4K_9H_8[Mo^{VI}_{11}V^{IV}_{7}O_{52}(\mu_9\text{-}SeO_3)]_2(H_2O)_{17}\}^{3-}$
5	2251.7	$\{(C_{16}H_{36}N)_7K_4[Mo^{VI}_{11}V^{V}_{5}V^{IV}_{2}O_{52}(\mu_9\text{-}SeO_3)](H_2O)_9\}^{3-}$

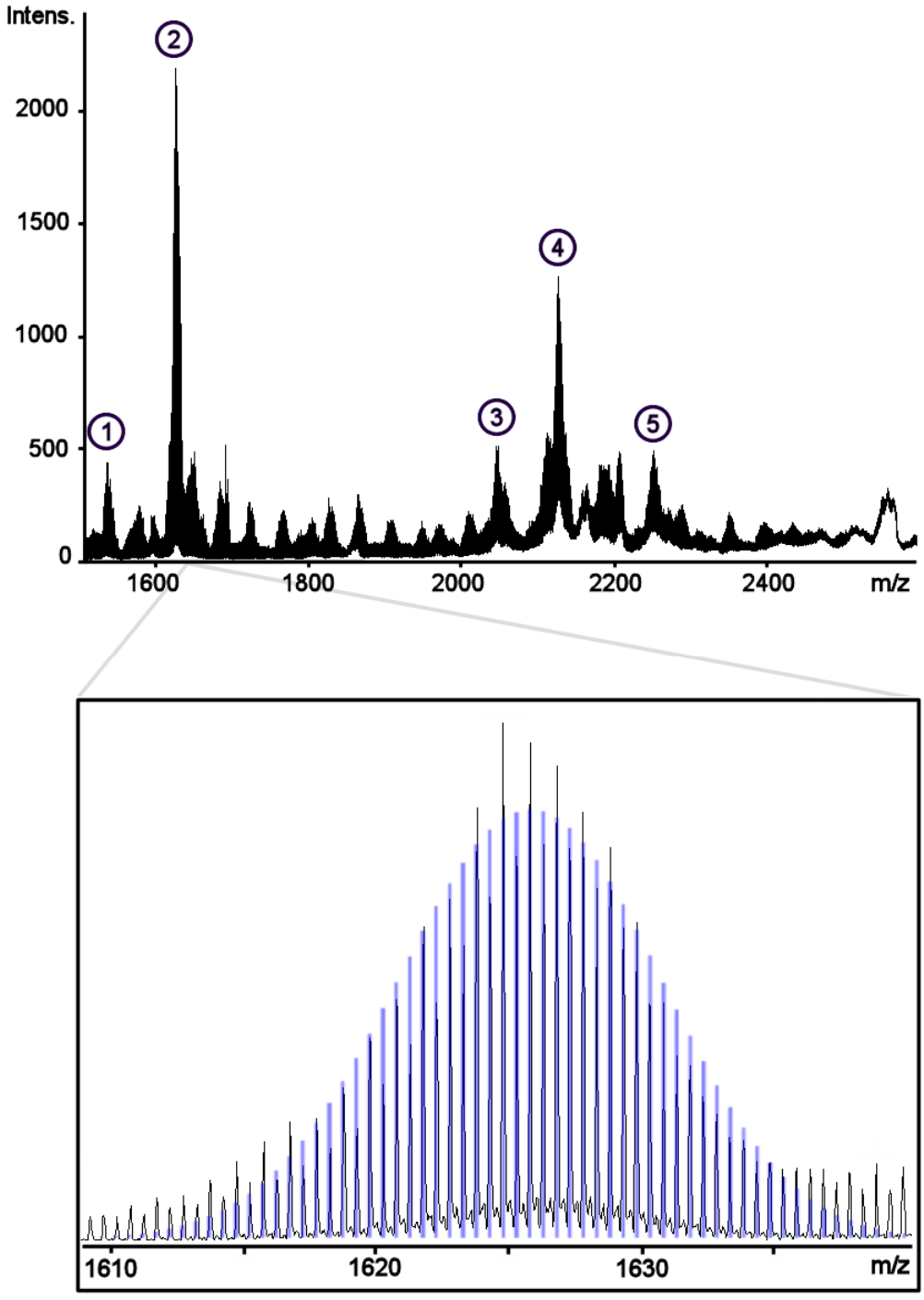

Figure 66: Negative ion mass spectrum for compound **6a** in acetonitrile (top) and expanded envelope centred at *m/z ca.* 1624.7 (with six V^{4+}). Black line: experimental data, blue line: profile line of the simulated isotope pattern.

Table 11: Selected *m/z* range of the ESI-MS of **7a**

Label	*m/z*	Formula
1	2088.9	$\{(C_{16}H_{36}N)_6K_3[Mo^{VI}_{11}V^{V}_{1}V^{IV}_{6}O_{52}(\mu_9\text{-}SeO_3)](H_2O)_{13}\}^{2-}$
2	2217.3	$\{(C_{16}H_{36}N)_{17}H_5[Mo^{VI}_{11}V^{IV}_{7}O_{52}(\mu_9\text{-}SeO_3)]_2\}^{4-}$
3	2369.9	$\{(C_{16}H_{36}N)_9K[Mo^{VI}_{11}V^{IV}_{7}O_{52}(\mu_9\text{-}SeO_3)](H_2O)_8\}^{2-}$
4	2547.5	$\{K_8H_4[Mo^{VI}_{11}V^{V}_{5}V^{IV}_{2}O_{52}(\mu_9\text{-}SeO_3)]_2(H_2O)_2\}^{2-}$
5	2707.6	$\{(C_{16}H_{36}N)K_{10}H_3[Mo^{VI}_{11}V^{V}_{4}V^{IV}_{3}O_{52}(\mu_9\text{-}SeO_3)]_2(H_2O)_2\}^{2-}$
6	2830.2	$\{(C_{16}H_{36}N)_2K_{11}H_3[Mo^{VI}_{11}V^{V}_{3}V^{IV}_{4}O_{52}(\mu_9\text{-}SeO_3)]_2\}^{2-}$
7	2990.3	$\{(C_{16}H_{36}N)_4KH_{13}[Mo^{VI}_{11}V^{V}_{2}V^{IV}_{5}O_{52}(\mu_9\text{-}SeO_3)]_2(H_2O)_{12}\}^{2-}$
8	3135.9	$\{(C_{16}H_{36}N)_8K_7H_9[Mo^{VI}_{11}V^{V}_{3}V^{IV}_{4}O_{52}(\mu_9\text{-}SeO_3)]_3(H_2O)_4\}^{2-}$
9	3593.2	$\{(C_{16}H_{36}N)_4K_5H_2[Mo^{VI}_{11}V^{IV}_{7}O_{52}(\mu_9\text{-}SeO_3)]\ (H_2O)_3\}^{2-}$

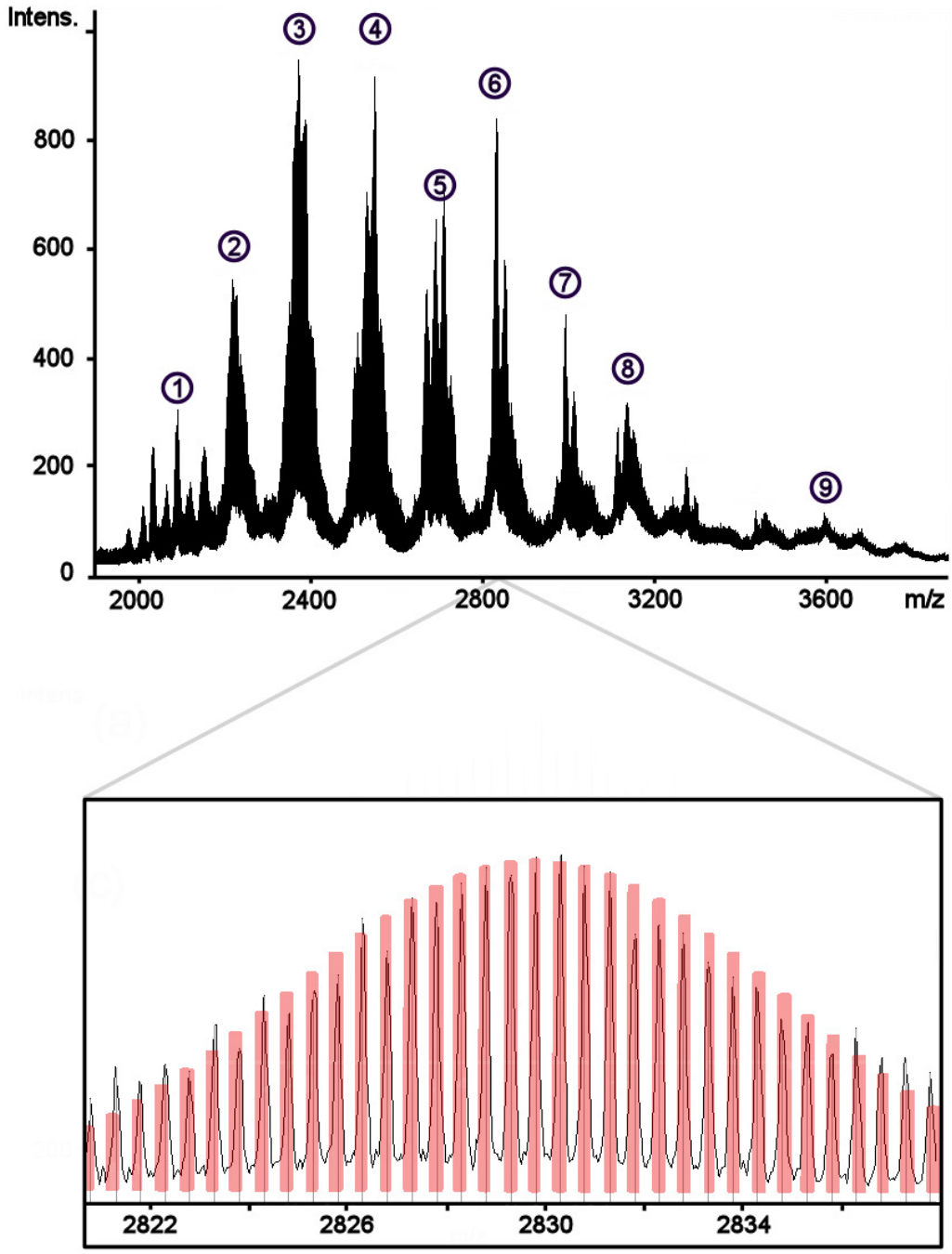

Figure 67: Negative mass spectrum for compound **7a** in acetonitrile (top) and expanded envelope centred at *m/z ca.* 2830.2 (with four V^{4+}). Black line: experimental data, red line: profile line of the simulated isotope pattern.

Additional studies on the stability of the different selenite cages in solution were performed using UV-Vis spectroscopy in aqueous solution. Figure 68 represents the four spectra which correspond to compounds (a) $\{Mo_{12}V_{10}Se_8\}$; (b) $\{Mo_{11}V_7Se\}$, (c) $\{Mo_{17}V_8Se\}$ and (d) $\{Mo_{20}V_{16}Se_{10}\}$. From Figure 68a we could say that $\{Mo_{12}V_{10}Se_8\}$ decomposes over an hour. The fast decomposition would then explain why there is a vast overlapping of low intensity envelopes in the mass spectra (Figure 64), which belong to the actual $\{Mo_{12}V_{10}Se_8\}$ cage and possibly to other species that form in solution upon decomposition of $\{Mo_{12}V_{10}Se_8\}$. It is well known that in POM chemistry several species may be in equilibrium, depending on the pH. Upon dissolution of $\{Mo_{12}V_{10}Se_8\}$ in water, the cage decomposes after one hour leading to other species as seen by the number of peaks in the mass spectra and in the difference in absorbance in the UV-Vis overtime. In the case of the $\{Mo_{11}V_7Se\}$ cage (Figure 68b) we can appreciate the stability of the cluster over at least one hour. This feature is corroborated by the mass spectrometry since in that case the highest peaks correspond to the $\{Mo_{11}V_7Se\}$ cage. The UV-Vis spectrum for compounds $\{Mo_{17}V_8Se\}$ and $\{Mo_{20}V_{16}Se_{10}\}$ (Figure 68c and 68d respectively) show how both compounds lose their integrity over an hour. In contrast to the $\{Mo_{12}V_{10}Se_8\}$ cage, no peaks were found in the corresponding mass spectra which suggested that the different archetypes decompose in solution. By running UV-Vis experiments we corroborated what the mass-spectrometry first suggested.

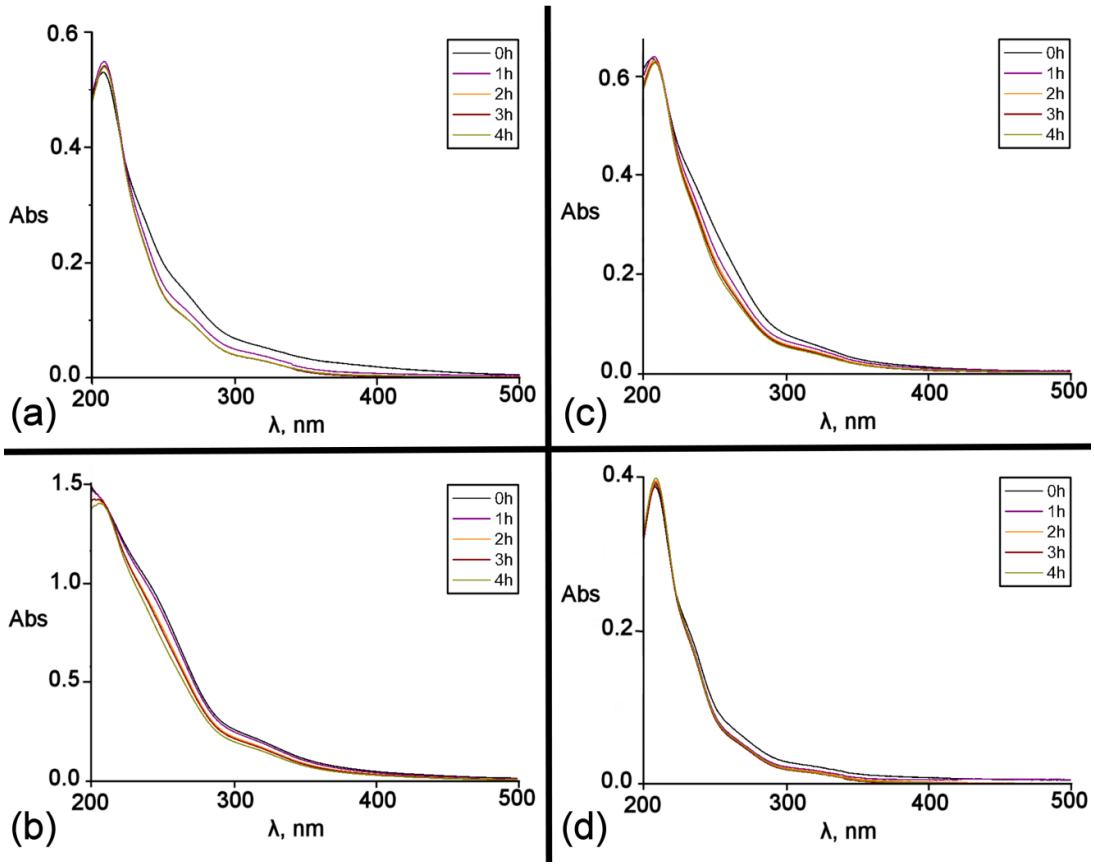

Figure 68: UV-Vis spectra ran over 4 hour to study the stability of the different selenite cages in aqueous solution: (a) $\{Mo_{12}V_{10}Se_8\}$; (b) $\{Mo_{11}V_7Se\}$, (c) $\{Mo_{17}V_8Se\}$ and (d) $\{Mo_{20}V_{16}Se_{10}\}$.

3.2.5 Vanado-selenite polyoxometalates: novel building blocks.

The incorporation of the pyramidal selenite heteroanion within the mixed-metal molybdovanadate systems has proved to have a significant effect on the self-assembly process of the different building units involved in the reaction mixture. The cooperation between the molybdenum and vanadium metal centres, which exhibit different coordination modes and geometries, as well as the ability of the selenite anion to act as a template and stabilizing ligand, has led to the formation of a new family of materials. Such results confirmed that the geometry and size of the heteroanion are critical parameters for the isolation of novel archetypes. In our effort to expand the selenite-based heteropolyoxometalate family, we studied the effect that SeO_3^{2-} has in the assembly of polyoxovanadates systems. As was described earlier in *Section 1.3.*, heteropolyoxovanadate chemistry is not as developed as that of molybdenum or tungsten. However, due to the ability that vanadates have to adopt different oxidation states and coordination modes, plus the several bridging modes that the pyramidal selenite heteroanion can display, we believed that the combination of both building units could lead to the discovery of novel materials with interesting architectures and properties. The C_{3v} symmetric selenite heteroanion contains a non-bonding but stereochemically active lone pair of electrons which can impart additional redox and photophysical properties.[42, 43]

3.2.5.1 Isolation of two reduced vanado-selenite cages: $\{V_{10}Se_4\}$ 14 and $\{V_{12}Se_4\}$ 15.

The sequential addition of K_2SeO_3 and $NH_2NH_2{\cdot}2HCl$ to an acidified aqueous (37% HCl in water, 1:4 v/v) solution of NH_4VO_3 resulted in the formation of a dark green solution from which crystals of $(NH_4)_8H_2[V^{V}_{8}V^{IV}_{2}O_{25}(SeO_3)_4]{\cdot}10H_2O$ **14** ($\{V_{10}Se_4\}$) were isolated after one week (Figure 69 top). The crystals were collected and the mother liquor was left to evaporate. After one week the mother liquor turned yellow and crystals of $[V_{10}O_{28}]^{6-}$ were isolated.[46] Crystals of **14** were obtained over a wide range of pH and V/Se ratios, at pH *ca.* 5 and V/Se 5/1 being the optimum conditions. When Na_2SeO_3 and $NH_2NH_2{\cdot}2HCl$ were sequentially added to an acidified aqueous (37% HCl in water, 1:4 v/v) solution of $NaVO_3$,

crystals of $(NH_4)_6Na[V^{V}_7V^{IV}_5O_{27}(SeO_3)_4]\cdot 8H_2O$ **15** $\{V_{12}Se_4\}$ (Figure 69 bottom) were obtained within 24 hours after the pH of the reaction was adjusted to 5 and using the V/Se ratio of 3/1. The formation of **15** was only possible when the solution was kept at 4 ºC for very slow evaporation. In some cases we obtained a mixture of **15** and $[V_{10}O_{28}]^{6-}$ crystals from the same batch. To avoid the co-crystallization of the reduced compound **15** with the oxidized $[V_{10}O_{28}]^{6-}$ cluster, we carefully degased the solution with N_2 gas.

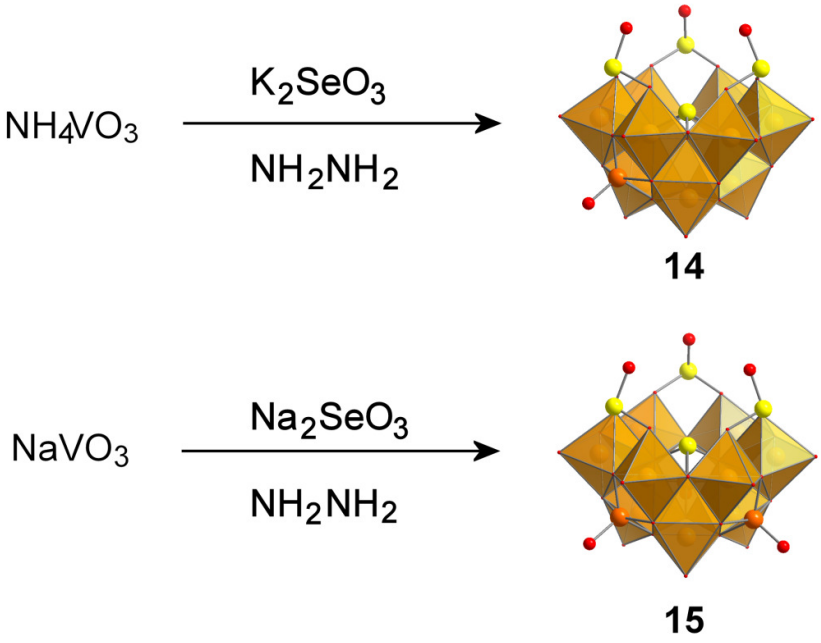

Figure 69: Combination of ball-and-stick and polyhedra representations of **14** (top) and **15** (bottom) and a summary of the synthetic procedures for their isolation. Both compounds where obtained at pH *ca.* 5 yielding the formation of dark green square crystals. VO_6: orange polyhedra; VO_5: orange spheres; Se: yellow spheres and O: red spheres.

It is interesting to point out that, even though the nuclearities of the two mixed-valence compounds are different, $\{V_{10}Se_4\}$ and $\{V_{12}Se_4\}$, they have analogous archetypes to the fully oxidized $[V_{10}O_{25}(SeO_3)_4]^{8-}$ cage, first discovered by Sasaki and co-workers.[140] Both compounds are related to the trivacant Keggin anion α-B-XM_9, where three SeO_3 trigonal pyramids are attached on top of the SeV_9 cage (where the $[M_3O_{13}]$ triad from the α-XM_{12} Keggin anion has been removed) and one μ_9-SeO_3 heteroanion is situated in the middle of the cage (Figure 70a). Moreover, the incorporation of the SeO_3^{2-} pyramidal heteroanions,

which have a lone pair of electrons, avoids the closure of the cage and introduces stability to the novel archetype. Another remarkable feature in these structures is the incorporation of vanadate metal centres with different coordination modes: compound **14** has one capping VO_5 square pyramid attached on one of the "windows" of the α-B-SeV_9 anion, whereas compound **15** has three VO_5 square pyramid capping moieties, one in each window (Figure 70b).

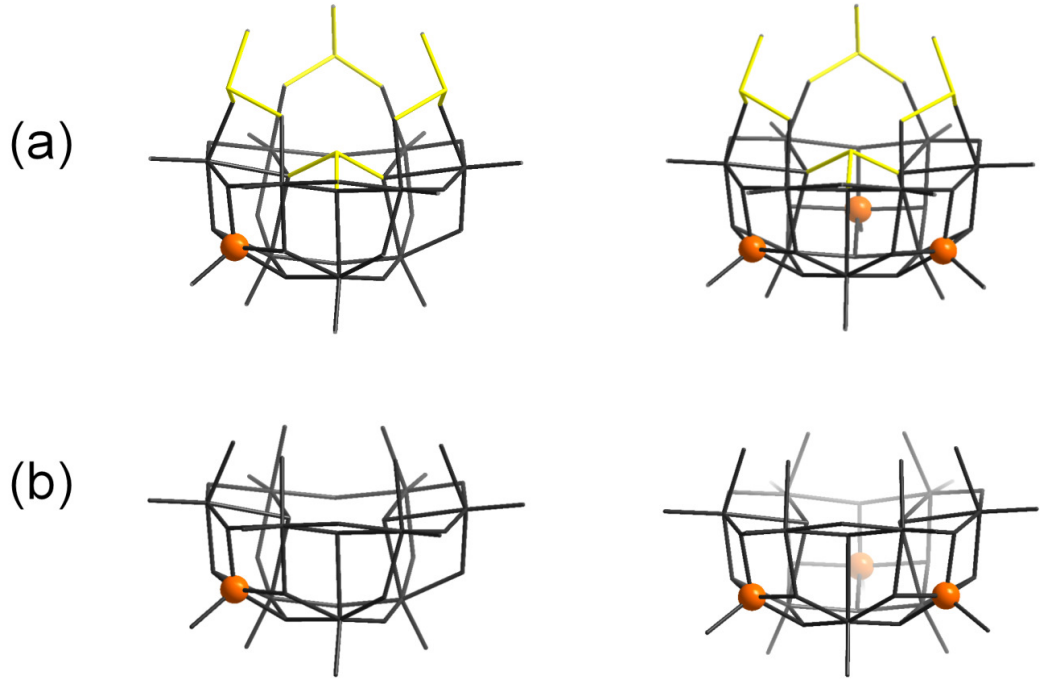

Figure 70: Combination of ball-and-stick and wire representations of **14** (left) and **15** (right): (a) comparison between the two frameworks where the VO_5 moieties are highlighted by the orange spheres; and (b) comparison of the vanadate cages where the selenites have been omitted for clarity. VO_6: black framework/light orange spheres; VO_5: orange spheres and SeO_3^{2-}: yellow framework.

3.2.5.2 Structural description

Crystallographic studies revealed that **14a** and **15a** can be formulated as $[V^{V}_{8}V^{IV}_{2}O_{25}(SeO_3)_4]^{10-}$ and $[V^{V}_{7}V^{IV}_{5}O_{27}(SeO_3)_4]^{7-}$ respectively, whereby the vanadate-

selenite anions adopt a "basket" like structure which consists of three triads of edge-sharing VO_6 octahedra, which are connected to each other by corner sharing (Figure 71 top). The cavity of the basket is occupied by one μ_9-SeO_3^{2-} anion with the lone pair of electrons pointing upwards, and three SeO_3 anions connected between the triads *via* two corner-sharing (Figure 70a). In the case of **14** one capping VO_5 square pyramidal units is capping one of the square faces of the "basket; whereas in compound **15** the three square windows are all capped by one VO_5 square pyramidal moiety each (Figure 71 bottom).

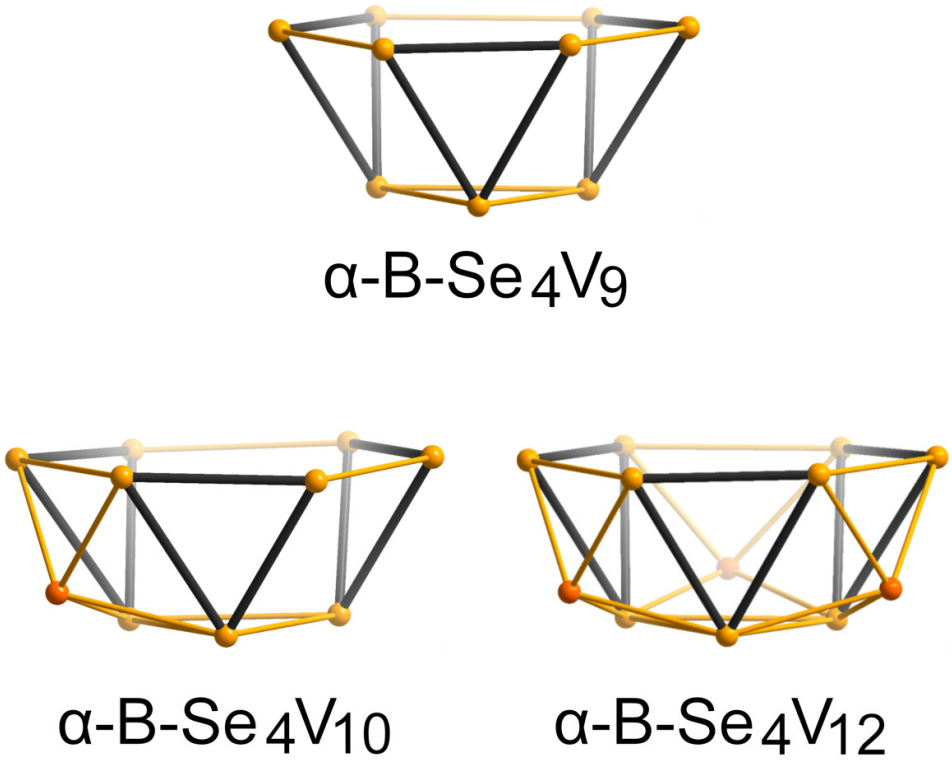

Figure 71: Ball-and-stick representation of the V-skeleton, α-B-Se_4V_9 (top) common framework of both compounds. Comparison between the cages in **14** and **15** (bottom) which have different nuclearities due to the difference in capping VO_5 units; one in **14** which is disordered over the three square windows, and three in **15**, one in each window. The selenite heteroanions have been deleted for clarity. The black triangles represent the three different triads which build up the "basket" cages. V centres from the VO_6 octahedra are light orange spheres whereas the V centres from the square pyramidal VO_5 are in orange.

As was mentioned before, compounds **14** and **15** are isostructural to each other but have different nuclearities due to the incorporation of one and three VO_5 square pyramid units within the basket like cage respectively. The encapsulation of such moieties within the Se_4V_9 archetype leads to the slight distortion of the respective cages. This fact is more pronounced in the case of $\{V_{10}Se_4\}$ because only one of the square windows is capped by the square pyramidal VO_5 unit; whereas in $\{V_{12}Se_4\}$ all the windows are occupied leading to a more symmetric basket-like cage. A comparison between the V-V distances within the cages is given in Table 12.

Table 12: V-V distances for compounds **14** and **15**. In compound **14** window A is occupied by the VO_5 capping unit whereas in compound **15** all the windows are capped.

	{$V_{10}Se_4$} /Å ***14***	*{$V_{12}Se_4$} /Å* ***15***
1	4.009(1)	3.991(2)
2	3.639(1)	3.744(2)
3	3.639(1)	3.744(2)

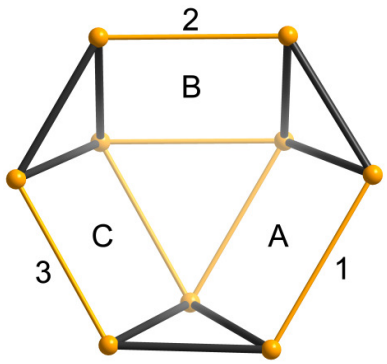

The assignment of formal charges of the metal ions on **14** and **15** was made on the basis of charge balance considerations for the entire compounds, combined with bond valance sum (BVS) calculations,[214] redox titrations, and elemental analysis. For compound **14** the V atoms in the VO_6 octahedra have the formal oxidation state V (BVS_{av} = 4.85), and the V atom in the square pyramidal VO_5 is in the oxidation state IV (BVS_{av} = 3.80). The V atoms in the VO_6 octahedra are coordinated by four μ_2-O^{2-}, one μ_4-O^{2-} and one oxo group if they belong to the triad not adjacent to the VO_5 unit; whereas if they belong to the triad next to the square window capped by the VO_5 unit, they are connected by two μ_2-O^{2-}, two μ_3-O^{2-} ,one μ_4-O^{2-} and one oxo group, depending on whether they belong to the triads where the VO_5 moiety is attached or not. The V atoms in the VO_5 square pyramid are coordinated by four μ_2-O^{2-} and one terminal oxo group. For compound **15** seven of the V atoms in the VO_6 octahedra have the formal oxidation state V (BVS_{av} = 4.67), and two are reduced V centres

with the formal oxidation state IV (BVS_{av} = 4.47); whereas the V atom in the square pyramidal VO_5 are in the oxidation state IV (BVS V7 = 4.08). The V atoms in the VO_6 octahedra belonging to the upper layer of the cage are coordinated by three μ_3-O^{2-}, two μ_2-O^{2-} and one terminal oxo group; the VO_6 from the lower layer are coordinated by four μ_3-O^{2-}, one μ_4-O^{2-} and one oxo group. The V atoms in the VO_5 square pyramid are coordinated by four μ_2-O^{2-} and one terminal oxo group. Average distances for compound **14** and **15** are given in Table 13.

Table 13: Selected interatomic distances relevant to the coordination sphere of VO_6 and VO_5 in compound **14** and **15** (see Appendix Section 7.13 and 7.14).

		{$V_{10}Se_4$} /Å ***14***	*{$V_{12}Se_4$}* /Å ***15***
VO_6	V=O	1.591(7) – 1.607(5)	1.594(7) – 1.618(7)
	μ_2-O^{2-}	1.744(5) – 2.108(2)	1.783(6) – 1.965(6)
	μ_3-O^{2-}	1.828(5) – 1.984(5)	1.896(6) – 2.096(3)
	μ_4-O^{2-}	2.308(4) – 2.385(4)	2.347(6) – 2.452(8)
VO_5	V=O	1.651(8)	1.632(9) – 1.739(10)
	μ_2-O^{2-}	1.725(6) – 1.960(5)	1.764(8) – 2.121(10)

All the Se atoms in the SeO_3^{2-} pyramids are in the oxidation state IV (BVS_{av} = 3.73 for compound **14** and BVS_{av} = 4.06 for compound **15**). As we previously observed in the mixed-metal compounds **5**, **6**, **9** and **10**, the selenite anion is acting as a template and stabilizing ligand within the same structure. The anion adopts a μ_9-coordination mode when it is centred at the cage, where each oxygen atom is connected to one $\{V_3O_{13}\}$ triad. The three Se atoms in (μ,μ)-coordination mode consist of two oxygen atoms connected to two VO_6 octahedra from adjacent triads *via* μ-O^{2-} bridges, and one oxygen atom uncoordinated and pointing upwards. The lone pair of electrons of the three (μ,μ)-SeO_3 anions are pointing outwards, forcing the unshared oxygen atoms from each moiety to face

each other. Selected interatomic distances and angles for the SeO_3^{2-} heteroanions in compound **14** and **15** are listed in Table 14 and 15 respectively.

Table 14: Selected interatomic distances and angles relevant to the coordination spheres of the selenite anions in **14** (see Appendix Section 7.13).

bond distance [Å]		angles [º]	
Se(1)-O(15)	1.662(6)	O(15)-Se(1)-O(12)	99.0(2)
Se(1)-O(12)	1.737(5)	O(15)-Se(1)-O(12A)	99.0(2)
Se(2)-O(13)	1.688(6)	O(12)-Se(1)-O(12A)	98.9(3)
Se(2)-O(7)	1.698(4)	O(13)-Se(2)-O(7)	98.70(19)
Se(3)-O(16)	1.672(5)	O(13)-Se(2)-O(7A)	98.70(19)
Se(3)-O(21)	1.719(5)	O(7)-Se(2)-O(7A)	99.5(3)
Se(3)-O(11)	1.724(5)	O(16)-Se(3)-O(21)	100.3(2)
		O(16)-Se(3)-O(11)	99.2(2)
		O(21)-Se(3)-O(11)	100.4(2)

Table 15: Selected interatomic distances and angles relevant to the coordination spheres of the selenite anions in **15** (see Appendix Section 7.14).

bond distance [Å]		angles [º]	
Se(1)-O(16)	1.663(8)	O(16)-Se(1)-O(12A)	97.9(3)
Se(1)-O(12)	1.718(6)	O(16)-Se(1)-O(12)	97.9(3)
Se(2)-O(8)	1.679(7)	O(12A)-Se(1)-O(12)	99.4(4)
Se(2)-O(9)	1.685(5)	O(8)-Se(2)-O(9A)	98.6(2)
Se(3)-O(15)	1.660(6)	O(8)-Se(2)-O(9)	98.6(2)
Se(3)-O(14)	1.705(7)	O(9A)-Se(2)-O(9)	98.6(3)
Se(3)-O(17)	1.718(6)	O(15)-Se(3)-O(14)	99.8(3)
		O(15)-Se(3)-O(17)	99.8(3)
		O(14)-Se(3)-O(17)	101.6(3)

3.2.5.3 Non-linear Optical Properties

The non-centrosymmetric structures of **14** and **15** implied that compounds $\{V_{10}Se_4\}$ and $\{V_{12}Se_4\}$ are expected to have non-linear optical properties (NLO). The materials were tested but unfortunately, SHG (second-harmonic generation) responses from these samples were extremely low, lower than sugar powder. We supposed that this was due to the anti-parallel alignment of the polarization vectors in the crystals, even though they crystallized in a non-centrosymmetric space group. This explanation is consistent with the packing modes of **14** and **15** as it is shown in Figure 72, where the disposal of the cages are opposite to each other which led to the cancelation of the crystal vectors.

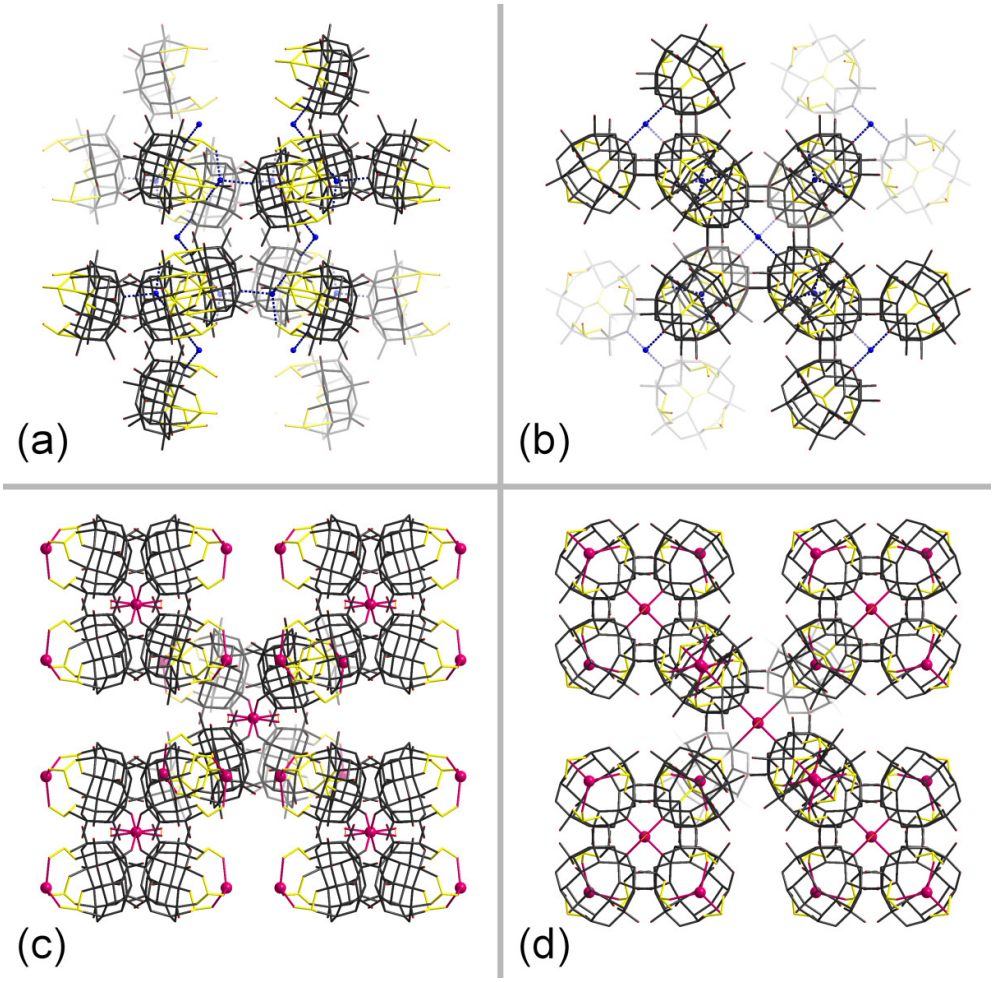

Figure 72: Packing modes of compound **14** in view of (a) *a* axis and (b) *c* axis; and of compound **15** from (c) *a* axis and (d) *c* axis. Vanadate inorganic framework: dark grey, SeO_3^{2-}: yellow, N: blue spheres and Na: pink spheres.

3.2.5.4 $\{V_{10}Se_4\}$ and $\{V_{12}Se_4\}$ as Secondary Building Units

As we described in *Section 1.5.1.,* one of the most widely used approaches to synthesise novel and larger archetypes is the use of lacunary polyoxometalates as secondary building units. Such methodologies have been extensively studied in the case of lacunary polyoxotungstates due to their stability in solution and ability to form large clusters based on smaller building units. On the contrary, molybdenum and vanadium based lacunary clusters are unknown, as a consequence of their lability. To date, almost all the reported polyoxovanadate clusters exhibit ball-like structures due to the incorporation of the square pyramidal VO_5 units, which impart flexibility to the cluster and hence lead to the closure of the archetype. Such structures are lacking in lacunary positions and so they cannot act as secondary building units. However, we believe that the isolation of compounds **14** and **15** opens a new route for the isolation of bigger and unprecedented archetypes based on such cages. As we previously discussed, the incorporation of the selenite heteroanion not only imparts additional stability to the cluster but avoids its closure, leading to the isolation of the two novel cages which exhibit lacunary positions.

In an attempt to use compounds **14** and **15** as secondary building units we used both compounds as starting materials. When compound **15** was reacted with solid $CoSO_4{\cdot}7H_2O$ in an ammonium acetate buffer solution (1M, pH ~ 4), crystals of $(NH_4)_5[Co(OH_2)_3V^{V}_9V^{IV}O_{25}(SeO_3)_4]{\cdot}15H_2O$ **16** ($\{CoV_{10}Se_4\}$) (Figure 73) where obtained within a week, when the solution was kept at 4 ºC in an open vessel, whereas if the reaction was done in aqueous solution without buffer no crystals were obtained. When compound **14** was used instead, no crystals were formed either in buffer or aqueous solution. The explanation of these results can be attributed to the stability of the different basket-like archetypes; as confirmed by our UV-Vis and mass-spectroscopy studies. When we performed UV-Vis analysis of both compounds, **14** and **15**, in aqueous solution over one hour, we observed that both species decompose during the first ten minutes (Figure 74a and 74b). On the contrary, when the UV-Vis analysis were performed in ammonium acetate buffer solution (1M, pH ~ 4) the cages were stable for hours (Figure 74c and 74d). Additionally, when we performed ESI-MS, either in aqueous media or by precipitating

solid from the reaction mixtures which yielded to **14** and **15** *via* cation exchange with organic salts, no peaks which corresponded to **14** or **15** where observed, leading to the conclusion that the vanado-selenite cages lose their integrity in solution.

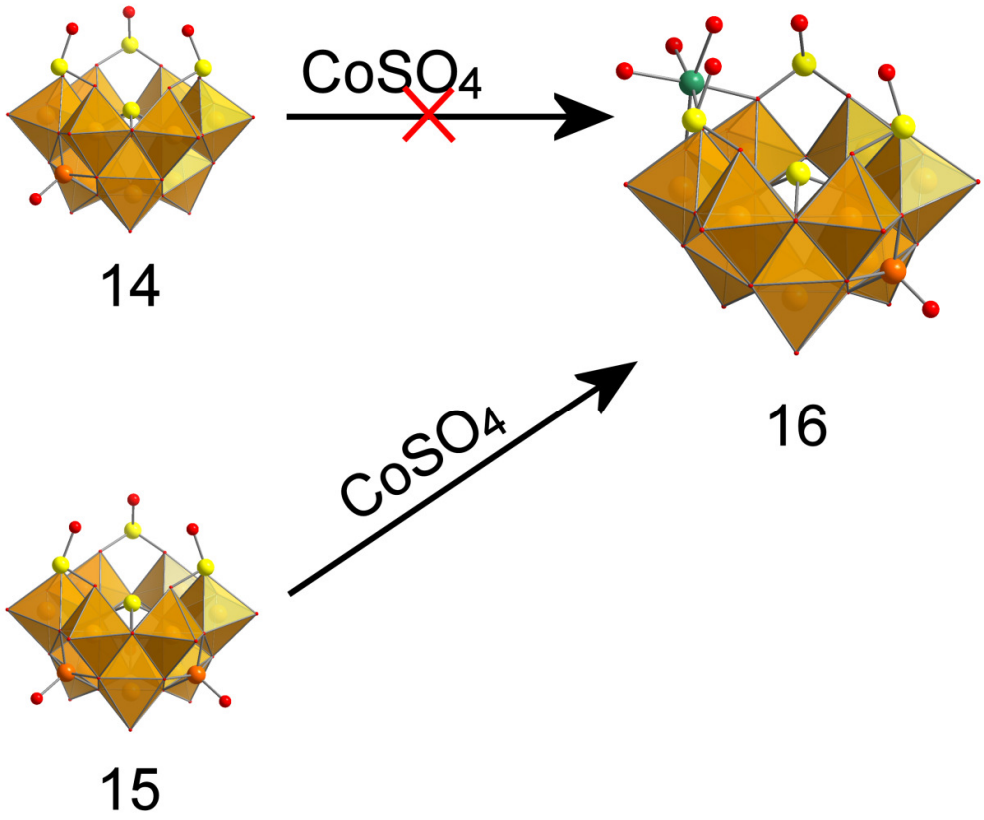

Figure 73: Combination of ball-and-stick and polyhedral representations of structure and the synthetic procedure for the formation of compound **16**; which it is only obtained if $\{V_{12}Se_4\}$ **15** is used as a starting material. VO_6: orange polyhedra, V in VO_5: orange spheres, Se: yellow spheres, Co: green sphere and O: red sphere.

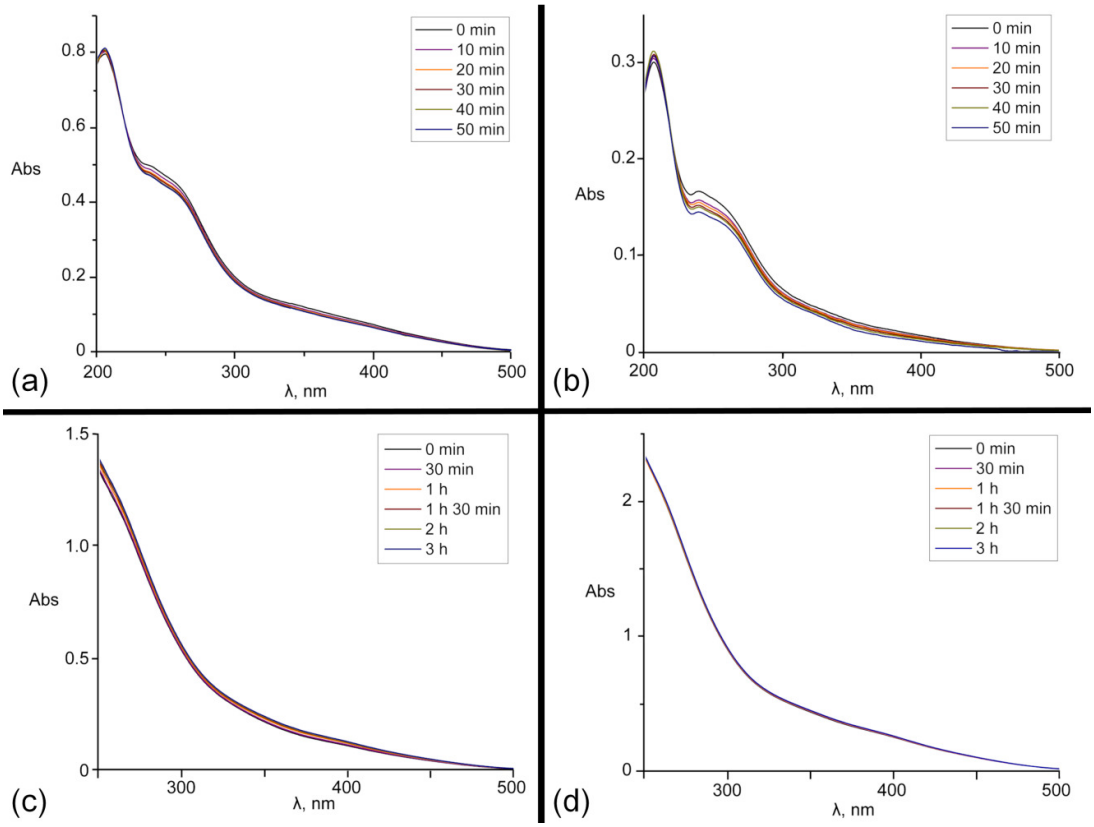

Figure 74: UV-Vis spectra of compound **14** in (a) water and (c) ammonium acetate buffer solution; and compound **15** also in (b) water and (d) ammonium acetate buffer solution (1M, pH~4). In aqueous solution both compounds decompose within the ten first minutes as observed by the decrease in intensity of the charge transfer (CT) band at *ca.* 270 nm; whereas in buffer solution compound **14** is stable over an hour and then starts to decompose, and compound **15** stayed stable for the 3 hours we ran the experiment.

Crystallographic studies revealed that compound **16** can be formulated as $[Co(OH_2)_3V^{V}_9V^{IV}O_{25}(SeO_3)_4]^{5-}$, where the anion **16a** retains the "basket"-like archetype from the parental structure **15**; isostructural to the lacunary Keggin anion α-B-XM_9. During formation, **16a** has lost two out of the three VO_5 square pyramidal moieties which were capping the square windows of the cage (Figure 75). However, one $\{CoO_3(OH_2)_3\}$ octahedral unit has been incorporated on top of the cage, opposite to the remaining VO_5 square pyramidal unit and between two of the (μ,μ)-SeO_3 heteroanions. The assignment of formal charges of the metal ions of **16** was made on the basis of charge balance considerations for the entire compound, combined with bond valance sum (BVS)

calculations,[214] and elemental analysis. Eight V atoms in the VO_6 octahedra have the formal oxidation state V (BVS_{av} = 4.78), and one has the oxidation state of IV (BVS V8 = 4.17). The V atoms in the VO_6 octahedra are coordinated by four μ_2-O^{2-} with V-O bonds spanning distances of the range 1.861(3) – 2.037(3) Å, one μ_4-O^{2-} with V-O distances between 2.320(3) – 2.355(3) Å, and one terminal oxo group with V=O distances of the range of 1.604(3) – 1.605(3) Å, when they are not coordinated to either the VO_5 or the $\{CoO_3(OH_2)_3\}$ unit. The V atoms in the VO_6 octahedra, which coordinate either with the square pyramidal VO_5 or the $\{CoO_3(OH_2)_3\}$ moiety, are connected by two μ_2-O^{2-} with V-O distances between 1.712(3) – 1.944(3) Å, two μ_3-O^{2-} with V-O bonds spanning distances in the range 1.945(3) – 2.096(3) Å, one μ_4-O^{2-} with V-O distances between 2.277(3) – 2.429(3) Å and one oxo group with V=O distances of the range of 1.604(3) – 1.625(3) Å. Selected interatomic distances for the V atom in VO_5 and the Co atom in $\{CoO_3(OH_2)_3\}$ are given in Table 16.

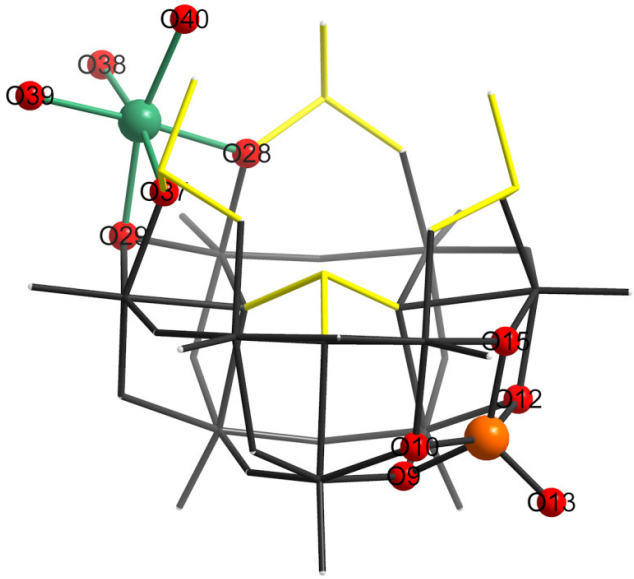

Figure 75: Combination of ball-and-stick and wire representation of the cobalt analogue "basket"-like cage where the incorporation of the V^{IV} atom in VO_5 square pyramid and the Co^{II} in the $\{CoO_3(OH_2)_3\}$ octahedral is highlighted. The V atom in the square pyramidal VO_5 is in the oxidation state V (BVS = 5.03); and the Co in the $\{CoO_3(OH_2)_3\}$ octahedra in the oxidation state II (BVS = 2.04). Vanadate inorganic framework: dark grey, pyramidal selenites: yellow, V in VO_5: orange sphere, Co: green sphere and O: red spheres (see Appendix Section 7.15).

Table 16: Selected interatomic distances relevant to the coordination spheres of the V in VO_5 and the Co cation in **16** (see Appendix Section 7.15).

Bond distance [Å]			
V(6)-O(13)	1.599(3)	Co(1)-O(38)	2.066(3)
V(6)-O(15)	1.784(3)	Co(1)-O(37)	2.083(3)
V(6)-O(9)	1.857(3)	Co(1)-O(40)	2.086(3)
V(6)-O(10)	1.892(3)	Co(1)-O(39)	2.098(3)
V(6)-O(12)	1.922(3)	Co(1)-O(29)	2.102(3)
		Co(1)-O(28)	2.106(3)

Table 17: Selected interatomic distances and angles relevant to the coordination spheres of the selenite atoms in **16** (see Appendix Section 7.15).

bond distance [Å]		angles [º]	
Se(1)-O(36)	1.660(3)	O(36)-Se(1)-O(33)	100.77(14)
Se(1)-O(33)	1.698(3)	O(36)-Se(1)-O(37)	100.70(13)
Se(1)-O(37)	1.765(3)	O(33)-Se(1)-O(37)	99.46(13)
Se(2)-O(21)	1.691(3)	O(21)-Se(2)-O(22)	100.28(13)
Se(2)-O(22)	1.698(3)	O(21)-Se(2)-O(23)	99.95(12)
Se(2)-O(23)	1.729(2)	O(22)-Se(2)-O(23)	99.18(12)
Se(3)-O(34)	1.658(3)	O(34)-Se(3)-O(26)	102.14(14)
Se(3)-O(26)	1.697(3)	O(34)-Se(3)-O(28)	100.49(14)
Se(3)-O(28)	1.746(3)	O(26)-Se(3)-O(28)	100.84(13)
Se(4)-O(35)	1.669(3)	O(35)-Se(4)-O(25)	99.84(14)
Se(4)-O(25)	1.718(3)	O(35)-Se(4)-O(27)	98.47(14)
Se(4)-O(27)	1.726(3)	O(25)-Se(4)-O(27)	99.77(14)

The incorporation of the cobalt cation within the inorganic framework alters the bridging modes of the SeO_3^{2-} previously observed in compounds **14** and **15**. Compound **16** retains the coordination mode of the central heteroanion μ_9-SeO_3 (Se(2)), where every oxygen atom is connected to one of the triads, but the symmetry of two of the (μ,μ)-SeO_3 anions is lowered to (η,μ)-SeO_3 (Se(1) and Se(3)) due to the additional coordination with the cobalt

metal centre. All the Se atoms in the SeO_3 pyramids are in the oxidation state IV (BVS_{av} = 3.94). Selected interatomic distances and angles for the Se atoms are given in Table 17.

In our attempt to use compound **16** as a tertiary building unit for the discovery of new materials, we first checked the stability of the compound in solution. UV-Vis spectroscopy confirmed that compound **16** is only stable in acetate buffer solution (1M, pH ~ 4) during the first 10 minutes and it decomposes afterwards (Figure 76).

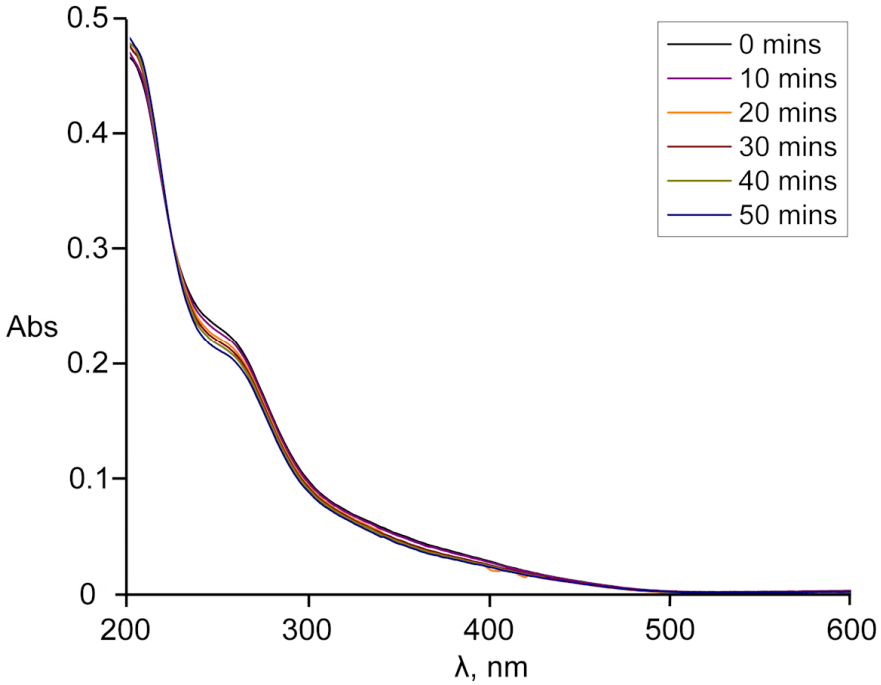

Figure 76: UV-Vis spectra ran over 1 hour to study the stability of the $\{CoV_{10}Se_4\}$ cages in ammonium acetate buffer solution (1M, pH ~ 4).

The isolation of **16** confirmed that compound **15** can be used as a future building unit for the isolation of unprecedented archetypes. We believe that the reason why only **15** lead to the crystallization of **16** is due to the stability of the cage in solution, as has been demonstrated by UV-Vis spectroscopy (Figure 74), which could be attributed to the presence of the three VO_5 moieties in **15** (two reduced V^{IV} and on V^{V}); whereas compound **14** has only one $V^{IV}O_5$ capping moiety.

3.2.6 Summary

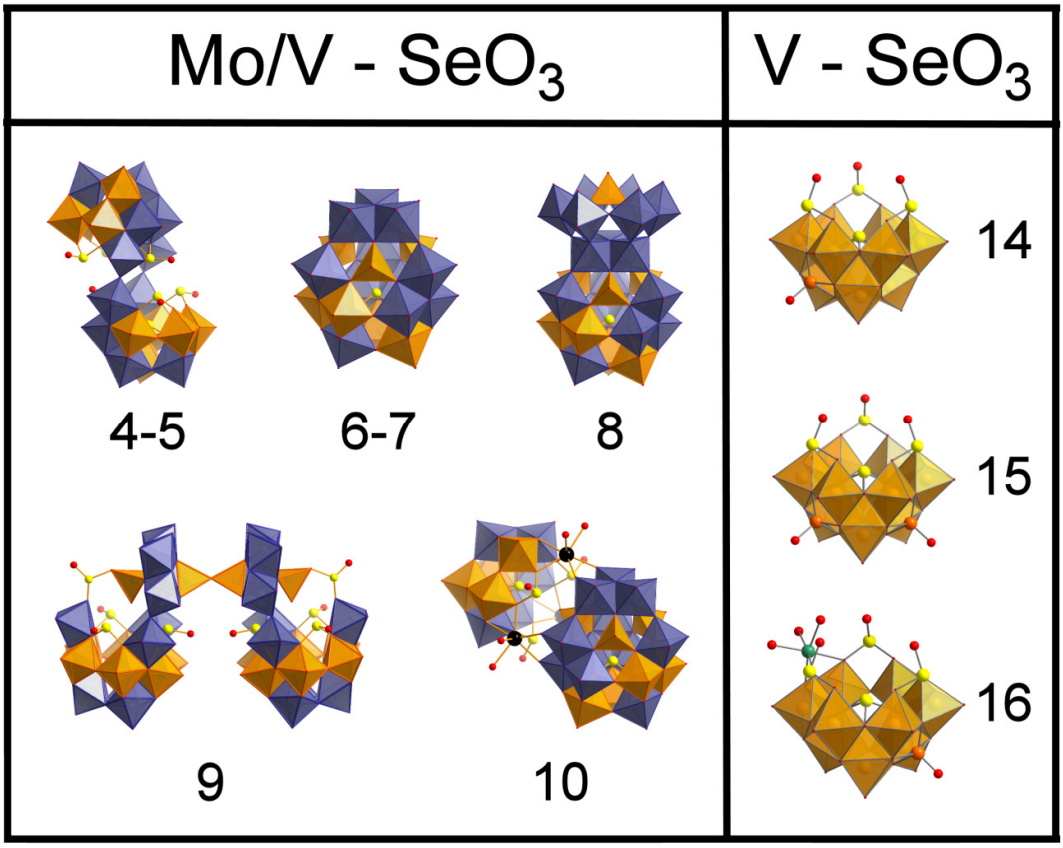

Figure 77: Summary of the different materials isolated from the one pot reactions when molybdate and vanadate are present in solution along with the pyramidal selenite heteroanion (left); and when only vanadium is participating in the self-assembly process with selenite acting as a template (right). Mo: purple polyhedra, V: orange polyhedra/spheres, Co: green sphere, Na: black spheres, Se: yellow spheres and O: red spheres.

Here is represented a summary of the eight novel archetypes that have been isolated based on the use of SeO_3^{2-} pyramidal heteroanion (Figure 77). It is interesting to point out that all the structures exhibit the common building unit $\{SeM_9\}$ where M can be either Mo or V in MO_6 octahedra. This unit consists of three triads of edge-sharing MO_6 octahedra, which are connected to each other *via* corner sharing; and its cavity is occupied by one μ_9-SeO_3 anion with the lone pair of electrons pointing upwards. On the other hand, all the structures except for $\{Mo_{11}V_7Se\}$ and $\{Mo_{17}V_8Se\}$ archetypes exhibit more than one coordination

mode of the selenite anion within the same structure. The heteroatom involved in the construction of these archetypes is not only templating the formation of the different cages but acting as a stabilizing ligand. The free oxygen atoms from the different SeO_3^{2-} moieties make compounds **4-5**, **9-10** and **14-16** excellent candidates for further polymerization, due to the possibility to coordinate other ligands to the uncoordinated oxygen atoms.

Another interesting aspect is the role of the molybdates in the self-assembly process of such materials. When molybdenum is involved in the reaction mixture we were able to isolate several structures with nuclearities ranging between 18-36; whereas when there is only vanadium, the formation of novel compounds is limited to the formation of "basket"-like cages with nuclearities between 10 and 12. In the mixed-metal systems, the V metal centres can adopt either a VO_6 octahedron or VO_4 tetrahedron; whereas in pure vanadium systems, the V metal centres exist as either a VO_6 octahedron or VO_5 square pyramid, which is not observed in the mixed-metal archetypes. So it is evident that the cooperation between the different species is necessary for the formation of higher nuclearity archetypes.

3.3 Tellurite-based Mixed-Metal Polyoxometalates

As was previously demonstrated in *Sections 3.1.* and *3.2.*, the incorporation of the sulfite heteroanion (r_{at} = 1.03 Å) led to the isolation of two unprecedented novel Dawson-based archetypes: $[Mo^{VI}_{11}V^{V}_{5}V^{IV}_{2}O_{52}(\mu_9\text{-}SO_3)]^{7-}$ and $[Mo^{VI}_{11}V^{V}_{5}V^{IV}_{2}O_{52}(\mu_9\text{-}SO_3)(Mo_6VO_{22})]^{10-}$ ($\{Mo_{11}V_7S\}$ and $\{Mo_{17}V_8S\}$ respectively), whereas when selenite was used instead (r_{at} = 1.17 Å), the self-assembly process was directed to form a new family of heteropolyoxometalate clusters based on the trivacant Keggin-like $\{SeMo_{9-x}V_x\}$ (x = 4-5) building unit where the heteroanion exhibits a plethora of coordination modes. The incorporation of the bigger pyramidal selenite anion allowed us to isolate the novel structural motifs $[Mo^{VI}_{12}V^{V}_{10}O_{58}(SeO_3)_8]^{10-}$ ($\{Mo_{12}V_{10}Se_8\}$), and $[Mo^{VI}_{20}V^{V}_{12}V^{IV}_{4}O_{99}(SeO_3)_{10}]^{21-}$ ($\{Mo_{20}V_{16}Se_{10}\}$); and the $[Mo^{VI}_{11}V^{V}_{5}V^{IV}_{2}O_{52}(\mu_9\text{-}SeO_3)]^{7-}$ and $[Mo^{VI}_{11}V^{V}_{5}V^{IV}_{2}O_{52}(\mu_9\text{-}SeO_3)(Mo_6VO_{22})]^{10-}$ anions ($\{Mo_{11}V_7Se\}$ and $\{Mo_{17}V_8Se\}$ respectively), isostructural to the sulfite-based archetypes. It is evident from the reported findings that the pyramidal geometry, in conjunction with the ionic radius of the heteroanion has an effect on the architectures that can be isolated. The bigger the heteroanion is, the more spatial restrictions are introduced, leading to the isolation of novel archetypes with higher nuclearities. Herein, in an effort to investigate further the effect of the geometry and the size of the incorporated heteroanions on the self-assembly process and the final structural motif, we have introduced the pyramidal TeO_3^{2-} anion as a principal heteroanion in the mixed-metal molybdovanadate system. As we have discussed earlier, the anionic radius of the different heteroanions, geometrically identical, has a profound effect on the isolated cluster. For that reason we believed that the incorporation of tellurium, which has a bigger atomic radius (r_{at} = 1.37 Å) than sulphur and selenium,[213] would lead to the discovery of unusual architectures; as it has been demonstrated by the isolation of three novel tellurite-based mixed-metal and mixed-valence polyoxometalates, namely: $(NH_4)_9K[Mo^{VI}_{12}V^{V}_{8}V^{IV}_{4}Te^{IV}O_{69}(\mu_9\text{-}Te^{IV}O_3)_2]\cdot 27H_2O$ **11**, $K_{14}[Mo^{VI}_{12}V^{V}_{8}V^{IV}_{4}O_{69}(\mu_9\text{-}Te^{IV}O_3)_2]\cdot 27H_2O$ **12,** which are isostructural with a tellurium centre gating the square shaped window on the cap of **11**; and $K_{10}[Mo^{VI}_{11}V^{V}_{5}V^{IV}_{2}O_{52}(\mu_9\text{-}Te^{IV}O_3)(Mo^{VI}_{6}V^{V}O_{22})]\cdot 15H_2O$ **13**.

3.3.1 Isolation of three novel $\{Mo_xV_yTe_z\}$ archetypes

The sequential addition of $NH_4V^VO_3$, $K_2Te^{IV}O_3$ and $NH_2NH_2{\cdot}2HCl$ in an aqueous solution of $(NH_4)_6Mo^{VI}_7O_{24}$, followed by the adjustment of the pH between 2 and 4, by addition of a 3M HCl solution, resulted in the formation of dark green crystals of $(NH_4)_9K[Mo^{VI}_{12}V^V_8V^{IV}_4Te^{IV}O_{69}(\mu_9\text{-}Te^{IV}O_3)_2]{\cdot}27H_2O$ $\{Mo_{12}V_{12}Te_3\}$ **11** after one week. When KV^VO_3 and K_2MoO_4 were used instead of the ammonium salts, crystals of $K_{14}[Mo^{VI}_{12}V^V_8V^{IV}_4O_{69}(\mu_9\text{-}Te^{IV}O_3)_2]{\cdot}27H_2O$ $\{Mo_{12}V_{12}Te_2\}$ **12** and $K_{10}[Mo^{VI}_{11}V^V_5V^{IV}_2O_{52}(\mu_9\text{-}Te^{IV}O_3)(Mo^{VI}_6V^VO_{22})]{\cdot}15H_2O$ $\{Mo_{17}V_8Te\}$ **13** were formed in similar yield after one week (Figure 78). In a similar fashion as in the previous pyramidal-based POM systems, the cation involved in the reaction mixture is crucial for the formation of the desired compound. Only when potassium is present in the system the formation of compounds **12** and **13** is possible, whereas when there are mixtures of ammonium and potassium, compound **11** is formed. For the isolation of compounds **12** and **13** it was necessary to accurately adjust the ratio between the K_2MoO_4 and K_2TeO_3 starting materials. When the Mo/Te ratio was 3/1 compound **12** was formed, whereas for compound **13** the Mo/V was 6/1. All the new tellurite-based archetypes exhibit Dawson-like structures where the different metal centres display diverse geometries and oxidation states: dioxo-/oxo-Mo^{VI} and octahedrally/tetrahedrally coordinated V^V/V^{IV} centres. V^V is rapidly reduced in the presence of the reducing agent $NH_2NH_2{\cdot}2HCl$ which leads to four V^{IV} in the case of **11** and **12**; and two V^{IV} in **13**.

As was previously demonstrated, even though sulphur, selenium and tellurium belong to the same group of the periodic table and present similar behaviour under the same experimental conditions, the difference of the heteroanion's size has a profound effect on the self-assembly process of the mixed-metal units and the architecture of the final product. The incorporation of the tellurite heteroatom within the molybdenum-vanadium system leads to the formation of the unprecedented $\{Mo_{12}V_{12}Te_x\}$ cage with x = 2 or 3, with nuclearity 24, which had not been observed in the case of the sulfite-/selenite-based mixed metal polyoxometalates. The integration of the TeO_3^{2-} anion (r_{at} = 1.37 Å), bigger in size than sulfite and selenite, does not lead to the formation of the analogous $\{Mo_{11}V_7X\}$ cage with X = S and Se, but to the Crown-Dawson archetype $\{Mo_{17}V_8Te\}$.

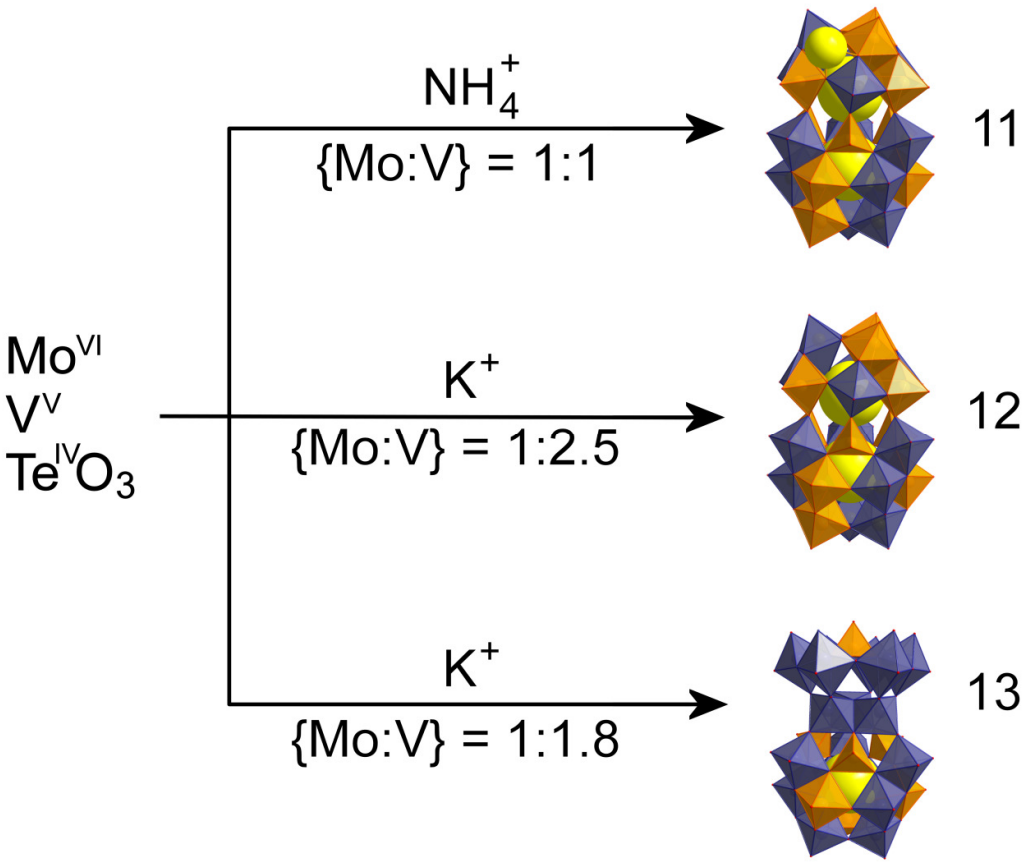

Figure 78: Synthetic procedure for the isolation of the three novel tellurite-based mixed-metal polyoxometalates **11**, **12** and **13**. The effect of the cations and the {Mo:V} ratios are highlighted. Mo: purple polyhedra, V: orange polyhedra and Se: yellow spheres.

Intriguingly, the three novel tellurite-based archetypes exhibit common chemical and structural information: (a) the existence of the oxidized form of V in the presence of a reducing agent, even though V^V is rapidly reduced to V^{IV} by hydrazine (in the present case there are 4 V^{IV} for compounds **11** and **12**, and 2 for compound **13**); (b) the plethora of geometries adopted by the metal centres in the same structure, as shown by structural analysis (dioxo-/oxo-Mo^{VI} and octahedrally/tetrahedrally coordinated $V^{IV/V}$ centres); and (c) the μ_9-$Te^{IV}O_3$ coordination mode that the tellurite anion exhibits in all three clusters.

3.3.2 Structural description of the tellurite-molybdovanadate clusters

3.3.2.1 The novel {$Mo_{12}V_{12}Te_3$} 11 and {$Mo_{12}V_{12}Te_2$} 12 cage-like archetypes

Crystallographic studies revealed that **11a** and **12a** can be formulated as $[Mo^{VI}_{12}V^{V}_{8}V^{IV}_{4}Te^{IV}O_{69}(\mu_9\text{-}Te^{IV}O_3)_2]^{10-}$ and $[Mo^{VI}_{12}V^{V}_{8}V^{IV}_{4}O_{69}(\mu_9\text{-}Te^{IV}O_3)_2]^{14-}$ respectively, whereby the molybdovanadate-tellurite anions **11a** and **12a** adopt a "capsule" like structure which consists of two hemispheres. The upper hemisphere, which is structurally related to the lacunary Keggin structure $[XM_9O_{34}]^{n-}$,[4] incorporates five V (3 V^V and 2 V^{IV}) and four Mo^{VI} centres crystallographically disordered over the nine positions, with its cavity occupied by one μ_9-$Te^{IV}O_3$ anion with the lone pair of electrons pointing downwards (Figure 79a). In the case of **11a** a tellurite ion gates one of the square shaped "windows" of the M_9 cage (Figure 79b). The upper hemisphere is connected to the lower half *via* the corners of alternating V^VO_4 tetrahedra and MoO_6 octahedra. The remaining four V positions (2 V^V and 2 V^{IV}) are crystallographically disordered over nine potential sites of the lower hemisphere, where another μ_9-$Te^{IV}O_3$ anion occupies the central cavity, with the lone pair of electrons pointing upwards (Figure 79c). The assignment of formal charges of the metal ions was made on the basis of charge balance considerations for the entire compound, combined with bond valence sum (BVS) calculations (Table 18),[214] elemental analysis, redox titrations and high resolution electrospray mass spectrometry. The V atoms in the VO_4 units are coordinated by two μ_3-O^{2-} moieties, with V–O bonds spanning the range 1.783(8)–1.810(8) Å, and one terminal oxo group with an average V=O distance of 1.597(9) Å. The MoO_6 units alternating with the V^VO_4 tetrahedra complete their coordination environment with two terminal oxo groups in *cis*-positions, with Mo=O bonds (1.694(9)–1.724(8) Å), one μ_2-O^{2-}, (2.062(8)–2.096(8) Å) and three μ_3-O^{2-} moieties in the range of 2.062(8)–2.250(8) Å. The Te atoms in the pyramidal TeO_3^{2-} are coordinated with three μ_3-O^{2-} moieties, with an average Te–O bond length of 1.877(8) Å while the Te atom in the TeO_4 unit is coordinated with four μ_2-O^{2-} in the range of 1.921(8) to 2.116(8) Å.

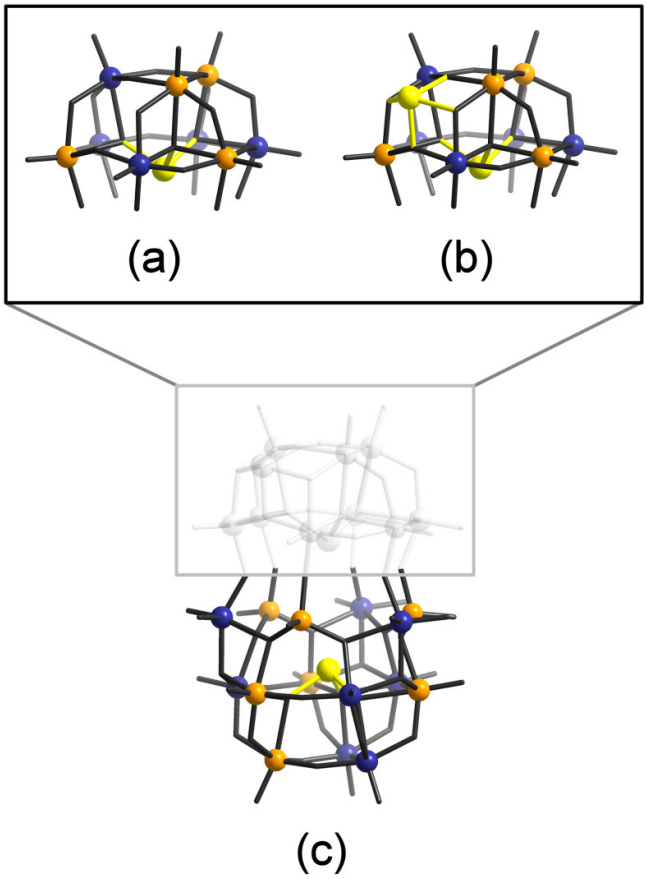

Figure 79: Ball-and-stick representation of the inorganic cage $\{Mo_{12}V_{12}Te_x\}$ with x = 2 or 3. The novel archetype is built up from two hemispheres: (a) $\{Mo^{VI}_4V^{V}_3V^{IV}_2Te^{IV}O_{33}\}$ and (b) $\{Mo^{VI}_4V^{V}_3V^{IV}_2Te^{IV}_2O_{33}\}$ illustrating the upper hemisphere for **12a** and **11a** respectively, where the only difference between them is the capping μ_8-TeO_4 unit that compound **11** exhibits on one of the square faces; (c) represents the isostructural lower hemisphere $\{Mo_8V^{V}_5V^{IV}_2O_{45}(\mu_9\text{-}TeO_3)\}$ common in **11a** and **12b**. Mo: purple spheres, V: orange spheres and Se: yellow spheres.

Table 18: BVS average calculations for Mo, V and Te in compounds **11a** and **12a.**

	11a	**12a**
Mo in MoO_6	5.88	5.77
V in VO_4	5.11	5.05
Te in μ_9-TeO_3	4.61	4.54
Te in μ_8-TeO_4	4.15	-

Compound **11** crystallized in the space group *C*2/*c* (Figure 80a) and compound **12** in *C*2/*m* (Figure 80b). In the former, each $\{Mo_{12}V_{12}Te_3\}$ anion is paired to its neighbour *via* H-bonds from the ammonium cations (blue arrows). The pair of anions are then connected to an adjacent pair *via* potassium cations (grey arrows). In the latter, each $\{Mo_{12}V_{12}Te_2\}$ cage is surrounded by potassium cations in a honeycomb fashion (grey hexagons). In compound **12** there is an important trigonal cap disorder over two positions in the upper hemisphere of the cage, as it is observed as hexagonal pattern in Figure 80b.

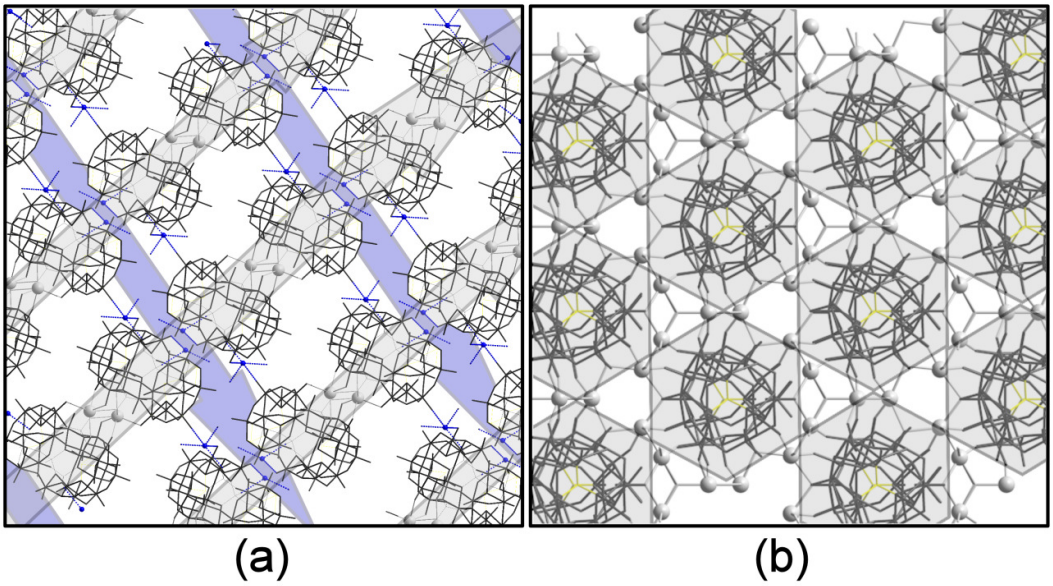

Figure 80: Ball-and-stick representation of the packing mode (a) for compound **11a** and (b) for compound **12a**. The inorganic framework is shown by dark grey sticks and the TeO_3 by yellow sticks. K: grey spheres and N: blue spheres. H-bonds: blue bonds.

The purity of both compounds was confirmed by powder X-ray diffraction (Figure 81 and Figure 82). The experimental PXRD data was compared with the simulated XRD pattern from the single crystal structure. The PXRD were collected at room temperature, whereas single crystal data were collected at 150 K. Due to temperature difference, the corresponding peaks in the two diffraction patterns have different shifts at different index space.

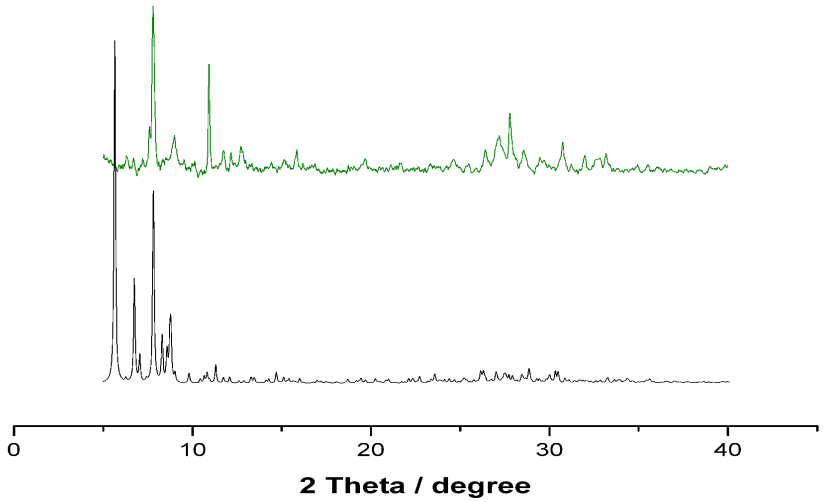

Figure 81: Comparison of the experimental (green line) and simulated (black line) X-ray diffraction powder patterns for compound **11**.

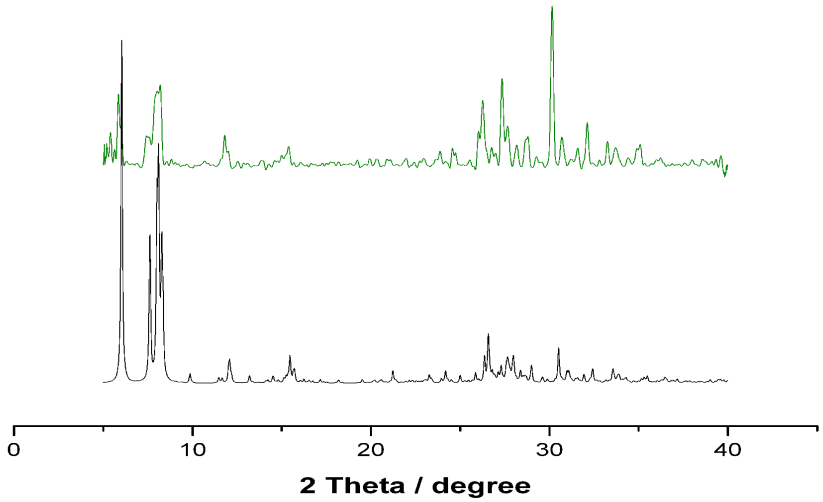

Figure 82: Comparison of the experimental (green line) and simulated (black line) X-ray diffraction powder patterns for compound **12**.

3.3.2.2 The Crown-Dawson {$Mo_{17}V_8Te$} 13

Compound **13a** can be formulated as $[Mo^{VI}_{11}V^{V}_{5}V^{IV}_{2}O_{52}(\mu_9\text{-}Te^{IV}O_3)(Mo^{VI}_{6}V^{V}O_{22})]^{10-}$ ({$Mo_{11}V_7Te$}) and adopts a "Crowned"-Dawson structural motif and is isostructural to the

sulfite- and selenite-based $\{Mo_{17}V_8X\}$ (X = S, Se) capsule. Furthermore, the structural similarities with compounds **11a** and **12a** become obvious since the lower part of their structures incorporates the same building block, $\{Mo^{VI}_8V^{V}_5V^{IV}_2Te^{IV}O_{48}\}$, see Figure 83. In the case of **13a** there is a triad of edge-shared MoO_6 octahedra capping the $\{Mo^{VI}_8V^{V}_5V^{IV}_2Te^{IV}O_{48}\}$ unit, connected further to the "crown"-shaped, $\{Mo^{VI}_6V^{V}O_{22}\}$, formation while in the case of **11a** and **12a** the common building unit is capped by a $\{Mo^{VI}_4V^{V}_3V^{IV}_2Te^{IV}_2O_{33}\}$ and $\{Mo^{VI}_4V^{V}_3V^{IV}_2Te^{IV}O_{33}\}$ units respectively. It is interesting to point out that the common part in all three compounds is also related with the egg-shaped Dawson-like archetype we observed in the $\{Mo_{17}V_8X\}$ (X = S, Se) cluster. The triad of MoO_6 octahedra that form the upper cap in $\{Mo_{17}V_8X\}$ has been replaced by the M_9 trivacant Keggin-like building unit in the case of compound **11a** and **12a**, whereas in compound **13a** the Dawson-like cage retains the $[Mo_{11}V_7O_{52}(\mu_9\text{-}SeO_3)]^{7-}$ cage (isostructural to $\{Mo_{11}V_7X\}$) and a six MoO_6 membered ring crown, with the VO_4 tetrahedron in the centre, has been attached on top.

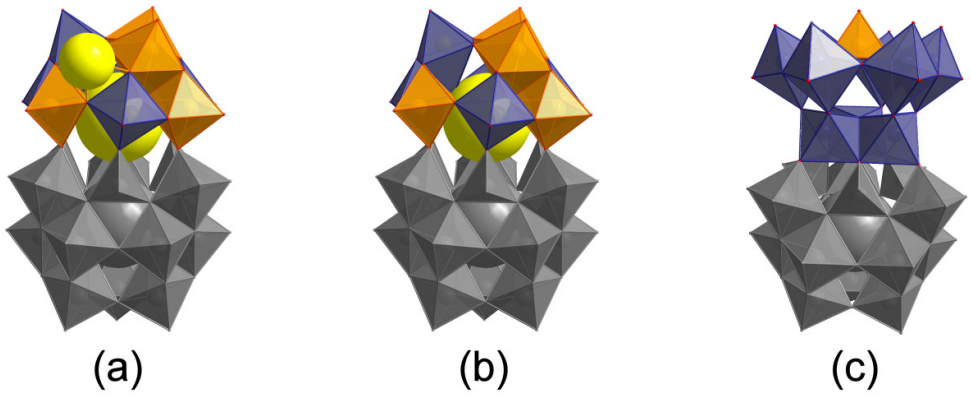

Figure 83: Polyhedral representations of the three tellurite-based polyoxometalates. The three archetypes exhibit the same structural motif $\{Mo^{VI}_8V^{V}_5V^{IV}_2Te^{IV}O_{48}\}$ (grey polyhedra) with different upper hemispheres represented by the colourful polyhedra: (a) $\{Mo^{VI}_4V^{V}_3V^{IV}_2Te^{IV}_2O_{33}\}$ in anion **11a**; (b) $\{Mo^{VI}_4V^{V}_3V^{IV}_2Te^{IV}O_{33}\}$ in anion **12a**; and (c) $\{Mo^{VI}_9V^{V}O_{34}\}$ in anion **13a**. Mo: purple polyhedra, V: orange polyhedra, Te: yellow spheres and O: red spheres.

In a similar fashion to **11a** and **12a**, the alternating belt of VO_4 tetrahedra and MoO_6 octahedra are crystallographically well resolved as its upper hemisphere, whereas the

remaining nine metal centres located at the lower hemisphere are crystallographically disordered. The "crown"-shaped, $\{Mo^{VI}_6V^{V}O_{22}\}$ fragment consists of three pairs of corner shared $Mo^{VI}O_6$ octahedra comprising two terminal oxo groups and the central cavity is occupied by a tetrahedral $V^{V}O_4$ unit via corner sharing interaction. The crown is further attached to the three $Mo^{VI}O_6$ centres located at the top of the 'egg-shaped' structure through six oxo-bridges. The $Mo^{VI}O_6$ triads are then connected *via* vertexes of alternating $V^{V}O_4$ tetrahedra and MoO_6 octahedra to the lower hemisphere, which is templated by a TeO_3^{2-} heteroanion in a μ_9-coordination bridging mode (Figure 84), which is the third μ_9-$Te^{VI}O_3$ reported example found in the literature.[36, 220] Further discussion of the tellurites coordination modes can be found in *Section 3.3.4*. The assignment of formal charges on the metals was made again on the basis of charge balance considerations for the entire compound, combined with BVS calculations,[214] elemental analysis and redox titrations. All the Mo are in the oxidation state VI (BVS_{av} = 5.97); the V in the VO_4 are have the formal oxidation state V (BVS_{av} = 5.05); and the Te atom in IV (BVS_{av} = 4.66). The Mo atoms in the MoO_6 belonging to the upper hemisphere are coordinated by two terminal oxo groups in *cis*-positions, with Mo=O bonds spanning 1.702(10)–1.731(12) Å, one μ-O^{2-}, with Mo–O bond lengths between 1.882(10)–1.905(14) Å, and three μ_3-O^{2-} bridges, with Mo–O bond lengths of 1.988(10)–2.280(10) Å. The V atoms in the VO_4 are coordinated by three μ_3-O^{2-} moieties, with V–O bonds spanning the range 1.730(6)–1.767(10) Å, and one terminal oxo group with V=O bonds in the range of 1.628(11)–1.647(14) Å.

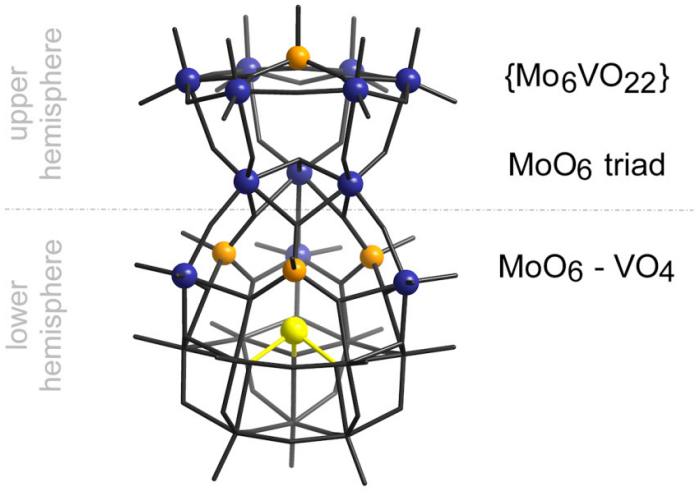

Figure 84: Ball-and-stick representation of the crystallographically well-defined MoO_6 octahedra and VO_4 tetrahedra in **13a**. Mo: purple spheres, V: orange spheres, Te: yellow

sphere. The crystallographically disordered lower hemisphere is represented by the dark grey framework (see Appendix Section 7.12).

Isostructural to the sulfite and selenite "Crown"-Dawson analogues, compound **13** crystallises in the space group *Pnma* (Figure 85); where the $\{Mo_{17}V_8Te\}$ units are connected to each other *via* potassium cations in an antiparallel arrangement and there is a mirror plane which passes across the *b* axis and parallel to *ac* plane.

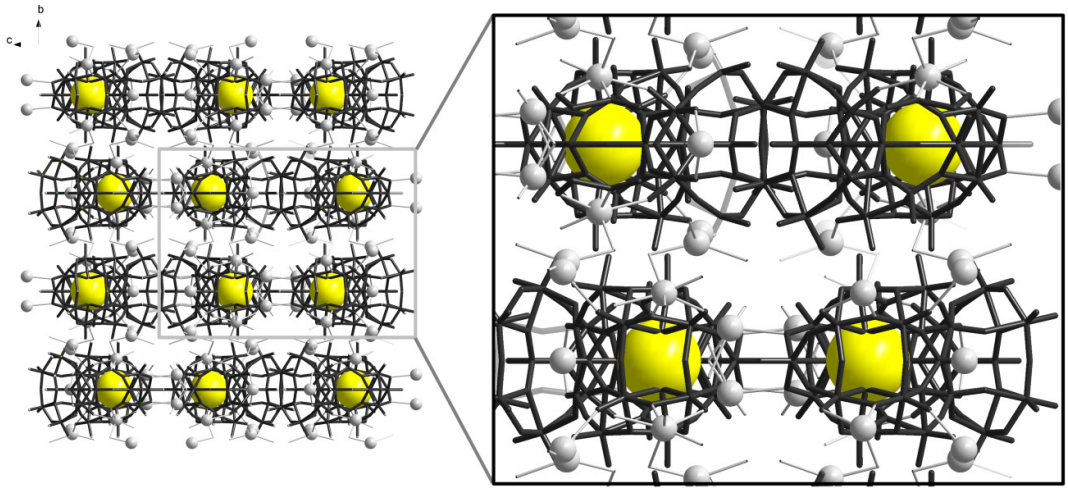

Figure 85: Combination of ball-and-stick and wire representations of the packing mode of compound **13a**. The inorganic framework is represented by dark grey wires. Te: yellow spheres and K: light grey spheres.

3.3.3 Solution identification of the tellurite-based cages

During the course of this study, ESI-MS has proved to be a valuable tool in our effort to characterize unambiguously the $\{Mo_{12}V_{12}Te_3\}$ **11** and $\{Mo_{12}V_{12}Te_2\}$ **12** clusters in solution. This was performed either directly in aqueous media or by ion exchange with tetrabutylammonium (TBA) and examined using mass spectrometry in CH_3CN. In this study, the TBA salt of the $\{Mo_{12}V_{12}Te_3\}$ cluster **11a**, dissolved in CH_3CN confirmed that the tellurite inorganic cage retains its integrity in solution (Figure 86 top). The observed isotopic envelopes were assigned to the $\{Mo_{12}V_{12}Te_3\}$ species with different protonation

and oxidation states. (Table 19). More specifically, the envelope of higher intensity signal consists of two overlapping species which can be formulated as $\{(C_{16}H_{36}N)_3K_6H_3[Mo^{VI}_{12}V^{V}_{4}V^{IV}_{8}O_{69}Te(TeO_3)_2]\cdot(H_2O)_8\}^{2-}$ at *m/z ca.* 2227.1 and $\{(C_{16}H_{36}N)_3K_4H_3[Mo^{VI}_{12}V^{V}_{6}V^{IV}_{6}O_{69}Te(TeO_3)_2]\cdot(H_2O)_{13}\}^{2-}$ at *m/z ca.* 2233.2, respectively (Figure 86 bottom).

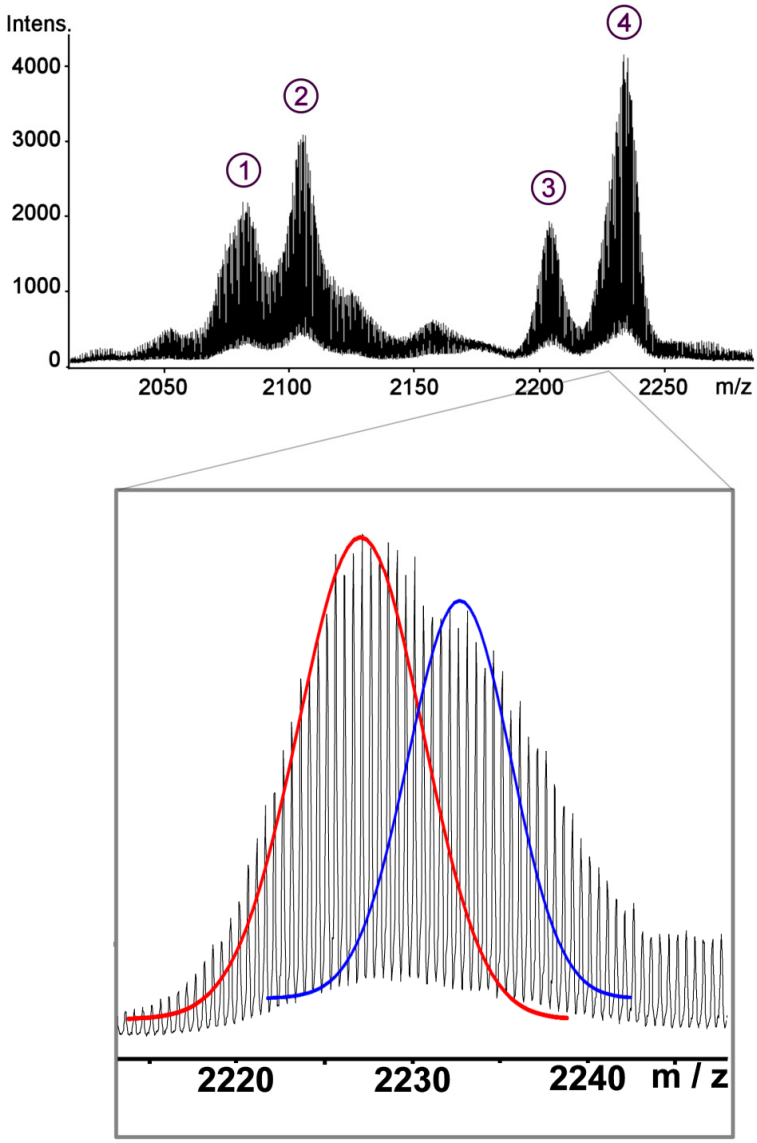

Figure 86: Negative ion mass spectrum of **11a** in acetonitrile solution (top); and expanded highest peak (bottom) which comprises two envelopes centred at *m/z ca.* 2271 (with 8 V^{IV}) and at *m/z ca.*2233.2 (with 6 V^{IV}). Black line: experimental data, red/blue lines: profile lines of the simulated isotope patterns.

Table 19: Selected *m/z* range of the ESI-MS of **11a**.

Label	m/z	Formula
1	2081.45	$\{(C_{16}H_{36}N)_2K_8[Mo^{VI}_{12}V^{V}_{6}V^{IV}_{6}O_{69}Te(TeO_3)_2]\cdot(H_2O)\}^{2-}$
2	2105.43	$\{(C_{16}H_{36}N)_2K_8[Mo^{VI}_{12}V^{V}_{6}V^{IV}_{6}O_{69}Te(TeO_3)_2]\cdot(H_2O)_4\}^{2-}$
3	2203.59	$\{(C_{16}H_{36}N)_2K_6[Mo^{VI}_{12}V^{V}_{8}V^{IV}_{4}O_{69}Te(TeO_3)_2]\cdot(H_2O)_{19}\}^{2-}$
4	2233.57	$\{(C_{16}H_{36}N)_2K_7H_2[Mo^{VI}_{12}V^{V}_{4}V^{IV}_{8}O_{69}Te(TeO_3)_2]\cdot(H_2O)_{20}\}^{2-}$

In the case of **12a** the studies were performed in aqueous medium. As was expected, the spectrum consists of a series of overlapping envelopes assigned to species of different extent of protonation and/or hydration (Figure 87). The main species observed gave envelopes centred at *m/z ca.* 1776.7 and 2350.3 and were formulated as dimers of **12a** species, $\{K_{12}H_4[(Mo_{12}V^{V}_{12}O_{69}(TeO_3)_2)]_2(H_2O)_{11}\}^{4-}$ and $\{K_{11}H_6[(Mo_{12}V^{V}_{12}O_{69}(TeO_3)_2)]_2(H_2O)_{10}\}^{3-}$ respectively.

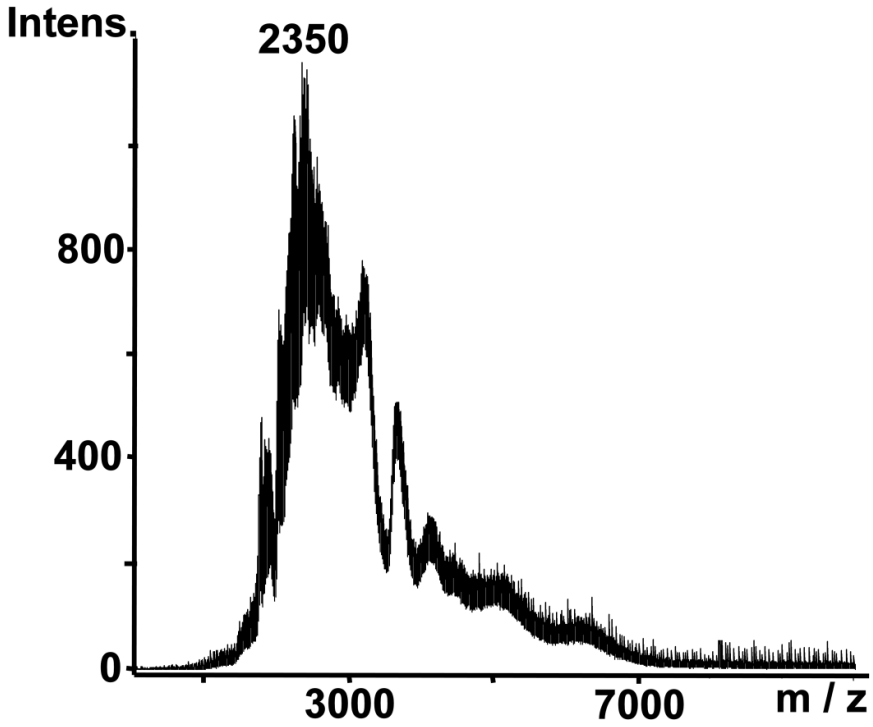

Figure 87: Negative ion mass spectrum in aqueous medium of **13**.

3.3.4 Tellurite coordination modes

The incorporation of the tellurite heteroanion within the mixed-metal system has led to the isolation of three novel archetypes. Such structures are templated by the TeO_3^{2-} heteroatoms which, as we previously observed in the selenite-based novel materials, adopt different coordination modes within the same cage (Figure 88): the μ_9-TeO_3, observed in **11**, **12** and **13**; and the μ_8-TeO_4^{2-} only seen in **11**. This is only the third example of μ_9-TeO_3 coordination found in the literature.[36, 220, 221] This coordination mode is characteristic for heteroanions possessing a lone pair of electrons as it has been observed not only in the previously discussed POMs templated by sulfite or selenite pyramidal heteroanions, but also in the already reported antimony, arsenic or bismuth based lacunary polyoxometalate clusters (see *Section 1.5.1*). The ability of such coordination modes to template a wide variety of materials, which display different nuclearities and structural geometries, unveils the possibility to use tellurites for the isolation of novel materials with interesting architectures and properties. Moreover, the incorporation of heteroatoms with a lone pair of electrons induces electrostatic repulsions during the interaction with the available building blocks in solution and consequently promotes the formation of novel archetypes.

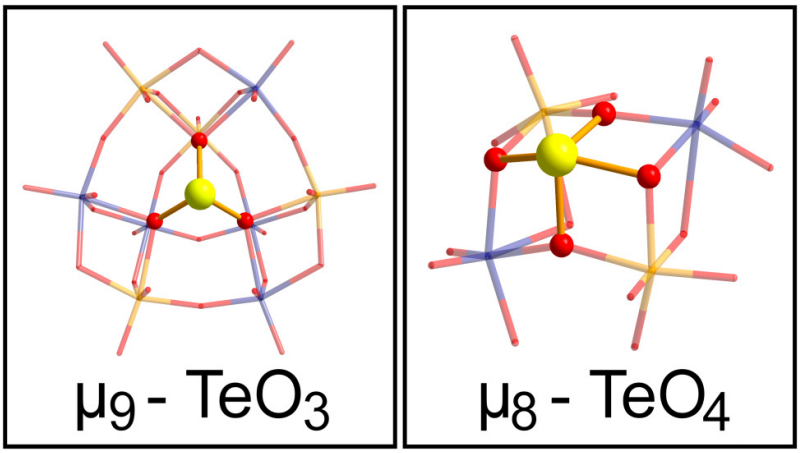

Figure 88: Wire-stick representation of the Te^{IV} coordination modes, μ_9-$Te^{IV}O_3$ (left) where each oxygen is linked to three metal centres, found in **11** and **12** upper and lower layer, and in **13** lower hemisphere. The bridging mode μ_8-$Te^{IV}O_4$ (right) is found in compound **11** where every oxygen atom is linked to two metal centres. Mo: purple sticks, V: orange sticks, Se: yellow spheres and O: red sticks/spheres.

In the previously described sulfite- and selenite-based mixed metal polyoxometalates the incorporated heteroanions adopt the μ_9- coordination mode (X = S or Se) and are encapsulated in the centre of the trivacant Keggin like cage M_9 (Figure 89); and two μ_9-SeO_3 in the case of the $\{Mo_{12}V_{10}Se_8\}$, which consists of two trivacant lacunary Keggin like cages are connected together *via* MoO_6 bridges. However, in the case of the tellurite-based cluster, the two $\{Mo_{12}V_{12}Te_3\}$ and $\{Mo_{12}V_{12}Te_2\}$ "capsules" are templated by two μ_9-TeO_3 heteroanions each. This is the first time that we observed two pyramidal heteroanions templating the mixed-metal cage. In the previous pyramidal-based archetypes only one μ_9-XO_3 anion was encapsulated. This feature is related to the bigger size of the tellurite anion and to the novel structural capping $\{Mo^{VI}_4V^{V}_3V^{IV}_2O_{30}\}$ motif, present in **11** and **12**, which has a cavity wide enough for the incorporation of the second μ_9-TeO_3 anion (see cavity distance in Table 20). In the case of the sulfite- and selenite-based Dawson-like structures, the incorporation of a second μ_9-XO_3 heteroanion is not possible due to the steric restrictions caused by the ring of alternating vertex sharing MoO_6 and VO_4 units. A direct comparison between the sulfite- and selenite-based Dawson-like cages and the conventional Dawson archetype reveals that the interatomic distance between the tetrahedral V centres of the upper hemisphere is *ca.* 4.751(2) Å, whereas the equivalent Mo centres in the classical Dawson lie 6.134(1) apart. In the case of **11** and **12** the equivalent interatomic distances between the tetrahedral V centres is *ca.* 5.485(2). The increased cavity size allows the incorporation of the novel capping $\{Mo^{VI}_4V^{V}_3V^{IV}_2O_{30}\}$ motif which is templated by the μ_9-TeO_3^{2-} anion, situated in the central cavity.

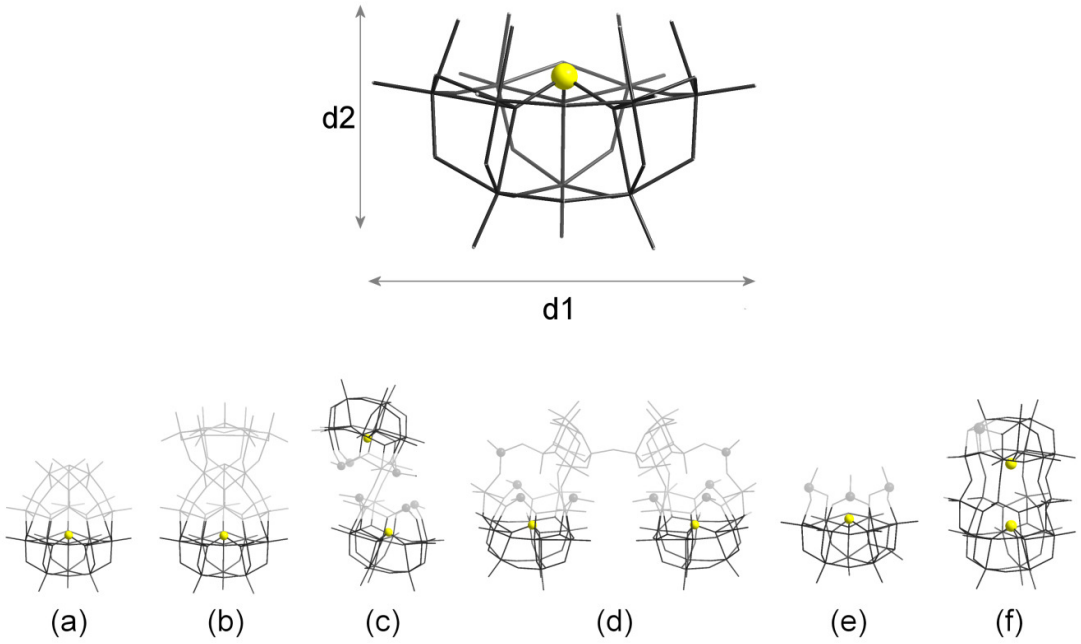

Figure 89: Wire representation of the common M_9 cage (top) templated by the μ_9-XO_3 heteroanion (yellow sphere). This building unit is common in the different mixed metal POMs template by pyramidal heteroanions from Group 16: (a) $\{Mo_{11}V_7X\}$ (X = S, Se); (b) $\{Mo_{17}V_8X\}$ (X = S, Se, Te); (c) $\{Mo_{12}V_{10}X_8\}$(x = Se); (d) $\{Mo_{20}V_{16}X_{10}\}$ (X = Se); (e) $\{V_{10}X_4\}$ (X = Se); and $\{Mo_{12}V_{12}X_3\}$ or $\{Mo_{12}V_{12}X_2\}$ (X = Te). The inorganic framework is shown in dark grey stick whereas the heteroanions are the yellow spheres.

At this point it is important to point out the different sizes of the cavities that the new family of pyramidal-based mixed-metal POM cluster exhibit and how it is related with the atomic radius of the related heteroanion (Figure 89, Table 20). Interestingly, in the case of the egg-shaped Dawson-like structures $\{Mo_{11}V_7X\}$, Figure 89a, the lower cavity sizes for both the sulfite- and selenite-based anions do not show major differences; whereas in the case of the Crown-Dawson archetype, Figure 89b, there appears to be a general trend to decrease the cavity size as you move down the group.

Table 20: Distances between metal centres of opposite MO_6 octahedra (d1) in the M_9 cage templated by the μ_9-XO_3 heteroanion in Figure 89. Only the largest distances are given.

	XO_3^{2-}	M – M distances [Å]
(a)	SO_3^{2-}	7.096(1)
	SeO_3^{2-}	7.109(3)
(b)	SO_3^{2-}	7.138(1)
	SeO_3^{2-}	7.072(2)
	TeO_3^{2-}	7.069(2)
(c)	SeO_3^{2-}	7.009(3)
(d)	SeO_3^{2-}	6.999(2)
(e)	SeO_3^{2-}	7.060(2)
(f) $\{Mo_{12}V_{12}X_3\}$	TeO_3^{2-} (lower hemisphere)	7.100(1)
	TeO_3^{2-} (upper hemisphere)	7.142(2)
(f) $\{Mo_{12}V_{12}X_2\}$	TeO_3^{2-} (lower hemisphere)	7.073(2)
	TeO_3^{2-} (upper hemisphere)	7.092(5)

Another interesting feature within the tellurite-based POMs is the incorporation of the μ_8-TeO_4 heteroanion in compound **11**, which is the first example of such a coordination mode in the case of tellurites. This type of coordination mode was previously observed in the bicapped Keggin polyoxoanion $[PMo_{12}O_{40}Sb^{III}_2]^{4-}$ in which the Sb atoms exhibit a rhombic pyramidal coordination geometry with coordination number 4.[222] In the present case, the tellurite heteroanion adopts an isostructural geometry also with a coordination number of 4, where each of the oxygen atoms is coordinated to two MO_6 (M = Mo or V) octahedra from the upper cage and the lone pair of electrons is pointing out of the plane (Figure 90). Such a coordination mode imparts additional stability to the inorganic cage as well as confirming the possibility to use tellurites as a coordinative ligand. Selected distances between the MO_6 metal centres that are coordinating with the tellurite anion are given in Table 21.

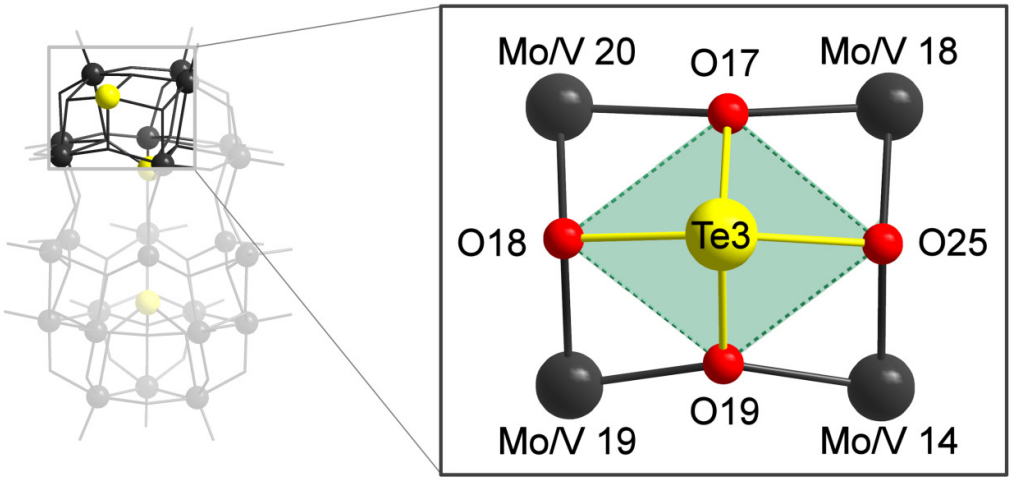

Figure 90: Ball-and-stick representation of the coordination mode of μ_8-TeO_4 heteroanion in compound **11**. The light green area represents the rhombic pyramidal coordination geometry that the heteroanion adopts.

Table 21: Bond distance between the MO_6 octahedra (M = Mo or V) that surround the μ_8-TeO_4 tellurite heteroanion in **11** (see Section 7.10).

	bond distance [Å]
M14 – M18	3.446(2)
M18 – M20	4.058(3)
M20 – M19	3.413(3)
M19 – M14	3.829(2)

The incorporation of the μ_8-TeO_4 heteroanion in **11** could explain the difference in size between the two "capsule" like structures $\{Mo_{12}V_{12}Te_3\}$ and $\{Mo_{12}V_{12}Te_2\}$. As described in Table 20 the d1 M – M distances in the lower and upper hemispheres in **11** and **12** are slightly different, with **11** being wider than **12**. The encapsulation of the third tellurite anion in **11** creates a distortion between the metal centres of the M_9 upper hemisphere elongating the M – M distances. This fact is not only reflected in the height of the M_9 cage but also in its length (d2 in Figure 89); 6.315(2) for **11** and 6.291(3) for **12**. All together this has an effect on the distances between the two μ_9-TeO_3 pyramidal heteroanions within the cage being 4.832(1) Å for **11** and 4.804(1) Å for **12**.

IR spectroscopy was used to study the different coordination modes of the TeO_3^{2-} anion. Assignment of some characteristic bands for compounds **11** – **13** are given in Table 22. The free pyramidal tellurite anion (C_{3v} symmetry) exhibits four fundamental vibrational modes: $\nu_1(A_1)$ = 758 cm^{-1}, $\nu_2(A_1)$ = 364 cm^{-1}, $\nu_3(E)$ = 703 cm^{-1} and $\nu_4(E)$ = 326cm^{-1}.[216] Due to the equivalent environment of the tellurite anion in compounds **11** – **13**, we expected to observe the TeO_3^{2-} bands near the above mentioned vibrational modes. However, because of the overlapping with the ν(M=O) bands, which appeared in the 1000 – 800 cm^{-1} region, we only observed two bands. From Table 22, the difference between the highest and the lowest TeO stretching vibrations, $\Delta|\nu_3 - \nu_1|$, for compounds **12** and **13** is ≈ 140 cm^{-1}. In both compound the tellurite anion is in μ_9-coordination mode. For compound **11** the $\Delta|\nu_3 - \nu_1|$ is ≈ 130 cm^{-1}. As in the case of the selenite anions, where the heteroanion exhibited more than one coordination mode within the same cluster, the distinction of the μ_9-bridging mode from the μ_8- in **11** was not possible by FT-IR spectroscopy. Interestingly, in the present case FT-IR spectroscopy offers an easy way to identify the μ_9-coordination mode of the tellurite heteroanion and to distinguish between the Crown-Dawson anion **13** and the M_{24} cages (**11** and **12**).

Table 22: Diagnostic IR bands [cm^{-1}] of the molybdovanadate sulfite compounds **11** - **13**. Intensity codes: vs = very strong; s = strong; sh = sharp; m = medium

Compound	Bonding modes of TeO_3^{2-}	$\nu_3(E)$	$\nu_1(A_1)$	$\Delta\|\nu_3 - \nu_1\|$ [cm^{-1}]	ν_2 (A_1)	ν_4 (E)	ν(V=O) ν(Mo=O)	Ref
11	μ_8-TeO_4^{2-} μ_9-TeO_3^{2-}	712	845s	133			967s 894s	This work
12	μ_9-TeO_3^{2--}	692	835s	143			968s 889s	This work
13	μ_9-TeO_3^{2-}	696	837s	141			964s 901s	This work

3.3.5 Summary

The incorporation of the tellurite heteroanion within the molybdovanadate mixed-valence system has led to the isolation of three novel archetypes: $[Mo^{VI}_{12}V^{V}_{8}V^{IV}_{4}Te^{IV}O_{69}(\mu_9\text{-}Te^{IV}O_3)_2]^{10-}$ **11a**, $[Mo^{VI}_{12}V^{V}_{8}V^{IV}_{4}O_{69}(\mu_9\text{-}Te^{IV}O_3)_2]^{14-}$ **12a**, and $[Mo^{VI}_{11}V^{V}_{5}V^{IV}_{2}O_{52}(\mu_9\text{-}Te^{IV}O_3)(Mo^{VI}_{6}V^{V}O_{22})]^{10-}$ **13a**. The three compounds belong to the Dawson-like family, templated by non-conventional pyramidal heteroanions from Group XVI. The pH and cation involved in the reaction mixture have proven to be crucial parameters for the isolation of the three compounds. So far, the above mentioned compounds are the largest reported mixed metal POMs which incorporate the pyramidal $Te^{IV}O_3$ anion. ESI-MS has proven to be decisive, not only for the discovery of the aforementioned compounds, but also to identify unambiguously the additional Te^{IV} atom which is incorporated in **11a**.

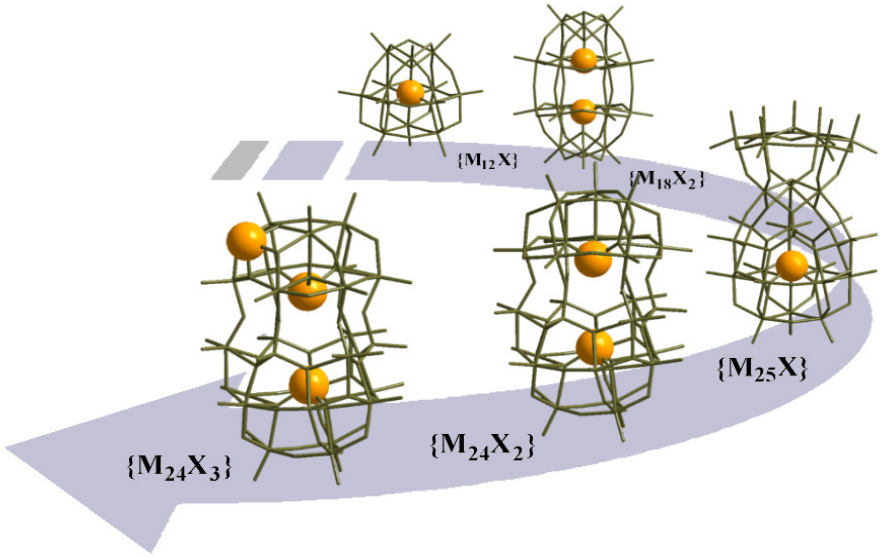

Figure 91: Wire representation of related heteropolyoxometalate clusters and their evolution from Keggin $\{M_{12}X\}$, Wells-Dawson $\{M_{18}X_2\}$ to the tellurite-based POMs $\{M_{25}X\}$ **13**, $\{M_{24}X_2\}$ **12** and $\{M_{24}X_3\}$ **11**. All the cages contain the same lower hemisphere built up from nine MO_6 octahedra and its cavity occupied by the heteroatom X (orange spheres). The inorganic framework of the different clusters is represented by dark-green wires.

Furthermore, the insertion of the pyramidal heteroanion within the mixed-metal and mixed-valence systems guided the self-assembly process of the different building blocks involved in the reaction mixture to the formation of the unprecedented “capsule” like structures. The isolation of such architectures highlights the structural evolution process from the well-know Keggin and Wells-Dawson heteroanions to the compounds described in this section (Figure 91). The Keggin anion is only known with tetrahedral heteroanions as a template, whereas no structure templated by a pyramidal heteroanion has been isolated, due to the electrostatic repulsions arising from the lone pair of electrons and the lack of additional O-coordination site which makes it potentially “less effective” during the templation process.

4 CONCLUSIONS

With the work presented here, we have demonstrated that the incorporation of non-conventional pyramidal heteroanions within mixed-valence molybdovanadate cages results in the isolation of a new family of materials with unprecedented architectures. Molybdenum and vanadium metal centres can exhibit a wide variety of coordination modes and geometries. Meanwhile the pyramidal heteroanions from Group XVI (SO_3^{2-}, SeO_3^{2-} and TeO_3^{2-}), which incorporate a lone pair of electrons, can act as a ligand, exhibit multiple coordination modes, and regulate the pH and act as mild reducing agent (in the case of the sulfites). The combination of molybdenum and vanadium metal centres with pyramidal heteroanions form group XVI can therefore lead to the formation of novel inorganic frameworks considerably different from the analogous structures templated by tetrahedral heteroanions. For the successful isolation of such novel materials it has been fundamental to control precisely the pH and cation involved in the formation mechanism, as well as the Mo:V metal ratio of the starting materials. The study of the interaction of the pyramidal anions on the self-assembly of POMs confirms the existence of a strong relationship between the heteroanion's size and its geometry. Even though sulphur, selenium and tellurium belong to the same group within the periodic table, the bigger the heteroanion is, the more steric restrictions are introduced within the system, as was observed in the formation of the final cluster.

The incorporation of the pyramidal SO_3^{2-} heteroanion within the molybdovanadate system has led to the isolation of two unique archetypes: $(NH_4)_7[Mo^{VI}_{11}V^{V}_{5}V^{IV}_{2}O_{52}(\mu_9\text{-}SO_3)]\cdot 12H_2O$ **1** and $(NH_4)_{10}[Mo^{VI}_{11}V^{V}_{5}V^{IV}_{2}O_{52}(\mu_9\text{-}SO_3)(Mo^{VI}_{6}V^{V}O_{22})]\cdot 14H_2O$ **2**. Both compounds are related to the $M_{18}(XO_4)_2$ Wells-Dawson anion but exhibit different structural features as a consequence of the presence of the sulfite heteroatom with its lone pair of electrons, and the participation of molybdenum and vanadium metal centres with different oxidation states and coordination modes. The use of mass spectrometry techniques have proven to be crucial in terms of observing the formation of the above mentioned compounds in solution, as well as to establish the existence of the sulfite-based

pyramidal template within the Dawson shell, and the number of reduced vanadium metal centres.

We have also successfully isolated compound **2** using **1** as a starting material, which demonstrates that it is possible to use **1** as secondary building unit (Figure 92). When compound **1** was first isolated, it was considered that the three di-oxo Mo units on the cap of the distorted Dawson structure were inert since the site on the cap was electronically saturated. However, the isolation of compound **2** demonstrates that such assumption was wrong and that the di-oxo units on the cap react efficiently with appropriate building units, giving bigger architectures while at the same time retaining the structural and chemical information from the parent molecule. Expanding our studies to better understand the formation mechanism of such materials, we plan to use **2** as a secondary building unit for designing and manufacturing novel and bigger species in the nano-scale. For the successful formation of the Keplerate ball, it was crucial to use triethanolamine (TEA) molecules ("shrink-wrapping" effect) along with Na^+ or K^+ cations; not only because TEA directs the self-assembly process but because it promotes the reduction of the V^V metal centres. Although it may seem ordinary that labile POM clusters show increased reactivity under appropriate reaction conditions, a systematic study of such ligand promoted transformation process leading to the isolation and characterization of the final product retaining the initial architectural and chemical information is quite extraordinary. This work shows that it is possible to use reactive but non-lacunary POM-based species as synthons to trigger the formation of new cluster types.

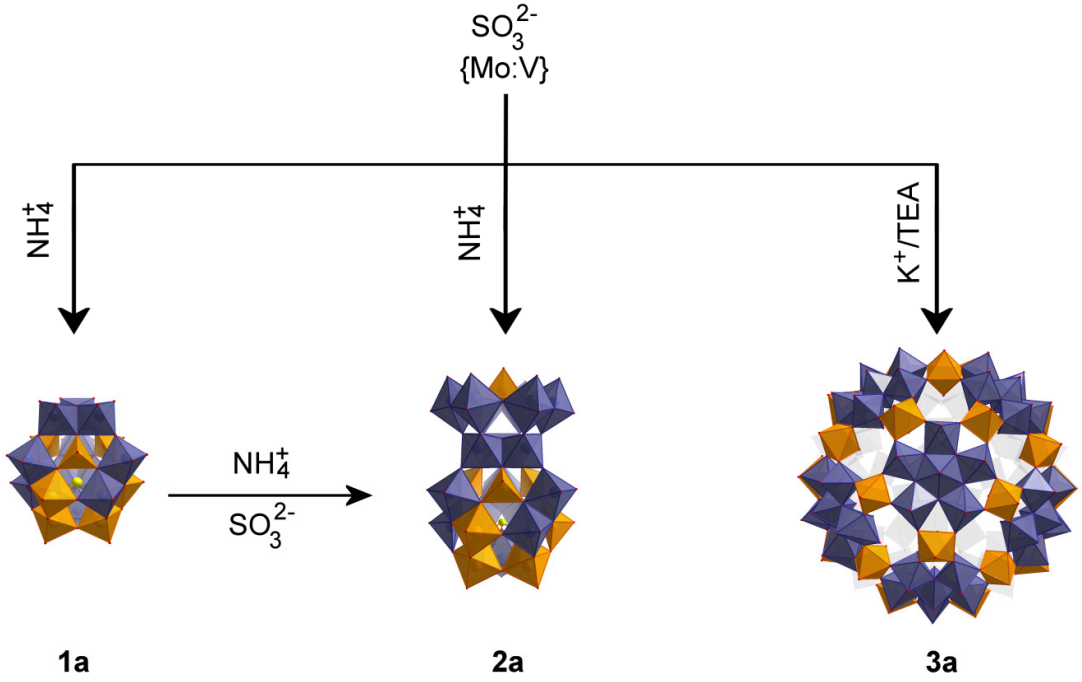

Figure 92: Schematic representation of the three sulfite-based polyoxometalates isolated under accurate control of the {Mo:V} ratio and cation involved in the reaction mixture. The template effect of the sulfite anion triggers the self-assembly of the different frameworks which exhibit novel structural features. Each of the three compounds can be isolated from different one pot reactions and at the same time each of them act as a building unit for the subsequent cluster, higher in nuclearity than its ancestor. Mo: purple polyhedra, V: orange polyhedra, Se: yellow spheres and O: red spheres.

In a similar fashion as in the case of the sulfite-based polyoxometalates, the selenite heteroanion triggered the self-assembly formation of four new inorganic cages, which contains the largest mixed-metal selenite-based POMs reported so far: $[Mo^{VI}_{12}V^{V}_{10}O_{58}(SeO_3)_8]^{10-}$ (**5a-6a**), $[Mo^{VI}_{11}V^{V}_{5}V^{IV}_{2}O_{52}(\mu_9\text{-}SeO_3)]^{7-}$ (**7a-8a**), $[Mo^{VI}_{11}V^{V}_{5}V^{IV}_{2}O_{52}(\mu_9\text{-}SeO_3)(Mo_6VO_{22})]^{10-}$ (**9a**), and $[Mo^{VI}_{20}V^{V}_{12}V^{IV}_{4}O_{99}(SeO_3)_{10}]^{22-}$ (**10a**). Accurate control of the experimental conditions such as pH and the cation involved in the reaction mixture helped us to direct the self-assembly process and give rise to the isolation of novel archetypes with high nuclearities (Figure 93). This new series of compounds is an extension of the family of mixed-metal polyoxometalates templated by heteroatoms from Group XVI. The plethora of coordination modes that the SeO_3^{2-}

heteroanion displays within the different compounds mentioned above demonstrates the ability of the selenite anion to act as a ligand and stabilize novel libraries of building blocks which led to the isolation of new materials. ESI-MS studies proved once more to be decisive for the unambiguous determination of the novel archetypes in solution along with FT-IR spectroscopy which proved to be a valuable technique for the identification of the different coordination modes of the selenites in solid state.

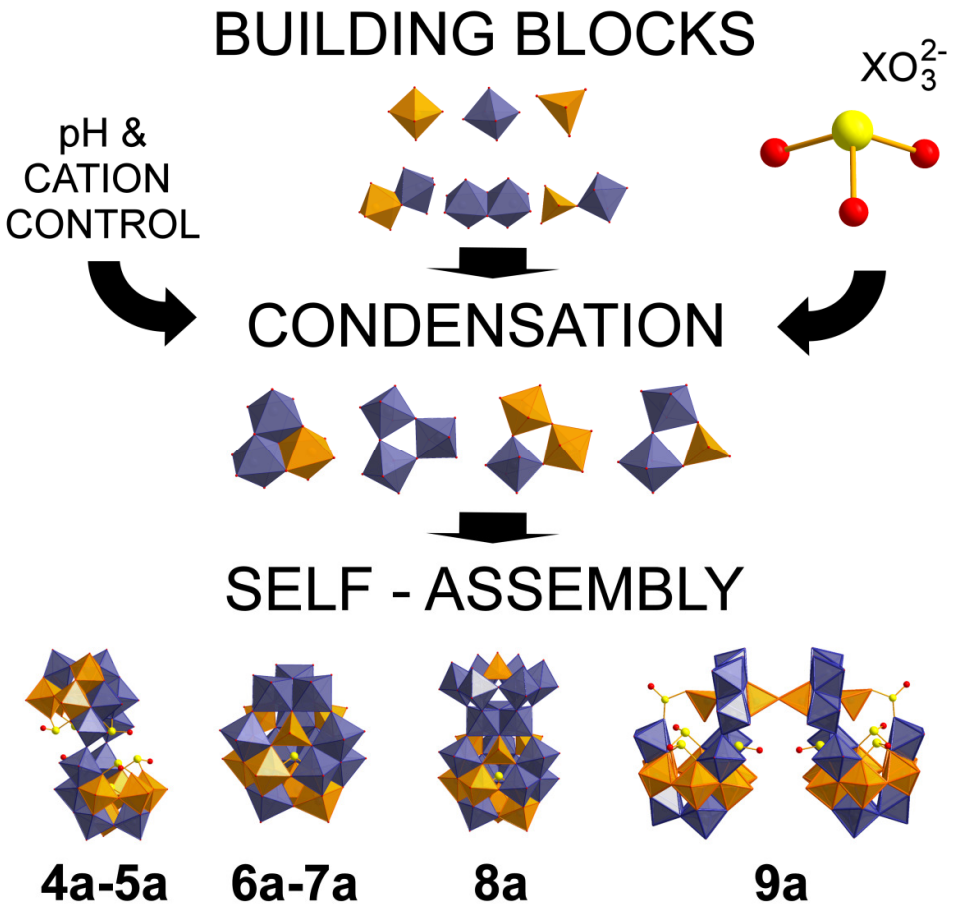

Figure 93: Representation of the self-assembly process by which the different building units involved in the reaction mixture leads to the isolation of the new family of selenite-based polyoxometalates. The template effect of the heteroanion along with the pH and cation control induces the formation of the four novel Dawson-like archetypes with the common M_9X building block. Mo: purple polyhedra, V: orange polyhedra, Se: yellow sphere and O: red sphere.

The exclusive use of vanadium as a principle metal addenda for the isolation of novel materials templated by the pyramidal selenite heteroanion has led to the formation of two unprecedented vanadate cages, related to the trivacant lacunary Keggin anion, and templated by one central μ_9-SeO_3 and three peripheral (μ,μ)-SeO_3 heteroanions with one free terminal oxo group: $[V^{V}_{8}V^{IV}_{2}O_{25}(SeO_3)_4]^{10-}$ **14a** and $[V^{V}_{7}V^{IV}_{5}O_{27}(SeO_3)_4]^{7-}$ **15a**. The isolation of these new inorganic metal oxide cages opens a new pathway for the isolation of larger and novel archetypes by using **14a** and **15a** as a building blocks, as we have verified by the isolation of the cobalt-analogue cage $[Co(OH_2)_3V^{V}_{9}V^{IV}O_{25}(SeO_3)_4]^{5-}$ **16** (Figure 94).

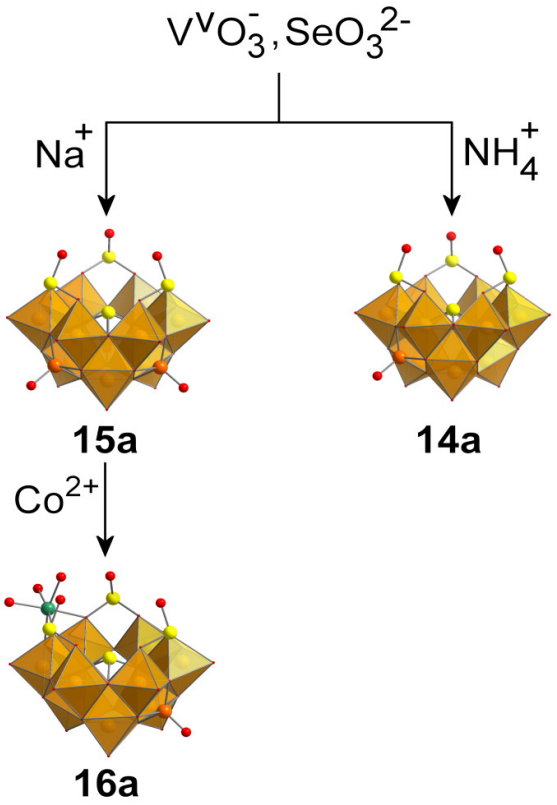

Figure 94: Schematic representation of the three vanadoselenite cages isolated from one pot reaction *via* cation control. In the case of **15a**, the cage acts as a secondary building unit for the formation of **16a** upon addition of cobalt(II) sulfate. The vanadates display two different geometries within the same archetype: the VO_6 octahedra (orange polyhedra) and the VO_5 square pyramid (orange spheres). Co: green sphere, Se: yellow spheres and O: red spheres.

The isolation of the three compounds mentioned above corroborates the fundamental role of the pyramidal heteroanion, that not only templates the formation of the mixed-valence basket-like cages but also displays different coordination modes within the same archetype. In the previous cases, when different molybdate building units were present in solution, the self-assembly process was directed towards the formation of higher nuclearity clusters related with to M_{18} Wells-Dawson archetypes. In the present case, the absence of the molybdenum centres led to the formation of novel cages related to the M_{12} Keggin anion instead. This could be a consequence of the tendency that vanadium has to adopt VO_5 square pyramidal geometry, which gives more flexibility to the frameworks and so the isolated archetypes display more ball-like structures. In this case, the incorporation of the heteroanion restricted the closure of the ball and provided the opportunity to isolate a lacunary Keggin-like cage which exhibited available coordination sites and could therefore be used as secondary building unit.

The isolation of the three novel mixed-metal, mixed-valence polyoxo-molybdenum/vanadium-tellurite clusters $[Mo^{VI}_{12}V^{V}_{8}V^{IV}_{4}Te^{IV}O_{69}(\mu_9\text{-}Te^{IV}O_3)_2]^{10-}$ **11a**, $[Mo^{VI}_{12}V^{V}_{8}V^{IV}_{4}O_{69}(\mu_9\text{-}Te^{IV}O_3)_2]^{14-}$ **12a** and $[Mo^{VI}_{11}V^{V}_{5}V^{IV}_{2}O_{52}(\mu_9\text{-}Te^{IV}O_3)(Mo^{VI}_{6}V^{V}O_{22})]^{10-}$ **13a**, which belong to the "Crown"-Dawson mixed-metal HPOM family templated by heteroanions from Group XVI, completes the series of investigations on the effect of the pyramidal heteroanions from the group of chalcogens (S, Se, Te) where we demonstrated that the pyramidal geometry has a profound effect on the self-assembly process and consequently on the products isolated. The above compounds are the largest mixed metal POMs reported so far which incorporate the pyramidal $Te^{IV}O_3$ anion. ESI-MS studies proved to be crucial not only for the discovery of the aforementioned compounds, but also to identify unambiguously the additional Te^{IV} atom which is incorporated in **11a**. Furthermore, we demonstrated the cooperative effect of the counterion along with the size of the heteroanion which allowed the discovery and isolation of such novel POM-based compounds (Figure 95).

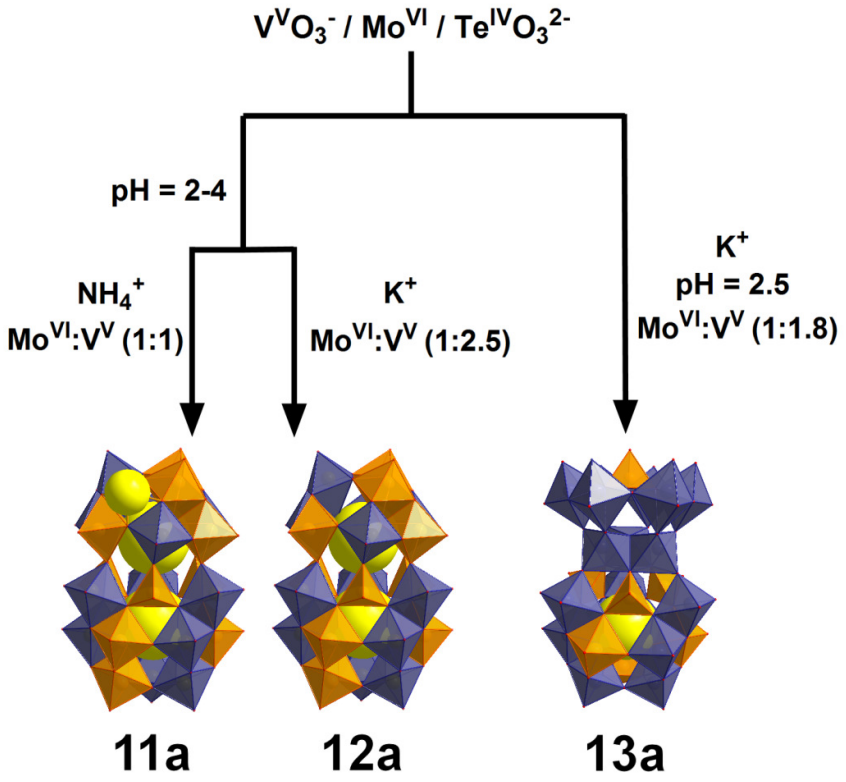

Figure 95: Schematic representation of the novel tellurite-based mixed-metal polyoxometalates where the cation and {Mo:V} ratios are highlighted as principal variables for the isolation of the different compounds. Mo: purple polyhedra, V: orange polyhedra, Te: yellow sphere and O: red sphere.

To conclude, we showed that the radius of the heteroanions used had a significant impact on the self-assembly process. As the size of the heteroanion increased, higher nuclearity structures were isolated (Table 23). The smaller sized (SO_3^{2-}) triggered the formation of the novel archetypes {$Mo_{11}V_7S$} and {$Mo_{17}V_8S$}; and its transformation process since it is used as reducing agent and pH-buffer control. The medium sized (SeO_3^{2-}) proved to be the most diverse one, as it gave us the opportunity to isolate a plethora of structures and nuclearities ranging from {$Mo_{11}V_7Se$} and {$Mo_{12}V_{10}Se_8$} to {$Mo_{17}V_8Se$} and {$Mo_{20}V_{16}Se_{10}$} respectively. The larger sized (TeO_3^{2-}) yielded the isostructural cages {$Mo_{12}V_{12}Te_3$} and {$Mo_{12}V_{12}Te_2$}, which had not been observed in the case of sulfite or selenite templating anions.

Table 23: Summary of the different inorganic archetypes built up from mixed-metal building units and templated by pyramidal heteroanions from Group XVI. It is also represented the nuclearity, heteroanion and bridging modes of the different heteroatoms participating in the cluster cage.

Compound	Nuclearity (with heteroanion)	Heteroanion XO_3^{2-}	Heteroanion Coordination Mode
$\{Mo_{11}V_7X\}$	18 (19)	SO_3^{2-} SeO_3^{2-}	μ_9- XO_3^{2-}
$\{Mo_{17}V_8X\}$	25 (26)	SO_3^{2-} SeO_3^{2-} TeO_3^{2-}	μ_9- XO_3^{2-}
$\{Mo_{12}V_{10}X_8\}$	22 (30)	SeO_3^{2-}	μ_9 - SeO_3^{2-} (μ,μ) - SeO_3^{2-} (η,μ) - SeO_3^{2-}
$\{Mo_{20}V_{16}Se_{10}\}$	36 (46)	SeO_3^{2-}	μ_9 - XO_3^{2-} (μ,μ) - XO_3^{2-} (η,η) - XO_3^{2-}
$\{Mo_{12}V_{12}X_3\}$	24 (27)	TeO_3^{2-}	μ_9- XO_3^{2-} μ_8- XO_4^{2-}
$\{Mo_{12}V_{12}X_2\}$	24 (26)	TeO_3^{2-}	μ_9- XO_3^{2-}
$\{V_{12}X_4\}$	12 (16)	SeO_3^{2-}	μ_9 - XO_3^{2-} (μ,μ) - XO_3^{2-}
$\{V_{10}X_4\}$	10 (14)	SeO_3^{2-}	μ_9 - XO_3^{2-} (μ,μ) - XO_3^{2-}
$\{CoV_{10}X_4\}$	11 (15)	SeO_3^{2-}	μ_9 - XO_3^{2-} (μ,μ) - XO_3^{2-}

Moreover, the use of FT-IR spectroscopy proved to be a useful tool for the study of the different coordination modes of the pyramidal heteroanions. It was demonstrated that the identification of the different bridging modes was only possible when the heteroanion is in an equivalent environment. Consequently, the comparison between the isostructural cages

templated by the μ_9- XO_3^{2-} anion (X = S, Se and Te) is possible. As it is shown in Table 24, the difference between the highest and the lowest XO stretching vibrations, $\Delta|\nu_3-\nu_1|$, is slightly larger in the sulfite-based material than in the tellurites. Such observations corroborate the trend that exists when going down in a group from the periodic table.

Table 24: Comparison between the $\Delta|\nu_3-\nu_1|$ of the isostructural Dawson-based cages $\{Mo_{11}V_7X\}$ and $\{Mo_{17}V_8X\}$, templated by different pyramidal heteroanions from Group XVI.

	$\Delta\|\nu_3-\nu_1\|$, [cm^{-1}]	
μ_9- XO_3^{2-}	$\{Mo_{11}V_7X\}$	$\{Mo_{17}V_8X\}$
μ_9- SO_3^{2-}	153	150
μ_9- SeO_3^{2-}	153	145
μ_9- TeO_3^{2-}	-	143

The versatility of mixed-valence polyoxometalate clusters that have been isolated during this work demonstrates the strong influence of the heteroanion's geometry and size in the assembly of the different building units involved in the reaction mixture. Furthermore, the ability of the heteroanions to act as ligands and the use of these materials as secondary building blocks open a new front for the development of novel synthetic strategies and the discovery of new materials with potential magnetic and redox properties. The use of ESI/CSI mass spectroscopy techniques have proved to be decisive not only to understand the behaviour of the different cages in solution but also to find stable species in solution for further use as secondary building units. Moreover, the demonstration of cation induced sizing of nanosized species opens the door towards the engineering of molecular nanoparticles of desirable size and pre-defined functionality.

5 EXPERIMENTAL

5.1 Materials

All reagents and chemicals were supplied by *Sigma Aldrich Chemical Company Ltd*., *Alfa Aesar, Fisher Scientific*, and *Lancaster Chemicals*. Unless stated otherwise, the materials were used without further purification. Solvents were supplied by *Fisher Chemicals*.

5.2 Instrumentation

The following instrumentation was used to obtain analytical and spectroscopic data herein:

Fourier-transform infrared (FT-IR) spectroscopy: Unless stated otherwise, the materials were prepared as KBr pellets and FT-IR spectra were collected in transmission mode using a JASCO FT-IR-410 spectrometer or a JASCO FT-IR 4100 spectrometer. Wavenumbers ($\tilde{\nu}$) are given in cm^{-1}; intensities as denoted as vs = very strong, s = strong, m = medium, w = weak, br = broad, sh = sharp.

Microanalysis: Nitrogen and hydrogen content were determined by the microanalysis services within the Department of Chemistry, University of Glasgow using a EA 1110 CHNS, CE-440 Elemental Analyser.

Mass Spectrometry: Electrospray-ionisation mass spectrometry (ESI-MS) and coldspray-ionisation mass spectrometry (CS-MS) were performed using a Bruker micrOTOF-Q quadrupole time-of -flight mass spectrometer.

Single Crystal X-ray Diffraction: Single crystal datasets were collected at 150(2) K on the following instruments:

- Bruker AXS Apex II QUAZAR ($\lambda_{MoK\alpha}$ = 0.71073Å) equipped with a graphite monochromator.
- Oxford Diffraction Gemini Ultra ($\lambda_{MoK\alpha}$ = 0.71073Å and $\lambda_{CuK\alpha}$ = 1.54178 Å) equipped with a graphite monochromator and ATLAS CCD detector.

Powder X-ray Diffraction (XRD): Powder XRD patterns were collected on a PANalytical X'PERT Pro diffractometer ($\lambda_{CuK\alpha}$ = 1.5405 Å) equipped with a graphite monochromator and a X'Celerator detector. Unless stated otherwise the datasets were collected in flat plate holder mode at room temperature.

UV-Vis spectroscopy: UV-Vis spectra were collected using a JASCO V-670 spectrometer equipped with an ISV723 60mm integrating sphere in diffuse reflectance mode.

Thermogravimetric analysis (TGA): Thermogravimetric analysis was performed on a TA Instruments Q 500 Thermogravimetric Analyzer under nitrogen flow at a typical heating rate of 5 °C min^{-1} or from room temperature to either 700 ºC or 1000 ºC.

Flame Atomic Absorption Spectroscopy Analysis: FAAS analysis was performed at the Environmental Chemistry Section, Department of Chemistry, The University of Glasgow on a Perkin-Elmer 1100B Atomic Absorption Spectrophotometer.

Redox Titrations where performed using a TOLEDO pH-meter with a conductivity probe. The corresponding materials were dissolved in water (previously degased with nitrogen) and the titrations were done using a solution of 0.01 M Ce^{IV} in 0.5 M of sulphuric acid solution.

5.3 Synthesis and Characterisation

5.3.1 Synthesis of compound $(NH_4)_7[Mo^{VI}_{11}V^{V}_{5}V^{IV}_{2}O_{52}(\mu_9\text{-}SO_3)]\cdot 12H_2O$ 1

$(NH_4)_6Mo^{VI}_7O_{24}\cdot 4H_2O$ (0.60 g, 0.4 mmol) was dissolved in an HCl solution (37 % HCl in water, 1:4 v/v, 25 ml, pH ~ 0) and then solid NH_4VO_3 (0.60 g, 5.1 mmol) was added in one portion to the solution under stirring. Upon dissolution of NH_4VO_3 the light red colour of the solution changed to light green and the pH changed to 0.7. Then, solid $(NH_4)_2SO_3$ (6.20 g, 46.2 mmol) was gradually added to it, under magnetic stirring. A series of colour changes ensued beginning from yellow-orange colour at pH=0, then light blue at pH = 1.5, followed by the formation of a deep violet (pH = 3) solution. The same crystalline material isolated in the range 2.5 – 5 of pH values. At pH value of 3 obtained the highest yield. The solution was filtered off and the filtrate left in an open vessel (a 250 ml beaker) at room temperature (~25 ^oC) for 3 days, during which deep green crystals suitable for X-ray structure analysis, were obtained. Yield: 0.95 g (21 % based on Mo).

Elemental analysis calcd for: $H_{52}Mo_{11}N_7O_{67}SV_7$: H: 1.97, N: 3.68, S: 1.20, Mo: 39.58, V: 13.37; found: H: 1.88, N: 3.82, S: 1.22, Mo: 39.48, V: 13.40.

FT-IR [(KBr) ν/cm^{-1}]: 3400 (br) [ν(O–H) from H_2O], 1401s [δ(NH_4^+)], 970 (sh) [ν(V=O)], 944 (s) [ν(Mo=O)], 886 (s) [ν(SO_3^{2-})], 861 (s) [ν(SO_3^{2-})], 817 (vs) [ν(SO_3^{2-})].

UV-Vis (in H_2O): λ_{max}, [nm, ($dm^3mol^{-1}cm^{-1}$)] = 243(21000), 587(530).

TGA data from **1** shows that weight loss between 25 – 200 ^oC can be assigned to approx. 12 water molecules in the crystal lattice, while between 200 – 400 °C, can be assigned to removal of 7 NH_4^+ cations as NH_3 molecules. The weight loss between 450 – 510 ^oC is assigned to the removal of SO_3^{2-} as gas SO_2).

5.3.2 Synthesis of compound $(NH_4)_{10}[Mo^{VI}_{11}V^{V}_{5}V^{IV}_{2}O_{52}(\mu_9\text{-}SO_3)(Mo^{VI}_{6}V^{V}O_{22})]\cdot 14H_2O$ 2

Ammonium molybdate tetrahydrate (0.60 g, 0.4 mmol) was dissolved in an HCl solution (37% HCl in water, 1:4 v/v, 25 mL, pH ~ 0), and then the solid ammonium metavanadate (0.40 g, 3.4 mmol) was added in one portion to the solution under stirring. Upon dissolution of the NH_4VO_3 the solution turns to light yellow colour and the pH changed to 0.7. Then, solid $(NH_4)_2SO_3$ (9.33 g, 69.5 mmol) was gradually added under magnetic stirring. A series of colour changes ensued, beginning from a green colour at pH 0.7, then light blue colour at pH 1.5, followed by a dark green colour at pH 2 and ending with a deep violet solution at pH 3. Compound **2** could be synthesized within the pH range of 2 - 4. The solution was filtered off and the filtrate left in an open vessel (a 100 mL beaker) at room temperature (~25 °C) for a week, during which time dark green crystals suitable for X-ray structure analysis were obtained. During the crystallization time the dark green solution turns to deep purple. At this point the solution needs to be filtered off to avoid formation of by-products. The first yield of crystals appears while the solution is purple. The crystallization process continues till the point where the mother liquor has light green colour. Yield 0.11 g (0.03 mmol, 56% based on Mo).

Elemental analysis for: $H_{72}Mo_{17}N_{12}O_{89}S_1V_8$ (3734.98); calcd (%): H: 1.84, Mo: 43.66, N: 3.75, V: 10.91; found (%): H: 1.65, Mo: 43.98, N: 4.25, V: 10.95.

FT-IR [(KBr) ν/cm^{-1}] 3442 (br) [ν(O–H) from H_2O], 1613 (s) [$\nu(H_2O)$], 1401 [$\delta(NH_4^+)$], 962 (sh) [ν(V=O)], 944 (s) [ν(Mo=O)], 895 (s) [$\nu(SO_3^{2-})$], 872 (s) [$\nu(SO_3^{2-})$], 812 (vs) [$\nu(SO_3^{2-})$].

UV-Vis (in H_2O): λ_{max}, [nm, (dm^{3}mol^{-1}cm^{-1})] = 610.5(2400), 800(1900).

TGA data from **2** shows that weight loss between 25 – 200 ^{o}C can be assigned to approx. 14 water molecules in the crystal lattice, while between 200 – 600 °C, can be assigned to removal of 10 NH_4^+ cations as NH_3 molecules which is overlapping with the removal of SO_3^{2-} as SO_2 gas), the remaining percentage (600 – 800 °C) can be assigned to the MoO_3 based phase transition.

5.3.3 Synthesis of compound $\{Mo_{72}V_{30}(SO_4)_{12}\}$ 3

Sodium molybdate dihydrate (0.60 g, 2.4 mmol) was dissolved in an HCl solution (37% HCl in water, 1:4 v/v, 25 mL, pH ~ 0), and then the solid sodium metavanadate (0.40 g, 3.2 mmol) was added in one portion to the solution under stirring. Upon dissolution of the $NaVO_3$ the solution turns to light yellow colour and the pH changed to 0.7. Then, solid triethanolamine (1.3 g, 8.7 mmol) added followed by Na_2SO_3 (9.33 g, 74.0 mmol) under magnetic stirring. A series of colour changes ensued, beginning from a green colour at pH 0.7, then light blue colour at pH 1.5, followed by a dark green colour at pH 2 and ending with a deep violet solution at pH 3.5. The Keplerate compound could be synthesized within the pH range of 2.5 – 4.5. The solution was filtered off and then treated with KCl (0.65 g, 8.72 mmol). The filtrate left in an open vessel (a 100 mL beaker) at room temperature (~25 °C) for 5 days, during which time dark purple crystals suitable for X-ray structure analysis were obtained. Yield: 0.20 g (30.4 % based on Mo). The unit cell determination revealed dimensions identical to the previously reported compound with formula, $Na_8K_{24}Mo_{72}V_{32}S_{12}O_{538}H_{412}$ ($\{Mo_{72}V_{30}\}$). IR (KBr): 1625 (H_2O), 1201 (w), 1129 (w), 1049 (w), 966 ν(Mo–O_t)/ν(V–O_t)), 795 (vs), 631 (m).

5.3.4 Synthesis of compound $K_{10}[Mo^{VI}_{12}V^{V}_{10}O_{58}(SeO_3)_8]\cdot 18H_2O$ 4

K_2MoO_4 (0.67 g, 2.8 mmol) was dissolved in 25 mL of deionised water. Then solid KVO_3 (0.70 g, 5.1 mmol) was added in one portion to the solution under stirring and the solution was heated to 90 °C for 10 minutes, during which time the vanadate salt completely dissolves. Solid K_2SeO_3 (0.19 g, 0.93 mmol) and $NH_2NH_2\cdot 2HCl$ (4.2 mg, 40 µmol) were successively added under stirring and the pH was adjusted by drop-wise addition of 3M HCl after the reaction was cooled down at room temperature. Compound **4** can be isolated between pH 0.5 and 2.5 being 1.5 the optimum pH. The dark brown solution was filtered off and the filtrate left in an open vessel (a 100 mL beaker) at room temperature (~ 25 ºC) for two days, during which time dark orange crystals suitable for X-ray structure analysis were obtained. Yield: 0.271 g (0.06 mmol, 27 % based on Mo).

Elemental analysis for: $H_{36}K_{10}Mo_{12}O_{100}Se_8V_{10}$ (4319.5); calcd (%): Mo 26.65, V 11.79, Se 14.62, K 9.05; found (%): Mo 26.75, V 11.44, Se 14.33, K 9.34.

FT-IR [(KBr) ν/cm^{-1}] 3425 (br) [ν(O–H) from H_2O], 1623 (s) [ν(H_2O)], 964 (sh) [ν(V=O)], 879 (s) [ν(Mo=O)], 803 (s) [ν(SeO_3^{2-})], 746 (s) [ν(SeO_3^{2-})], 699 (vs) [ν(SeO_3^{2-})], 564 (vs) [ν(SeO_3^{2-})].

UV-Vis (in H_2O): λ_{max}, [nm, (dm^{3}mol^{-1}cm^{-1})] = 210(110000), 238(54000)

TGA data from **4** shows that weight loss between 25 – 200 ^{o}C can be assigned to approx. 18 water molecules in the crystal lattice, while between 200 – 500 °C, can be assigned to removal of 8 SeO_3^{2-} as SeO_2 gas.

5.3.5 Synthesis of compound $(NH_4)_6K_4[Mo^{VI}_{12}V^{V}_{10}O_{58}(SeO_3)_8]\cdot 18H_2O$ 5

Solid NH_4VO_3 (0.40 g, 3.4 mmol) was added in one portion to a stirred solution of $(NH_4)_6Mo_7O_{24}\cdot 4H_2O$ (0.60 g, 0.4 mmol) in water (25 mL); and the solution was heated to 90 °C until the vanadate salt is completely dissolved. The reaction is allowed to cool down at room temperature and then solid K_2SeO_3 (0.19 g, 0.93 mmol) was added. After 5 minutes of stirring $NH_2NH_2\cdot 2HCl$ (4.2 mg, 40 µmol) was slowly added. The reaction mixture was stirred for 10 min and the pH was adjusted to 1.5 by addition of concentrated HCl to the solution. The dark brown solution was filtered and the filtrate was left crystallise for two weeks in an open vessel at room temperature. Dark orange crystals were filtered and dried in air. Yield: 0.253 g (0.06 mmol, 26 % based on Mo).

Elemental analysis for: $H_{60}K_4Mo_{12}N_6O_{100}Se_8V_{10}$ (4193.12); calcd (%):Mo 27.46, V 12.15, Se 15.06, K 3.76, N: 2.00; found (%):Mo 27.10, V 12.31, Se 15.00, K 3.77, N 2.73.

FT-IR [(KBr) ν/cm^{-1}] 3444 (br) [ν(O–H) from H_2O], 1611 (s) [ν(H_2O)], 1402 (s) [ν(NH_4^+)], 971 (s) [ν(V=O)], 863 (s) [ν(Mo=O)], 754 (s) [ν(SeO_3^{2-})], 665 (s) [ν(SeO_3^{2-})], 569 (m) [ν(SeO_3^{2-})], 533 (m) [ν(SeO_3^{2-})].

UV-Vis (in H_2O): λ_{max}, [nm, (dm^{3}mol^{-1}cm^{-1})] = 209(140000), 240.2(81000), 269.6(47000).

TGA data from **5** shows that weight loss between 25 – 200 ^{o}C can be assigned to approx. 18 water molecules in the crystal lattice, while between 200 – 400 °C, can be assigned to

removal of 6 NH_4^+ cations as NH_3 molecules which is overlapping with the removal of 8 SeO_3^{2-} as SeO_2 gas.

5.3.6 Synthesis of compound $K_7[Mo^{VI}_{11}V^{V}_{5}V^{IV}_{2}O_{52}(\mu_9\text{-}SeO_3)]\cdot 31H_2O$ 6

K_2MoO_4 (0.67 g, 2.8 mmol) was dissolved in 25 mL of deionised water. Then solid KVO_3 (0.70 g, 5.1 mmol) was added in one portion to the solution under stirring and the solution was heated to 90 °C for 10 minutes, during which time the vanadate salt completely dissolves. Solid K_2SeO_3 (0.19 g, 0.93 mmol) and $NH_2NH_2\cdot 2HCl$ (4.2 mg, 40 µmol) were successively added under stirring and the pH was adjusted by drop-wise addition of 3M HCl to 3. The dark brown solution was filtered off and the filtrate left in an open vessel (a 100 mL beaker) at room temperature (~ 25 ºC) for one week, during which time brown hexagonal crystals suitable for X-ray structure analysis were obtained. Yield: 0.075 g (0.02 mmol, 10 % based on Mo).

Elemental analysis for: $H_{62}K_7Mo_{11}O_{86}SeV_7$ (3202.92); calcd (%): Mo 33.32, V 11.26, Se 2.49, K 8.64; found: Mo 34.00, V 11.31, Se 2.36, K 9.01.

FT-IR [(KBr) ν/cm^{-1}] 3454 (br) [ν(O–H) from H_2O], 1618 (s) [$\nu(H_2O)$], 964 (sh) [ν(V=O)], 858 (s) [ν(Mo=O)], 814 (s) [$\nu(SeO_3^{2-})$], 747 (s) [$\nu(SeO_3^{2-})$], 568 (vs) [$\nu(SeO_3^{2-})$].

UV-Vis (in H_2O): λ_{max}, [nm, (dm^{3}mol^{-1}cm^{-1})] = 206.4(110000), 264.6(48000), 326.8(14000).

TGA data from **6** shows that weight loss between 25 – 400 ^{o}C can be assigned to approx. 31 water molecules in the crystal lattice which is overlapping with the removal of 1 SeO_3^{2-} as SeO_2 gas.

5.3.7 Synthesis of compound $(NH_4)_4K_3[Mo^{VI}_{11}V^{V}_{5}V^{IV}_{2}O_{52}(\mu_9\text{-}SeO_3)]\cdot 29H_2O$ 7

Solid NH_4VO_3 (0.36 g, 3.1 mmol) was added in one portion to a stirred solution of $(NH_4)_6Mo_7O_{24}\cdot 4H_2O$ (0.60 g, 0.4 mmol) in water (25 mL). Then, the solid K_2SeO_3 (0.19 g,

0.93 mmol) was added and after 5 minutes of stirring $NH_2NH_2 \cdot 2HCl$ (4.2 mg, 40 µmol) was slowly added. The reaction mixture was stirred for 10 min and the pH was adjusted to 4.0 by addition of concentrated HCl to the solution. The dark green solution was filtered and the filtrate was left crystallise for two weeks in an open vessel at room temperature. The green hexagonal crystals were filtered and dried in air. Yield: 0.314 g (0.10 mmol, 41 % based on Mo).

Elemental analysis for: $H_{74}K_3Mo_{11}N_4O_{84}Se_1V_7$ (3061.6); calcd (%): Mo 34.47, V 11.65, Se 2.58, K 2.55, N: 2.29; found: Mo 34.71, V 12.31, Se 3.09, K 2.51, N 3.01.

FT-IR [(KBr) ν/cm^{-1}] 3444 (br) [ν(O–H) from H_2O], 1401 (s) [$\nu(NH_4^+)$], 952 (s) [ν(V=O)], 862 (s) [ν(Mo=O)], 818 (m) [$\nu(SeO_3^{2-})$], 747 (m) [$\nu(SeO_3^{2-})$], 580 (m) [$\nu(SeO_3^{2-})$], 546 (m) [$\nu(SeO_3^{2-})$].

UV-Vis (in H_2O): λ_{max}, [nm, (dm^{3}mol^{-1}cm^{-1})] = 210(120000), 266(53000), 326(16000).

TGA data for **7** shows that weight loss between 25 – 350 °C can be assigned to approx. 29 water molecules in the crystal lattice which is overlapping with the removal of 4 NH_4^+ cations as NH_3 molecules, while between 350 – 400 °C, can be assigned to the removal of 1 SeO_3^{2-} as SeO_2 gas.

5.3.8 Synthesis of compound $(NH_4)_7K_3[Mo^{VI}_{11}V^{V}_{5}V^{IV}_{2}O_{52}(\mu_9\text{-}SeO_3)(Mo_6VO_{22})]\cdot 40H_2O$ 8

Solid NH_4VO_3 (0.40 g, 3.4 mmol) was added in one portion to a stirred solution of $(NH_4)_6Mo_7O_{24}\cdot 4H_2O$ (0.60 g, 0.4 mmol) in water (25 mL). Then, the solid K_2SeO_3 (0.19 g, 0.93 mmol) was added and after 5 minutes of stirring $NH_2NH_2 \cdot 2HCl$ (4.2 mg, 40 µmol) was slowly added. The reaction mixture was stirred for 10 min and the pH was adjusted to 2.8 by addition of concentrated HCl to the solution. The dark green solution was filtered and the filtrate was left crystallise for two weeks in an open vessel at room temperature, during which time dark green needles suitable for X-ray structure analysis were obtained. Yield: 0.011 g (2.55 µmol, ~2 % based on Mo).

Elemental analysis for: $H_{108}K_3Mo_{17}N_7O_{117}Se_1V_8$ (4313.45); calcd (%): Mo 37.81, V 9.45, Se 1.83, K 2.72, N: 2.27; found: Mo: 37.42, V: 9.53, Se: 2.55, K: 3.11, N: 2.64.

FT-IR [(KBr) ν/cm^{-1}] 3433 (br) [ν(O–H) from H_2O], 1402 (s) [$\nu(NH_4^+)$], 966 (sh) [ν(V=O)], 905 (s) [ν(Mo=O)], 862 (sh) [$\nu(SeO_3^{2-})$], 762 (s) [$\nu(SeO_3^{2-})$], 589 (vs) [$\nu(SeO_3^{2-})$], 480 (vs) [$\nu(SeO_3^{2-})$], 462 (vs) [$\nu(SeO_3^{2-})$].

UV-Vis (in H_2O): λ_{max}, [nm, (dm^{3}mol^{-1}cm^{-1})] = 210(27000), 262(9700), 327(2200).

TGA data from **8** shows that weight loss between 25 – 450 °C can be assigned to approx. 40 water molecules in the crystal lattice which is overlapping with the removal with the removal of 7 NH_4^+ cations as NH_3 molecules and 1 SeO_3^{2-} as SeO_2 gas.

5.3.9 Synthesis of compound $(NH_4)_{19}K_3[Mo^{VI}_{20}V^{V}_{12}V^{IV}_{4}O_{99}(SeO_3)_{10}]\cdot 36H_2O$ 9

Solid NH_4VO_3 (0.40 g, 3.4 mmol) was added in one portion to a stirred solution of $(NH_4)_6Mo_7O_{24}\cdot 4H_2O$ (0.60 g, 0.4 mmol) in water (25 mL). Then, the solid K_2SeO_3 (0.19 g, 0.93 mmol) was added and after 5 minutes of stirring $NH_2NH_2\cdot 2HCl$ (4.2 mg, 40 µmol) was slowly added. The reaction mixture was stirred for 10 min and the pH was adjusted to 5.0 by addition of concentrated HCl to the solution. The dark green solution was filtered and the filtrate was left crystallise for two weeks in an open vessel at room temperature, during which time green prism crystals suitable for X-ray structure analysis were obtained. Yield: 0.03 g (5 µmol, ~5 % based on Se).

Elemental analysis for: $H_{148}K_3Mo_{20}N_{19}O_{165}Se_{10}V_{16}$ (6696.11); calcd (%): Mo 28.65, V 12.17, Se 11.79, K 1.75, N: 3.98; found: Mo: 29.04, V: 11.55, Se: 12.64, K: 1.99, N 5.28.

FT-IR [(KBr) ν/cm^{-1}] 3434 (br) [ν(O–H) from H_2O], 1615 (s) [$\nu(H_2O)$], 1399 (s) [$\nu(NH_4^+)$], 954 (sh) [ν(V=O)], 852 (s) [ν(Mo=O)], 727 (sh) [$\nu(SeO_3^{2-})$], 579 (w) [$\nu(SeO_3^{2-})$], 537 (m) [$\nu(SeO_3^{2-})$].

UV-Vis (in H_2O): λ_{max}, [nm, (dm^{3}mol^{-1}cm^{-1})] = 210(133101), 240(54000), 277(18000), 324(7700).

TGA data from **9** shows that weight loss between 25 – 200 °C can be assigned to approx. 36 water molecules in the crystal lattice, while between 200 – 400 °C, can be assigned to removal of 19 NH_4^+ cations as NH_3 molecules and the removal of 10 SeO_3^{2-} as SeO_2 gas.

5.3.10 Synthesis of compound $(NH_4)_{15}[Na_3(Mo^{VI}_{11}V^{V}_{5}V^{IV}_{2}O_{52}(\mu_9\text{-}SeO_3))(Mo^{VI}_{5}V^{V}_{2}V^{IV}_{2}O_{24}(SeO_3)_4)]\cdot 10H_2O$ 10

Solid NH_4VO_3 (0.40 g, 3.4 mmol) was added in one portion to a stirred solution of $(NH_4)_6Mo_7O_{24}\cdot 4H_2O$ (0.60 g, 0.4 mmol) in water (25 mL); and the solution was heated to 90 °C until the vanadate salt is completely dissolved. The reaction is allowed to cool down at room temperature and then solid Na_2SeO_3 (0.21 g, 0.93 mmol) was added. After 5 minutes of stirring $NH_2NH_2\cdot 2HCl$ (4.2 mg, 40 µmol) was slowly added. The reaction mixture was stirred for 10 min and the pH was adjusted between 2.5 and 4 by addition of concentrated HCl to the solution. The dark green solution was filtered and the filtrate was left crystallise for two weeks in an open vessel at room temperature. Dark orange crystals were filtered and dried in air. Yield: 0.02 g (5 µmol, 3 % based on Se).

Elemental analysis for: $H_{90}Mo_{16}N_{15}Na_3O_{106}Se_5V_{11}$ (4556.02); calcd (%): Mo 33.69, V 12.30, Se 8.67, Na 1.51, N: 4.61; found: Mo 24.52, V 19.79, Se 8.14, Na 1.38, N 4.20.

FT-IR [(KBr) ν/cm^{-1}] 3477 (br) [ν(O–H) from H_2O], 1409 (s) [$\nu(NH_4^+)$], 954 (s) [ν(V=O)], 841 (s) [ν(Mo=O)], 744 (s) [$\nu(SeO_3^{2-})$], 596 (vs) [$\nu(SeO_3^{2-})$].

UV-Vis (in H_2O): λ_{max}, [nm, (dm^{3}mol^{-1}cm^{-1})] = 210(19000), 276(7600).

TGA data for **10** shows that weight loss between 25 – 150 °C can be assigned to approx. 15 water molecules in the crystal lattice which is overlapping with the removal of 15 NH_4^+ cations as NH_3 molecules, while between 150 – 400 °C, can be assigned to the removal of 5 SeO_3^{2-} as SeO_2 gas.

5.3.11 Synthesis of compound $(NH_4)_9K[Mo^{VI}_{12}V^{V}_{8}V^{IV}_{4}Te^{IV}O_{69}(\mu_9\text{-}Te^{IV}O_3)_2]\cdot 27H_2O$ 11

Ammonium molybdate tetrahydrate (0.60 g, 0.4 mmol) was dissolved in an HCl solution (37% HCl in water, 1:4 v/v, 25 mL, pH ≈ 0), and then solid ammonium metavanadate (0.35 g, 2.9 mmol) was added in one portion to the solution under stirring. The solid potassium tellurite hydrate (0.24 g, 0.93 mmol) was gradually added under stirring,

followed by the addition of solid $NH_2NH_2 \cdot 2HCl$ (4.2 mg, 40 μmol). Compound (**1**) could be synthesized within pH 2 and 4. The solution was refluxed overnight at 90 ºC. The solution was then cool down at room temperature (~ 25 ºC) and filtered off. The filtrate was left in an open vessel (a 100 mL beaker) at room temperature (~ 25 ºC) for a week, during which time dark green rhomboid shape crystals from **11**, suitable for X-ray structure analysis, were obtained. Yield 0.08 g (0.02 mmol, 10 % based on V).

Elemental analysis for: $H_{90}KMo_{12}N_9O_{102}Te_3V_{12}$ (4033.1); calcd (%): H: 2.25, N: 3.13, K: 0.97, Te: 9.49, Mo: 28.54, V: 15.16; found (%): H: 2.08, N: 3.68, K: 0.86, Te: 9.10, Mo: 28.84, V: 15.80.

FT-IR [(KBr), cm^{-1}] 3444 (br) [ν(O-H) from H_2O], 1400 (s) [$\nu(NH_4)$], 967 (s) [ν(V=O)], 894 (s) [ν(Mo=O)], 845 (s) [$\nu(TeO_3^{2-})$], 768 [$\nu(TeO_3^{2-})$].

UV-Vis (in H_2O): λ_{max}, [nm, ($dm^3mol^{-1}cm^{-1}$)] = 262(81000), 318(33000).

TGA data from **11** shows that weight loss between 25 – 400 ºC can be assigned to approx. 27 water molecules in the crystal lattice which is overlapping the removal of 9 NH_4^+ cations as NH_3 molecules.

5.3.12 Synthesis of compound $K_{14}[Mo^{VI}_{12}V^{V}_{8}V^{IV}_{4}O_{69}(\mu_9\text{-}Te^{IV}O_3)_2] \cdot 27H_2O$ 12

Potassium molybdate dihydrate (0.67 g, 2.8 mmol) was dissolved in 25 mL of deionized water and the solid potassium metavanadate (0.6 g, 7 mmol) was added in one portion to the solution under stirring. Then, solid $K_2TeO_3 \cdot xH_2O$ (0.24 g, 0.93 mmol) was gradually added under stirring; followed by (4.2 mg, 40 μmol) of hydrazine hydrochloride. The pH to 2.5 by addition of a 3M HCl aqueous solution and the solution was refluxed overnight at 90 ºC. The solution was then cool down at room temperature (~ 25 ºC) and filtered off. The filtrate was left in an open vessel (a 100 mL beaker) at room temperature (~ 25 ºC) for a week, during which time green hexagonal crystals suitable for X-ray structure analysis were obtained. Yield 0.08 g (0.02 mmol, 10.4 % based on Mo).

Elemental analysis for: $H_{54}K_{14}Mo_{12}O_{102}Te_2V_{12}$ (4251.42); calcd (%): Te: 6.00, K: 12.78, Mo: 27.08, V: 14.38; found (%): Te: 5.74, K: 12.41, Mo: 27.61, V: 14.45.

FT-IR [(KBr), cm^{-1}] 3433 (br) [ν(O-H) from H_2O], 968 (s) [ν(V=O)], 889 (s) [ν(Mo=O)], 842 (s) [$\nu(TeO_3^{2-})$], 763 [$\nu(TeO_3^{2-})$].

UV-Vis (in H_2O): λ_{max}, [nm, ($dm^3mol^{-1}cm^{-1}$)] = 263(72000), 317(32000).

TGA data from **12** shows that weight loss between 0 – 200 ºC can be assigned to approx. 27 water molecules in the crystal lattice. The cluster is stable up to 700 ºC.

5.3.13 Synthesis of compound $K_{10}[Mo^{VI}_{11}V^{V}_{5}V^{IV}_{2}O_{52}(\mu_9\text{-}Te^{IV}O_3)(Mo^{VI}_{6}V^{V}O_{22})]\cdot 15H_2O$ 13

$K_2TeO_3\cdot xH_2O$ (0.12 g, 0.47 mmol) were dissolved in 25 mL of deionized water and the pH of the solution was adjusted to 2 by addition of 3 M HCl solution. At this point, white precipitate appeared and the reaction was heat at 90 °C to dissolve the precipitate. Potassium molybdate dihydrate (0.67 g, 2.8 mmol) was then added to the solution under stirring, followed by the addition of solid potassium metavanadate (0.70 g, 5.1 mmol) and the pH was readjusted to 2 by addition of 3 M HCl solution. Finally, solid $NH_2NH_2\cdot 2HCl$ (4.2 mg, 40 µmol) was gradually added under stirring and the solution turned from yellow to green. Compound **13** could be synthesized within the pH range 2.8-3.5. After adjusting the pH, solid KCl (2.0 g, 0.03 mol) was added under stirring. The solution was filtered off and the filtrate left in an open vessel (100 mL beaker) at room temperature (~25 °C) for a week, during which time dark green crystals suitable for X-ray structure analysis were obtained. Yield 0.07g (0.02 mmol, 12% based on Mo).

Elemental analysis for: $H_{30}K_{10}Mo_{17}O_{92}TeV_8$ (4059.13); calcd (%): K: 9.63, Te: 3.14, Mo: 40.18, V: 10.04; found (%): K: 9.10, Te: 3.74, Mo: 39.62, V: 10.62.

FT-IR [(KBr), cm^{-1}] 3434 (br) [ν(O-H) from H_2O], 964 (s) [ν(V=O)], 901 (s) [ν(Mo=O)], 850 (s) [$\nu(TeO_3^{2-})$], 818 [$\nu(TeO_3^{2-})$].

TGA data from **13** shows that weight loss between 0 – 175 C° can be assigned to approx. 15 water molecules in the crystal lattice.

5.3.14 Synthesis of compound $(NH_4)_8H_2[V^V_8V^{IV}_2O_{25}(SeO_3)_4]\cdot 10H_2O$ 14

Solid K_2SeO_3 (0.23 g, 1.13 mmol) was added to a stirred solution of NH_4VO_3 (0.40 g, 3.4 mmol) in aqueous HCl solution (37 % HCl in water, 1:4 v/v, 25 mL, pH ≈ 0). Subsequently $NH_2NH_2\cdot 2HCl$ (4.2 mg, 40 μmol) were added slowly to the yellow solution. The pH was adjusted between 3 and 5 by addition of a 6M NH_3 aqueous solution. The reaction mixture was stirred for 5 minutes and then filtered. The filtrate was left to crystallise at room temperature in an open vessel (100 mL), where dark-green square crystals appeared within 1 week. Yield 0.24 g (0.14 mmol, 49 % based on Se).

Elemental analysis for: $H_{54}N_8O_{47}Se_4V_{10}$ (1743.75); calcd (%): N: 6.42, Se: 18.11, V: 29.21; found (%): N: 5.77, Se: 17.51, V: 28.48.

FT-IR [(KBr), cm^{-1}] 3432 (br) [ν(O-H) from H_2O], 1401 (s) [$\nu(NH_4)$], 954 (s) [ν(V=O)], 827 (s) [$\nu(SeO_3^{2-})$], 754 (s) [$\nu(SeO_3^{2-})$], 698 [$\nu(SeO_3^{2-})$], 561 [$\nu(SeO_3^{2-})$].

UV-Vis (in H_2O): λ_{max}, [nm, ($dm^3mol^{-1}cm^{-1}$)] = 206(52000), 269(22000).

TGA data from **14** shows that weight loss between 25 – 300 ºC can be assigned to approx. 10 water molecules in the crystal lattice which is overlapping the removal of 8 NH_4^+ cations as NH_3 molecules, while between 300 – 400 °C, can be assigned to removal of 4 SeO_3^{2-} as SeO_2 gas.

5.3.15 Synthesis of compound $(NH_4)_6Na[V^V_7V^{IV}_5O_{27}(SeO_3)_4]\cdot 8H_2O$ 15

Solid Na_2SeO_3 (0.57 g, 3.3 mmol) was added to a stirred solution of $NaVO_3$ (1.22 g, 10 mmol) in aqueous HCl solution (37 % HCl in water, 1:4 v/v, 25 mL, pH ≈ 0). Subsequently $NH_2NH_2\cdot 2HCl$ (0.03 g, 0.28 mmol) were added slowly to the yellow solution. The pH was adjusted to 5 by addition of a 6M NH_3 aqueous solution. The reaction mixture was stirred for 5 minutes and then filtered. The filtrate was left to crystallise at 4 °C in a sealed vessel (100 mL), where dark-green square crystals appeared after 24 hours. Yield 0.26 g (0.14 mmol, 17 % based on Se).

Elemental analysis for: $H_{64}N_5Na_1O_{61}Se_4V_{12}$ (1826.49); calcd (%): N: 4.60, Na: 1.25, Se: 17.29, V: 33.46; found (%): N: 5.53, Na: 0.28, Se: 17.79, V: 32.88.

FT-IR [(KBr), cm^{-1}] 3156 (br) [ν(O-H) from H_2O], 1402 (s) [$\nu(NH_4)$], 958 (s) [ν(V=O)], 828 (s) [$\nu(SeO_3^{2-})$], 752 (s) [$\nu(SeO_3^{2-})$], 690 [$\nu(SeO_3^{2-})$], 562 [$\nu(SeO_3^{2-})$].

UV-Vis (in H_2O): λ_{max}, [nm, ($dm^3mol^{-1}cm^{-1}$)] = 209(59000), 243(33000), 262(29000).

TGA data from **15** shows that weight loss between 25 – 300 ºC can be assigned to approx. 8 water molecules in the crystal lattice which is overlapping the removal of 6 NH_4^+ cations as NH_3 molecules, while between 300 – 400 °C, can be assigned to removal of 4 SeO_3^{2-} as SeO_2 gas.

5.3.16 Synthesis of compound $(NH_4)_5[Co(OH_2)_3V^V_9V^{IV}O_{25}(SeO_3)_4]\cdot 15H_2O$ 16

Solid $CoSO_4\cdot 7H_2O$ (0.10 g, 0.35 mmol) was added in one portion to a 10 mL ammonium acetate buffer solution (1M, pH ~ 4) containing $(NH_4)_6Na[V^V_{10}V^{IV}_2O_{27}(SeO_3)_4]\cdot 22H_2O$ (0.04 g, 0.02 mmol). The reaction mixture was stirred for 10 minutes and then filtered. The filtrate was left to crystallise at 4 °C in a sealed vessel (25 mL), where dark-green needles appeared within 1 week. Yield 0.02 g (12 μmol, 50 % based on Se).

Elemental analysis for: $H_{56}CoN_5O_{55}Se_4V_{10}$ (1890.67); calcd (%): N: 3.70, Co: 3.11, Se: 16.71, V: 26.94; found (%): N: 3.88, Co: 2.34, Se: 16.04, V: 27.02.

FT-IR [(KBr), cm^{-1}] 3150 (br) [ν(O-H) from H_2O], 1402 (s) [$\nu(NH_4)$], 983 (s) [ν(V=O)], 954 (s) [ν(V=O)], 824 (s) [$\nu(SeO_3^{2-})$], 751 (s) [$\nu(SeO_3^{2-})$], 562 [$\nu(SeO_3^{2-})$].

UV-Vis (in H_2O): λ_{max}, [nm, ($dm^3mol^{-1}cm^{-1}$)] = 263(24000).

TGA data from **16** shows that weight loss between 25 – 300 ºC can be assigned to approx. 18 water molecules in the crystal lattice which is overlapping the removal of 5 NH_4^+ cations as NH_3 molecules, while between 300 – 450 °C, can be assigned to removal of 4 SeO_3^{2-} as SeO_2 gas.

5.4 IR – spectroscopy

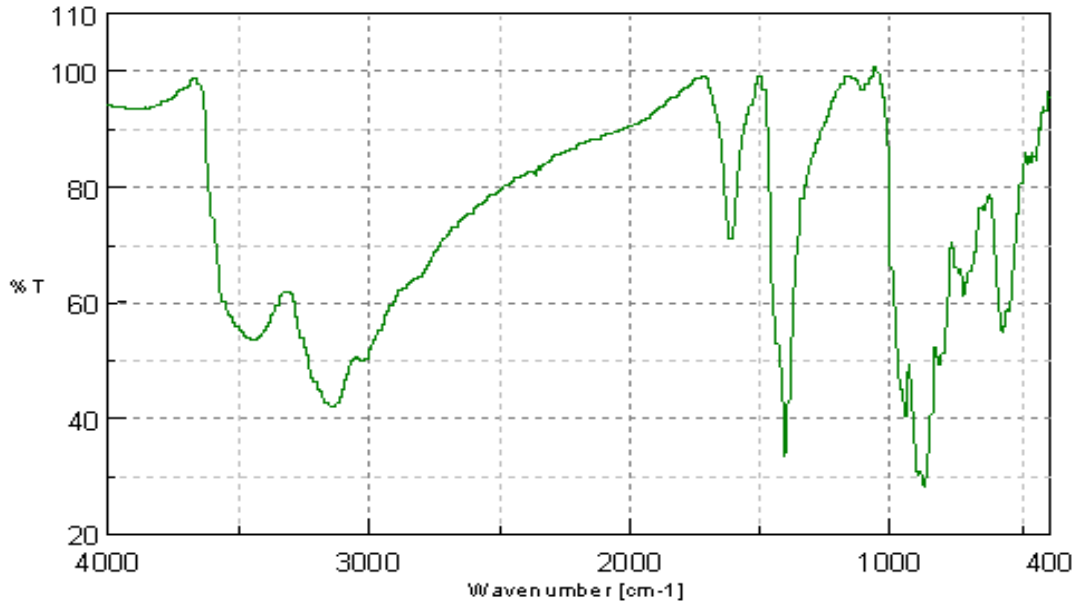

Figure 96: Infrared spectrum of compound **2**.

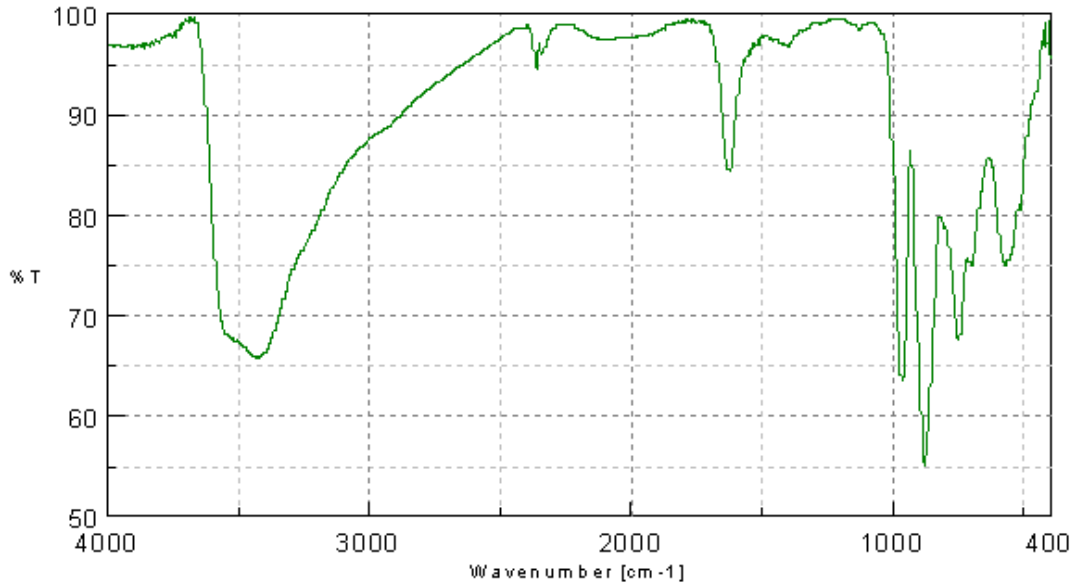

Figure 97: Infrared spectrum of compound **4**.

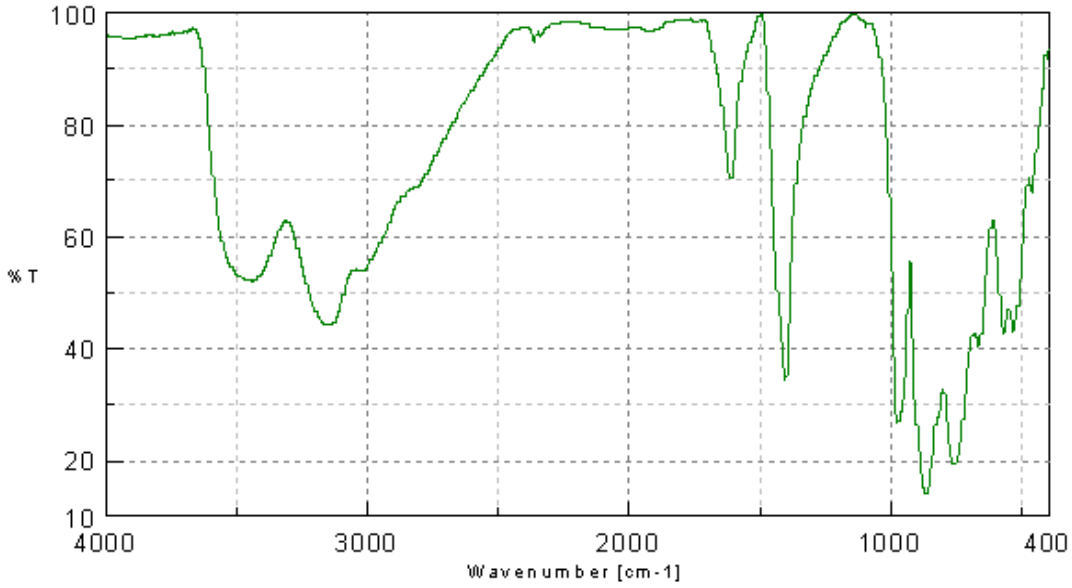

Figure 98: Infrared spectrum of compound **5**.

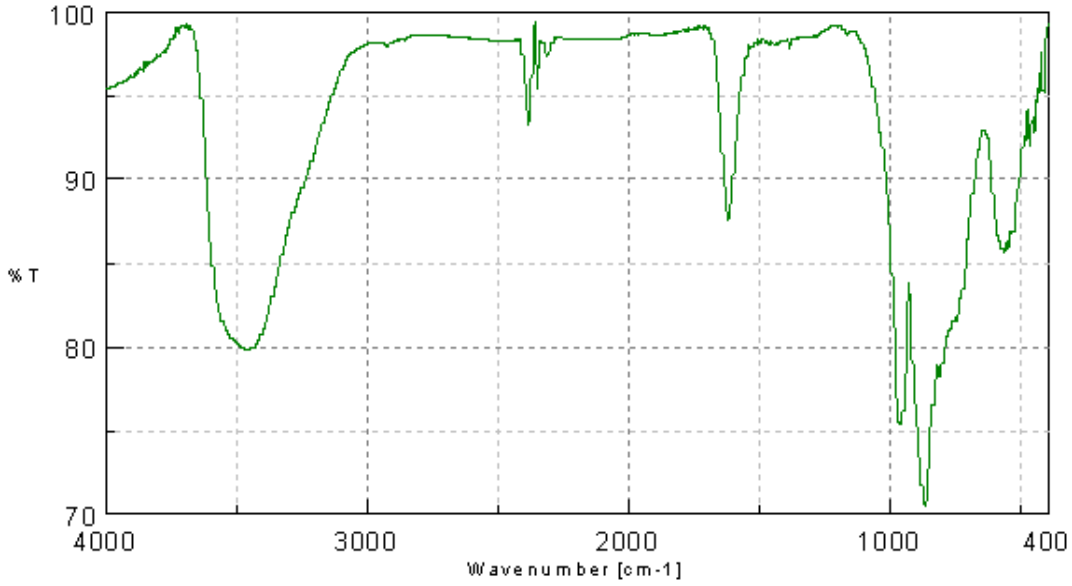

Figure 99: Infrared spectrum of compound **6**.

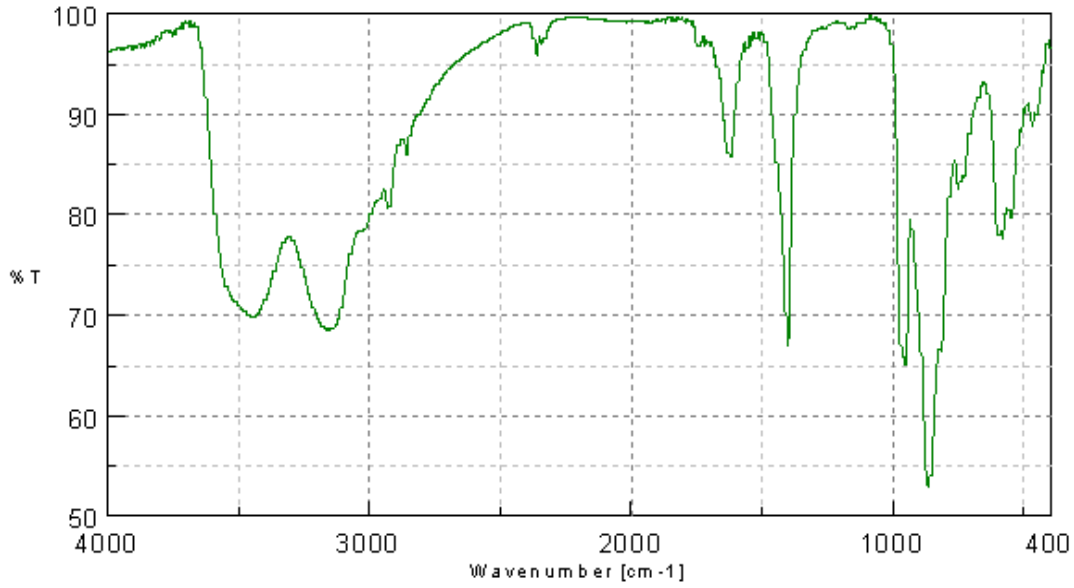

Figure 100: Infrared spectrum of compound **7**.

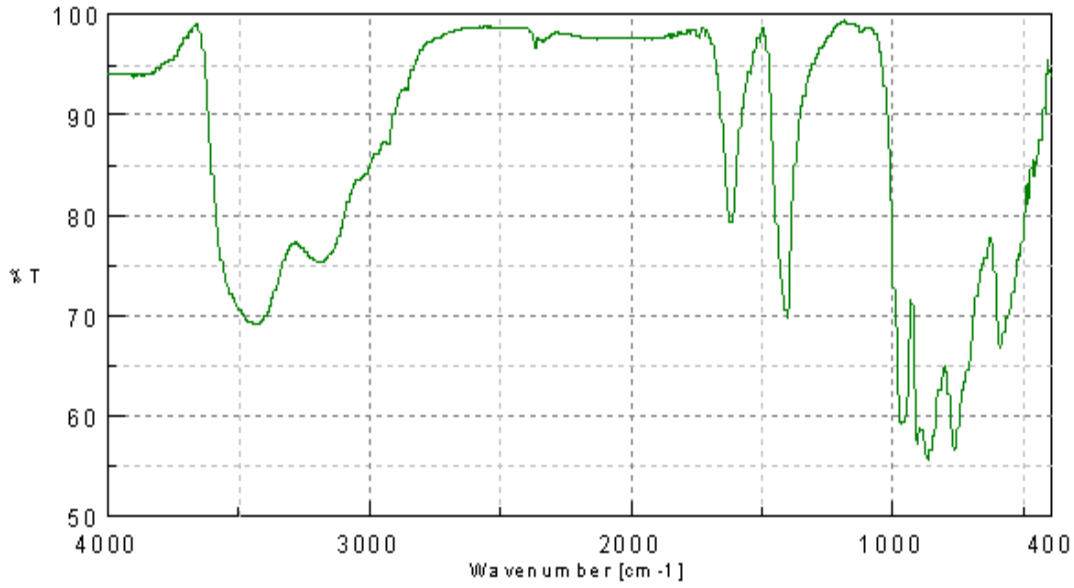

Figure 101: Infrared spectrum of compound **8**.

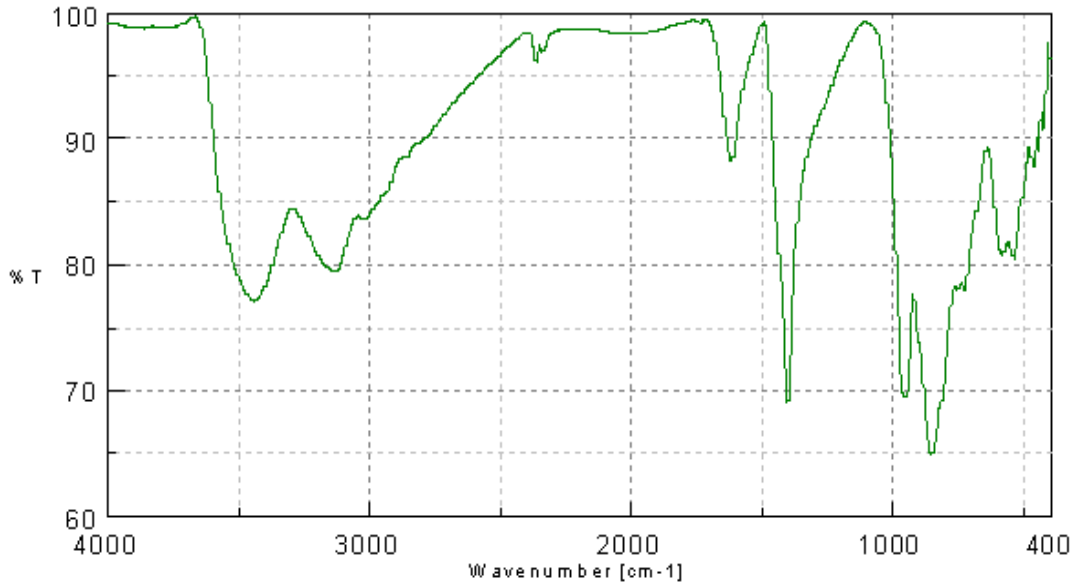

Figure 102: Infrared spectrum of compound **9**.

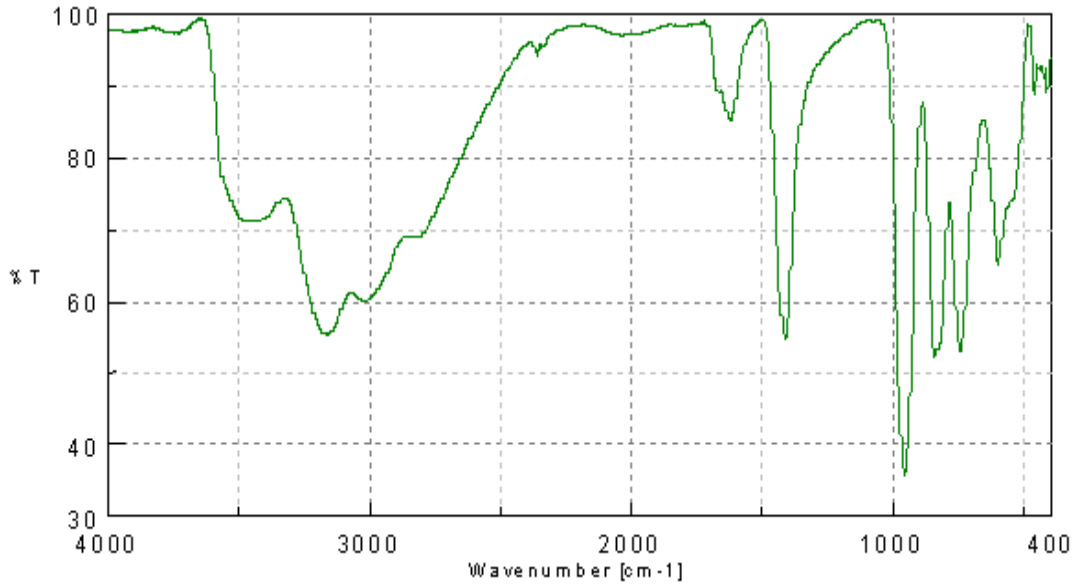

Figure 103: Infrared spectrum of compound **10**.

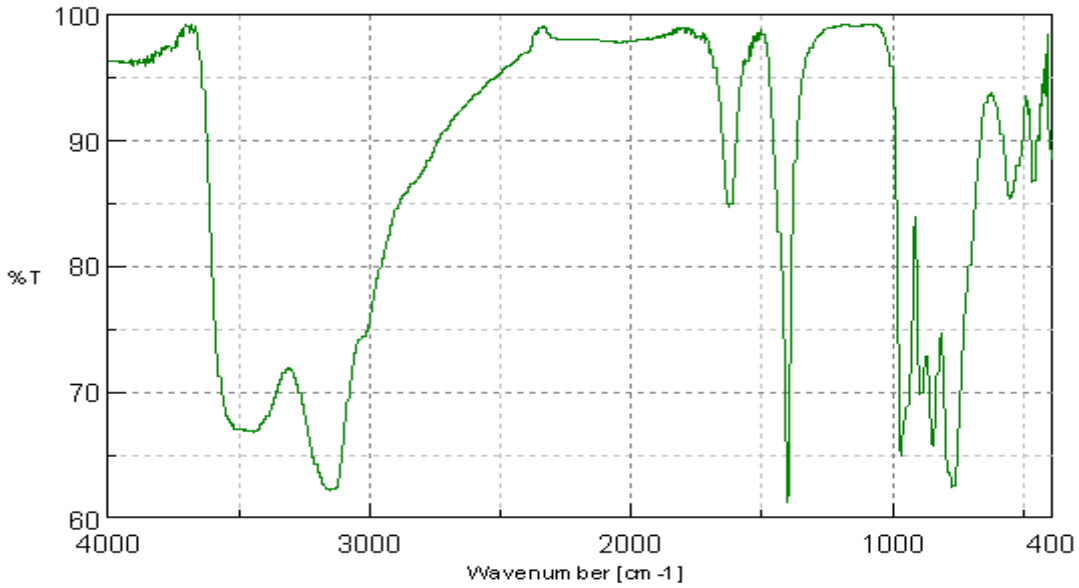

Figure 104: Infrared Spectrum of compound **11**.

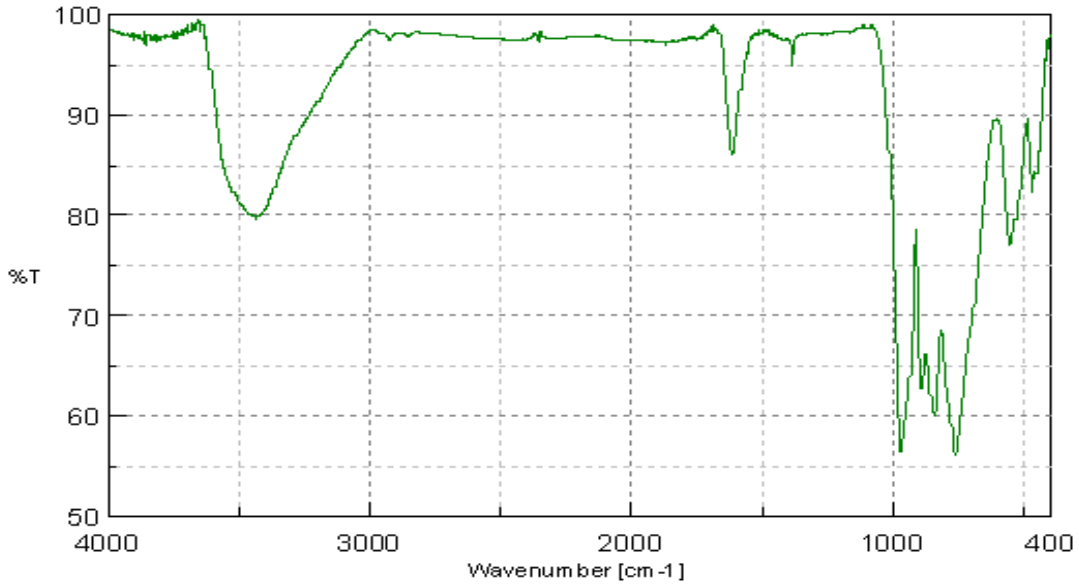

Figure 105: Infrared Spectrum of compound **12**.

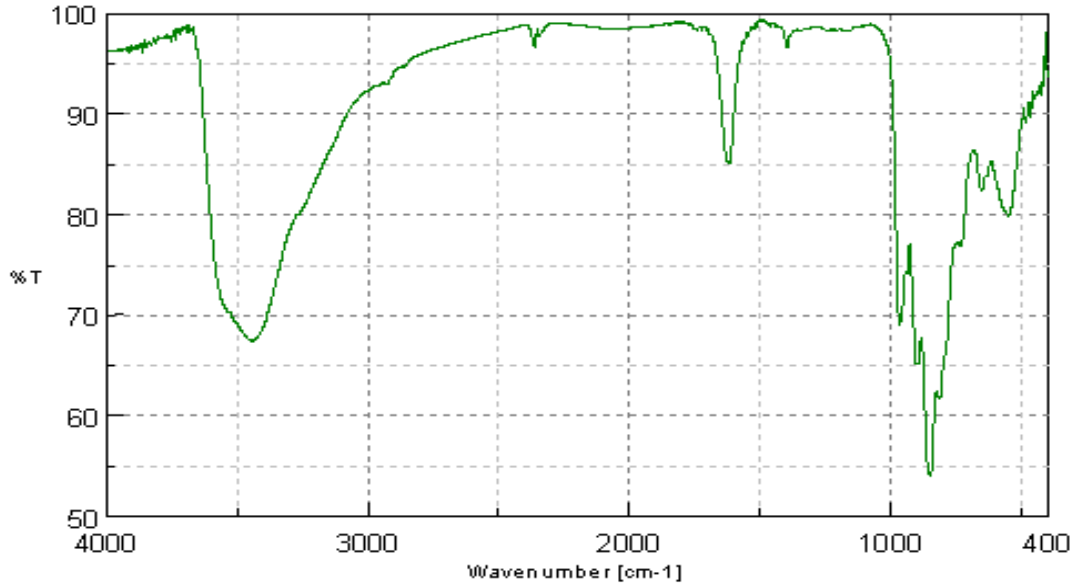

Figure 106: Infrared Spectrum of compound **13**.

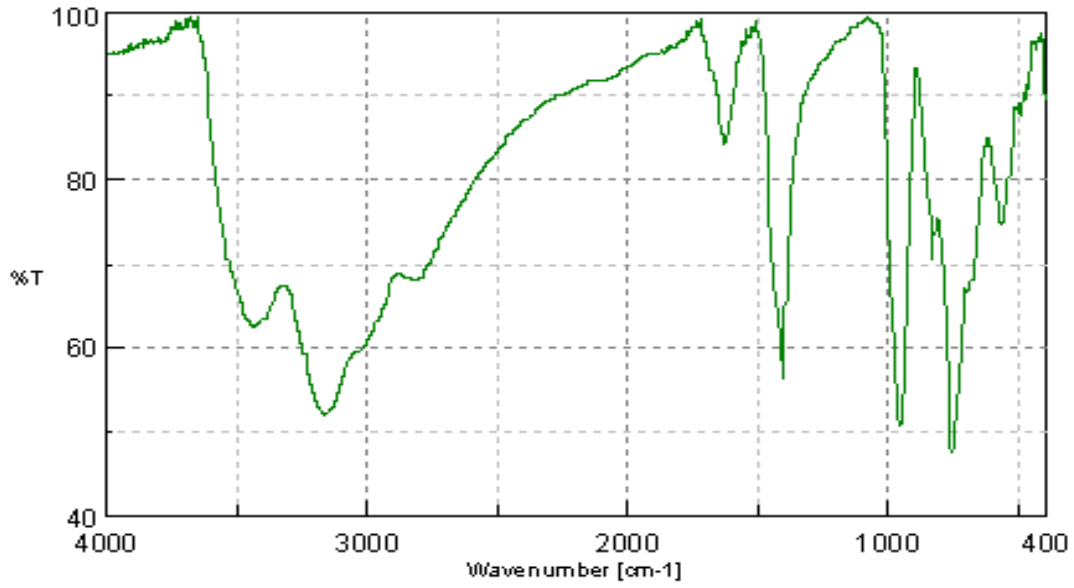

Figure 107: Infrared Spectrum of compound **14**.

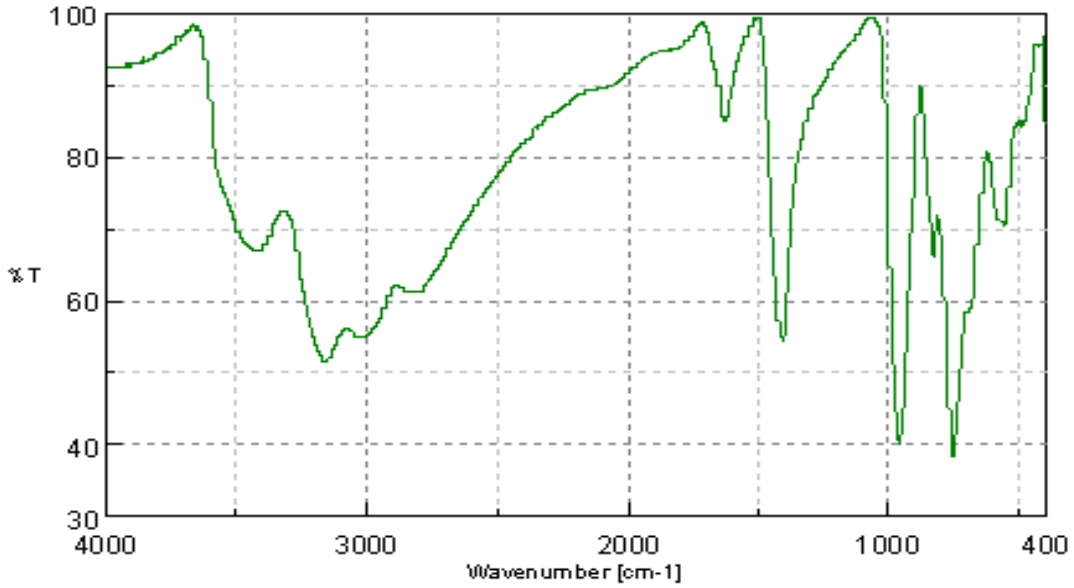

Figure 108: Infrared Spectrum of compound **15**.

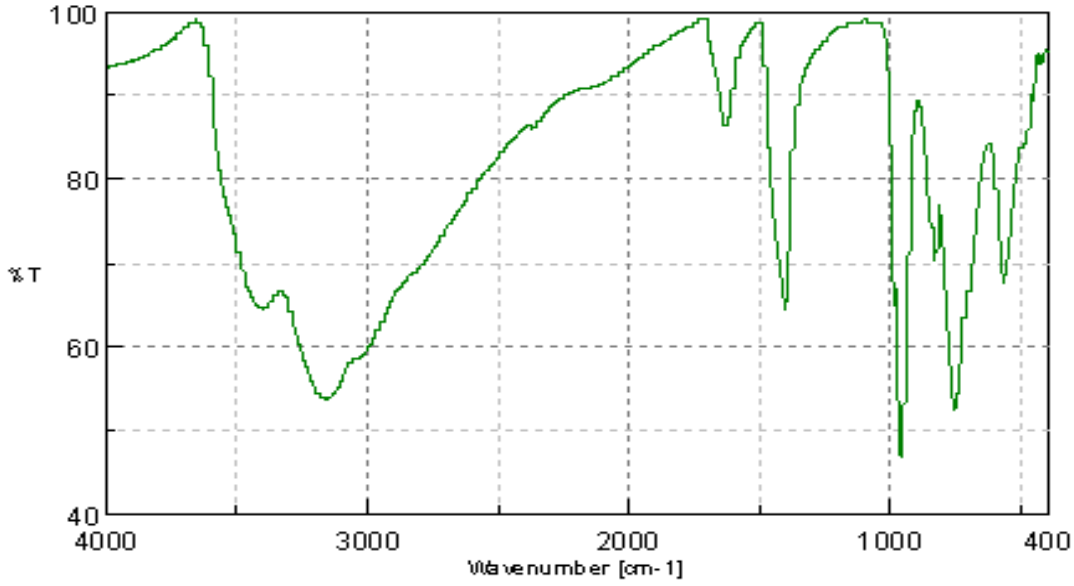

Figure 109: Infrared Spectrum of compound **16**.

5.5 UV – spectroscopy

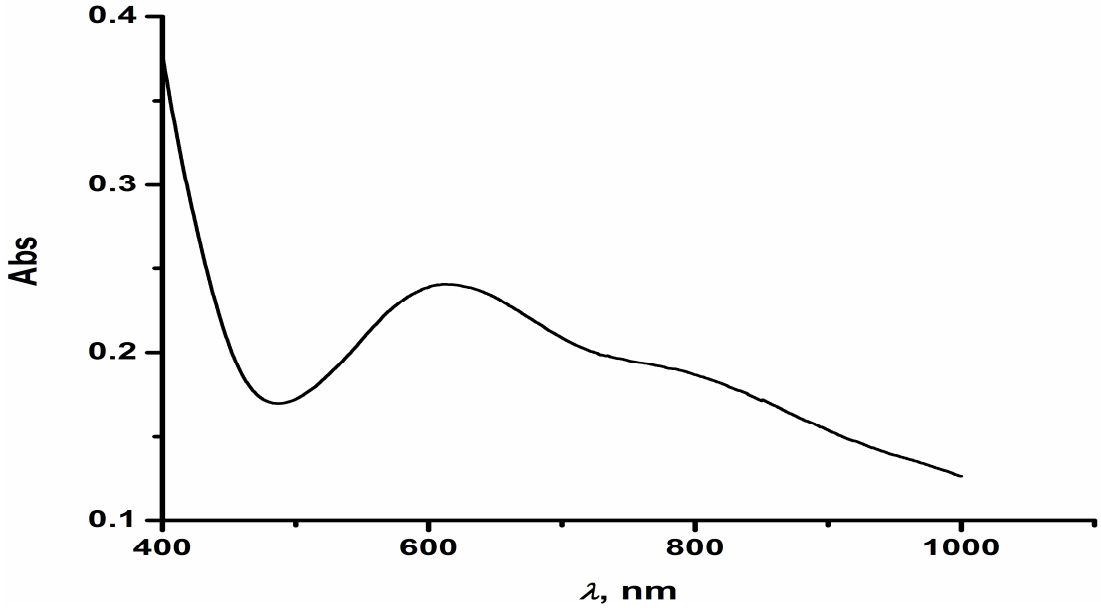

Figure 110: Visible spectrum of compound **2**. The bands can be assigned to ML and IV charge transfer.[223-226]

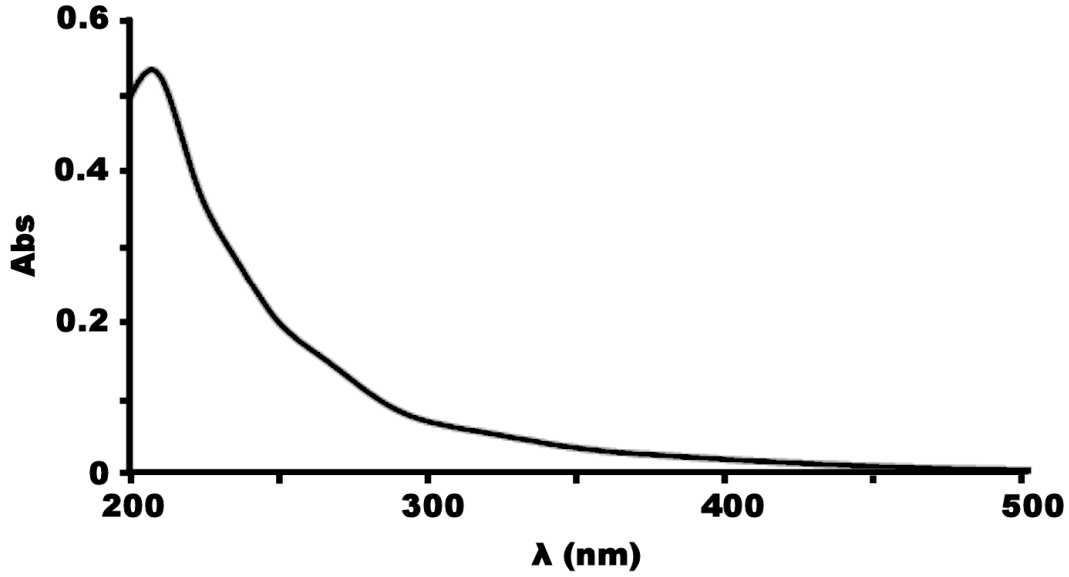

Figure 111: Visible spectrum of compound **4**. The bands can be assigned to ML and IV charge transfer.[223-226]

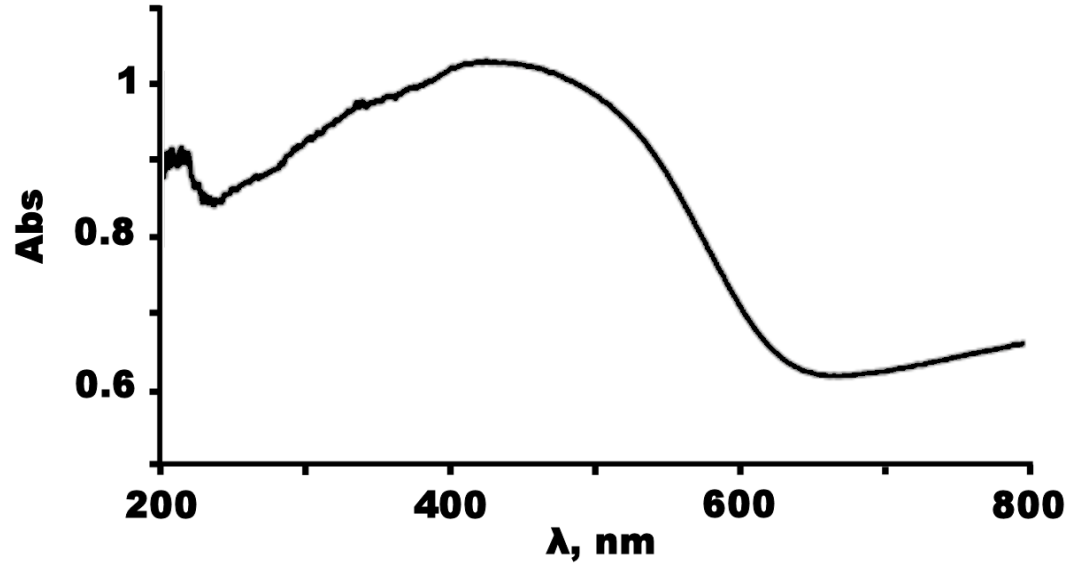

Figure 112: UV-vis reflectance spectrum of compound **4**. A series of broad overlapping bands can be observed at 266, 332 and 457 nm respectively, assignable to O→M and IV charge transfers.[223-226]

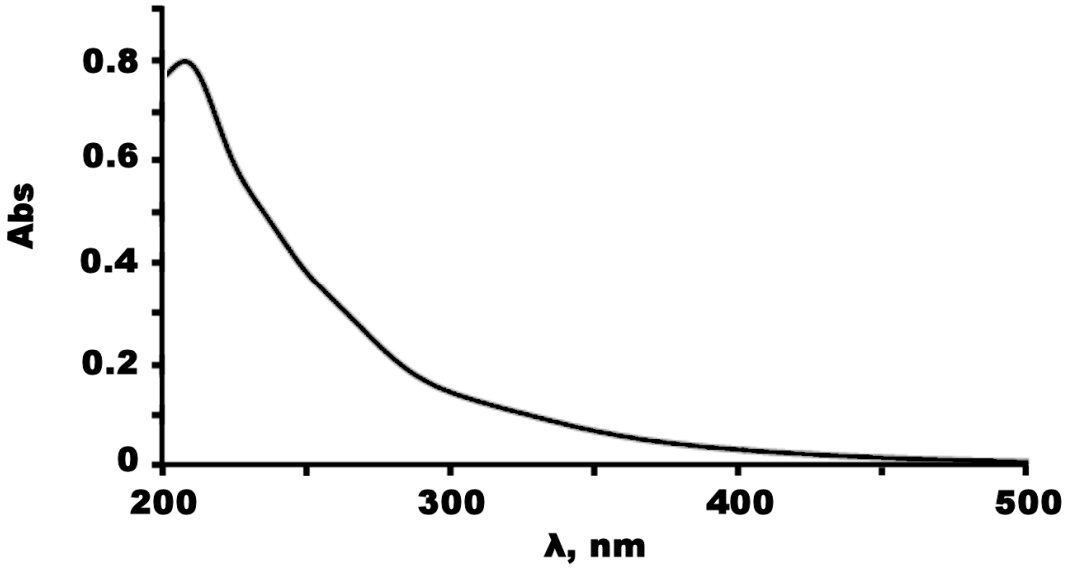

Figure 113: Visible spectrum of compound **5**. The bands can be assigned to ML and IV charge transfer.[223-226]

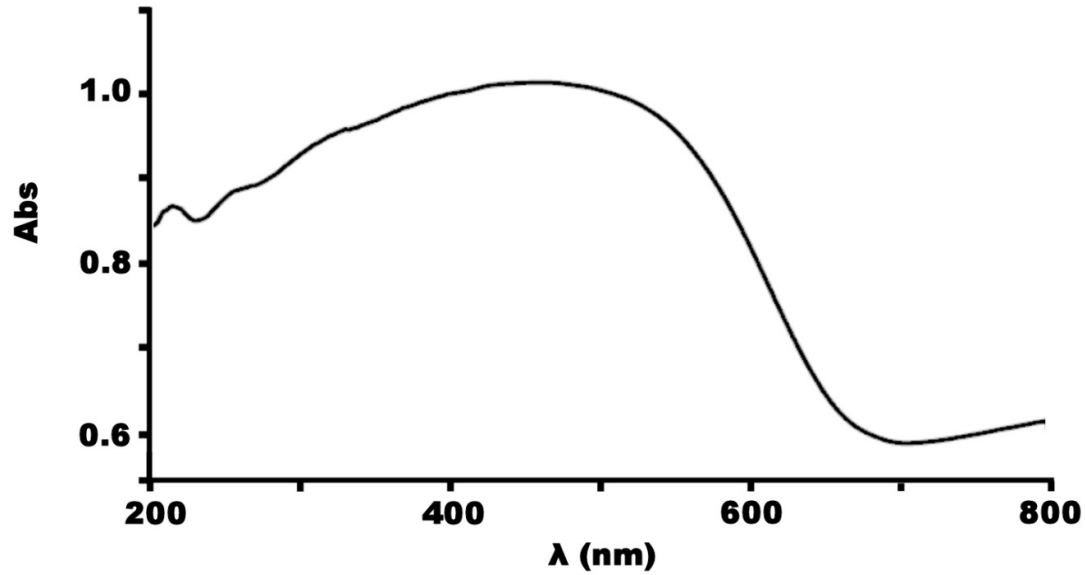

Figure 114: UV-vis reflectance spectrum of compound **5**. A series of broad overlapping bands can be observed at 272, 350 and 480 nm respectively, assignable to O→M and IV charge transfers.[223-226]

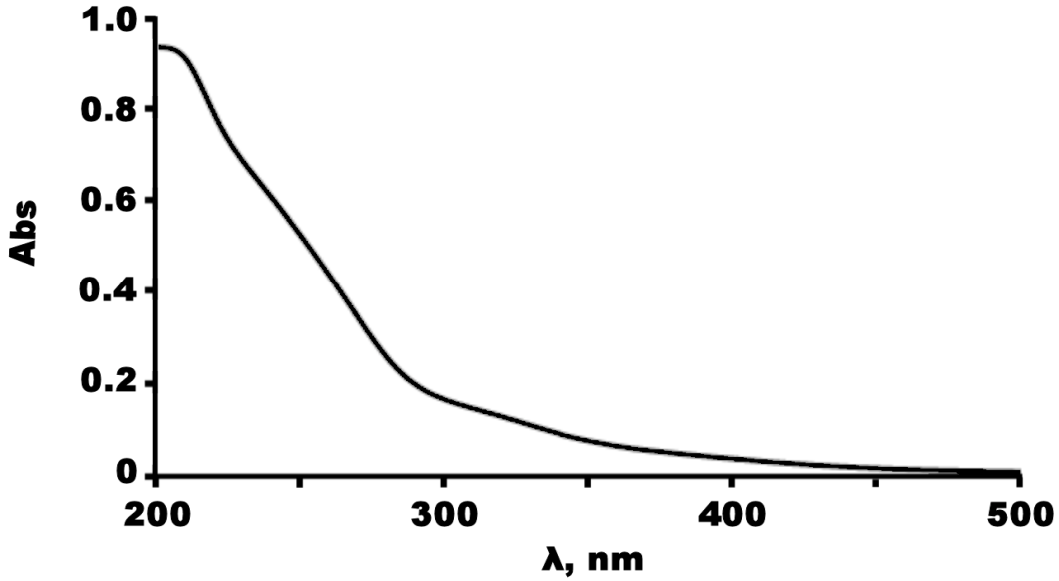

Figure 115: Visible spectrum of compound **6**. The bands can be assigned to ML and IV charge transfer.[223-226]

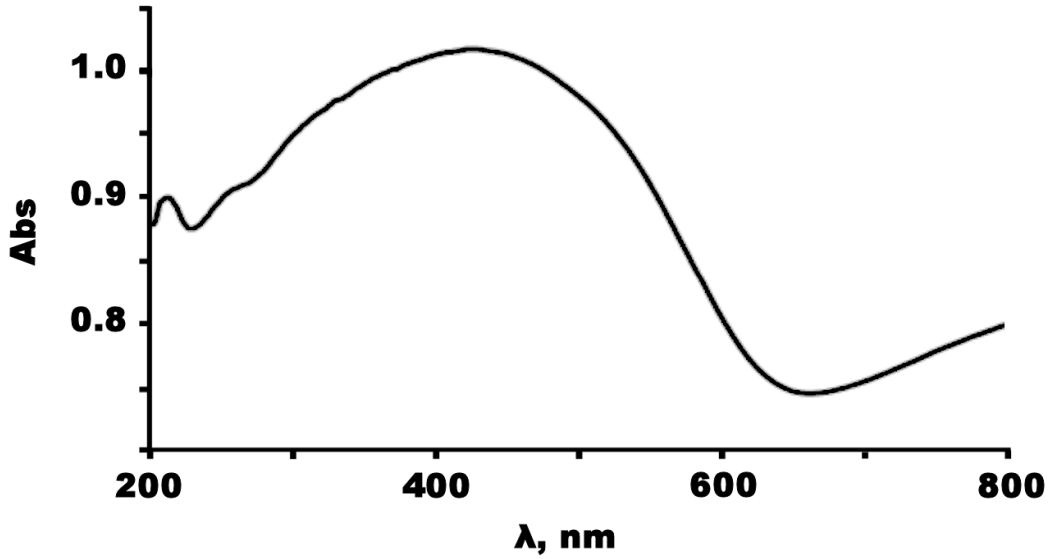

Figure 116: UV-vis reflectance spectrum of compound **6**. A series of broad overlapping bands can be observed at 260, 324 and 434 nm respectively, assignable to O→M and IV charge transfers.[223-226]

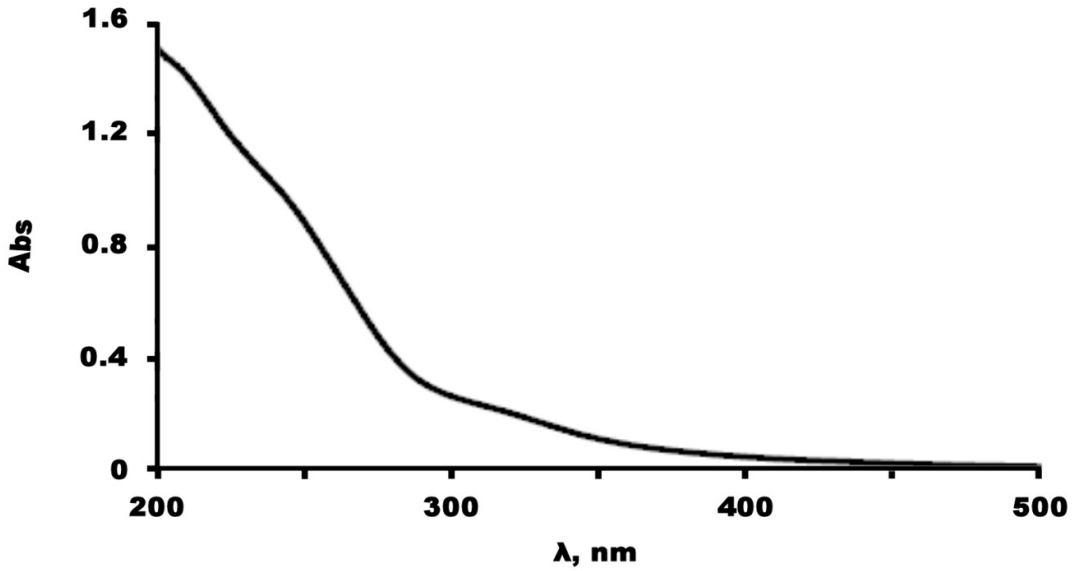

Figure 117: Visible spectrum of compound **7**. The bands can be assigned to ML and IV charge transfer.[223-226]

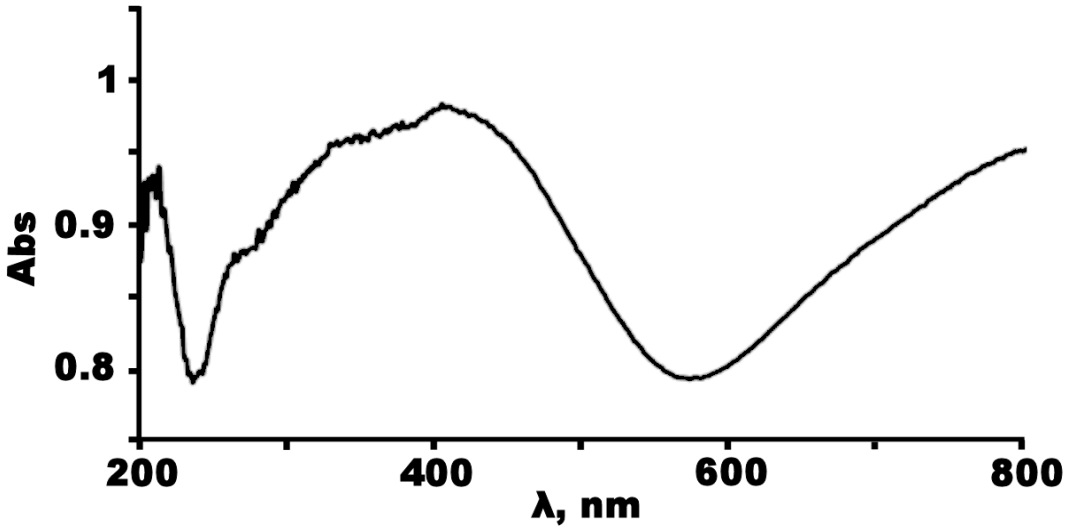

Figure 118: UV-vis reflectance spectrum of compound **7**. A series of broad overlapping bands can be observed at 255, 306, 369 and 432 nm respectively, assignable to O→M and IV charge transfers.[223-226]

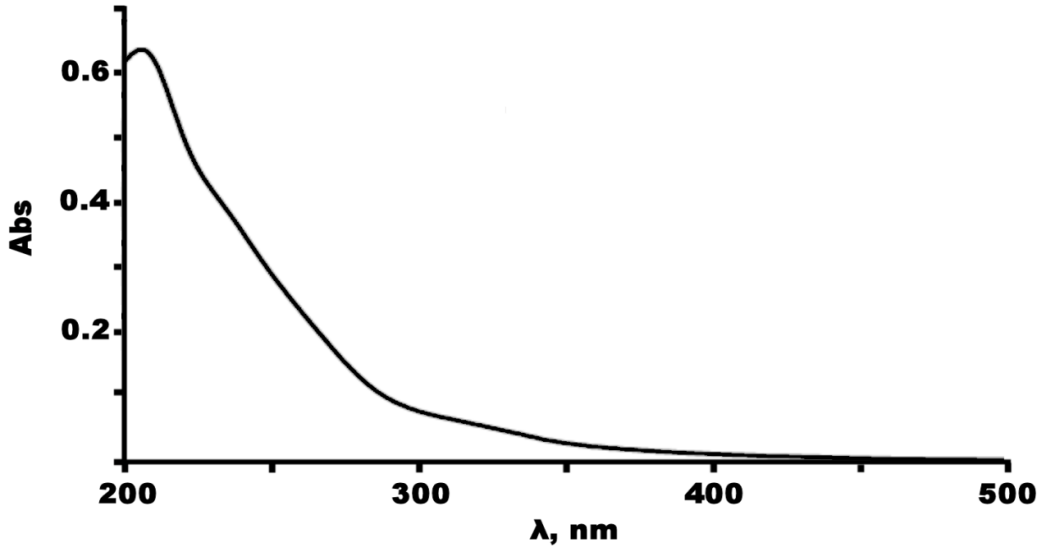

Figure 119: Visible spectrum of compound **8**. The bands can be assigned to ML and IV charge transfer.[223-226]

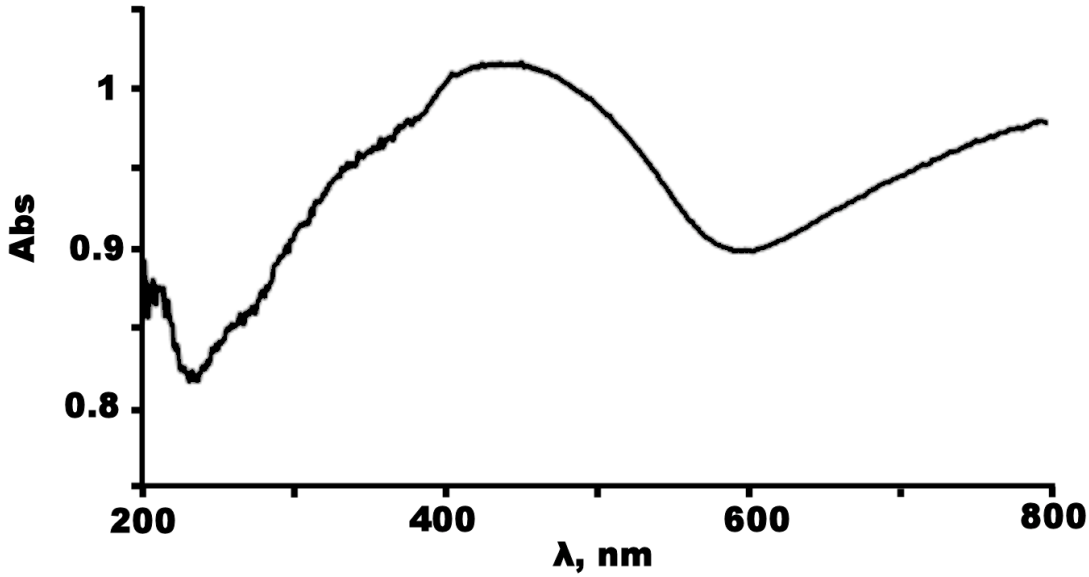

Figure 120: UV-vis reflectance spectrum of compound **8**. A series of broad overlapping bands can be observed at 264, 309, 360 and 451 nm respectively, assignable to O→M and IV charge transfers.[223-226]

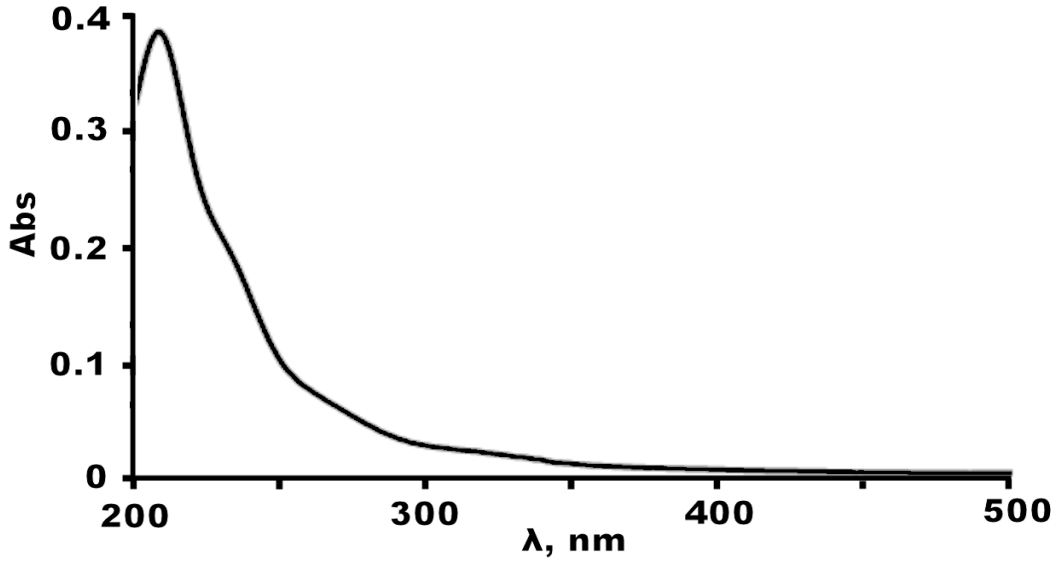

Figure 121: Visible spectrum of compound **9**. The bands can be assigned to ML and IV charge transfer.[223-226]

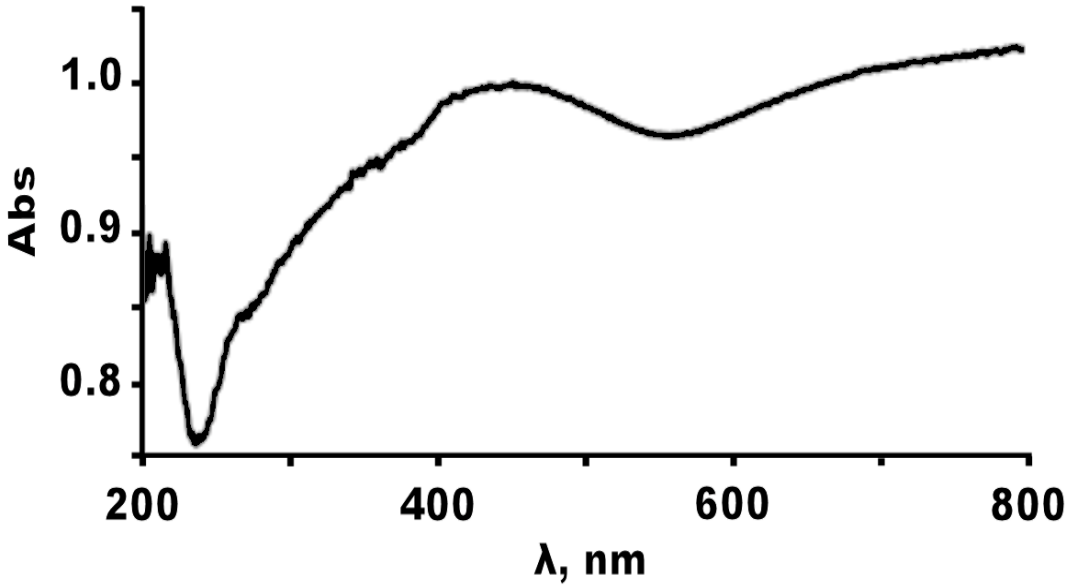

Figure 122: UV-vis reflectance spectrum of compound **9**. A series of broad overlapping bands can be observed at 269, 316, 383 and 470 nm respectively, assignable to O→M and IV charge transfers.[223-226]

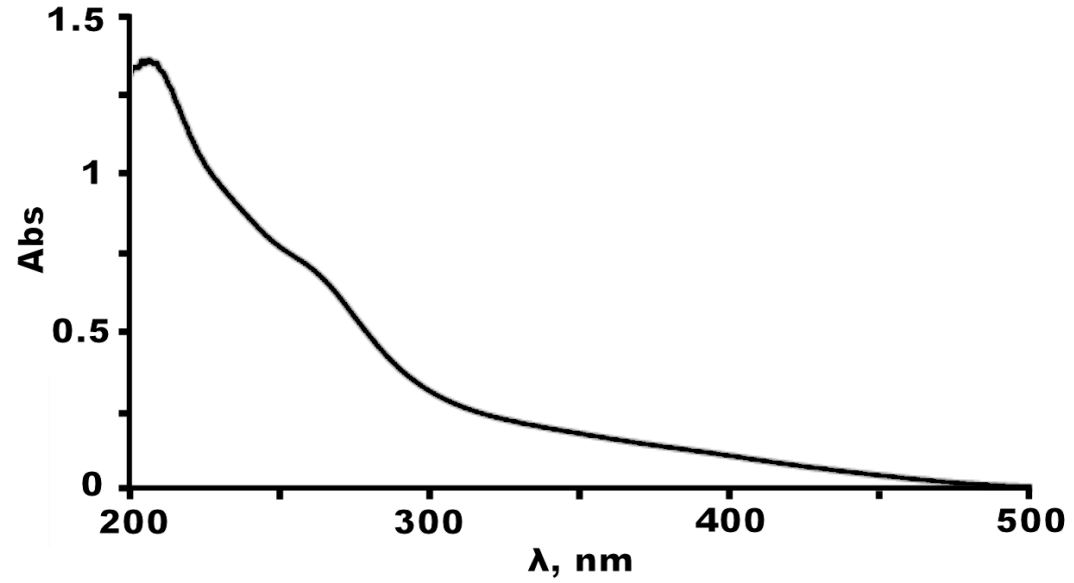

Figure 123: Visible spectrum of compound **10**. The bands can be assigned to ML and IV charge transfer.[223-226]

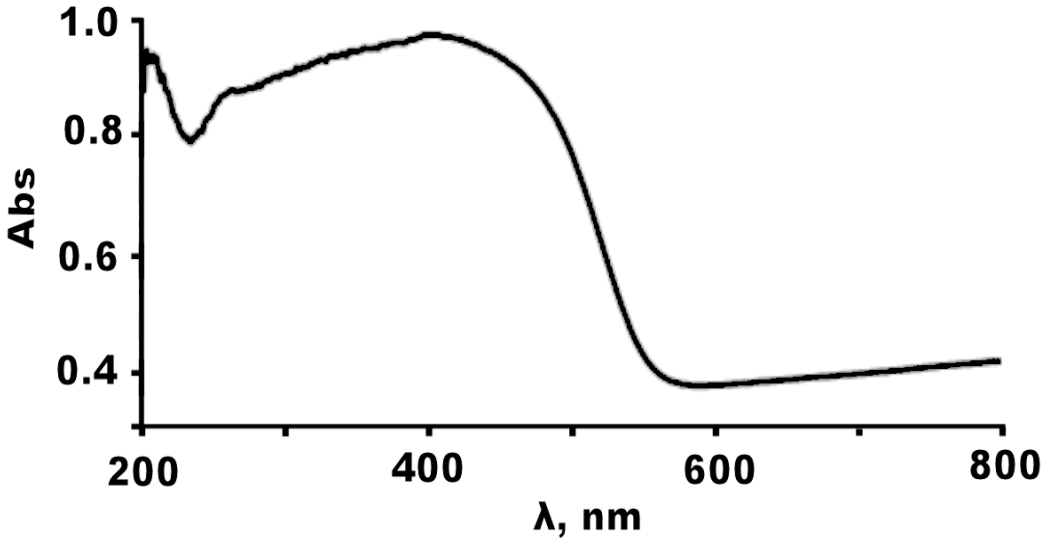

Figure 124: UV-vis reflectance spectrum of compound **10**. A series of broad overlapping bands can be observed at 273, 350 and 448 nm respectively, assignable to O→M and IV charge transfers.[223-226]

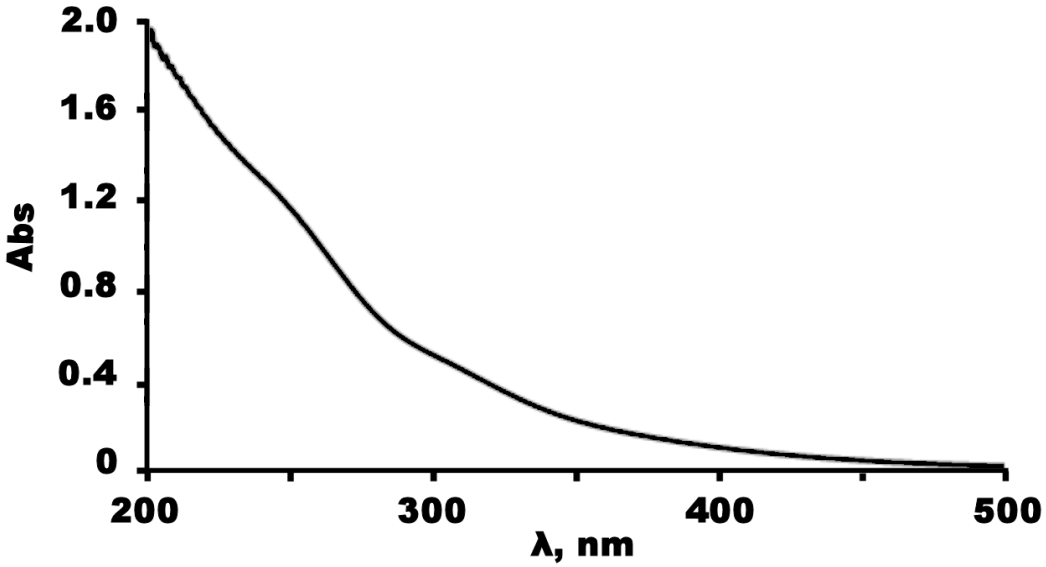

Figure 125: UV-vis spectrum of compound **11**. The bands can be assigned to ML and IV charge transfers.[223-226]

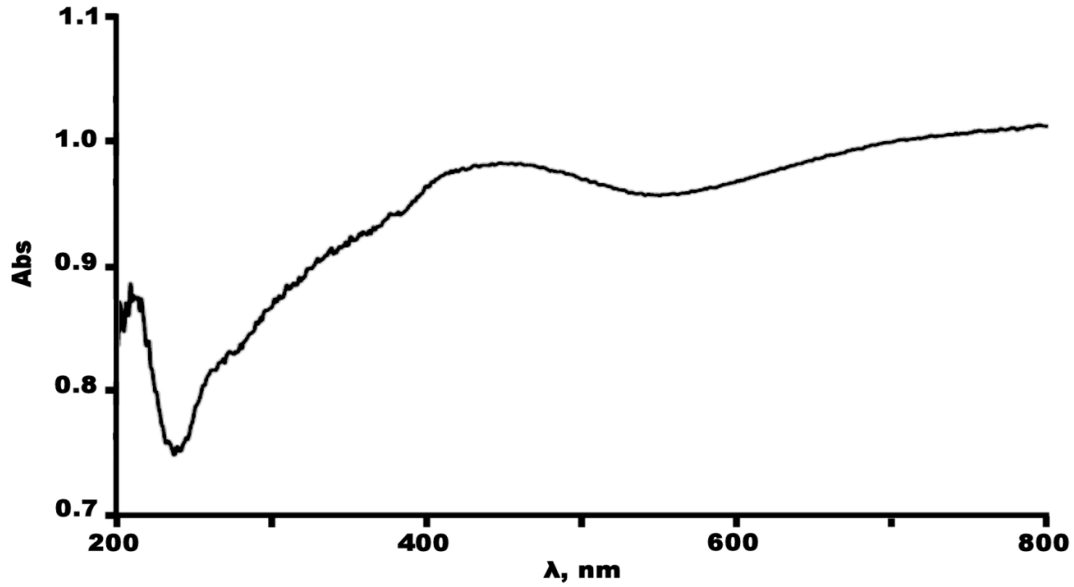

Figure 126: UV-vis reflectance spectrum of compound **11**. A series of broad overlapping bands can be observed at 269, 339 and 447 nm respectively, assignable to O→M and IV charge transfers.[223-226]

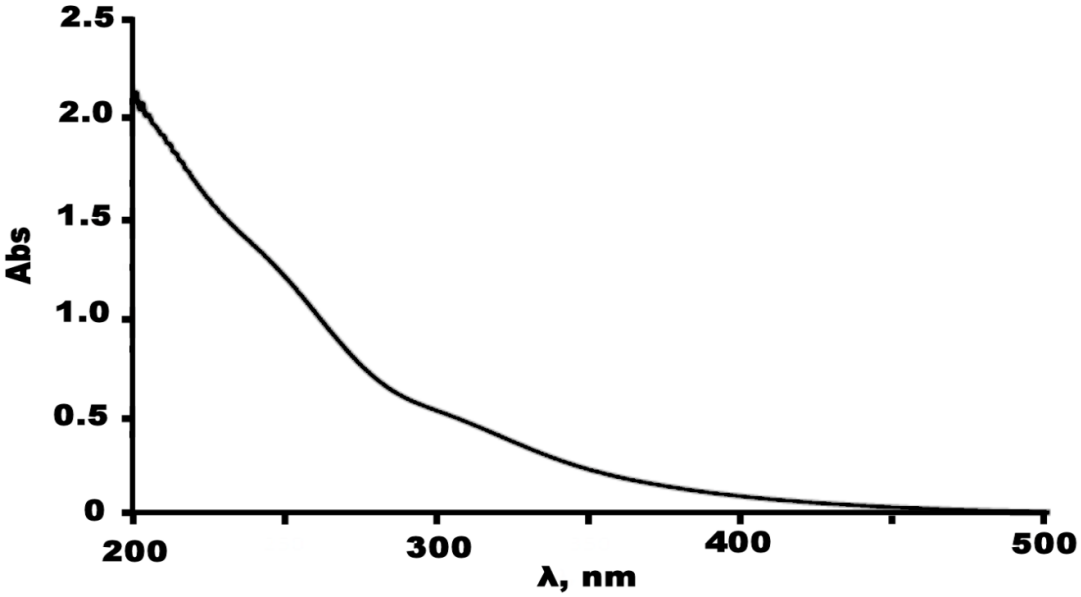

Figure 127: UV-vis spectrum of compound **12**. The bands can be assigned to ML and IV charge transfers.[223-226]

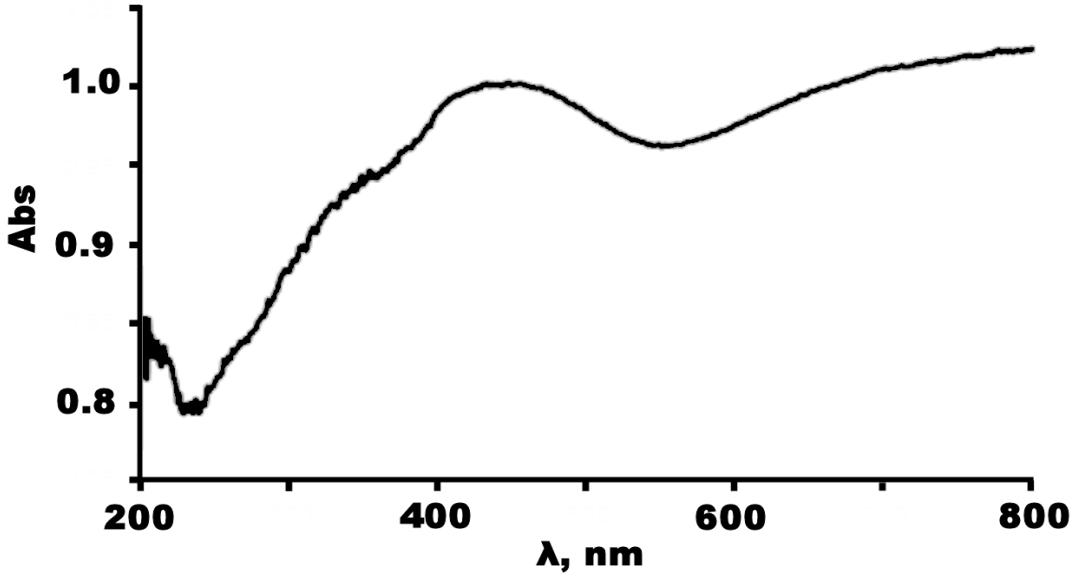

Figure 128: Visible spectrum of compound **12**. A series of broad overlapping bands can be observed at 273, 337 and 444 nm respectively, assignable to O→M and IV chargetransfers.[223-226]

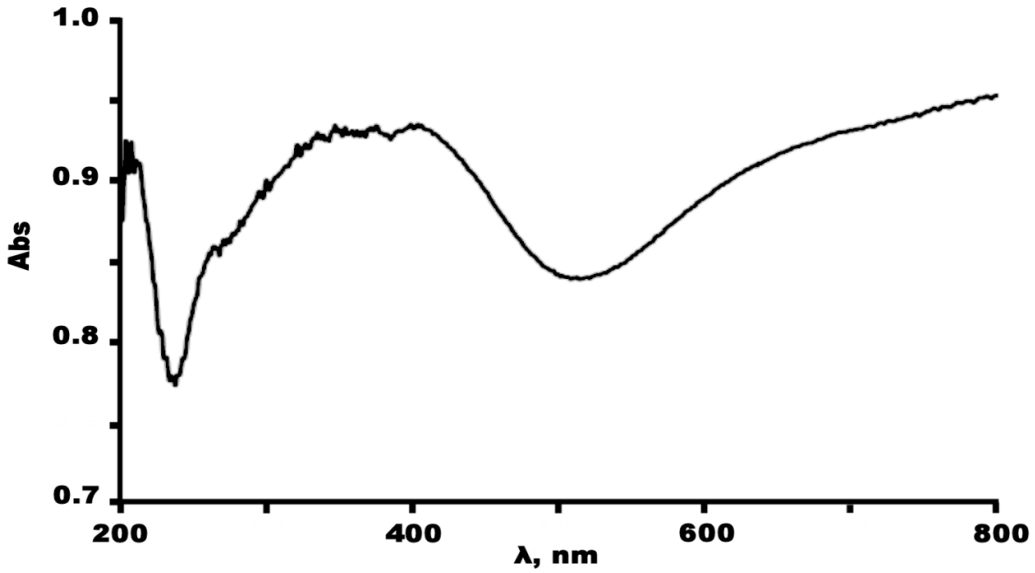

Figure 129: Visible spectrum of compound **13**. A series of broad overlapping bands can be observed at 272, 306, 339 and 410 nm respectively, assignable to O→M and IV charge transfers.[223-226]

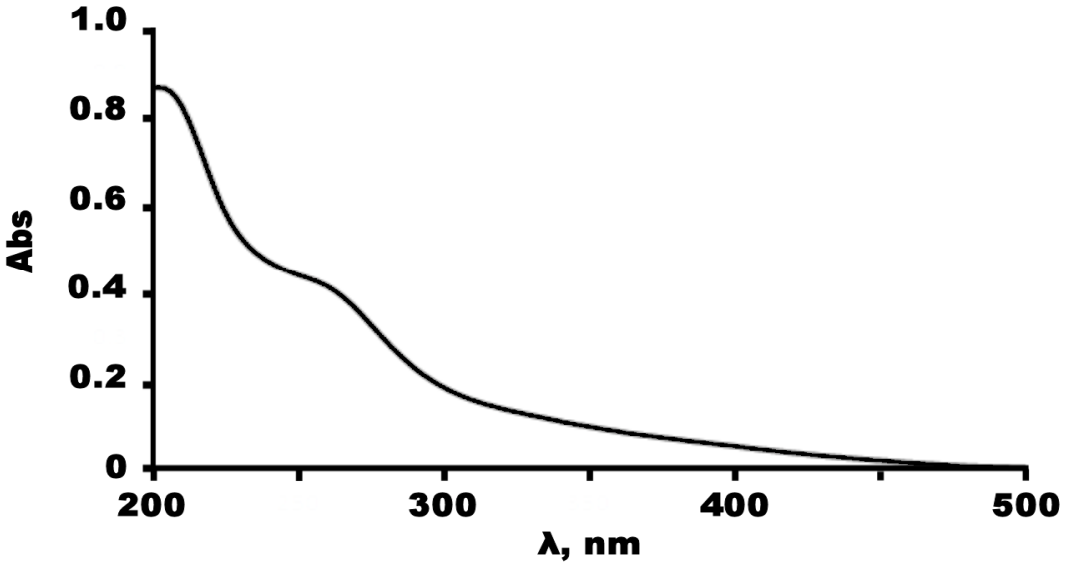

Figure 130: UV-vis spectrum of compound **14**. The bands can be assigned to ML and IV charge transfers.[223-226]

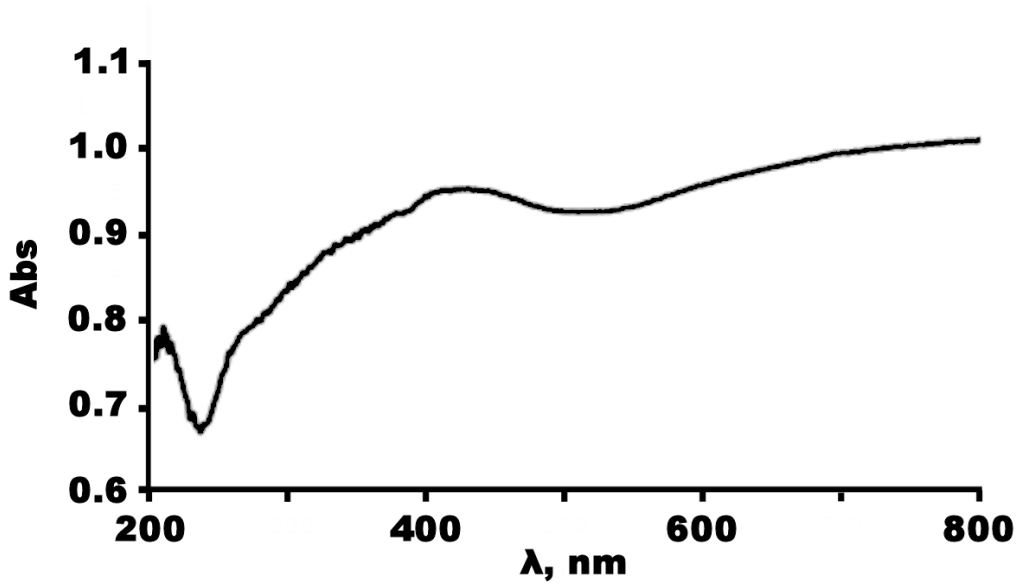

Figure 131: Visible spectrum of compound **14**. A series of broad overlapping bands can be observed at 262, 311, 364 and 437 nm respectively, assignable to O→M and IV charge transfers.[223-226]

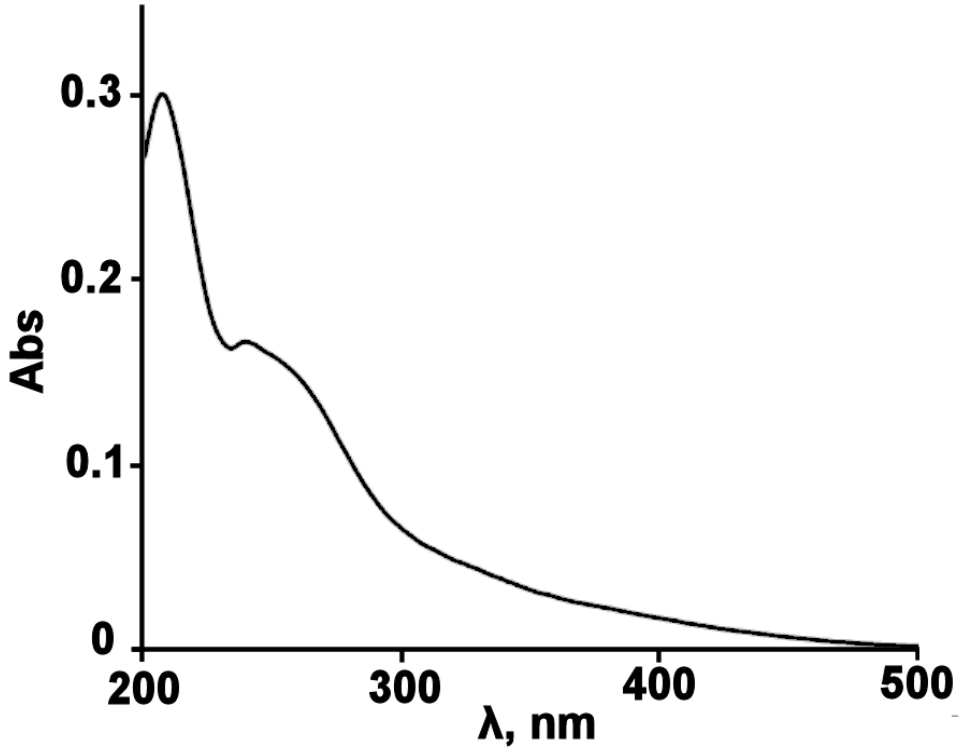

Figure 132: UV-vis spectrum of compound **15**. The bands can be assigned to ML and IV charge transfers.[223-226]

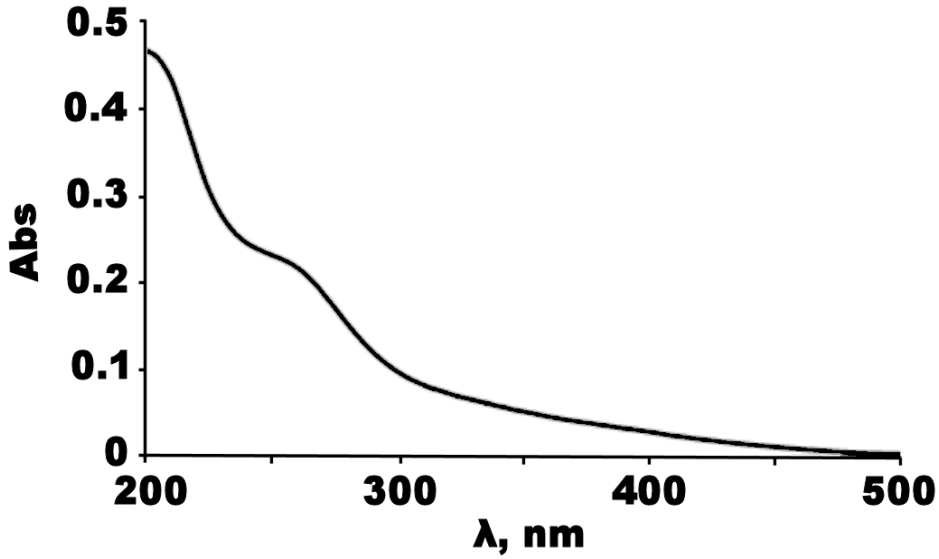

Figure 133: UV-vis spectrum of compound **16**. The bands can be assigned to ML and IV charge transfers.[223-226]

5.6 Thermogravimetric Analysis (TGA)

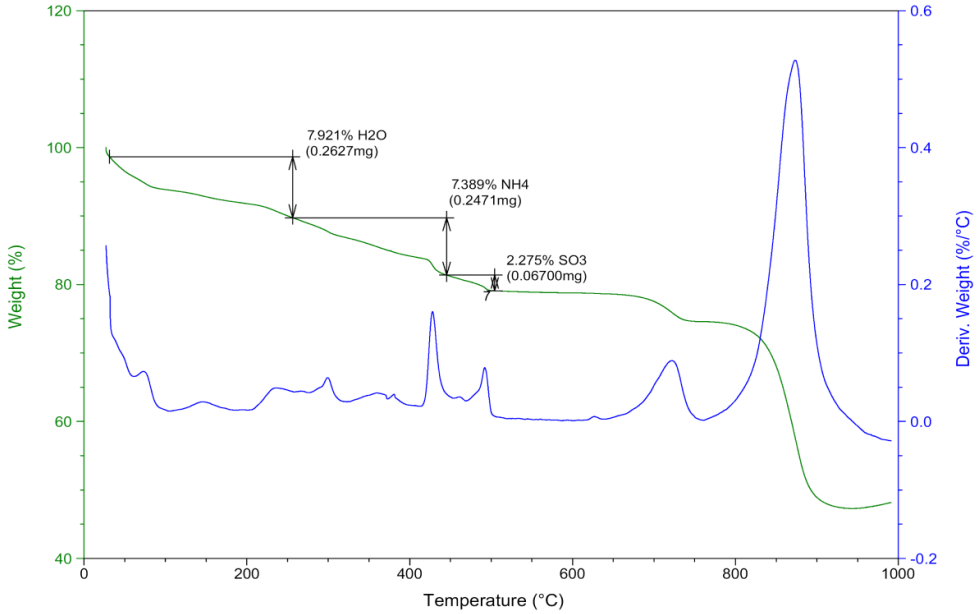

Figure 134: Thermal gravimetric analysis of **2**, showing the loss of solvent content (RT - 180 °C) as well as of the NH_4^+ and SO_3^{2-} as SO_2 (200 - 600 °C) followed by the decomposition of the compound at temperature beyond 700°C. A phase transition is taking place at higher temperatures (m.p MoO_3 = 795 ^oC).

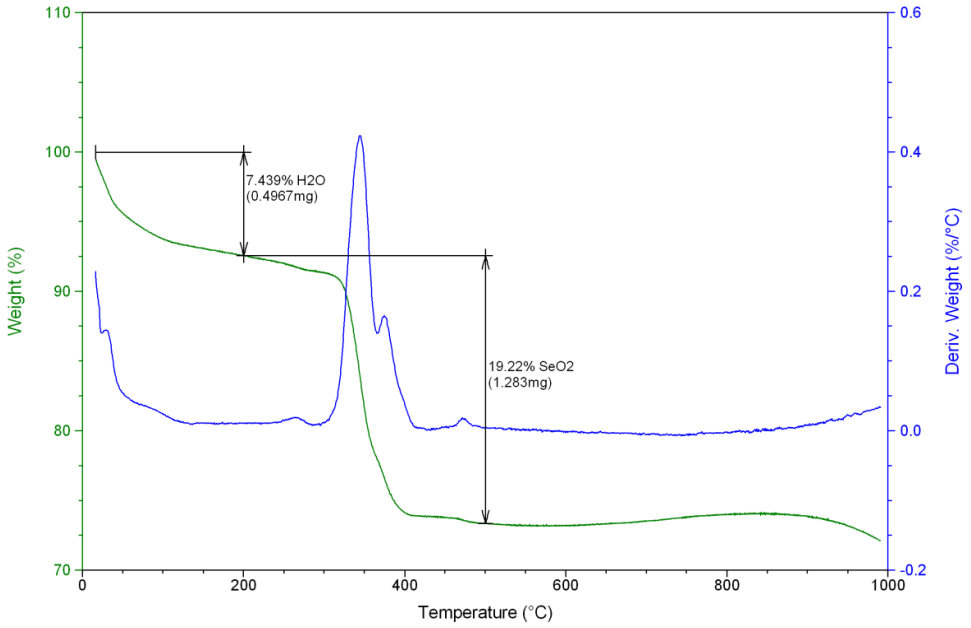

Figure 135: Thermal gravimetric analysis of **4**, showing the loss of solvent content (RT - 2000 °C) as well as of the SeO_3^{2-} as SeO_2 (200 - 500 °C).

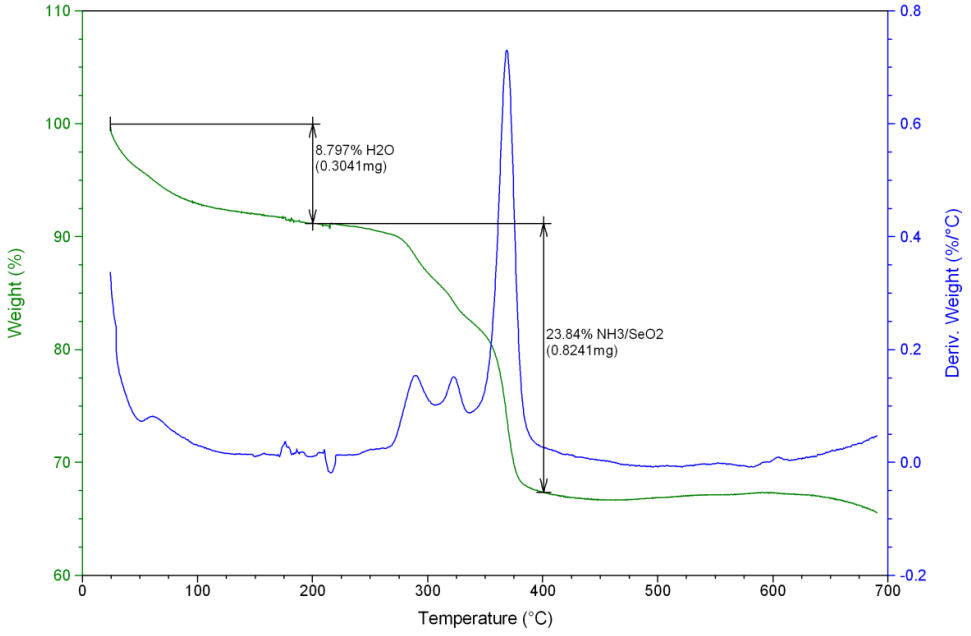

Figure 136: Thermal gravimetric analysis of **5**, showing the loss of solvent content (RT - 200 °C) as well as of the NH_4^+ and SeO_3^{2-} as SeO_2 (200 - 400 °C).

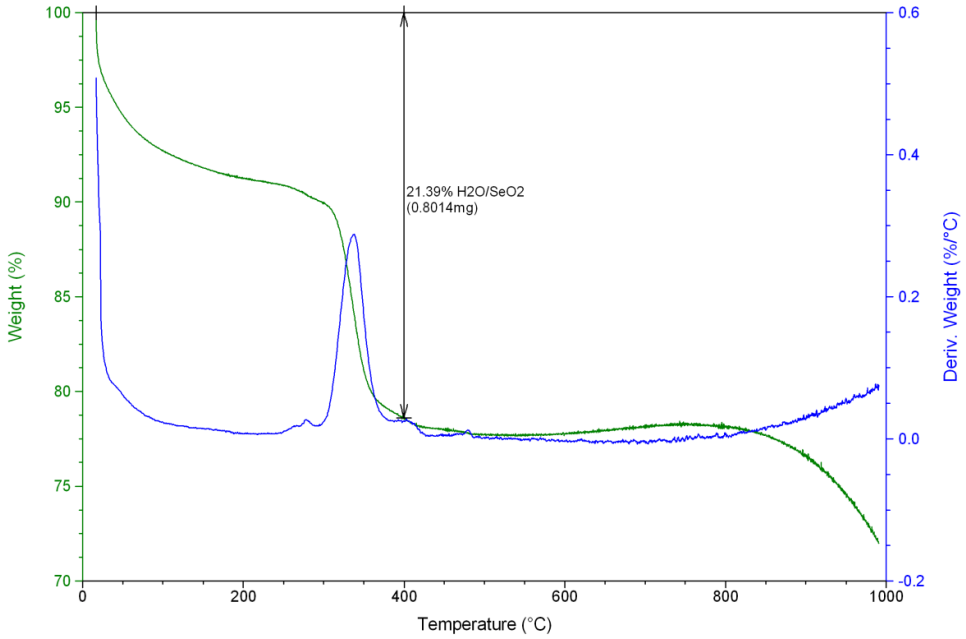

Figure 137: Thermal gravimetric analysis of **6**, showing the loss of solvent content as well as of the SeO_3^{2-} as SeO_2 (RT - 400 °C).

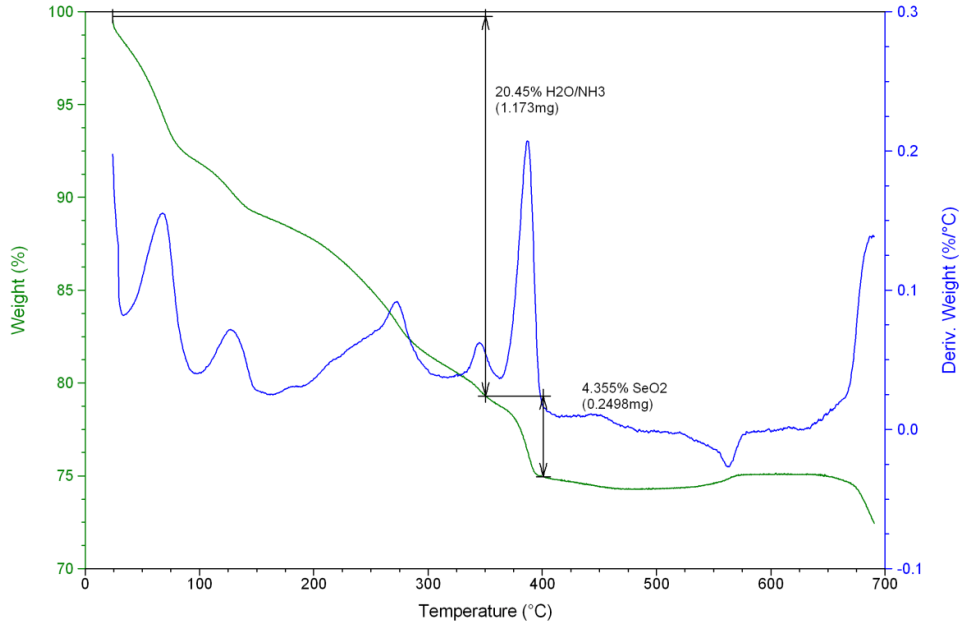

Figure 138: Thermal gravimetric analysis of **7**, showing the loss of solvent content and NH_4^+ (RT - 350 °C) as well as of the SeO_3^{2-} as SeO_2 (350 - 400 °C).

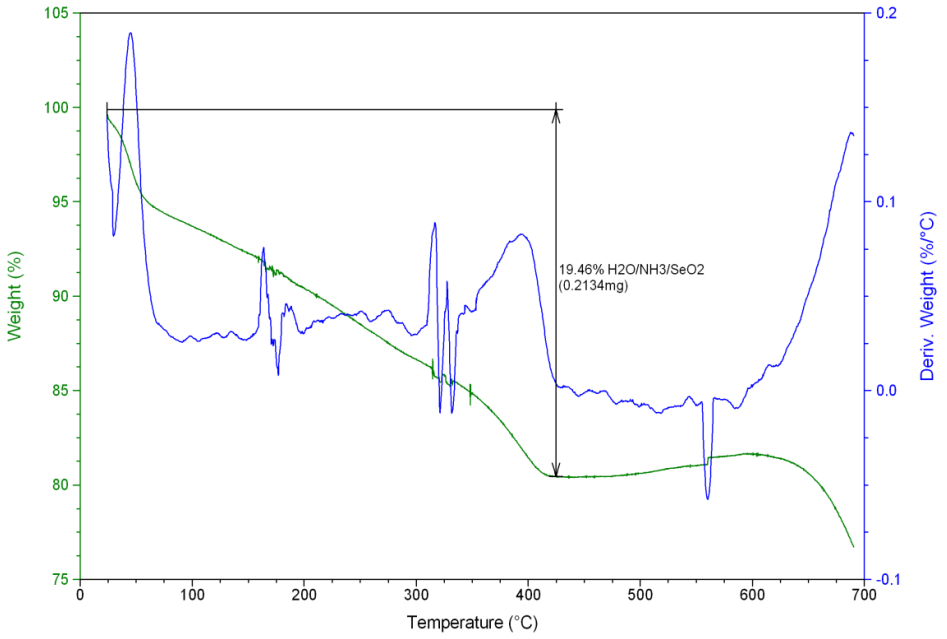

Figure 139: Thermal gravimetric analysis of **8**, showing the loss of solvent content and NH_4^+ as well as of the SeO_3^{2-} as SeO_2 (RT - 450 °C).

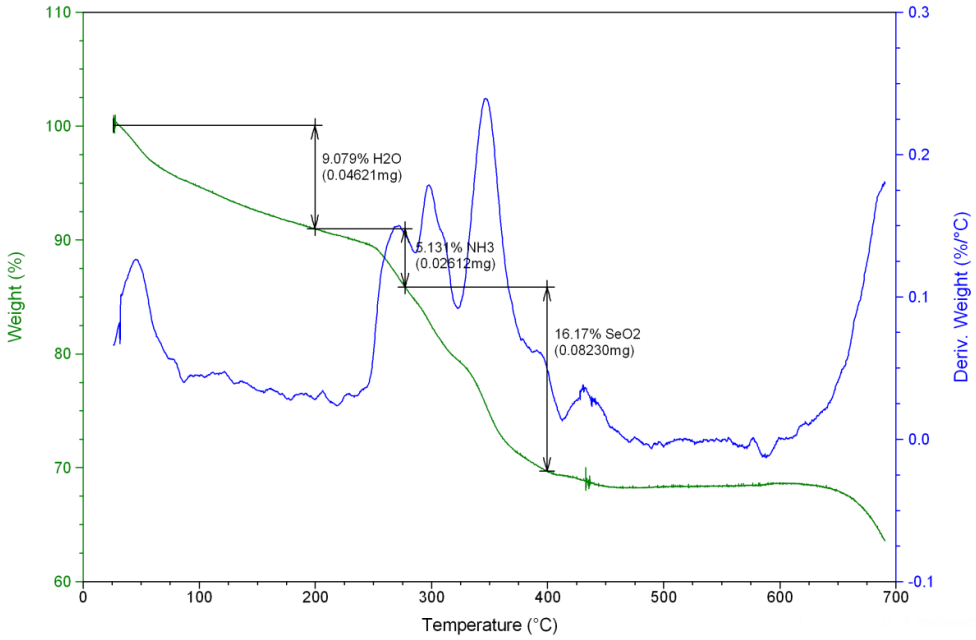

Figure 140: Thermal gravimetric analysis of **9**, showing the loss of solvent content (RT - 200 °C) as well as of the NH_4^+ and SeO_3^{2-} as SeO_2 (200 - 400 °C).

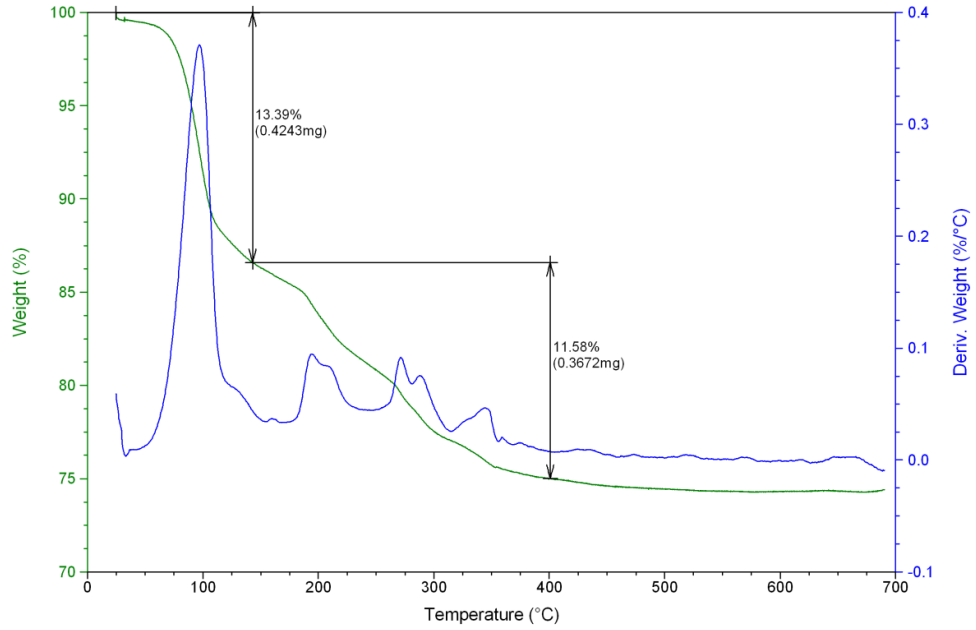

Figure 141: Thermal gravimetric analysis of **10**, showing the loss of solvent content and NH_4^+ (RT – 150) as well as of the SeO_3^{2-} as SeO_2 (150 - 400 °C).

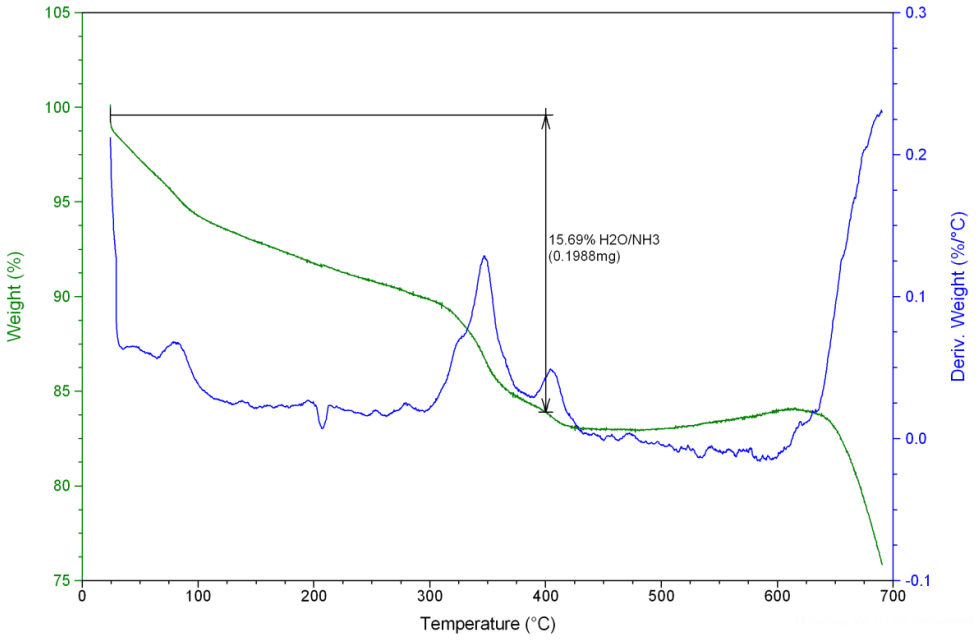

Figure 142: Thermal gravimetric analysis of **11**, showing the loss of solvent content as well as of the NH_4^+ (RT – 180 ºC).

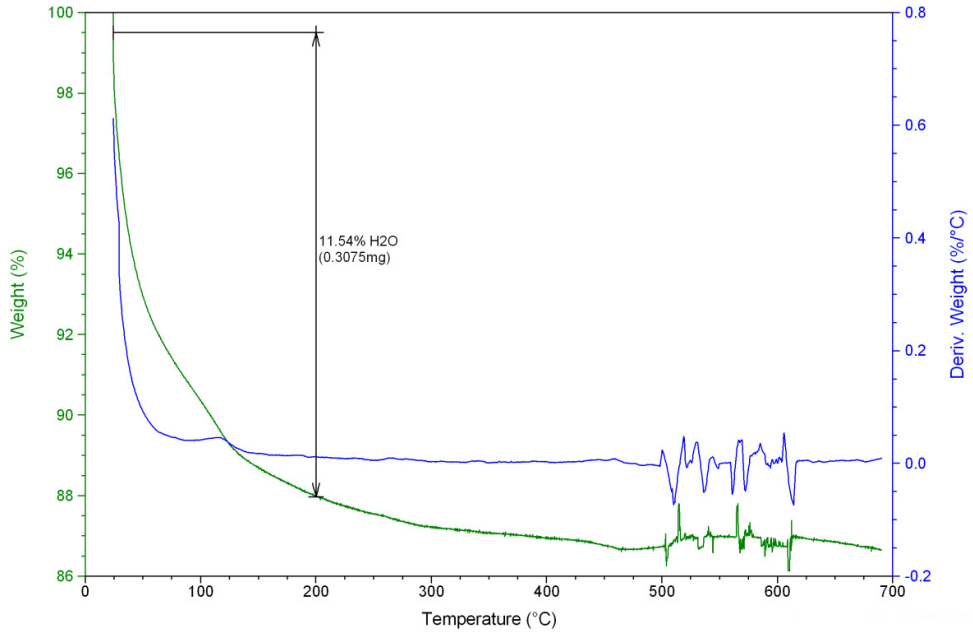

Figure 143: Thermal gravimetric analysis of **12**, show the loss of solvent content (RT – 200 ºC).

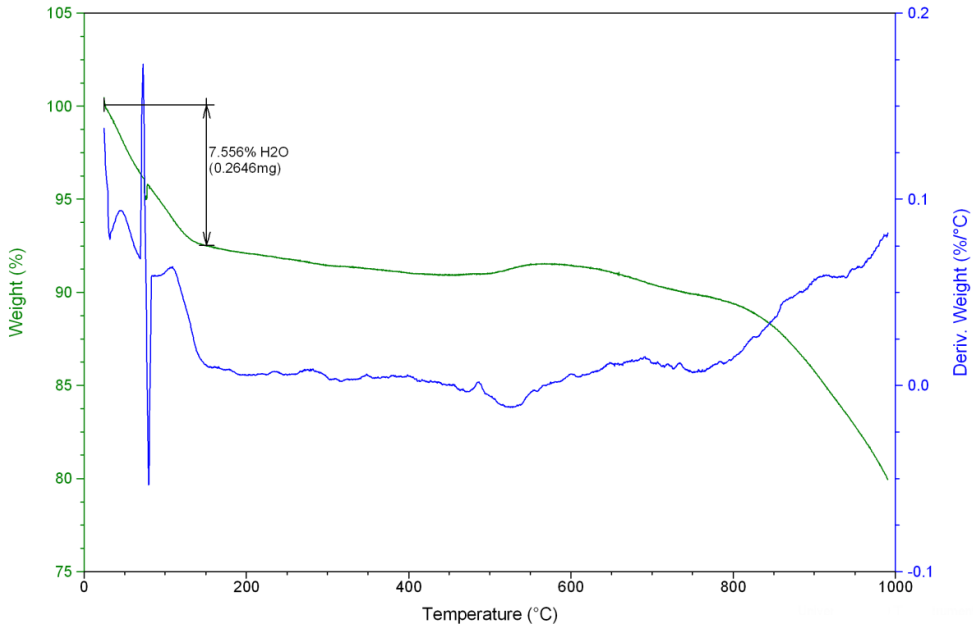

Figure 144: Thermal gravimetric analysis of **13**, showing the loss of solvent content (RT - 175 °C). The compound is stable up until 800 °C.

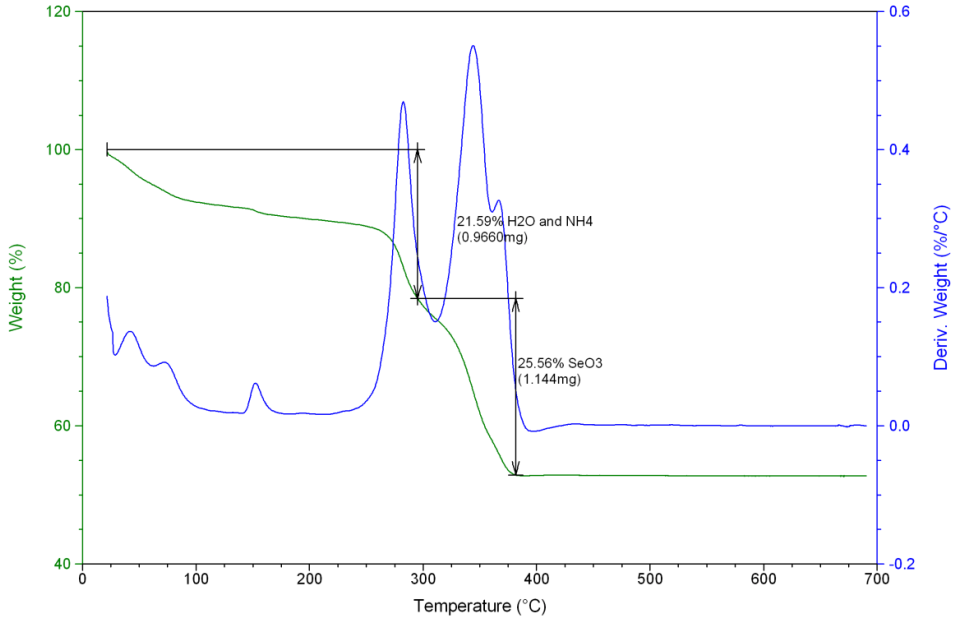

Figure 145: Thermal gravimetric analysis of **14**, showing the loss of solvent content and NH_4^+ (RT – 300 °C) and SeO_3^{2-} as SeO_2 (300 - 400 °C).

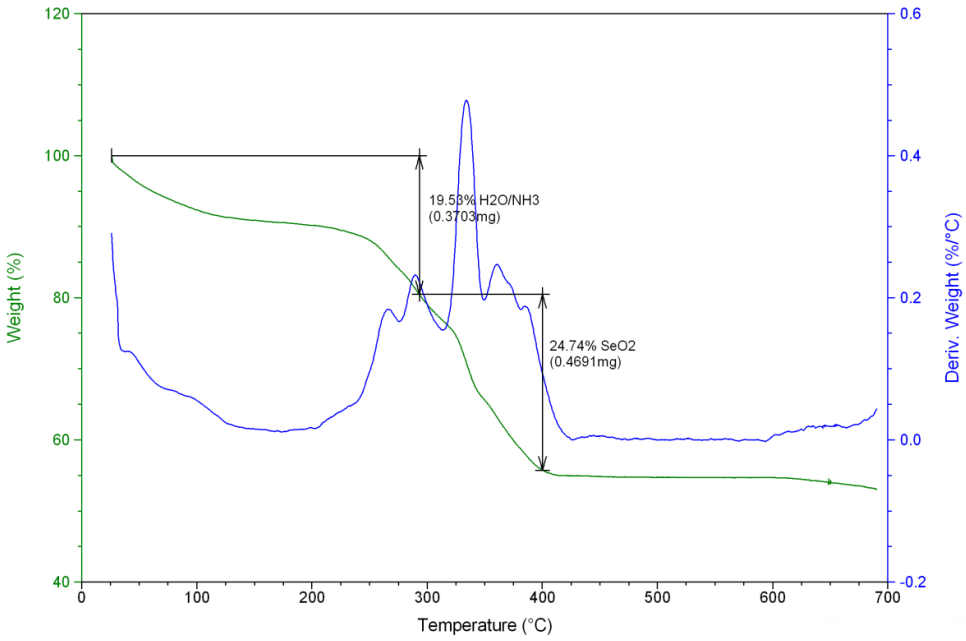

Figure 146: Thermal gravimetric analysis of **15**, showing the loss of solvent content and NH_4^+ (RT - 300 °C) as well as of the SeO_3^{2-} as SeO_2 (300 - 400 °C).

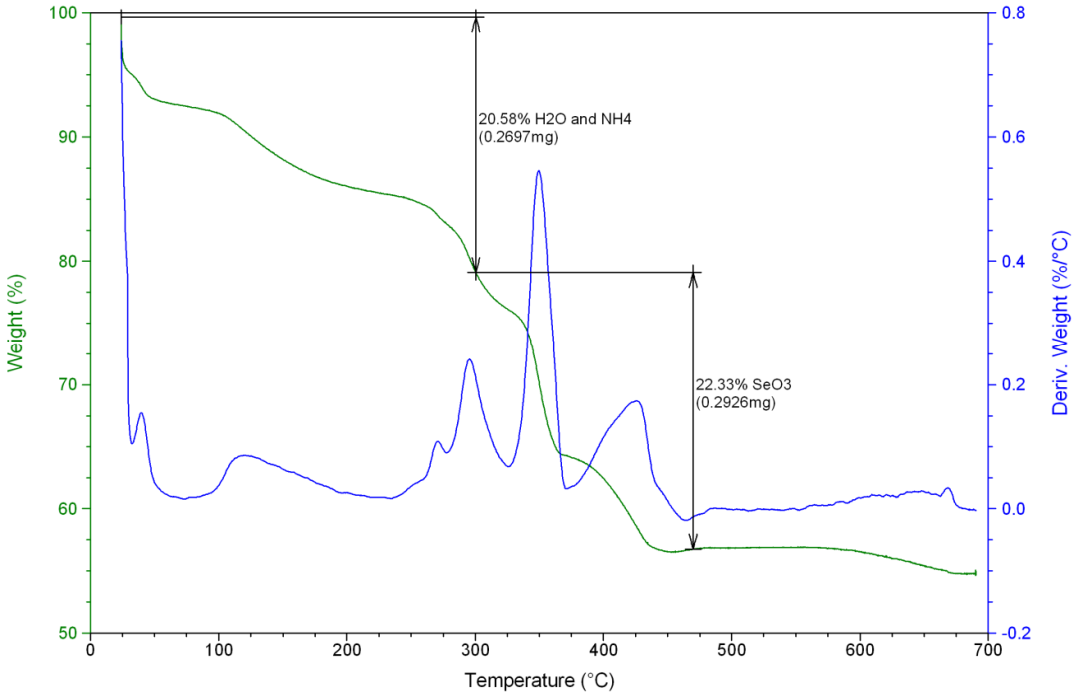

Figure 147: Thermal gravimetric analysis of **16**, showing the loss of solvent content and NH_4^+ (RT - 300 °C) as well as of the SeO_3^{2-} as SeO_2 (300 - 450 °C).

5.7 Powder X-ray Diffraction

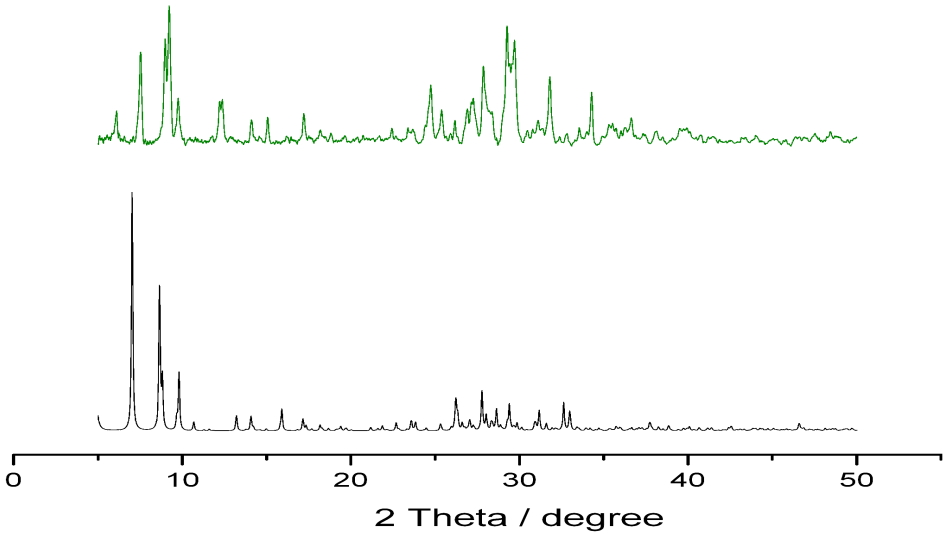

Figure 148: Comparison of the experimental (green line) and simulated (black line) X-ray diffraction powder patterns for compound **4**.

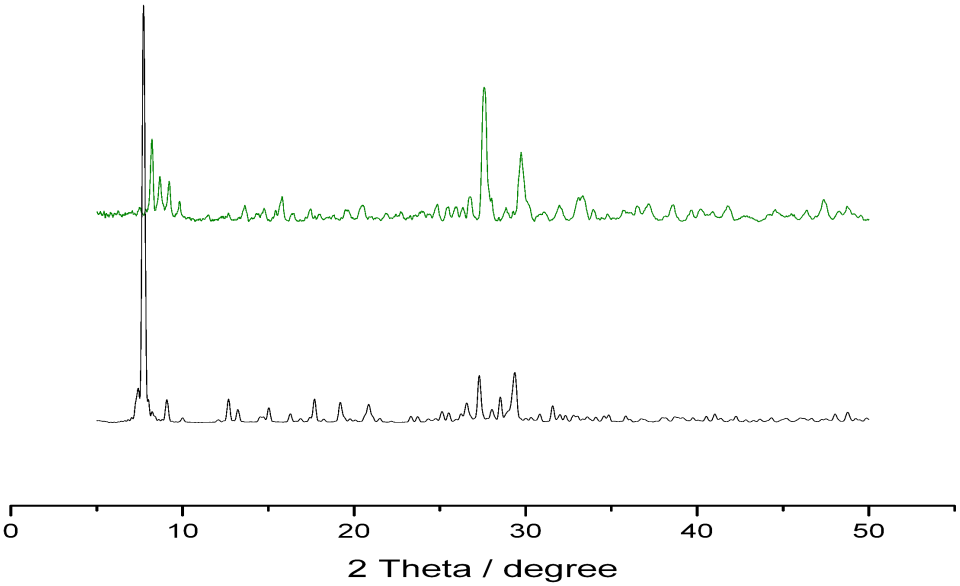

Figure 149: Comparison of the experimental (green line) and simulated (black line) X-ray diffraction powder patterns for compound **6**.

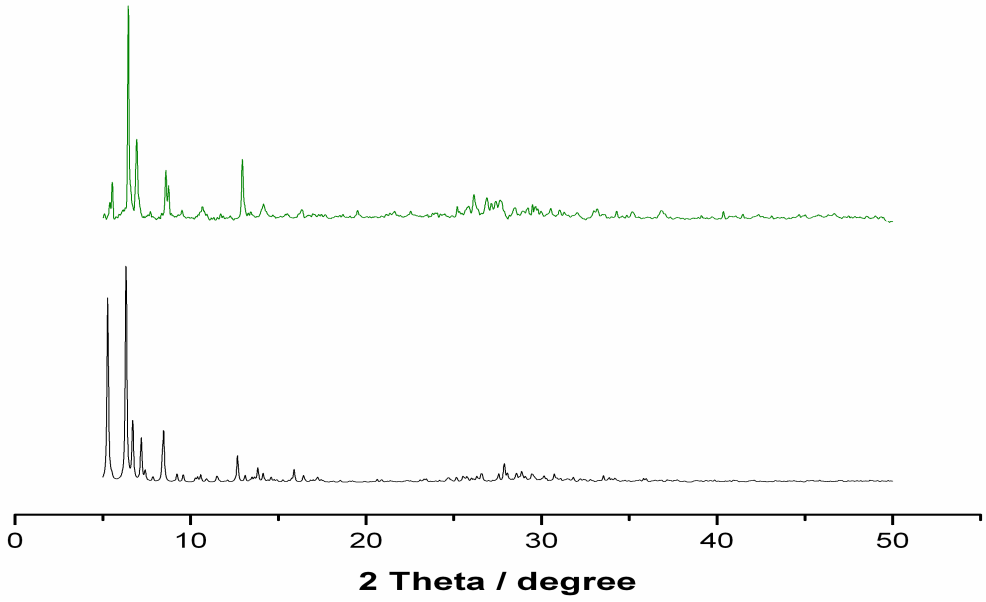

Figure 150: Comparison of the experimental (green line) and simulated (black line) X-ray diffraction powder patterns for compound **9**.

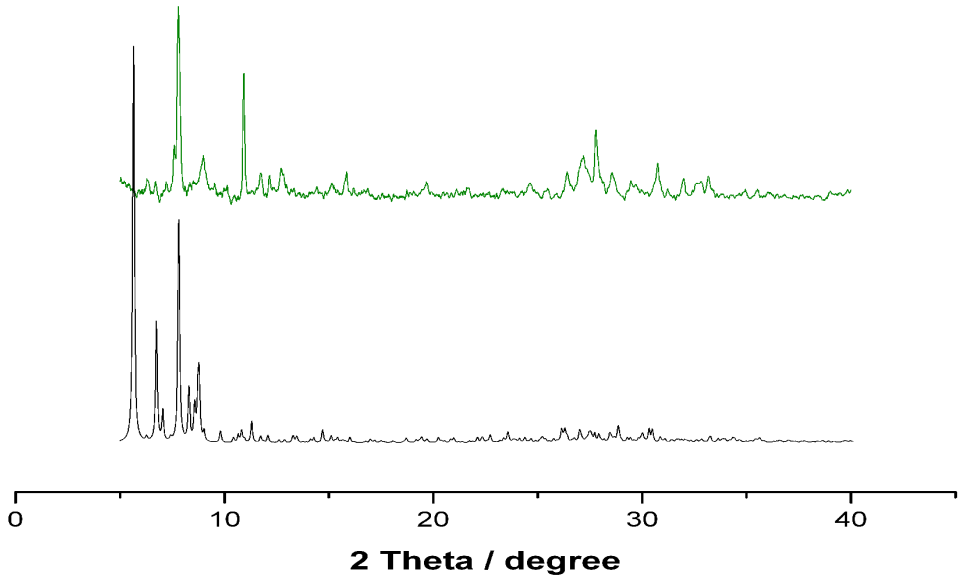

Figure 151: Comparison of the experimental (green line) and simulated (black line) X-ray diffraction powder patterns for compound **11**.

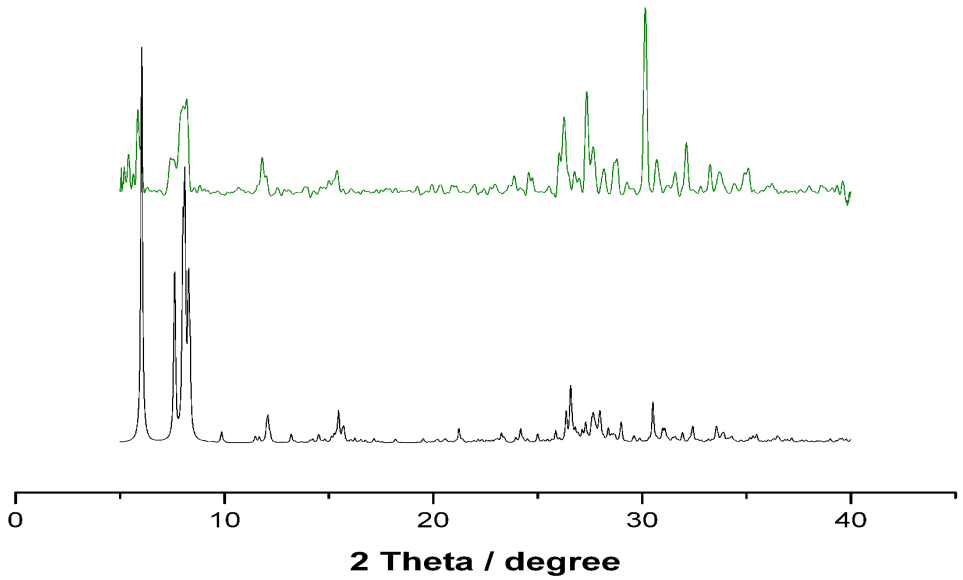

Figure 152: Comparison of the experimental (green line) and simulated (black line) X-ray diffraction powder patterns for compound **12**.

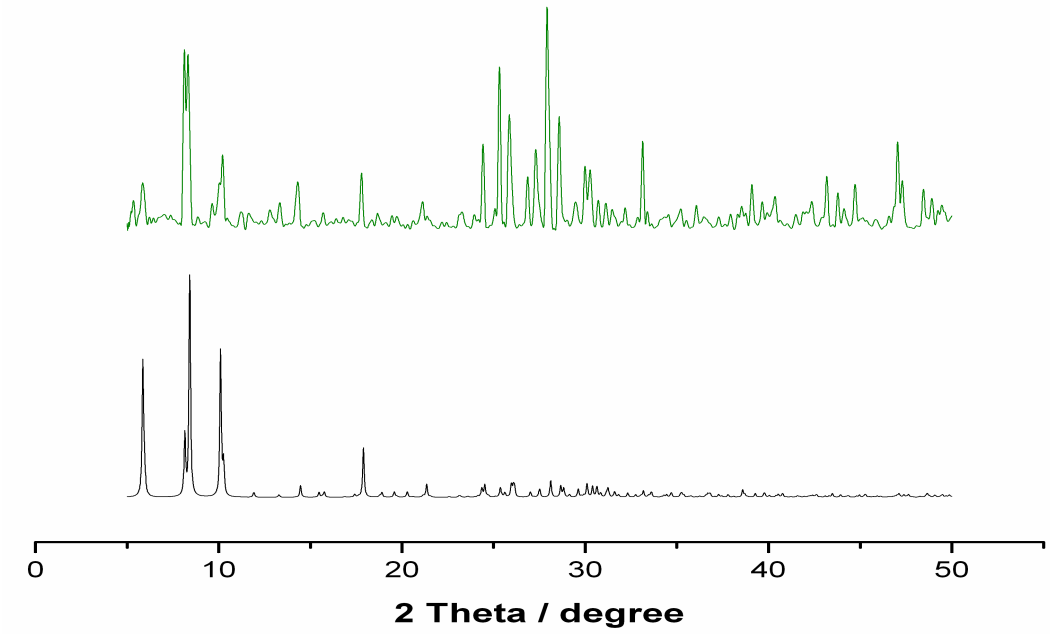

Figure 153: Comparison of the experimental (green line) and simulated (black line) X-ray diffraction powder patterns for compound **14**.

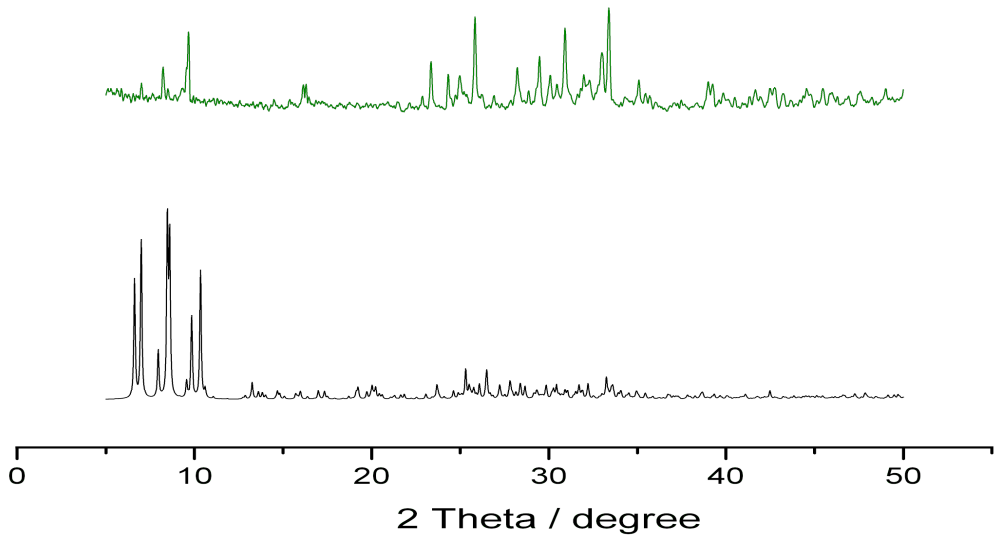

Figure 154: Comparison of the experimental (green line) and simulated (black line) X-ray diffraction powder patterns for compound **16**.

5.8 Mass Spectrometry

5.8.1 ESI – MS for compound 2

The distribution envelope observed for **1**, is the result of the contribution of two species with different extent of protonation. More specifically, the first envelope can be assigned to the isolated species with three reduced vanadium centres, $\{(Pr_4N)_7(NH_4)_2[Mo^{VI}_{11}V^{V}_{4}V^{IV}_{3}O_{52}(\mu_9\text{-}SO_3)(Mo^{VI}_{6}V^{V}O_{22})](CH_3CN)\}^{2-}$ which gives an envelope centred at m/z *ca.* 2342.1, while the second envelope can be assigned to the singly protonated analogue with four reduced vanadium centres, $\{(Pr_4N)_7(NH_4)_2[HMo^{VI}_{11}V^{V}_{3}V^{IV}_{4}O_{52}(\mu_9\text{-}SO_3)(Mo^{VI}_{6}V^{V}O_{22})](CH_3CN)\}^{2-}$ which gives an envelope centred at m/z *ca.* 2342.6. During the course of the ESI-MS studies and due to the low intensity of the observed envelope for compound **2**, was not possible the graphic representation of two well resolved species. For the above reason, only the profile of the fitted envelopes is shown, highlighted red for $\{(Pr_4N)_7(NH_4)_2[Mo^{VI}_{11}V^{V}_{4}V^{IV}_{3}O_{52}(\mu_9\text{-}SO_3)(Mo^{VI}_{6}V^{V}O_{22})](CH_3CN)\}^{2-}$ and blue for $\{(Pr_4N)_7(NH_4)_2[HMo^{VI}_{11}V^{V}_{3}V^{IV}_{4}O_{52}(\mu_9\text{-}SO_3)(Mo^{VI}_{6}V^{V}O_{22})](CH_3CN)\}^{2-}$ respectively.

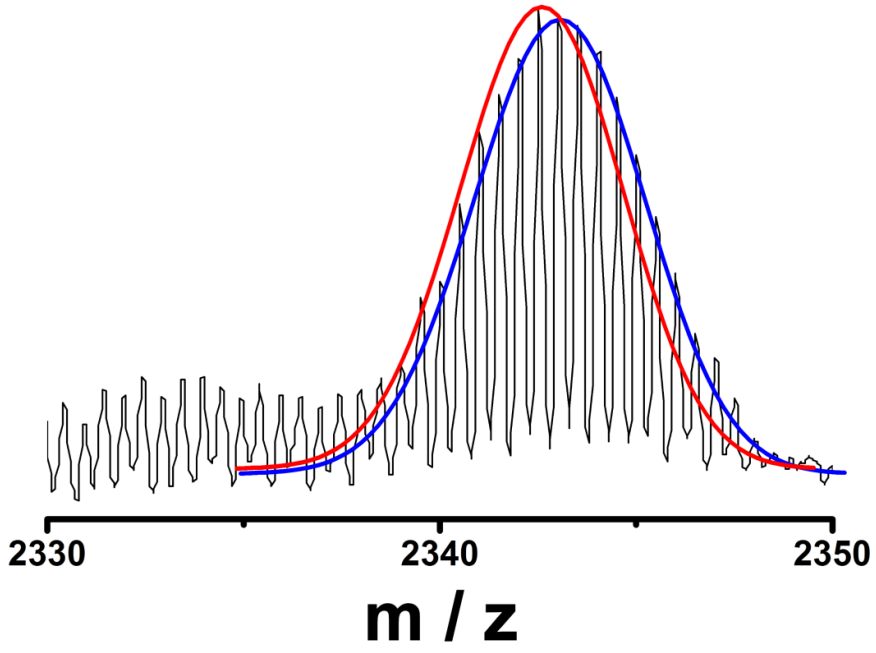

Figure 155: Negative ion mass spectrum in acetonitrile solution of $\{(Pr_4N)_7(NH_4)_2[H_n Mo_{11}V^{V}_{4-n}V^{IV}_{3+n}O_{52}(SO_3)(Mo^{VI}_{6}V^{V}O_{22})](CH_3CN)\}^{2-}$. Two envelopes can be seen where n

= 0 (with three vanadium ions in oxidation state IV) giving an envelope centred at m/z *ca.* 2342.1, and where n =1 (with four vanadium ions in oxidation state IV, requiring one proton) giving an envelope centred at m/z *ca.* 2342.6. Black line: experimental data, red/blue lines: profile lines of the simulated isotope patterns.

5.8.2 ESI – MS for compound 4

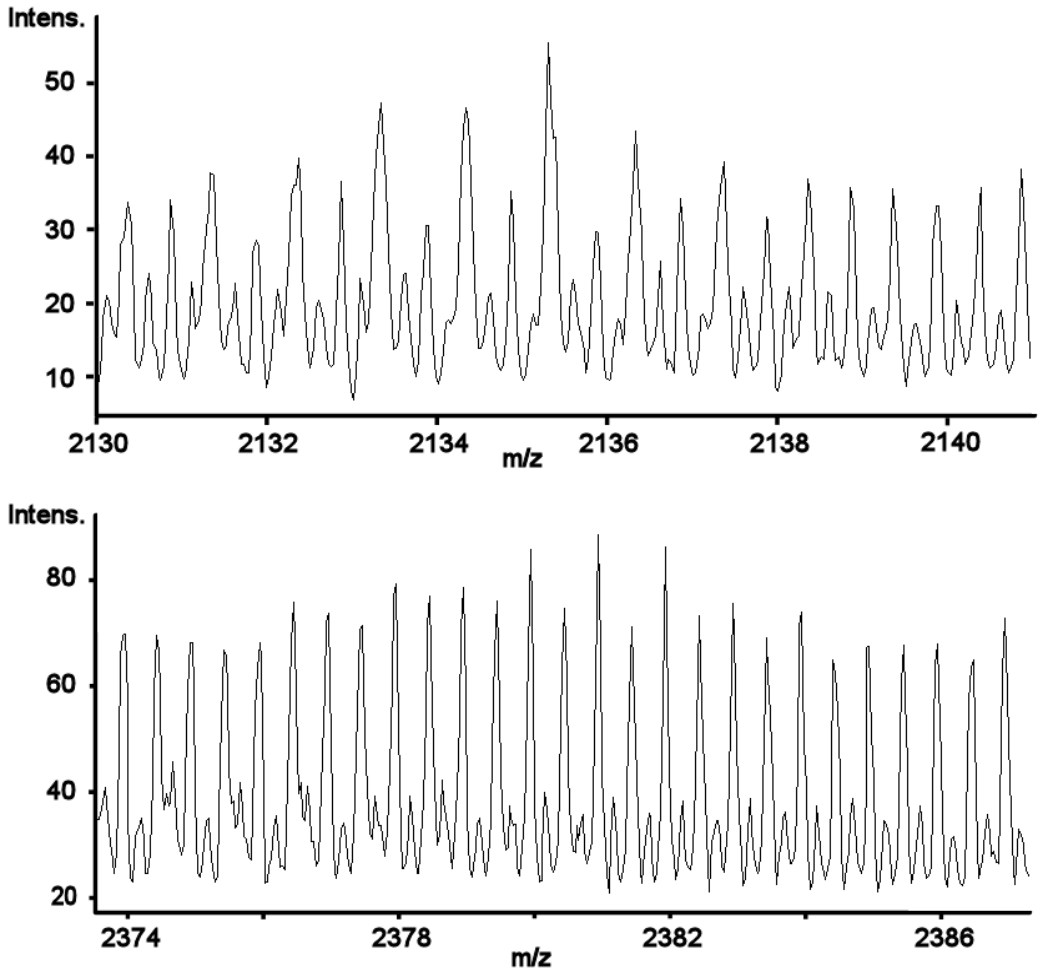

Figure 156: Negative ion mass spectrum in acetonitrile solution of $\{(C_{16}H_{36}N)_2K_4[H_7Mo_{12}V^{V}_5V^{IV}_5O_{58}(SeO_3)_8)(H_2O)\}^{2-}$ (top) giving an envelope centred at m/z *ca.* 2135.3 and of $\{(C_{16}H_{36}N)_3K_9[H_5Mo_{12}V^{V}V^{IV}_9O_{58}(SeO_3)_8)(H_2O)_4\}^{2-}$ (bottom) giving an envelope centred at m/z *ca.* 2380.9.

5.8.3 ESI – MS of compound 5

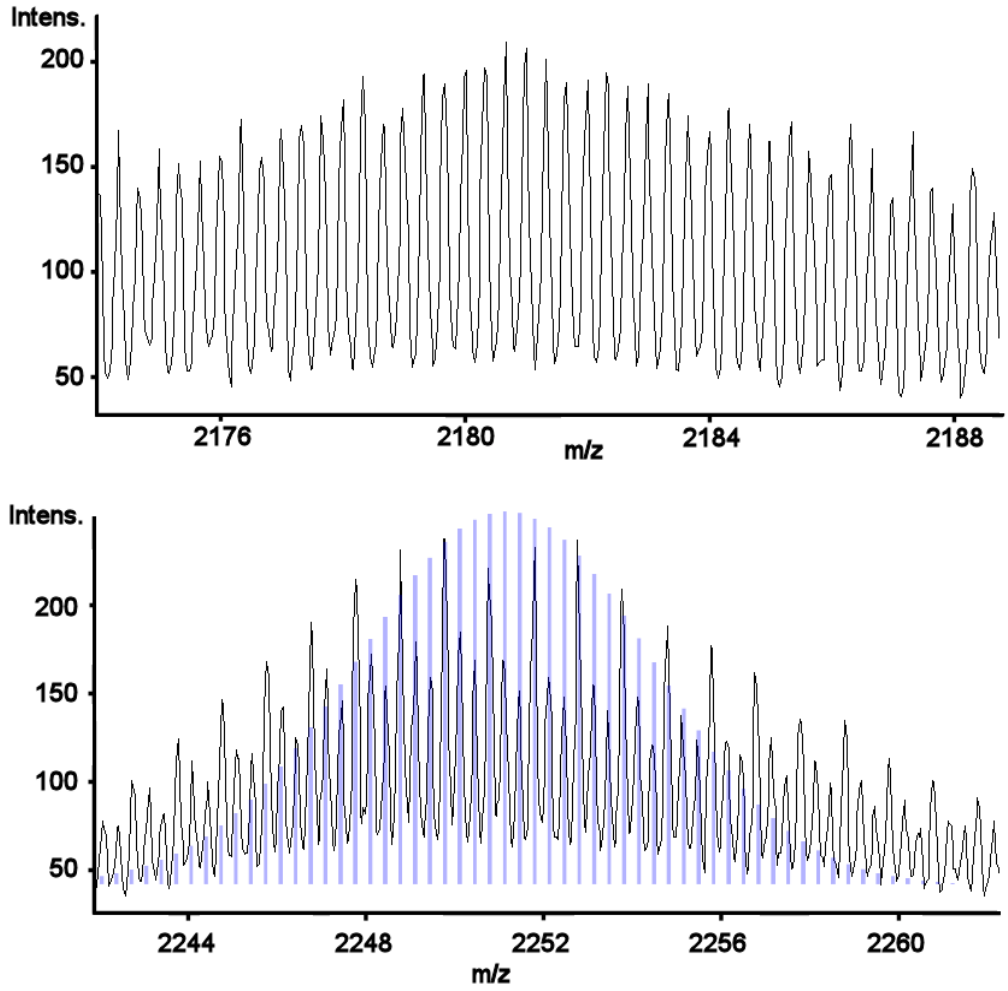

Figure 157: Negative ion mass spectrum in acetonitrile solution of $\{(C_{16}H_{36}N)_{11}K_6[Mo_{12}V^{V}V^{IV}_{9}O_{58}(SeO_3)_8)(H_2O)_2\}^{3-}$ (top) giving an envelope centred at m/z *ca.* 2180.6 and of $\{(C_{16}H_{36}N)_{11}K_7[H_5Mo_{12}V^{IV}_{10}O_{58}(SeO_3)_8)(H_2O)_{12}\}^{3-}$ (bottom) giving an envelope centred at m/z *ca.* 2251.7. Black line: experimental data, blue lines: profile line of the simulated isotope pattern.

5.8.4 ESI – MS of compound 6

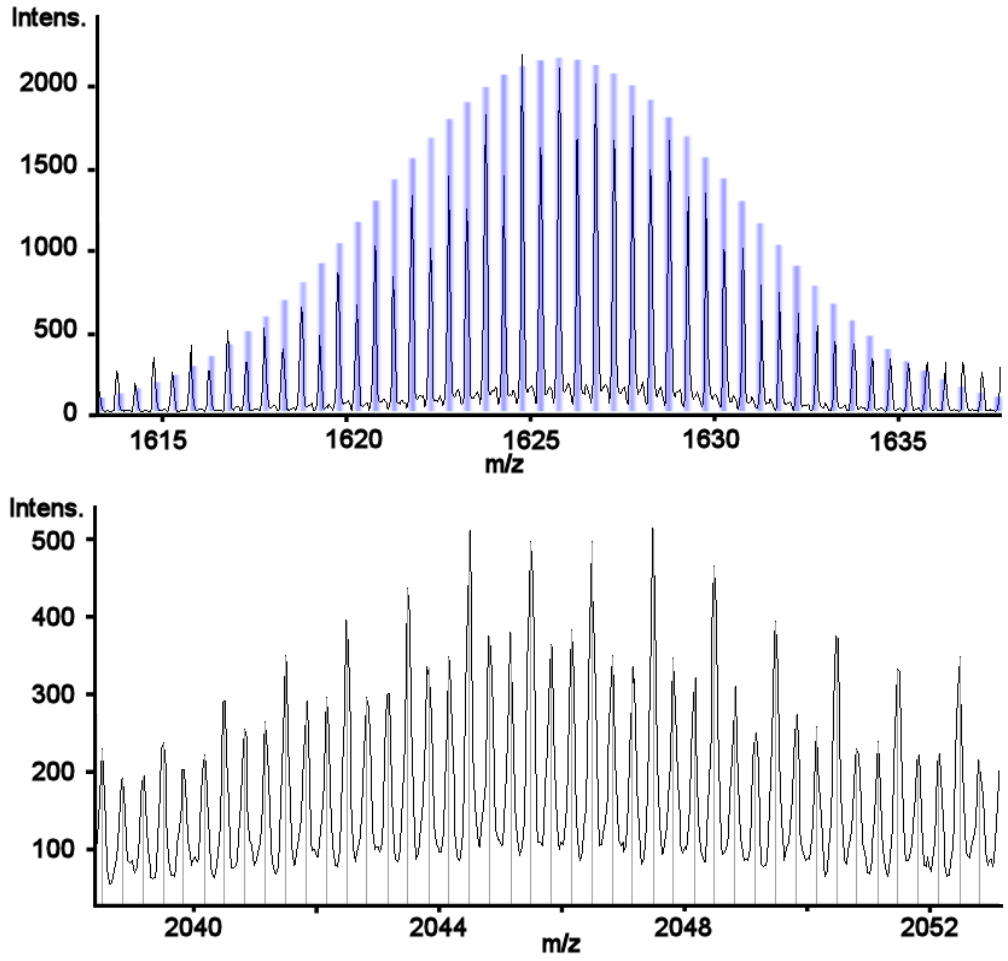

Figure 158: Negative ion mass spectrum in acetonitrile solution of $\{(C_{16}H_{36}N)K_7[HMo_{11}V^{V}V^{IV}{}_6O_{52}(SeO_3))(H_2O)_{20}\}^{2-}$ (top) giving an envelope centred at m/z *ca.* 1624.7 and of $\{(C_{16}H_{36}N)_5[H_5Mo_{11}V^{V}{}_3V^{IV}{}_4O_{52}(SeO_3)]_2(H_2O)_{10}\}^{3-}$ (bottom) giving an envelope centred at m/z *ca.* 2047.6. Black line: experimental data, blue lines: profile line of the simulated isotope pattern.

5.8.5 ESI – MS of compound 7

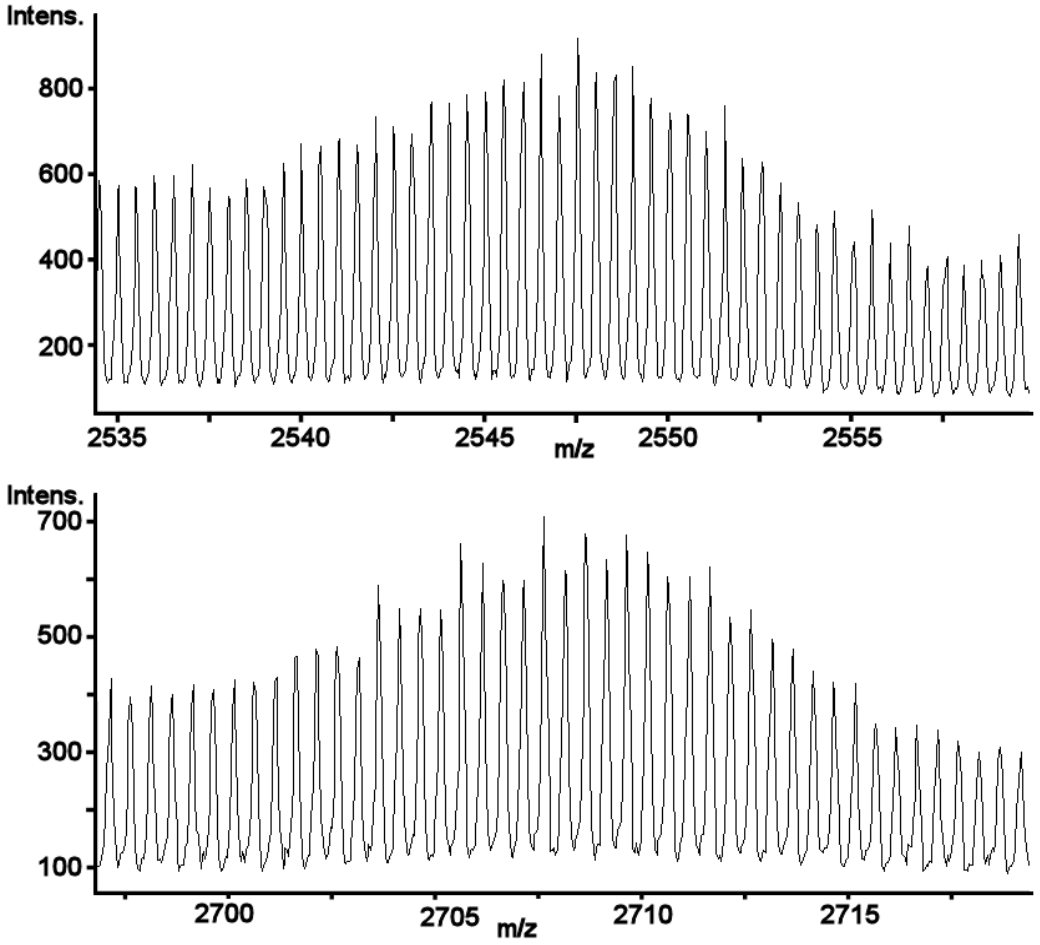

Figure 159: Negative ion mass spectrum in acetonitrile solution of $\{K_8[H_2Mo_{11}V^{V}_5V^{IV}_2O_{52}(SeO_3))(H_2O)_2\}^{2-}$ (top) giving an envelope centred at m/z *ca.* 2547.5 and of $\{(C_{16}H_{36}N)K_{10}H_3[Mo_{11}V^{V}_4V^{IV}_3O_{52}(SeO_3)]_2(H_2O)_2\}^{2-}$ (bottom) giving an envelope centred at m/z *ca.* 2707.6.

5.8.6 ESI –MS of compound 11

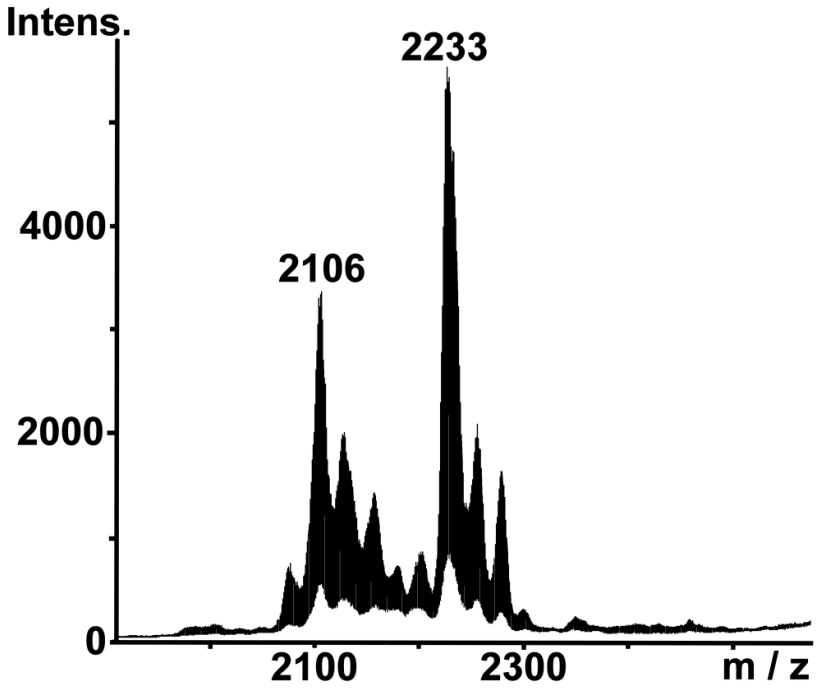

Figure 160: Negative ion mass spectrum in acetonitrile solution of **11**.

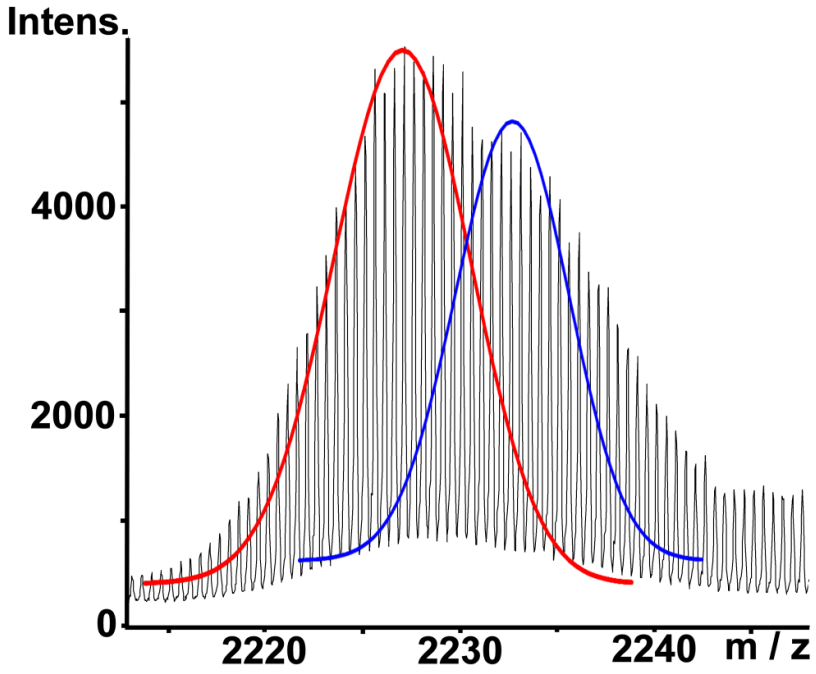

Figure 161: Expanded MS for compound **11**. Two overlapping species which can be formulated as $\{(C_{16}H_{36}N)_3K_6H_3\ [Mo^{VI}_{12}V^{V}_{4}V^{IV}_{8}O_{69}Te(TeO_3)_2]\cdot(H_2O)_8\}^{2-}$ at *m/z ca.* 2227.1

and $\{(C_{16}H_{36}N)_3K_4H_3[Mo^{VI}_{12}V^{V}_{6}V^{IV}_{6}O_{69}Te(TeO_3)_2]\cdot(H_2O)_{13}\}^{2-}$ at *m/z ca.* 2233.2, respectively. Black line: experimental data, red/blue lines: profile lines of the simulated isotope patterns.

5.8.7 ESI – MS of compound 12

In the case of **12** the MS was performed in aqueous medium. As was expected the spectrum consists of a plethora of overlapping envelopes assigned to species of different extent of protonation and hydration. The main species observed give envelopes at *m/z ca.* 1776.7 and 2350.3 and are formulated as dimers of **12** species, $\{K_{12}H_4[(Mo_{12}V^{V}_{12}O_{69}(TeO_3)_2)]_2(H_2O)_{11}\}^{4-}$ and $\{K_{11}H_6[(Mo_{12}V^{V}_{12}O_{69}(TeO_3)_2)]_2(H_2O)_{10}\}^{3-}$ respectively.

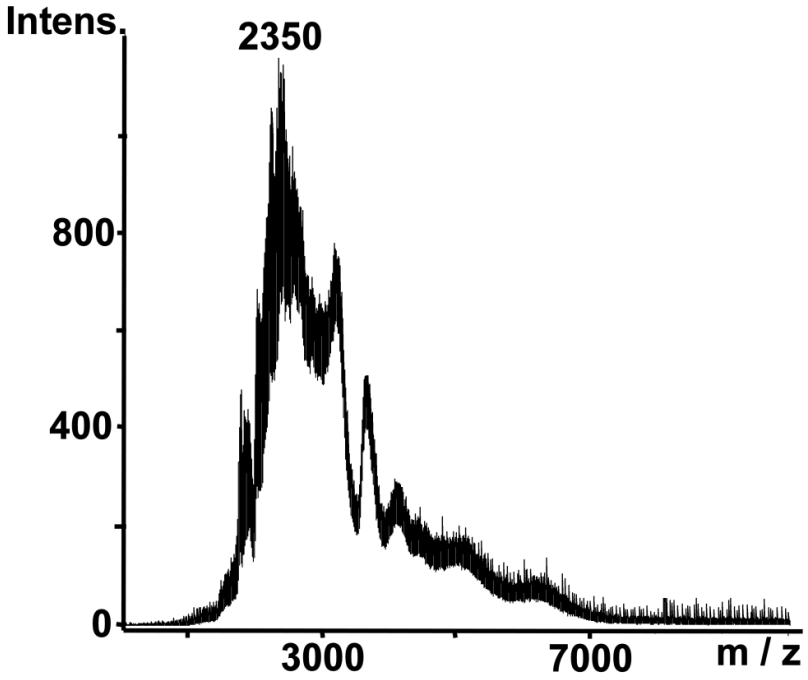

Figure 162: Negative ion mass spectrum in aqueous medium of **12**.

5.9 Redox Titrations

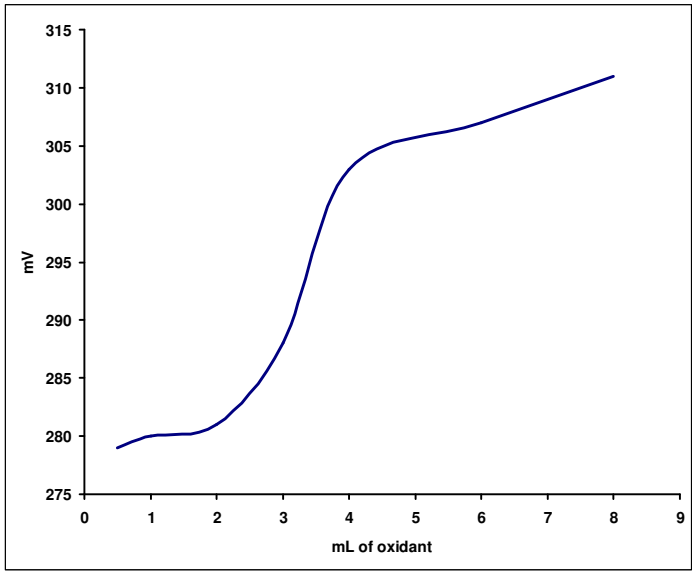

Figure 163: Redox titration curve of compound **2**. Compound **2** $(NH_4)_{10}[Mo^{VI}_{11}V^{V}_{5}V^{IV}_{2}O_{52}(\mu_9\text{-}SO_3)]\cdot 14H_2O$, mass used = 62 mg. Oxidant = 0.01 M Ce^{IV} in 0.5 M of sulphuric acid solution. Theoretical amount of oxidant for 2 electron reduced species in mL: 3.18. Experimental amount used in mL: 3.35.

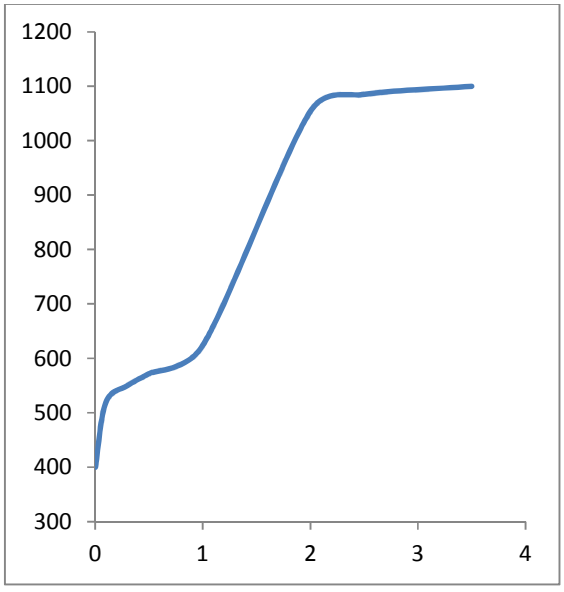

Figure 164: Redox titration curve of compound **6**. Compound **6** $K_7[Mo^{VI}_{11}V^{V}_{5}V^{IV}_{2}O_{52}(\mu_9\text{-}SeO_3)]\cdot 31H_2O$, mass used = 22 mg. Oxidant = 0.01 M Ce^{IV} in 0.5 M of sulphuric acid solution. Theoretical amount of oxidant for 2 electron reduced species in mL: 1.37. Experimental amount used in mL: 1.40.

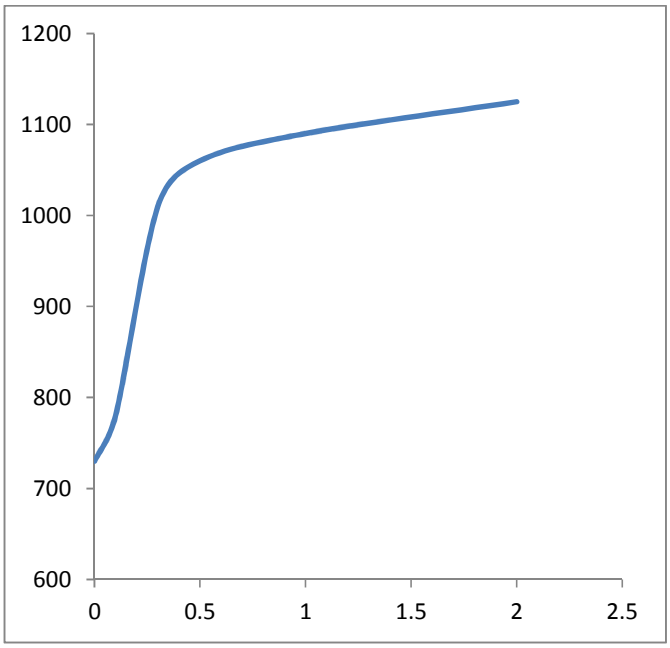

Figure 165: Redox titration curve of compound **7**. Compound **7** $(NH_4)_5K_2[Mo^{VI}_{11}V^{V}_{5}V^{IV}_{2}O_{52}(\mu_9\text{-}SeO_3)]\cdot 29H_2O$, mass used = 3 mg. Oxidant = 0.01 M Ce^{IV} in 0.5 M of sulphuric acid solution. Theoretical amount of oxidant for 2 electron reduced species in mL: 0.19. Experimental amount used in mL: 0.20.

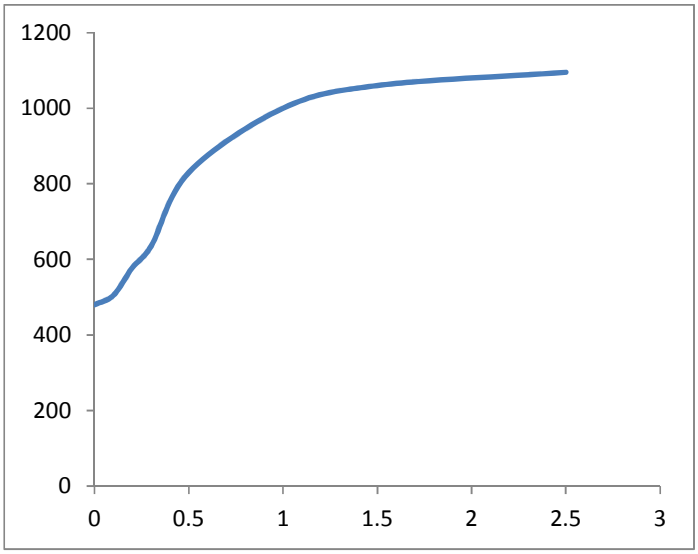

Figure 166: Redox titration curve of compound **8**. Compound **8** $(NH_4)_7K_3[Mo^{VI}_{11}V^{V}_{5}V^{IV}_{2}O_{52}(\mu_9\text{-}SeO_3)(Mo^{VI}_{6}V^{V}O_{22})]\cdot 40H_2O$, mass used = 8 mg. Oxidant = 0.01 M Ce^{IV} in 0.5 M of sulphuric acid solution. Theoretical amount of oxidant for 2 electron reduced species in mL: 0.51. Experimental amount used in mL: 0.37.

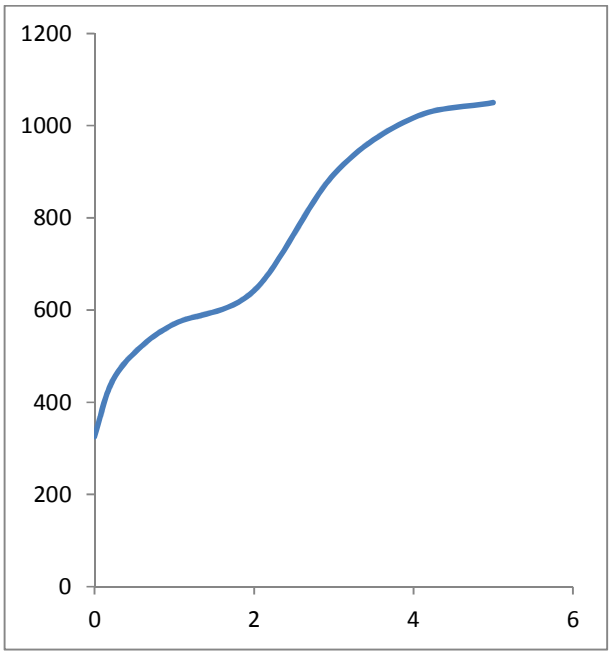

Figure 167: Redox titration curve of compound **9**. Compound **9** $(NH_4)_{19}K_3[Mo^{VI}_{20}V^{V}_{12}V^{IV}_{4}O_{99}(SeO_3)_{10}]\cdot 36H_2O$, mass used = 42 mg. Oxidant = 0.01 M Ce^{IV} in 0.5 M of sulphuric acid solution. Theoretical amount of oxidant for 4 electron reduced species in mL: 2.50. Experimental amount used in mL: 2.55.

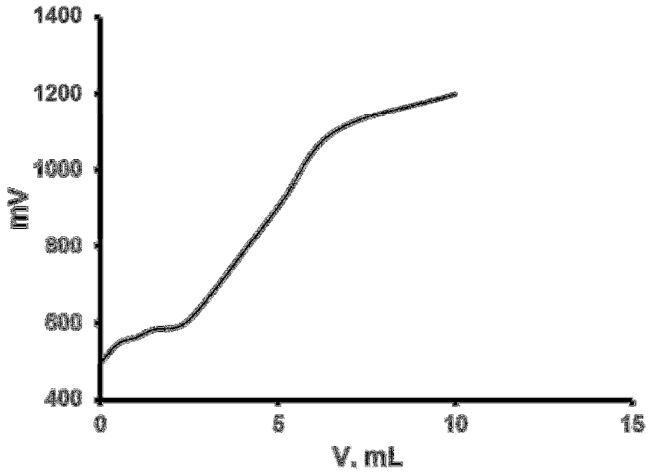

Figure 168: Redox titration curve of compound **11**. Compound **11** $(NH_4)_9K[Mo^{VI}_{12}V^{V}_{8}V^{IV}_{4}Te^{IV}O_{69}(\mu_9\text{-}Te^{IV}O_3)_2]\cdot 27H_2O$, mass used = 12 mg. Oxidant = 0.01 M Ce^{IV} in 0.5 M of sulphuric acid solution. Theoretical amount of oxidant for 4 electron reduced species in mL: 1.19. Experimental amount used in mL: 1.24.

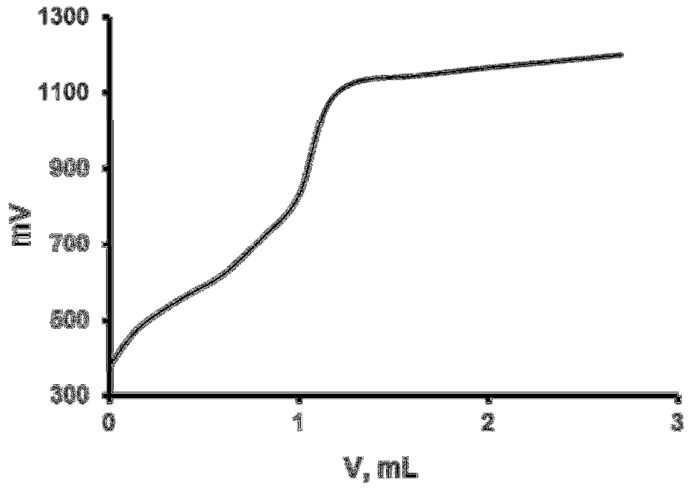

Figure 169: Redox titration curve of compound **12**. Compound **12** $K_{14}[Mo^{VI}_{12}V^{V}_{8}V^{IV}_{4}O_{69}(\mu_9\text{-}Te^{IV}O_3)_2]\cdot 27H_2O$, mass used = 50 mg. Oxidant = 0.01 M Ce^{IV} in 0.5 M of sulphuric acid solution. Theoretical amount of oxidant for 4 electron reduced species in mL: 4.7. Experimental amount used in mL: 4.55.

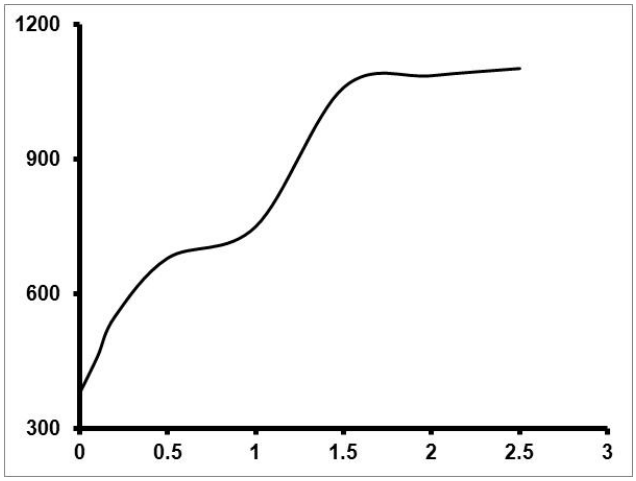

Figure 170: Redox titration curve of compound **13**. Compound **13** $K_{10}[Mo^{VI}_{11}V^{V}_{5}V^{IV}_{2}O_{52}(\mu_9\text{-}Te^{IV}O_3)(Mo^{VI}_{6}V^{V}O_{22})]\cdot 15H_2O$, mass used = 25 mg. Oxidant = 0.01 M Ce^{IV} in 0.5 M of sulphuric acid solution. Theoretical amount of oxidant for 2 electron reduced species in mL: 1.23. Experimental amount used in mL: 1.35.

6 CRYSTALLOGRAPHIC SECTION

14 single-crystal X-ray diffraction datasets are presented in this thesis. This section contains only the refinement details of each structure. For full bonding distances and angles the reader is referred to the supplementary data which is deposited with this thesis and can be obtained from the University of Glasgow. Structures were solved using Patterson or Direct methods with SHELXS-97[227] using WinGX routines.[5] Refinement was accomplished by full matrix least-squares on F^2 *via* SHELXL-97.[3] Analytical absorption corrections were done using a multi-faced crystal model based on expressions derived by R. C. Clark and J. S. Reid;[228] whereas empirical absorption corrections were done using SADABS program on expression derived by R. H. Blessing.[229] All non-hydrogen atoms were refined anisotropically unless stated otherwise. Hydrogen positions were calculated using standard geometric criteria and refined using riding model. All data manipulation and presentation steps were performed using WinGX.[5] Details about the structure refinement are given in tables. The following quantities are given in the information for each structure and were calculated as follows:

Goodness-of-fit (GooF) = $\left(\sqrt{\sum \frac{w(F_0^2 - F_c^2)^2}{(n-p)}}\right)$

Weighting scheme $w = \frac{1}{[\sigma^2(\mathrm{F}_0)^2 + (\mathrm{A}\,\mathrm{P})^2 + (\mathrm{BP})]}$ with $P = \frac{[\max(I_{obs,O}) + 2F_c^2]}{3}$

and p: number of parameters; n: number of reflection data; A, B: weighting scheme parameters

The residual factor R(int) for symmetry-equivalent reflections is defined as:

$$\mathrm{R(int)} = \frac{\Sigma\left|F_0^2 - F_c^2(mean)\right|}{\Sigma\left|F_0^2\right|}$$

Where both summations involve reflections for which more than one symmetry equivalent is averaged.

The final R-factors R1 and wR2 are defined as follows:

$$R1 = \frac{\Sigma \| F_0 | - | F_c \|}{\Sigma | F_o |} \qquad wR2 = \sqrt{\frac{\Sigma[w(F_0^2 - F_c^2)^2]}{\Sigma w(F_0^2)^2}}$$

Where both summations involve reflections for which more than one symmetry equivalent is averaged; and weighting scheme *w* is shown as above.

6.1 $(NH_4)_{10}[Mo^{VI}_{11}V^{V}_{5}V^{IV}_{2}O_{52}(\mu_9\text{-}SO_3)(Mo^{VI}_{6}V^{V}O_{22})]\cdot 14H_2O$ (2)

Identification code	**2**	
Empirical formula	$H_{68}Mo_{17}N_{10}O_{91}SV_8$	
Formula weight	3735.20	
Temperature	150(2) K	
Wavelength	0.71073 Å	
Crystal system	Orthorhombic	
Space group	*Pnma*	
Unit cell dimensions	a = 15.6986(5) Å	α = 90 º.
	b = 21.4976(3) Å	β = 90 º.
	c = 25.9861(3) Å	γ = 90 º.
Volume	8769.8(3) $Å^3$	
Z	4	
Calculated density	2.829 Mg/m^3	
Absorption coefficient	3.299 mm^{-1}	
F(000)	7120	
Crystal size	0.16 x 0.10 x 0.08 mm	
Theta range for data collection	3.14 to 26.00 º.	
Limiting indices	-10<=h<=17, -26<=k<=19, -32<=l<=31	
Reflections collected / unique	32247 / 7900 [R(int) = 0.0616]	
Completeness to theta = 26.00 º	89.2 %	
Absorption correction	Analytical	
Max. and min. transmission	0.778 and 0.620	
Refinement method	Full-matrix least-squares on F^2	
Data / restraints / parameters	7900 / 0 / 552	
Goodness-of-fit on F^2	1.036	
Final R indices [I>2sigma(I)]	R1 = 0.0544, wR2 = 0.1414	
R indices (all data)	R1 = 0.0907, wR2 = 0.1518	
Extinction coefficient	none	
Largest diff. peak and hole	1.83 and -1.71 e.$Å^{-3}$	

6.2 $K_{10}[Mo^{VI}_{12}V^{V}_{10}O_{58}(SeO_3)_8]\cdot 18H_2O$ (4)

Identification code	**4**	
Empirical formula	$H_{36}K_{10}Mo_{12}O_{100}Se_8V_{10}$	
Formula weight	4319.65	
Temperature	150(2) K	
Wavelength	1.54178 Å	
Crystal system	Monoclinic	
Space group	*C2/m*	
Unit cell dimensions	a = 37.717(2) Å	α = 90 º.
	b = 13.3912(7) Å	β = 104.169(6) º.
	c = 10.5375(6) Å	γ = 90 º.
Volume	5160.4(5) $Å^3$	
Z	2	
Calculated density	2.780 Mg/m^3	
Absorption coefficient	26.689 mm^{-1}	
F(000)	4064	
Crystal size	0.10 x 0.04 x 0.02 mm	
Theta range for data collection	3.51 to 51.68 º.	
Limiting indices	-38<=h<=38, -13<=k<=10, -10<=l<=10	
Reflections collected / unique	9505 / 2978 [R(int) = 0.0580]	
Completeness to theta = 51.68 º	98.8 %	
Absorption correction	Analytical	
Max. and min. transmission	0.661 and 0.279	
Refinement method	Full-matrix least-squares on F^2	
Data / restraints / parameters	2978 / 0 / 357	
Goodness-of-fit on F^2	1.076	
Final R indices [I>2sigma(I)]	R1 = 0.0756, wR2 = 0.1969	
R indices (all data)	R1 = 0.1087, wR2 = 0.2300	
Extinction coefficient	none	
Largest diff. peak and hole	1.83 and -1.11 e.$Å^{-3}$	

6.3 $(NH_4)_6K_4[Mo^{VI}_{12}V^{V}_{10}O_{58}(SeO_3)_8]\cdot 18H_2O$ (5)

Identification code	**5**	
Empirical formula	$H_{60}K_4Mo_{12}N_6O_{100}Se_8V_{10}$	
Formula weight	4193.30	
Temperature	150(2) K	
Wavelength	0.71073 Å	
Crystal system	Monoclinic	
Space group	*C2/c*	
Unit cell dimensions	a = 28.1611(9) Å	α = 90 º.
	b = 10.9062(3) Å	β = 105.586(4) º.
	c = 32.9468(12) Å	γ = 90 º.
Volume	9746.9(5) $Å^3$	
Z	4	
Calculated density	2.858 Mg/m^3	
Absorption coefficient	5.683 mm^{-1}	
F(000)	7936	
Crystal size	0.21 x 0.10 x 0.06 mm	
Theta range for data collection	2.94 to 24.41 º.	
Limiting indices	-32<=h<=32, -12<=k<=12, -38<=l<=38	
Reflections collected / unique	39936 / 8012 [R(int) = 0.0839]	
Completeness to theta = 24.41 º	99.7 %	
Absorption correction	Analytical	
Max. and min. transmission	0.7267 and 0.3816	
Refinement method	Full-matrix least-squares on F^2	
Data / restraints / parameters	8012 / 3 / 603	
Goodness-of-fit on F^2	0.936	
Final R indices [I>2sigma(I)]	R1 = 0.0593, wR2 = 0.1638	
R indices (all data)	R1 = 0.1130, wR2 = 0.1796	
Extinction coefficient	none	
Largest diff. peak and hole	1.76 and -1.98 e.$Å^{-3}$	

6.4 $K_7[Mo^{VI}_{11}V^{V}_{5}V^{IV}_{2}O_{52}(\mu_9\text{-}SeO_3)]\cdot 31H_2O$ (6)

Identification code	**6**	
Empirical formula	$H_{62}K_7Mo_{11}O_{86}SeV_7$	
Formula weight	3203.08	
Temperature	150(2) K	
Wavelength	1.54184 Å	
Crystal system	Tetragonal	
Space group	$P\bar{4}b2$	
Unit cell dimensions	a = 25.7061(2) Å	α = 90 °.
	b = 25.7061(2) Å	β = 90 °.
	c = 19.9182(2) Å	γ = 90 °.
Volume	13162.0(2) $Å^3$	
Z	8	
Calculated density	3.233 Mg/m^3	
Absorption coefficient	30.548 mm^{-1}	
F(000)	12320	
Crystal size	0.17 x 0.16 x 0.03 mm	
Theta range for data collection	3.29 to 67.54 °.	
Limiting indices	-30<=h<=29, -30<=k<=19, -23<=l<=23	
Reflections collected / unique	50907 / 11667 [R(int) = 0.0894]	
Completeness to theta = 67.54 °	99.8 %	
Absorption correction	Analytical	
Max. and min. transmission	0.4609 and 0.0783	
Refinement method	Full-matrix least-squares on F^2	
Data / restraints / parameters	11667 / 0 / 853	
Goodness-of-fit on F^2	1.028	
Final R indices [I>2sigma(I)]	R1 = 0.0685, wR2 = 0.1882	
R indices (all data)	R1 = 0.0826, wR2 = 0.2001	
Extinction coefficient	none	
Largest diff. peak and hole	2.07 and -2.24 e.$Å^{-3}$	

6.5 $(NH_4)_5K_2[Mo^{VI}_{11}V^{V}_{5}V^{IV}_{2}O_{52}(\mu_9\text{-}SeO_3)]\cdot 29H_2O$ (7)

Identification code	**7**
Empirical formula	$H_{74}K_3Mo_{11}N_4O_{84}SeV_7$
Formula weight	3082.81
Temperature	150(2) K
Wavelength	0.71073 Å
Crystal system	Rhombohedral
Space group	$R\bar{3}c$
Unit cell dimensions	a = 14.1424(2) Å α = 90 º. b = 14.1424(2) Å β = 90 º. c = 127.7889(4) Å γ = 120 º.
Volume	22134.5(4) $Å^3$
Z	12
Calculated density	2.775 Mg/m^3
Absorption coefficient	3.443 mm^{-1}
F(000)	17856
Crystal size	0.23 x 0.14 x 0.09 mm
Theta range for data collection	2.87 to 24.20 º.
Limiting indices	-16<=h<=15, -15<=k<=15, -146<=l<=146
Reflections collected / unique	74173 / 3839 [R(int) = 0.0434]
Completeness to theta = 24.20 º	96.7 %
Absorption correction	Analytical
Max. and min. transmission	0.7469 and 0.5048
Refinement method	Full-matrix least-squares on F^2
Data / restraints / parameters	3839 / 0 / 310
Goodness-of-fit on F^2	1.115
Final R indices [I>2sigma(I)]	R1 = 0.0513, wR2 = 0.1718
R indices (all data)	R1 = 0.0651, wR2 = 0.1792
Extinction coefficient	none
Largest diff. peak and hole	1.76 and -2.08 $e.Å^{-3}$

6.6 $(NH_4)_7K_3[Mo^{VI}_{11}V^{V}_{5}V^{IV}_{2}O_{52}(\mu_9\text{-}SeO_3)(Mo^{VI}_{6}V^{V}O_{22})]\cdot 40H_2O$ (8)

Identification code	**8**
Empirical formula	$H_{108}K_3Mo_{17}N_7O_{117}SeV_8$
Formula weight	4313.69
Temperature	150(2) K
Wavelength	1.54184 Å
Crystal system	Orthorhombic
Space group	*Pnma*
Unit cell dimensions	a = 15.4044(6) Å α = 90 º. b = 21.3761(9) Å β = 90 º. c = 25.8412(10) Å γ = 90 º.
Volume	8509.1(6) $Å^3$
Z	4
Calculated density	3.367 Mg/m^3
Absorption coefficient	30.168 mm^{-1}
F(000)	8328
Crystal size	0.16 x 0.11 x 0.10 mm
Theta range for data collection	3.34 to 62.59 º.
Limiting indices	-17<=h<=17, -24<=k<=21, -25<=l<=29
Reflections collected / unique	26149 / 6904 [R(int) = 0.0855]
Completeness to theta = 62.59 º	98.4 %
Absorption correction	Analytical
Max. and min. transmission	0.1524 and 0.0858
Refinement method	Full-matrix least-squares on F^2
Data / restraints / parameters	6904 / 0 / 624
Goodness-of-fit on F^2	1.067
Final R indices [I>2sigma(I)]	R1 = 0.0698, wR2 = 0.2041
R indices (all data)	R1 = 0.0878, wR2 = 0.2253
Extinction coefficient	none
Largest diff. peak and hole	2.25 and -2.53 e.$Å^{-3}$

6.7 $(NH_4)_{19}K_3[Mo^{VI}_{20}V^{V}_{12}V^{IV}_{4}O_{99}(SeO_3)_{10}]\cdot 36H_2O$ (9)

Identification code	**9**	
Empirical formula	$H_{148}K_3Mo_{20}N_{19}O_{165}Se_{10}V_{16}$	
Formula weight	6696.11	
Temperature	150(2) K	
Wavelength	1.54178 Å	
Crystal system	Monoclinic	
Space group	$P2_1/m$	
Unit cell dimensions	a = 16.0462(2) Å	α = 90 º.
	b = 27.9052(4) Å	β = 94.1060(10) º.
	c = 20.9112(2) Å	γ = 90 º.
Volume	9339.4(2) $Å^3$	
Z	2	
Calculated density	2.381 Mg/m^3	
Absorption coefficient	20.874 mm^{-1}	
F(000)	6412	
Crystal size	0.20 x 0.07 x 0.05 mm	
Theta range for data collection	3.18 to 65.00 º.	
Limiting indices	-18<=h<=18, -32<=k<=32, -24<=l<=24	
Reflections collected / unique	70886 / 16230 [R(int) = 0.0955]	
Completeness to theta = 65.00 º	99.9 %	
Absorption correction	Analytical	
Max. and min. transmission	0.4217 and 0.1028	
Refinement method	Full-matrix least-squares on F^2	
Data / restraints / parameters	16230 / 0 / 1074	
Goodness-of-fit on F^2	1.025	
Final R indices [I>2sigma(I)]	R1 = 0.0619, wR2 = 0.1652	
R indices (all data)	R1 = 0.0874, wR2 = 0.1862	
Extinction coefficient	none	
Largest diff. peak and hole	2.25 and -1.97 e.$Å^{-3}$	

6.8 $(NH_4)_{15}[Na_3(H_2O)_5(Mo_{11}V_7O_{52}(\mu_9\text{-}SeO_3)(Mo_5V_4O_{24}(SeO_3)_4)]\cdot 10H_2O$ (10)

Identification code	**10**	
Empirical formula	$H_{90}Mo_{16}N_{15}Na_3O_{106}Se_5V_{11}$	
Formula weight	4556.02	
Temperature	150(2) K	
Wavelength	0.71073 Å	
Crystal system	Triclinic	
Space group	$P\bar{1}$	
Unit cell dimensions	a = 14.2068(2) Å	α = 93.1140(10) º.
	b = 20.4415(4) Å	β = 93.3370(10) º.
	c = 22.2928(3) Å	γ = 105.596(2) º.
Volume	6208.57(17) $Å^3$	
Z	2	
Calculated density	2.437 Mg/m^3	
Absorption coefficient	3.927 mm^{-1}	
F(000)	4342	
Crystal size	0.36 x 0.18 x 0.04 mm	
Theta range for data collection	2.87 to 26.00 º.	
Limiting indices	-17<=h<=17, -25<=k<=25, -27<=l<=27	
Reflections collected / unique	100614 / 24407 [R(int) = 0.0721]	
Completeness to theta = 26.00 º	99.9 %	
Absorption correction	Analytical	
Max. and min. transmission	0.8587 and 0.3322	
Refinement method	Full-matrix least-squares on F^2	
Data / restraints / parameters	24407 / 0 / 1453	
Goodness-of-fit on F^2	1.068	
Final R indices [I>2sigma(I)]	R1 = 0.0666, wR2 = 0.1988	
R indices (all data)	R1 = 0.1028, wR2 = 0.2193	
Extinction coefficient	none	
Largest diff. peak and hole	2.23 and -2.02 e.$Å^{-3}$	

6.9 $(NH_4)_9K[Mo^{VI}_{12}V^{V}_{8}V^{IV}_{4}Te^{IV}O_{69}(\mu_9\text{-}TeO_3)_2]\cdot 27H_2O$ (11)

Identification code	**11**	
Empirical formula	$H_{90}KMo_{12}N_9O_{102}Te_3V_{12}$	
Formula weight	4033.27	
Temperature	150(2) K	
Wavelength	1.54184 Å	
Crystal system,	Monoclinic	
Space group	*C2/c*	
Unit cell dimensions	a = 50.9979(13) Å	α = 90 º.
	b = 13.6827(3) Å	β = 117.550(3) º.
	c = 31.7935(8) Å	γ = 90 º.
Volume	19669.5(8) $Å^3$	
Z	8	
Calculated density	2.724 Mg/m^3	
Absorption coefficient	29.639 mm^{-1}	
F(000)	15392	
Crystal size	0.31 x 0.11 x 0.09 mm	
Theta range for data collection	3.14 to 62.24 º.	
Limiting indices	-58<=h<=58, -15<=k<=14, -36<=l<=36	
Reflections collected / unique	60988 / 15368 [R(int) = 0.0812]	
Completeness to theta = 62.24 º	98.6 %	
Absorption correction	Analytical	
Max. and min. transmission	0.191 and 0.034	
Refinement method	Full-matrix least-squares on F^2	
Data / restraints / parameters	15368 / 0 / 1169	
Goodness-of-fit on F^2	1.085	
Final R indices [I>2sigma(I)]	R1 = 0.0712, wR2 = 0.1938	
R indices (all data)	R1 = 0.0877, wR2 = 0.2172	
Extinction coefficient	none	
Largest diff. peak and hole	3.03 and -1.07 e.$Å^{-3}$	

6.10 $K_{14}[Mo^{VI}_{12}V^{V}_{8}V^{IV}_{4}O_{69}(\mu_9\text{-}TeO_3)_2]\cdot 27H_2O$ (12)

Identification code	**12**	
Empirical formula	$H_{54}K_{14}Mo_{12}O_{102}Te_2V_{12}$	
Formula weight	4251.59	
Temperature	150(2) K	
Wavelength	0.71073 Å	
Crystal system	Monoclinic	
Space group	*C2/m*	
Unit cell dimensions	a = 23.2791(7) Å	α = 90 º.
	b = 13.3972(4) Å	β = 93.479(2) º.
	c = 29.3216(8) Å	γ = 90 º.
Volume	9127.8(5) $Å^3$	
Z	4	
Calculated density	3.094 Mg/m^3	
Absorption coefficient	4.153 mm^{-1}	
F(000)	8080	
Crystal size	0.28 x 0.15 x 0.03 mm	
Theta range for data collection	2.78 to 25.68 º.	
Limiting indices	-28<=h<=28, -15<=k<=16, -35<=l<=35	
Reflections collected / unique	36456 / 9042 [R(int) = 0.0745]	
Completeness to theta = 25.68 º	99.5 %	
Absorption correction	Analytical	
Max. and min. transmission	0.895 and 0.529	
Refinement method	Full-matrix least-squares on F^2	
Data / restraints / parameters	9042 / 0 / 689	
Goodness-of-fit on F^2	1.055	
Final R indices [I>2sigma(I)]	R1 = 0.0859, wR2 = 0.2250	
R indices (all data)	R1 = 0.1186, wR2 = 0.2540	
Extinction coefficient	none	
Largest diff. peak and hole	2.85 and -1.62 e.$Å^{-3}$	

6.11 $K_{10}[Mo^{VI}_{11}V^{V}_{5}V^{IV}_{2}O_{52}(\mu_9\text{-}TeO_3)(Mo^{VI}_{6}V^{V}O_{22})]\cdot 15H_2O$ (13)

Identification code	**13**	
Empirical formula	$H_{30}K_{10}Mo_{17}O_{92}TeV_8$	
Formula weight	4059.34	
Temperature	150(2) K	
Wavelength	1.54184 Å	
Crystal system	Orthorhombic	
Space group	*Pnma*	
Unit cell dimensions	a = 15.3491(2) Å	α = 90 º.
	b = 21.2977(2) Å	β = 90 º.
	c = 25.9883(2) Å	γ = 90 º.
Volume	8495.59(15) $Å^3$	
Z	4	
Calculated density	3.174 Mg/m^3	
Absorption coefficient	35.062 mm^{-1}	
F(000)	7624	
Crystal size	0.07 x 0.07 x 0.04 mm	
Theta range for data collection	3.34 to 62.49 º.	
Limiting indices	-17<=h<=17, -20<=k<=23, -29<=l<=29	
Reflections collected / unique	23939 / 6889 [R(int) = 0.0437]	
Completeness to theta = 62.49 º	98.5 %	
Absorption correction	Analytical	
Max. and min. transmission	0.376 and 0.198	
Refinement method	Full-matrix least-squares on F^2	
Data / restraints / parameters	6889 / 0 / 635	
Goodness-of-fit on F^2	1.069	
Final R indices [I>2sigma(I)]	R1 = 0.0678, wR2 = 0.1907	
R indices (all data)	R1 = 0.0840, wR2 = 0.2054	
Extinction coefficient	none	
Largest diff. peak and hole	2.86 and -2.31 e.$Å^{-3}$	

6.12 $(NH_4)_8H_2[V^V_8V^{IV}_2O_{25}(SeO_3)_4]\cdot 10H_2O$ (14)

Identification code	**14**	
Empirical formula	$H_{54}N_8O_{47}Se_4V_{10}$	
Formula weight	1743.75	
Temperature	150(2) K	
Wavelength	0.71073 Å	
Crystal system	Tetragonal	
Space group	$I\bar{4}2m$	
Unit cell dimensions	a = 20.8351(6) Å	α = 90 º.
	b = 20.8351(6) Å	β = 90 º.
	c = 21.5108(6) Å	γ = 90 º.
Volume	9337.9(5) $Å^3$	
Z	8	
Calculated density	2.481 Mg/m^3	
Absorption coefficient	5.154 mm^{-1}	
F(000)	6816	
Crystal size	0.16 x 0.10 x 0.06 mm	
Theta range for data collection	1.95 to 26.00 º.	
Limiting indices	-25<=h<=25, -23<=k<=25, -26<=l<=26	
Reflections collected / unique	20737 / 4619 [R(int) = 0.0662]	
Completeness to theta = 26.00 º	99.7 %	
Absorption correction	Empirical	
Max. and min. transmission	0.7473 and 0.4927	
Refinement method	Full-matrix least-squares on F^2	
Data / restraints / parameters	4619 / 0 / 336	
Goodness-of-fit on F^2	1.064	
Final R indices [I>2sigma(I)]	R1 = 0.0399, wR2 = 0.0960	
R indices (all data)	R1 = 0.0492, wR2 = 0.0995	
Extinction coefficient	none	
Largest diff. peak and hole	1.50 and -0.61 e.$Å^{-3}$	

6.13 $(NH_4)_6Na[V^V_7V^{IV}_5O_{27}(SeO_3)_4]\cdot 8H_2O$ (15)

Identification code	**15**	
Empirical formula	$H_{40}N_6NaO_{47}Se_4V_{12}$	
Formula weight	1826.49	
Temperature	150(2) K	
Wavelength	0.71073 Å	
Crystal system	Tetragonal	
Space group	$I\bar{4}2m$	
Unit cell dimensions	a = 20.9768(7) Å	α = 90 º.
	b = 20.9768(7) Å	β = 90 º.
	c = 21.6626(8) Å	γ = 90 º.
Volume	9532.1(6) $Å^3$	
Z	8	
Calculated density	2.545 Mg/m^3	
Absorption coefficient	5.424 mm^{-1}	
F(000)	7048	
Crystal size	0.15 x 0.12 x 0.10 mm	
Theta range for data collection	2.33 to 26.00 º.	
Limiting indices	-25<=h<=25, -25<=k<=25, -26<=l<=26	
Reflections collected / unique	72569 / 4868 [R(int) = 0.0485]	
Completeness to theta = 26.00 º	99.6 %	
Absorption correction	Empirical	
Max. and min. transmission	0.6131 and 0.4967	
Refinement method	Full-matrix least-squares on F^2	
Data / restraints / parameters	4868 / 0 / 315	
Goodness-of-fit on F^2	1.068	
Final R indices [I>2sigma(I)]	R1 = 0.0487, wR2 = 0.1514	
R indices (all data)	R1 = 0.0502, wR2 = 0.1529	
Extinction coefficient	none	
Largest diff. peak and hole	1.63 and -2.42 $e.Å^{-3}$	

6.14 $(NH_4)_5[Co(OH_2)_3V^{V}_9V^{IV}O_{25}(SeO_3)_4]\cdot 15H_2O$ (16)

Identification code	**16**	
Empirical formula	$H_{56}CoN_5O_{55}Se_4V_{10}$	
Formula weight	1890.67	
Temperature	150(2) K	
Wavelength	0.71073 Å	
Crystal system	Monoclinic	
Space group	$P2_1/m$	
Unit cell dimensions	a = 14.2240(9) Å	α = 90 º.
	b = 18.4971(12) Å	β = 102.403(3) º.
	c = 19.7416(12) Å	γ = 90 º.
Volume	5072.8(6) $Å^3$	
Z	4	
Calculated density	2.476 Mg/m^3	
Absorption coefficient	5.076 mm^{-1}	
F(000)	3696	
Crystal size	0.14 x 0.10 x 0.05 mm	
Theta range for data collection	2.11 to 26.00 º.	
Limiting indices	-17<=h<=17, -22<=k<=22, -24<=l<=24	
Reflections collected / unique	142318 / 9972 [R(int) = 0.0412]	
Completeness to theta = 26.00 º	99.9 %	
Absorption correction	Empirical	
Max. and min. transmission	0.7854 and 0.5368	
Refinement method	Full-matrix least-squares on F^2	
Data / restraints / parameters	9972 / 0 / 662	
Goodness-of-fit on F^2	1.090	
Final R indices [I>2sigma(I)]	R1 = 0.0305, wR2 = 0.0788	
R indices (all data)	R1 = 0.0355, wR2 = 0.0827	
Extinction coefficient	none	
Largest diff. peak and hole	0.90 and -0.70 $e.Å^{-3}$	

7 APPENDIX

7.1 Atom numbering for compound 1

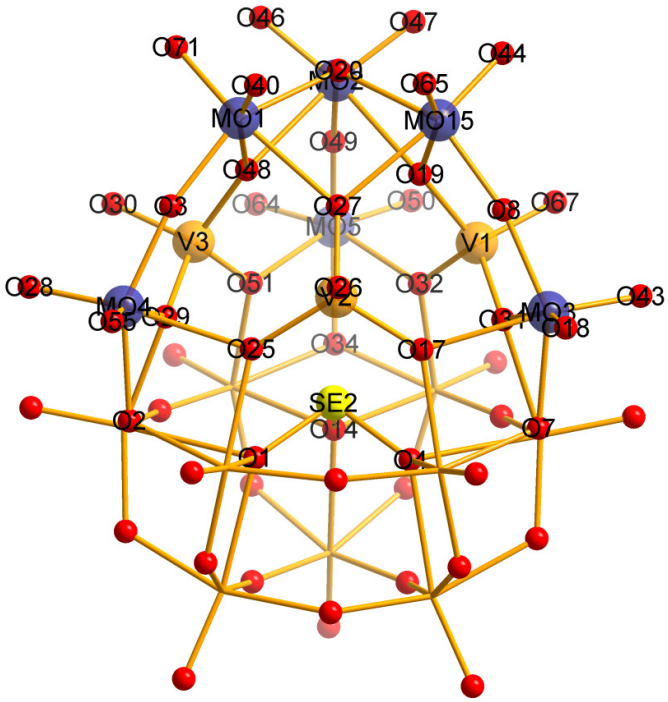

Figure 171: Atom numbering scheme for compound **1**.

7.2 Bond-valence sum for compound 2

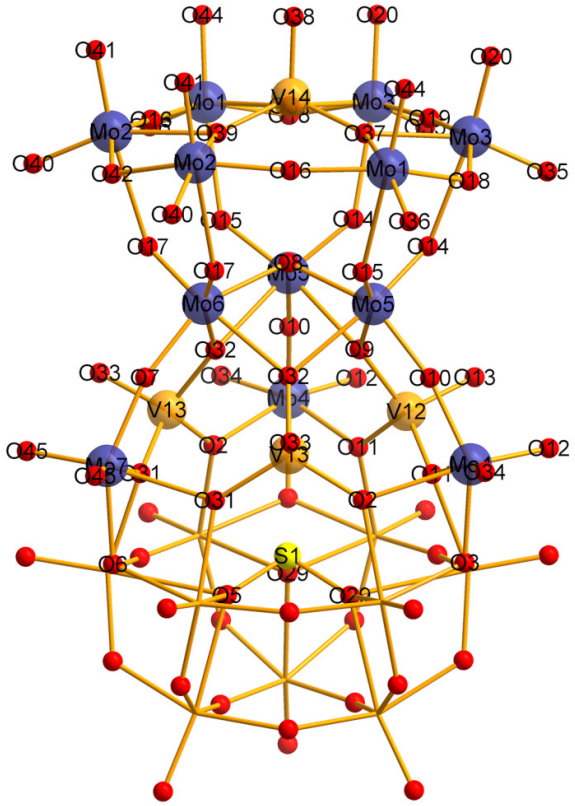

Figure 172: Atom numbering scheme for compound **2**.

Table 25: Bond-valence sum calculation for the non-disordered atoms in **2**.

Atom	BVS	Atom	BVS
Mo1	5.85	V12	5.01
Mo2	5.91	V13	4.73
Mo3	5.90	V14	4.65
Mo4	5.98		
Mo5	6.08		
Mo6	6.04		
Mo7	5.90		

7.3 Bond-valence sum for compound 4

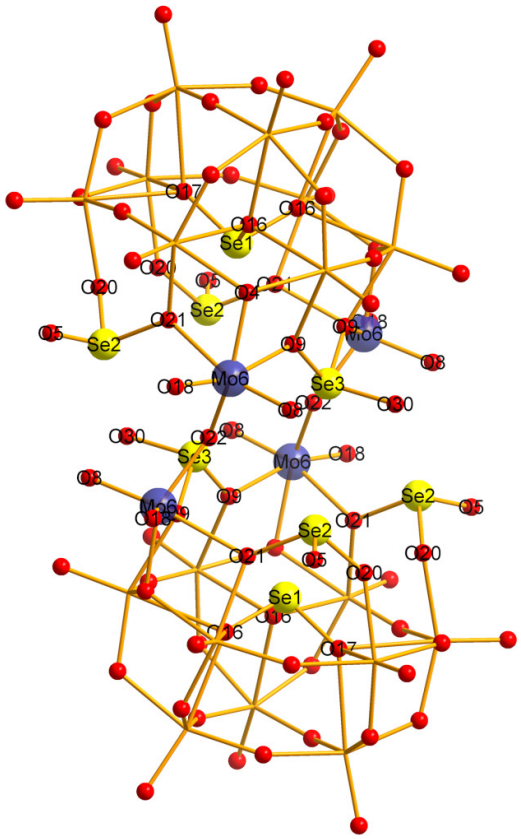

Figure 173: Atom numbering scheme for compound **4**.

Table 256: Bond-valence sum calculation for the non-disordered atoms in **4**.

Atom	BVS
Mo6	5.79
Se1	3.90
Se2	4.07
Se3	3.90

7.4 Bond-valence sum for compound 5

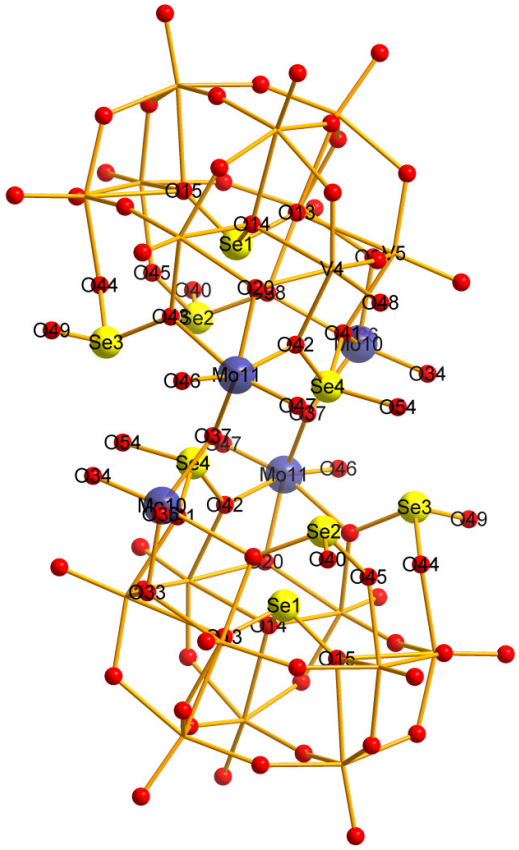

Figure 174: Atom numbering scheme for compound **5**.

Table 27: Bond-valence sum calculation for the non-disordered atoms in **5**.

Atom	BVS
Mo10	5.93
Mo11	6.07
Se1	4.00
Se2	4.05
Se3	4.08
Se4	3.66

7.5 Bond-valence sum for compound 6

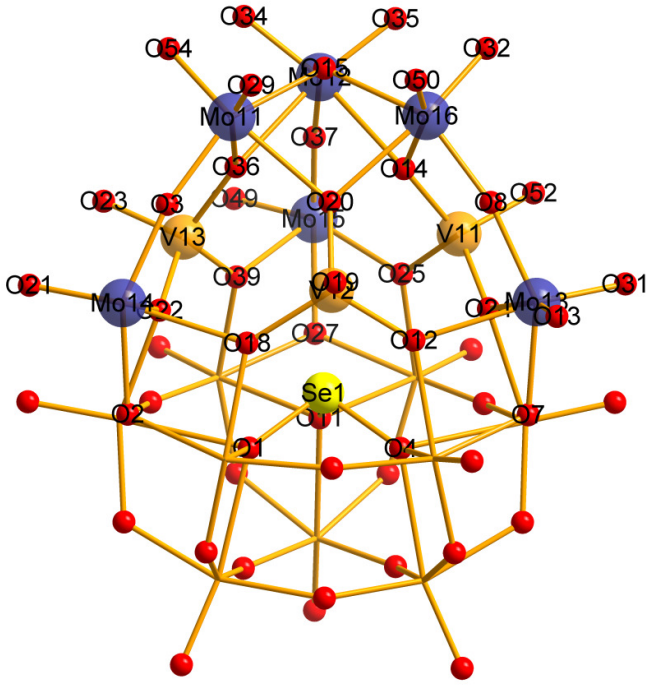

Figure 175: Atom numbering scheme for compound **6**.

Table 28: Bond-valence sum calculation for the non-disordered atoms in **6**.

Atom	BVS	Atom	BVS
Mo11	6.07	V11	5.51
Mo12	5.95	V12	5.25
Mo13	5.89	V13	5.20
Mo14	5.84		
Mo15	6.24		
Mo16	5.96		

7.6 Bond-valence sum for compound 7

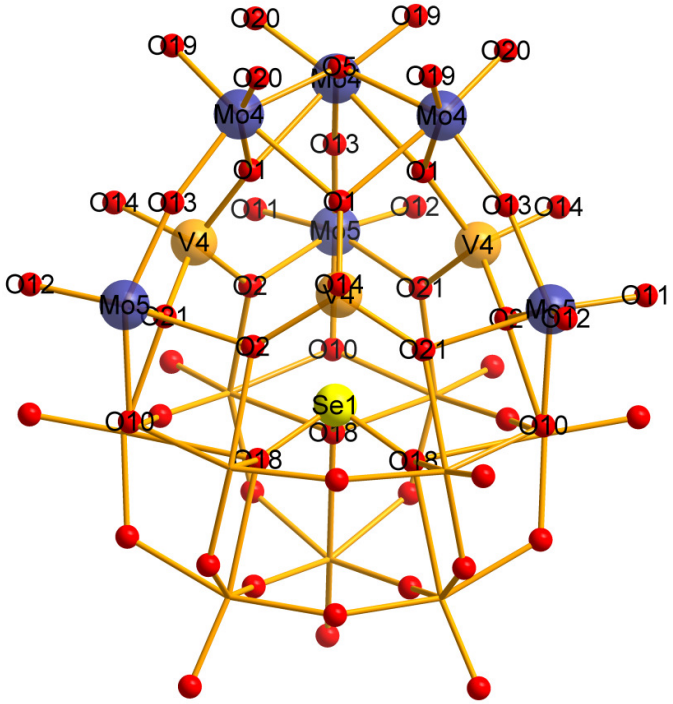

Figure 176: Atom numbering scheme for compound **7**.

Table 29: Bond-valence sum calculation for the non-disordered atoms in **7**.

Atom	BVS
Mo4	5.80
Mo5	5.90
V4	5.19

7.7 Bond-valence sum for compound 8

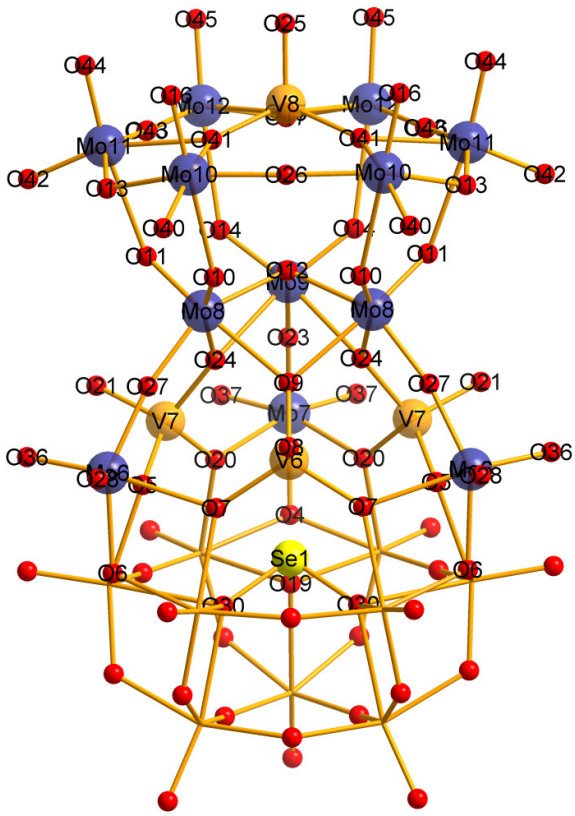

Figure 177: Atom numbering scheme for compound **8**.

Table 30: Bond-valence sum calculation for the non-disordered atoms in **8**.

Atom	BVS	Atom	BVS
Mo6	6.27	V6	5.19
Mo7	6.12	V7	5.03
Mo8	6.28	V8	5.21
Mo9	6.13		
Mo10	6.08		
Mo11	6.05		
Mo12	5.88		

7.8 Bond-valence sum for compound 9

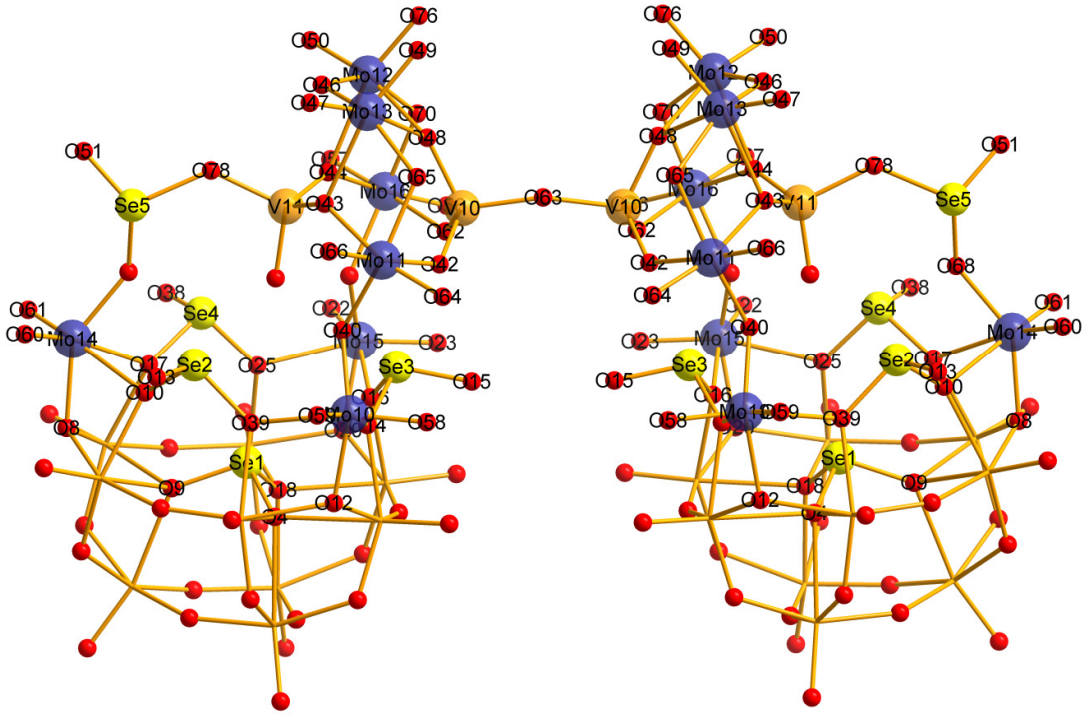

Figure 178: Atom numbering scheme for compound **9**.

Table 31: Bond-valence sum calculation for the non-disordered atoms in **9**.

Atom	BVS	Atom	BVS
Mo10	5.95	V10	5.29
Mo11	6.01	V11	5.01
Mo12	6.00	Se1	3.99
Mo13	5.81	Se2	3.97
Mo14	5.91	Se3	3.85
Mo15	5.91	Se4	3.89
Mo16	6.07	Se5	3.89

7.9 Bond-valence sum for compound 10

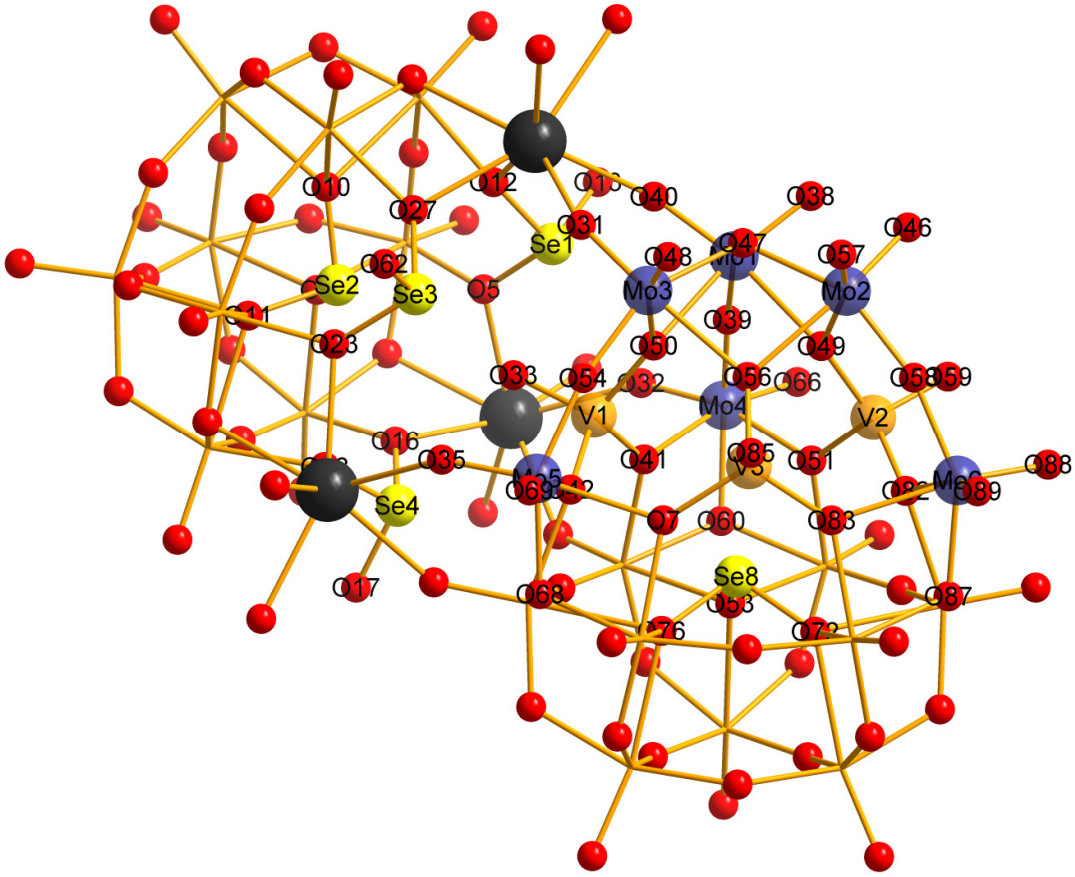

Figure 179: Atom numbering scheme for compound **10**.

Table 32: Bond-valence sum calculation for the non-disordered atoms in **10**.

Atom	BVS	Atom	BVS
Mo1	6.00	V2	5.07
Mo2	5.91	V3	5.17
Mo3	5.98	Se1	3.95
Mo4	6.10	Se2	4.01
Mo5	5.91	Se3	3.93
Mo6	5.84	Se4	3.94
V1	5.03	Se8	3.99

7.10 Bond-valence sum for compound 11

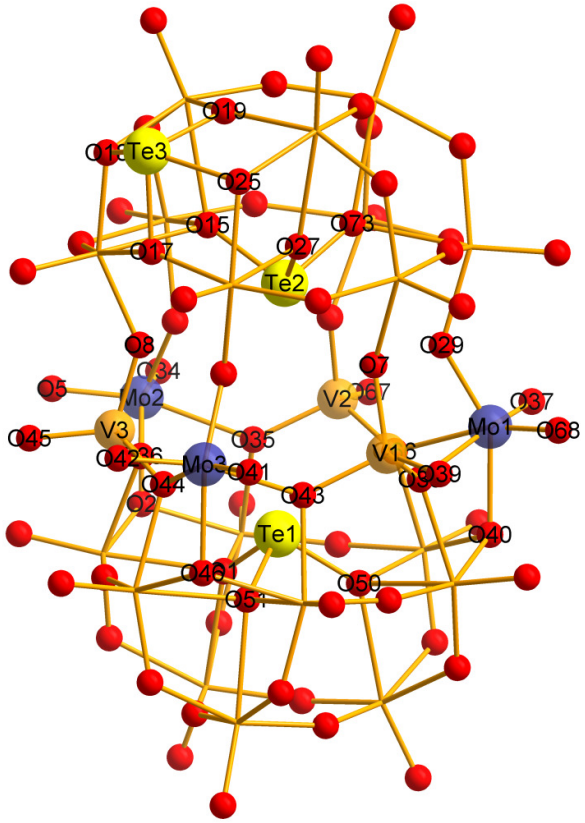

Figure 180: Atom numbering scheme for compound **11**.

Table 33: Bond-valence sum calculation for the non-disordered atoms in **11**.

Atom	BVS	Atom	BVS
Mo1	5.89	V3	5.05
Mo2	5.92	Te1	4.73
Mo3	5.87	Te2	4.51
V1	5.07	Te3	4.15
V2	5.22		

7.11 Bond-valence sum for compound 12

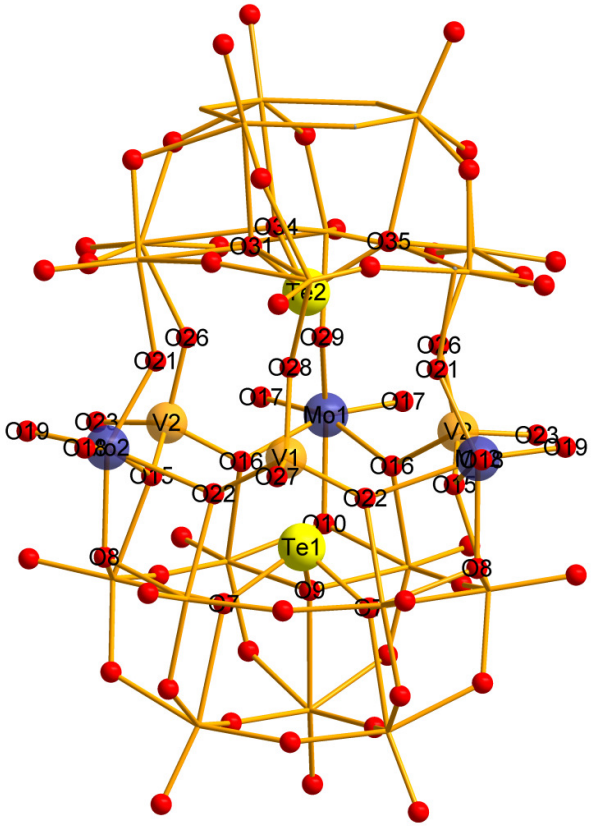

Figure 181: Atom numbering scheme for compound **12**.

Table 34: Bond-valence sum calculation for the non-disordered atoms in **12**.

Atom	BVS
Mo1	5.82
Mo2	5.73
V1	4.93
V2	5.17
Te1	4.55
Te2	4.54

7.12 Bond-valence sum for compound 13

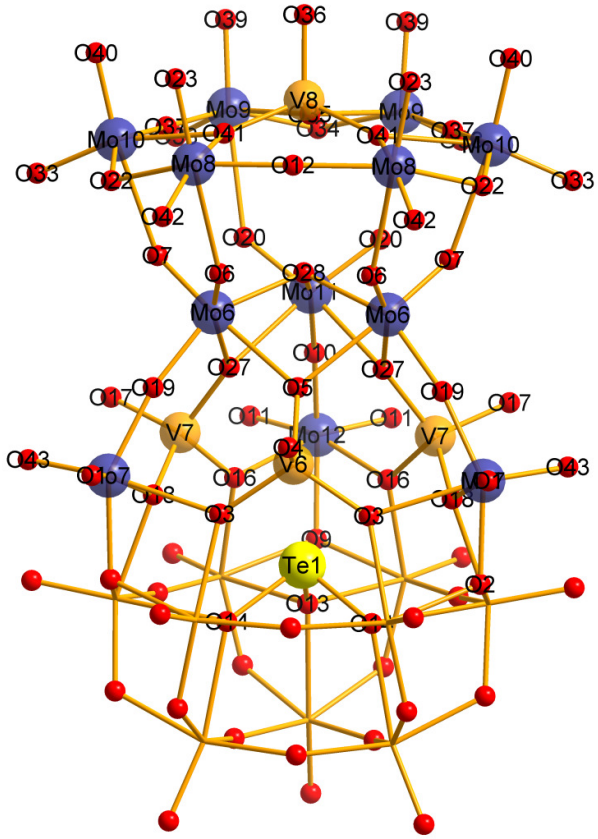

Figure 182: Atom numbering scheme for compound **13**.

Table 35: Bond-valence sum calculation for the non-disordered atoms in **13**.

Atom	BVS	Atom	BVS
Mo6	6.14	V6	5.08
Mo7	6.30	V7	5.16
Mo8	5.74	V8	4.85
Mo9	5.97		
Mo10	5.72		
Mo11	6.24		
Mo12	6.02		

7.13 Bond-valence sum for compound 14

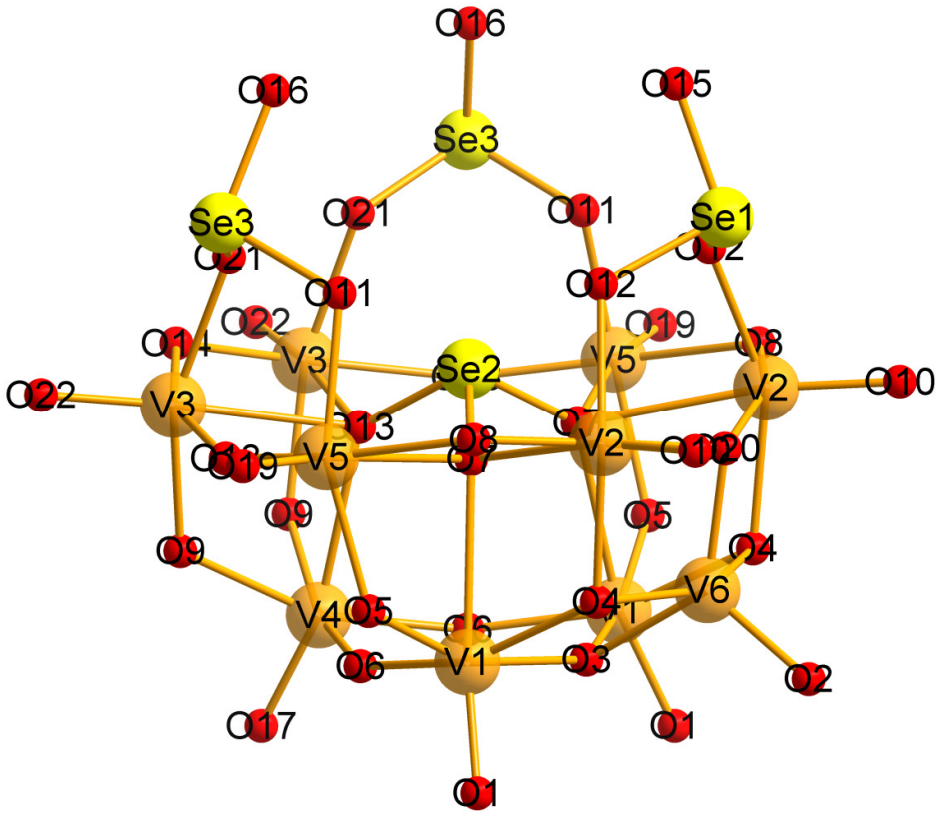

Figure 183: Atom numbering scheme for compound **14**.

Table 36: Bond-valence sum calculation for the non-disordered atoms in **14**.

Atom	BVS	Atom	BVS
V1	4.89	Se1	3.87
V2	4.79	Se2	4.04
V3	4.87	Se3	3.93
V4	4.90		
V5	4.86		
V6	4.65		

7.14 Bond-valence sum for compound 15

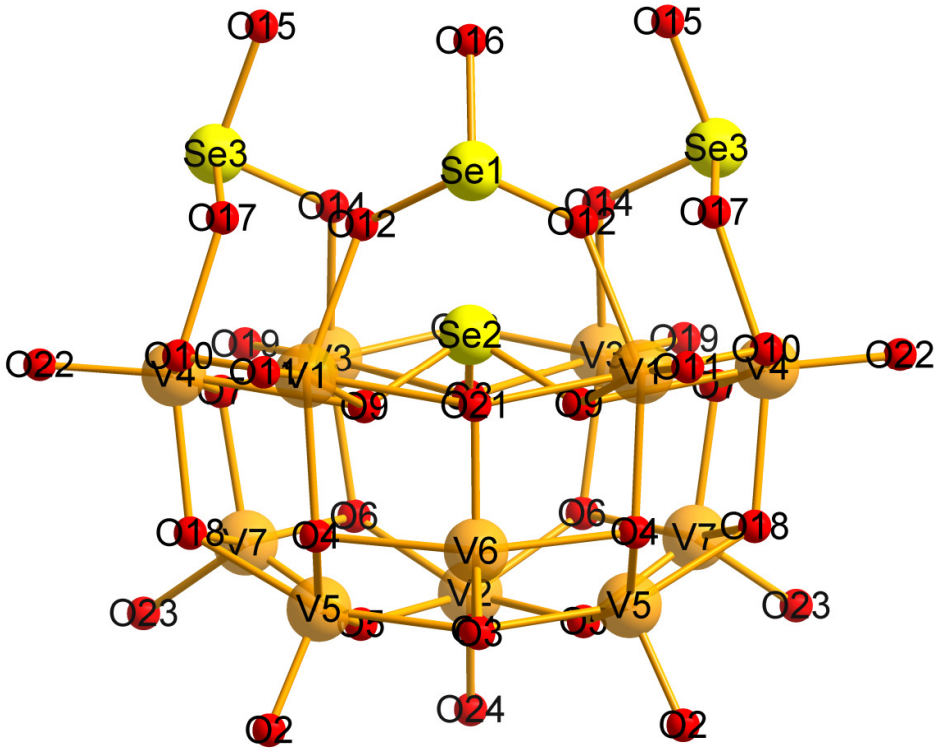

Figure 184: Atom numbering scheme for compound **15**.

Table 37: Bond-valence sum calculation for the non-disordered atoms in **15**.

Atom	BVS	Atom	BVS
V1	4.63	Se1	3.99
V2	4.74	Se2	4.17
V3	4.70	Se3	4.05
V4	4.48		
V5	4.54		
V6	4.67		
V7	3.79		

7.15 Bond-valence sum for compound 16

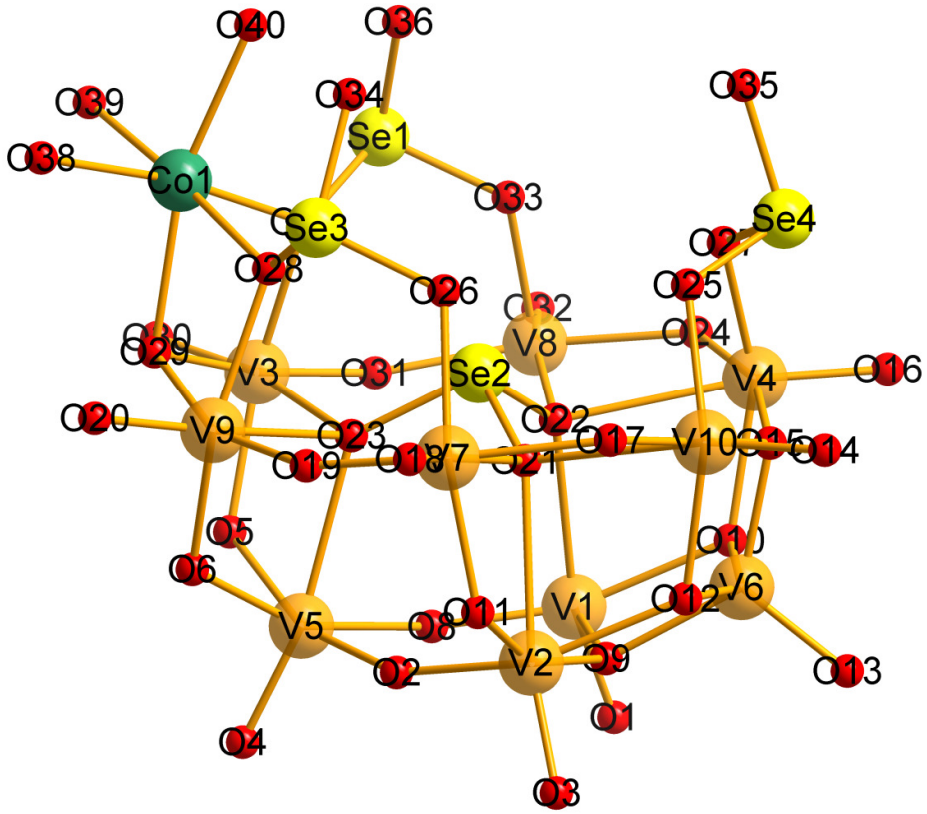

Figure 185: Atom numbering scheme for compound **16**.

Table 38: Bond-valence sum calculation for the non-disordered atoms in **16**.

Atom	BVS	Atom	BVS
V1	4.85	V9	4.76
V2	4.78	V10	4.82
V3	4.79	Co1	2.05
V4	4.80	Se1	3.92
V5	4.74	Se2	3.92
V6	5.04	Se3	4.00
V7	4.48	Se4	3.94
V8	4.17		

8 REFERENCES

[1] A. Müller, M. Koop, H. Bogge, M. Schmidtmann, F. Peters and P. Kogerler, *Chem. Comm.* **1999**, 1885-1886.

[2] D.-L. Long, R. Tsunashima and L. Cronin, *Angew. Chem., Int. Ed.* **2010**, *49*, 1736-1758.

[3] D.-L. Long, E. Burkholder and L. Cronin, *Chem. Soc. Rev* **2007**, *36*, 105-121.

[4] M. T. Pope and A. Müller, *Angew. Chem. Int. Ed. Engl.* **1991**, *30*, 34-48.

[5] L. Farrugia, *J. Appl. Cryst.* **1999**, *32*, 837-838.

[6] C. L. Hill, *Chem. Rev.* **1998**, *98*, 1-2.

[7] D.-L. Long and L. Cronin, *Chem. Eur. J.* **2006**, *12*, 3698-3706.

[8] M. I. Khan, *J. Solid State Chem.* **2000**, *152*, 105-112.

[9] H. Ma, J. Peng, Z. Han, X. Yu and B. Dong, *J. Solid State Chem.* **2005**, *178*, 3735-3739.

[10] M. V. Vasylyev and R. Neumann, *J. Am. Chem. Soc.* **2003**, *126*, 884-890.

[11] K. Kamata, K. Yonehara, Y. Sumida, K. Yamaguchi, S. Hikichi and N. Mizuno, *Science* **2003**, *300*, 964-966.

[12] J. J. Berzelius, *Poggendorfs Ann. Phys. Chem.* **1826**, *6*, 369.

[13] C. Marignac, *Ann. Chim. Phys.* **1864**, *3*, 1.

[14] M. T. Pope, *Heteropoly and Isopoly Oxometalates*, Springer-Verlag, Berlin Heidelberg New York Tokyo, **1983**.

[15] L. Pauling, *J. Am. Chem. Soc.* **1929**, *51*, 2868-2880.

[16] J. F. Keggin, *Nature (London)* **1933**, *131*, 908.

[17] J. F. Keggin, *Proc. R. Soc. London Ser. A* **1934**, *144*, 75-100.

[18] R. J. Errington, S. S. Petkar, B. R. Horrocks, A. Houlton, L. H. Lie and S. N. Patole, *Angew. Chem. Int. Ed.* **2005**, *44*, 1254-1257.

[19] I. M. Mbomekalle, B. Keita, L. Nadjo, P. Berthet, K. I. Hardcastle, C. L. Hill and T. M. Anderson, *Inorg. Chem.* **2003**, *42*, 1163-1169.

[20] D. Volkmer, B. Bredenkötter, J. Tellenbröker, P. Kögerler, D. G. Kurth, P. Lehmann, H. Schnablegger, D. Schwahn, M. Piepenbrink and B. Krebs, *J. Am. Chem. Soc.* **2002**, *124*, 10489-10496.

[21] E. Coronado, C. Giménez-Saiz and C. J. Gómez-García, *Coord. Chem. Rev.* **2005**, *249*, 1776-1796.

[22] G. Chaidogiannos, D. Velessiotis, P. Argitis, P. Koutsolelos, C. D. Diakoumakos, D. Tsamakis and N. Glezos, *Microelectron. Eng.* **2004**, *73-74*, 746-751.

[23] S. Liu, H. Möhwald, D. Volkmer and D. G. Kurth, *Langmuir* **2006**, *22*, 1949-1951.

[24] M. Luban, F. Borsa, S. Bud'ko, P. Canfield, S. Jun, J. K. Jung, P. Kögerler, D. Mentrup, A. Müller, R. Modler, D. Procissi, B. J. Suh and M. Torikachvili, *Phys. Rev. B: Condens. Matter* **2002**, *66*, 054407.

[25] H. N. Miras, E. F. Wilson and L. Cronin, *Chem. Commun.* **2009**, 1297-1311.

[26] M. T. Pope, A. Mueller and Editors, *Polyoxometalate Chemistry From Topology via Self-Assembly to Applications*, Kluwer Academic Publishers, **2001**.

[27] M. I. Khan, Q. Chen and J. Zubieta, *Inorg. Chem.* **1993**, *32*, 2924-2928.

[28] P. J. Hagrman, D. Hagrman and J. Zubieta,'Perspectives in the solid state coordination chemistry of the molybdenum oxides' in *Polyoxometalate Chemistry From Topology via Self-Assembly to Applications* (Eds.: M. T. Pope, A. Müller), Kluwer Academic Publishers, Dordrecht, The Netherlands, **2001**, pp. 269-300.

[29] M. I. Khan, Q. Chen and J. Zubieta, *Inorg. Chim. Acta* **1993**, *212*, 199-206.

[30] C. J. Warren, D. J. Rose, R. C. Haushalter and J. Zubieta, *Inorg. Chem.* **1998**, *37*, 1140-1141.

[31] E. Burkholder and J. Zubieta, *Inorg. Chim. Acta* **2004**, *357*, 301-304.

[32] H. Ichida and Y. Sasaki, *Acta Cryst.* **1983**, *39*, 529-533.

[33] D.-L. Long, P. Koegerler, L. J. Farrugia and L. Cronin, *Angew. Chem., Int. Ed.* **2003**, *42*, 4180-4183.

[34] C. P. Pradeep, D.-L. Long and L. Cronin, *Dalton Trans.* **2010**, *39*, 9443-9457.

[35] H. N. Miras, J. Yan, D.-L. Long and L. Cronin, *Angew. Chem. Int. Ed.* **2008**, *47*, 8420-8423.

[36] J. Yan, D.-L. Long, E. F. Wilson and L. Cronin, *Angew. Chem. Int. Ed.* **2009**, *48*, 4376-4380.

[37] H. N. Miras, G. J. T. Cooper, D.-L. Long, H. Bögge, A. Müller, C. Streb and L. Cronin, **2010**, *327*, 72-74.

[38] W. Clegg, G. M. Sheldrick, C. D. Garner and I. B. Walton, *Acta Cryst. B* **1982**, *38*, 2906-2909.

[39] J. Fuchs, W. Freiwald and H. Hartl, *Acta Cryst. B* **1978**, *34*, 1764-1770.

[40] B. Dawson, *Acta Cryst.* **1953**, *6*, 113-126.

[41] A. Müller, E. Krickemeyer, J. Meyer, H. Bögge, F. Peters, W. Plass, E. Diemann, S. Dillinger, F. Nonnenbruch, M. Randerath and C. Menke, *Angew. Chem. Int. Ed. Eng.* **1995**, *34*, 2122-2124.

[42] A. Müller, F. Peters, M. T. Pope and D. Gatteschi, *Chem. Rev.* **1998**, *98*, 239-272.

[43] W. G. Klemperer, T. A. Marquart and O. M. Yaghi, *Angew. Chem. Int. Ed. Engl.* **1992**, *31*, 49-51.

[44] J. Fuchs, S. Mahjour and J. Pickardt, *Angew. Chem. Int. Ed. Engl.* **1976**, *15*, 374-375.

[45] V. W. Day, W. G. Klemperer and O. M. Yaghi, *J. Am. Chem. Soc.* **1989**, *111*, 4518-4519.

[46] H. T. Evans, *Inorg. Chem.* **1966**, *5*, 967-977.

[47] V. W. Day, W. G. Klemperer and O. M. Yaghi, *J. Am. Chem. Soc.* **1989**, *111*, 5959-5961.

[48] D. Hou, K. S. Hagen and C. L. Hill, *J. Am. Chem. Soc.* **1992**, *114*, 5864-5866.

[49] D.-L. Long, D. Orr, G. Seeber, P. Kögerler, L. J. Farrugia and L. Cronin, *J. Cluster Sci.* **2003**, *14*, 313-324.

[50] Y. Hayashi, K. Fukuyama, T. Takatera and A. Uehara, **2000**, *29*, 770-771.

[51] A. Müller, M. Penk, E. Krickemeyer, H. Bögge and H.-J. Walberg, *Angew. Chem. Int. Ed. Engl.* **1988**, *27*, 1719-1721.

[52] A. Müller, M. Penk, R. Rohlfing, E. Krickemeyer and J. Döring, *Angew. Chem. Int. Ed. Engl.* **1990**, *29*, 926-927.

[53] A. Müller, E. Krickemeyer, M. Penk, R. Rohlfing, A. Armatage and H. Bögge, *Angew. Chem. Int. Ed. Engl.* **1991**, *30*, 1674-1677.

[54] B. Dong, C. J. Gómez-García, J. Peng, S. Benmansour and J. Ma, **2007**, *26*, 1310-1316.

[55] A. Müller, R. Rohlfing, J. Döring and M. Penk, *Angew. Chem. Int. Ed. Engl.* **1991**, *30*, 588-590.

[56] Z. Zheng, A. S. Juodawlkis, S. S. Wirtz, R. F. Schinazi, H. Zeng, C. Bellavia, F. Wudl and C. L. Hill, *Proc. - Electrochem. Soc.* **1998**, *98-8*, 1222-1226.

[57] J. Livage, *J. Chem. Mater.* **1991**, *3*, 578-593.

[58] A. R. Raju and C. N. R. Rao, *J. Chem. Soc., Chem. Commun.* **1991**, 1260-1261.

[59] A. L. Rheingold, C. B. White, B. S. Haggerty and E. A. Maatta, *Acta Cryst.* **1993**, *49*, 756-758.

[60] I. Lindqvist, *Acta. Cryst.* **1950**, *3*, 159-160.

[61] J. Fuchs and H. Hartl, *Angew. Chem. Int. Ed. Engl.* **1976**, *15*, 375-376.

[62] T. Yamase, *J. Chem. Soc. Dalton Trans.* **1985**, 2585-2590.

[63] B. Krebs and I. Paulat-Boschen, *Acta Cryst.* **1982**, *38*, 1710-1718.

[64] M. I. Khan, A. Müller, S. Dillinger, H. Bögge, Q. Chen and J. Zubieta, *Angew. Chem. Int. Ed. Engl.* **1993**, *32*, 1780-1782.

[65] D.-L. Long, P. Kögerler, L. J. Farrugia and L. Cronin, *Angew. Chem. Int. Ed.* **2003**, *42*, 4180-4183.

[66] W. N. Lipscomb, *Inorg. Chem.* **1965**, *4*, 132-134.

[67] J. Fuchs, R. Palm and H. Hartl, *Angew. Chem. Int. Ed.* **1996**, *35*, 2651-2653.

[68] R. Bhattacharyya, S. Biswas, J. Armstrong and E. M. Holt, *Inorg. Chem.* **1989**, *28*, 4297-4300.

[69] H. Hartl, R. Palm and J. Fuchs, *Angew. Chem. Int. Ed.* **1993**, *32*, 1492-1494.

[70] J. J. Hastings and O. W. Howarth, *J. Chem. Soc. Dalton Trans.* **1992**, 209-215.

[71] J. Fuchs, H. Hartl, W. Schiller and U. Gerlach, *Acta Cryst.* **1976**, *32*, 740-749.

[72] T. Lehmann and J. Z. HFuchs, *Z. Naturforsch. B* **1988**, *43*, 89.

[73] R. Signer and H. Gross, *Helvetica Chim. Acta.* **1934**, *17*, 1076-1080.

[74] R. Allmann, *Acta Crystallogr., Sect. B* **1971**, *27*, 1393.

[75] I. Brüdgam, J. Fuchs, H. Hartl and R. Palm, *Angew. Chem. Int. Ed.* **1998**, *37*, 2668-2671.

[76] D.-L. Long, H. Abbas, P. Kögerler and L. Cronin, *J. Am. Chem. Soc.* **2004**, *126*, 13880-13881.

[77] D.-L. Long, P. Kögerler, A. D. C. Parenty, J. Fielden and L. Cronin, *Angew. Chem. Int. Ed.* **2006**, *45*, 4798-4803.

[78] A. Björnberg, *Acta Cryst.* **1979**, *35*, 1995-1999.

[79] M. Cindrić, N. Strukan and B. Kamenar, *Polyhedron* **1999**, *18*, 2781-2785.

[80] M. Cindric´, N. Strukan, Z. Veksli and B. Kamenar, *Polyhedron* **1996**, *15*, 2121-2126.

[81] Q.-Z. Zhang, C.-Z. Lu, W.-B. Yang, C.-D. Wu, Y.-Q. Yu, Y. Yan, J.-H. Liu and X. He, *J. Cluster Sci.* **2003**, *14*, 381-390.

[82] D.-D. Liang, S.-X. Liu, Y.-H. Ren, C.-D. Zhang and L. Xu, *Inorg. Chem. Commun.* **2007**, *10*, 933-935.

[83] M. Ishaque Khan, S. Cevik and R. Hayashi, *J. Chem. Soc., Dalton Trans.* **1999**, 1651-1654.

[84] C. Wang, L. Weng, Y. Ren, C. Du, B. Yue, M. Gu and H. He, *Z. Anorg. Allg. Chem.* **2011**, *637*, 472-477.

[85] H. N. Miras, D.-L. Long, P. Kogerler and L. Cronin, *Dalton Trans.* **2008**, 214-221.

[86] I. A. Weinstock, J. J. Cowan, E. M. G. Barbuzzi, H. Zeng and C. L. Hill, *J. Am. Chem. Soc.* **1999**, *121*, 4608-4617.

[87] C. Hu, M. Hashimoto, T. Okuhara and M. Misono, *J. Catal.* **1993**, *143*, 437-448.

[88] I. V. Kozhevnikov, K. R. Kloetstra, A. Sinnema, H. W. Zandbergen and B. H. van, *J. Mol. Catal. A: Chem.* **1996**, *114*, 287-298.

[89] X. Lopez, C. Bo and J. M. Poblet, *J. Am. Chem. Soc.* **2002**, *124*, 12574-12582.

[90] C. Rocchiccioli-Deltcheff, M. Fournier, R. Franck and R. Thouvenot, *Inorg. Chem.* **1983**, *22*, 207-216.

[91] M. Sadakane and E. Steckhan, *Chem. Rev. (Washington, D. C.)* **1998**, *98*, 219-237.

[92] G. Herve and A. Teze, *Inorg. Chem.* **1977**, *16*, 2115-2117.

[93] L. E. Briand, G. T. Baronetti and H. J. Thomas, **2003**, *256*, 37-50.

[94] L. C. W. Baker and J. S. Figgis, *J. Am. Chem. Soc.* **1970**, *92*, 3794-3797.

[95] R. Contant and R. Thouvenot, **1993**, *212*, 41-50.

[96] F.-Q. Zhang, W. Guan, L.-K. Yan, Y.-T. Zhang, M.-T. Xu, E. Hayfron-Benjamin and Z.-M. Su, *Inorg. Chem.* **2011**, *50*, 4967-4977.

[97] A. Durif and M. T. Averbuch-Pouchot, *Acta Cryst.* **1979**, *35*, 1441-1444.

[98] M. I. Khan, J. Zubieta and P. Toscano, **1992**, *193*, 17-20.

[99] G.-Q. Huang, S.-W. Zhang, Y.-G. Wei and M.-C. Shao, **1993**, *12*, 1483-1485.

[100] K. Nomiya, T. Takahashi, T. Shirai and M. Miwa, *Polyhedron* **1987**, *6*, 213-218.

[101] G. Rozantsev, S. Radio, N. Gumerova, V. Baumer and O. Shishkin, *J. StrucT. Chem.* **2009**, *50*, 296-305.

[102] A. Perloff, *Inorg. Chem.* **1970**, *9*, 2228-2239.

[103] A. L. Nolan, R. C. Burns, G. A. Lawrance and D. C. Craig, *Acta Crystllogr. C* **2000**, *56*, 729-730.

[104] P. A. Lorenzo-Luis, P. Gili, A. Sánchez, E. Rodriguez-Castellón, J. Jiménez-Jiménez, C. Ruiz-Pérez and X. Solans, *Trans. Metal Chem.* **1999**, *24*, 686-692.

[105] D. Honda, S. Ikegami, T. Inoue, T. Ozeki and A. Yagasaki, *Inorg. Chem.* **2007**, *46*, 1464-1470.

[106] U. Lee, A. Kobayashi and Y. Sasaki, *Acta Crystallogr., Sect. C: Cryst. Struct. Commun.* **1983**, *C39*, 817-819.

[107] I. L. Botto, A. C. Garcia and H. J. Thomas, *J. Phys. Chem. Solids* **1992**, *53*, 1075-1080.

[108] C. I. Cabello, I. L. Botto, F. Cabrerizo, M. G. Gonzalez and H. J. Thomas, *Adsorpt. Sci. Technol.* **2000**, *18*, 591-608.

[109] V. Shivaiah, R. P. V. Narasimha, L. Cronin and S. K. Das, *J. Chem. Soc., Dalton Trans.* **2002**, 3781-3782.

[110] H. An, D. Xiao, E. Wang, C. Sun, Y. Li and L. Xu, *J. Mol. Struct.* **2005**, *751*, 184-189.

[111] H. An, Y. Li, D. Xiao, E. Wang and C. Sun, *Cryst. Growth Des.* **2006**, *6*, 1107-1112.

[112] Y.-F. Song, H. Abbas, C. Ritchie, N. McMillian, D.-L. Long, N. Gadegaard and L. Cronin, *J. Mater. Chem.* **2007**, *17*, 1903-1908.

[113] T. Kurata, A. Uehara, Y. Hayashi and K. Isobe, *Inorg. Chem.* **2005**, *44*, 2524-2530.

[114] S. Inami, M. Nishio, Y. Hayashi, K. Isobe, H. Kameda and T. Shimoda, *Eur. J. Inorg. Chem.* **2009**, *2009*, 5253-5258.

[115] D.-L. Long, Y.-F. Song, E. F. Wilson, P. Kögerler, S.-X. Guo, A. M. Bond, J. S. J. Hargreaves and L. Cronin, *Angew. Chem., Int. Ed.* **2008**, *47*, 4384-4387.

[116] S. Aime, M. Fasano and E. Terreno, *Chem. Soc. Rev.* **1998**, *27*, 19-29.

[117] M. Elhabiri, R. Scopelliti, J.-C. G. Bünzli and C. Piguet, *J. Am. Chem. Soc.* **1999**, *121*, 10747-10762.

[118] W. P. Griffith, N. Morley-Smith, H. I. S. Nogueira, A. G. F. Shoair, M. Suriaatmaja, A. J. P. White and D. J. Williams, **2000**, *607*, 146-155.

[119] D. D. Dexter and J. V. Silverton, *J. Am. Chem. Soc.* **1968**, *90*, 3589-3590.

[120] V. N. Molchanov, I. V. Tatjanina, E. A. Torchenkova and L. P. Kazansky, *J. Chem. Soc., Chem. Commun.* **1981**, 93-94.

[121] C.-D. Wu, C.-Z. Lu, H.-H. Zhuang and J.-S. Huang, *J. Am. Chem. Soc.* **2002**, *124*, 3836-3837.

[122] J. Iball, J. N. Low and T. J. R. Weakley, *J. Chem. Soc., Dalton Trans.* **1974**, 2021-2024.

[123] T. Li, F. Li, J. Lü, Z. Guo, S. Gao and R. Cao, *Inorg. Chem.* **2008**, *47*, 5612-5615.

[124] R. Villanneau, H. Carabineiro, X. Carrier, R. Thouvenot, P. Herson, F. Lemos, F. Ramôa Ribeiro and M. Che, *J. Phys. Chem. B* **2004**, *108*, 12465-12471.

[125] K. Y. Matsumoto, M. Kato and Y. Sasaki, *Bull. Chem. Soc. Jpn.* **1976**, *49*, 106-110.

[126] M.-L. Feng and J.-G. Mao, *Eur. J. Inorg. Chem.* **2004**, *2004*, 3712-3717.

[127] N. I. Kapakoglou, B. I. Panagiotis, S. E. Kazianis, C. E. Kosmidis, C. Drouza, M. J. Manos, M. P. Sigalas, A. D. Keramidas and T. A. Kabanos, *Inorg. Chem.* **2007**, *46*, 6002-6010.

[128] C. Robl and K. Haake, *J.Chem. Soc., Chem. Commun.* **1993**, 397-399.

[129] C. Baffert, J. F. Boas, A. M. Bond, P. Kögerler, D.-L. Long, J. R. Pilbrow and L. Cronin, *Chem. Eur. J.* **2006**, *12*, 8472-8483.

[130] J. Yan, D.-L. Long, H. N. Miras and L. Cronin, *Inorg. Chem.* **2010**, *49*, 1819-1825.

[131] Y. Jeannin and J. Martin-Frere, *Inorg. Chem.* **1979**, *18*, 3010-3014.

[132] D.-L. Long, C. Streb, Y.-F. Song, S. Mitchell and L. Cronin, *J. Am. Chem. Soc.* **2008**, *130*, 1830-1832.

[133] Y. Ozawa and Y. Sasaki, *Chemistry Letters* **1987**, 923-926.

[134] B. Krebs, E. Droste, M. Piepenbrink and G. Vollmer, *C. R. Acad. Sci. Paris, Serie IIc, Cimie* **2000**, *3*, 205-210.

[135] D.-L. Long, P. Kögerler and L. Cronin, *Angew. Chem., Int. Ed.* **2004**, *43*, 1817-1820.

[136] D.-L. Long, H. Abbas, P. Kögerler and L. Cronin, *Angew. Chem., Int. Ed.* **2005**, *44*, 3415-3419.

[137] M. J. Manos, J. D. Woollins, A. M. Z. Slawin and T. A. Kabanos, *Angew. Chem. Int. Ed.* **2002**, *41*, 2801-2805.

[138] J. Yan, D.-L. Long and L. Cronin, *Angew. Chem. Int. Ed.* **2010**, *49*, 4117-4120.

[139] J. Gao, J. Yan, S. G. Mitchell, H. N. Miras, A. G. Boulay, D.-L. Long and L. Cronin, **2011**, *2*, 1502-1508.

[140] T. Ozeki, H. Ichida and Y. Sasaki, **1987**, *43*, 1662-1665.

[141] G. Huan, M. A. Greaney and A. J. Jacobson, *J. Chem. Soc., Chem. Commun.* **1991**, 260-261.

[142] H. N. Miras, R. Raptis, P. Baran, N. Lalioti, A. Harrison and T. A. Kabanos, *C. R. Chimie* **2005**, *8*, 957-962.

[143] A. Müller, J. Meyer, E. Krickemeyer and E. Diemann, *Angew. Chem. Int. Ed. Engl.* **1996**, *35*, 1206-1208.

[144] C.-C. Jiang, Y.-G. Wei, Q. Liu, S.-W. Zhang, M.-C. Shao and Y.-Q. Tang, *Chem. Commun.* **1998**, 1937-1938.

[145] A. Müller and S. Roy,'Oxomolybdates: From Structures to Functions in a New Era of Nanochemistry' in *The Chemistry of Nanomaterials*, Wiley-VCH Verlag GmbH & Co. KGaA, **2005**, pp. 452-475.

[146] A. Müller, E. Krickemeyer, H. Bögge, M. Schmidtmann, F. Peters, C. Menke and J. Meyer, *Angew. Chem. Int. Ed. Engl.* **1997**, *36*, 484-486.

[147] A. Muller, S. Q. N. Shah, H. Bogge and M. Schmidtmann, *Nature* **1999**, *397*, 48-50.

[148] A. Müller, E. Krickemeyer, H. Bögge, M. Schmidtmann and F. Peters, *Angew. Chem. Int. Ed. Engl.* **1998**, *37*, 3359-3363.

[149] A. Müller, P. Kögerler and A. W. M. Dress, **2001**, *222*, 193-218.

[150] A. Müller, E. Beckmann, H. Bögge, M. Schmidtmann and A. Dress, *Angew. Chem., Int. Ed.* **2002**, *41*, 1162-1167.

[151] B. Krebs, E. Droste and M. Piepenbrink,'Synthesis and Crystal Structure Studies of Novel Selenium- and Tellurium-Substituted Lacunary Polyoxometalates.' in *Polyoxometalate Chemistry From Topology via Self-Assembly to Applications* (Eds.: M. T. Pope, A. Müeller), Kluwer Academic Publishers, Dordrecht, The Netherlands, **2001**, pp. 89-99.

[152] K. Wassermann and M. T. Pope, *Inorg. Chem.* **2001**, *40*, 2763-2768.

[153] P. Mialane, L. Lisnard, A. Mallard, J. Marrot, E. Antic-Fidancev, P. Aschehoug, D. Vivien and F. Sécheresse, *Inorg. Chem.* **2003**, *42*, 2102-2108.

[154] K.-C. Kim and M. T. Pope, *J. Chem. Soc., Dalton Trans.* **2001**, 986-990.

[155] M. Bösing, I. Loose, H. Pohlmann and B. Krebs, *Chem. Eur. J.* **1997**, *3*, 1232-1237.

[156] A. Müller, E. Krickemeyer, S. Dillinger, J. Meyer, H. Bögge and A. Stammler, *Angew. Chem. Int. Ed.* **1996**, *35*, 171-173.

[157] U. Kortz, M. G. Savelieff, B. S. Bassil, B. Keita and L. Nadjo, *Inorg. Chem.* **2002**, *41*, 783-789.

[158] D. Drewes, M. Piepenbrink and B. Krebs, *J. Cluster. Sci.* **2006**, *17*, 361-374.

[159] K. Wassermann, M. H. Dickman and M. T. Pope, *Angew. Chem. Int. Ed.* **1997**, *36*, 1445-1448.

[160] F. Hussain, R. W. Gable, M. Speldrich, P. Kogerler and C. Boskovic, *Chem. Commun.* **2009**, 328-330.

[161] K. Fukaya and T. Yamase, *Angew. Chem. Int. Ed.* **2003**, *42*, 654-658.

[162] E. Cadot, B. Salignac, A. Dolbecq and F. Secheresse,'From the first sulfurated Keggin anion to a new class of compounds based on the [M2O2S2]2+ building block M = Mo, W' in *Polyoxometalate Chemistry From Topology via Self-Assembly to Applications* (Eds.: M. T. Pope, A. Müller), Kluwer Academic Publishers, Dordrecht, The Netherlands, **2001**, pp. 39-53.

[163] E. Cadot, B. Salignac, S. Halut and F. Sécheresse, *Angew. Chem. Int. Ed.* **1998**, *37*, 611-613.

[164] J.-F. Lemonnier, S. Duval, S. Floquet and E. Cadot, *Isr. J. Chem.* **2011**, *51*, 290-302.

[165] B. Salignac, S. Riedel, A. Dolbecq, F. Sécheresse and E. Cadot, *J. Am. Chem. Soc.* **2000**, *122*, 10381-10389.

[166] E. Cadot, A. Dolbecq, B. Salignac and F. Sécheresse, *Chem. Eur. J.* **1999**, *5*, 2396-2403.

[167] E. Cadot, B. Salignac, T. Loiseau, A. Dolbecq and F. Sécheresse, *Chem. Eur. J.* **1999**, *5*, 3390-3398.

[168] J. Marrot, M. A. Pilette, F. Sécheresse and E. Cadot, *Inorg. Chem.* **2003**, *42*, 3609-3615.

[169] E. Cadot, M.-A. Pilette, J. Marrot and F. Sécheresse, *Angew. Chem. Int. Ed.* **2003**, *42*, 2173-2176.

[170] C. Bustos, B. Hasenknopf, R. Thouvenot, J. Vaissermann, A. Proust and P. Gouzerh, *Eur. J. Inorg. Chem.* **2003**, 2757-2766.

[171] A. Proust, R. Thouvenot and P. Gouzerh, *Chem. Commun. (Cambridge, U. K.)* **2008**, 1837-1852.

[172] A. Proust, R. Villanneau, R. Delmont, V. Artero and P. Gouzerh,'Organometallic oxometal clusters' in *Polyoxometalate Chemistry From Topology via Self-Assembly to Applications* (Eds.: M. T. Pope, A. Mueller), Kluwer Academic Publishers, Dordrecht, The Netherlands, **2001**, pp. 55-67.

[173] A. Proust, R. Thouvenot, S.-G. Roh, J.-K. Yoo and P. Gouzerh, *Inorg. Chem.* **1995**, *34*, 4106-4112.

[174] V. Artero, D. Laurencin, R. Villanneau, R. Thouvenot, P. Herson, P. Gouzerh and A. Proust, *Inorg. Chem.* **2005**, *44*, 2826-2835.

[175] Y. V. Geletii, C. Besson, Y. Hou, Q. Yin, D. G. Musaev, D. Quinonero, R. Cao, K. I. Hardcastle, A. Proust, P. Kogerler and C. L. Hill, *J. Am. Chem. Soc.* **2009**, *131*, 17360-17370.

[176] A. Proust, R. Thouvenot and P. Gouzerh, **2008**, 1837-1852.

[177] C. P. Pradeep, D.-L. Long, G. N. Newton, Y.-F. Song and L. Cronin, *Angew. Chem. Int. Ed.* **2008**, *47*, 4388-4391.

[178] R. C. Finn and J. Zubieta, *Inorg. Chem.* **2001**, *40*, 2466-2467.

[179] C. Sanchez, S.-I. G. J. de, F. Ribot, T. Lalot, C. R. Mayer and V. Cabuil, *Chem. Mater.* **2001**, *13*, 3061-3083.

[180] E. Burkholder, V. Golub, C. J. O'Connor and J. Zubieta, *Chem. Commun. (Cambridge, U. K.)* **2003**, 2128-2129.

[181] Y.-F. Song, D.-L. Long and L. Cronin, **2010**, *12*, 109-115.

[182] D. E. Katsoulis, *Chem. Rev.* **1998**, *98*, 359-387.

[183] I. V. Kozhevnikov and K. I. Matveev, *Appl. Catal.* **1983**, *5*, 135-150.

[184] L. E. Briand, G. T. Baronetti and H. J. Thomas, *Appl. Catal., A* **2003**, *256*, 37-50.

[185] D.-L. Long, R. Tsunashima and L. Cronin, *Angew. Chem., Int. Ed.* **2010**, *49*, 1736-1758.

[186] J. Piera and J.-E. Bäckvall, *Angew. Chem., Int. Ed.* **2008**, *47*, 3506-3523.

[187] K. Kamata, M. Kotani, K. Yamaguchi, S. Hikichi and N. Mizuno, *Chem.-Eur. J.* **2007**, *13*, 4133.

[188] C. L. Hill, M. S. Weeks and R. F. Schinazi, *J. Med. Chem.* **1990**, *33*, 2767-2772.

[189] N. Yamamoto, D. Schols, C. E. De, Z. Debyser, R. Pauwels, J. Balzarini, H. Nakashima, M. Baba, M. Hosoya and a. et, *Mol. Pharmacol.* **1992**, *42*, 1109-1117.

[190] T. Yamase, *Mol. Eng.* **1993**, *3*, 241-262.

[191] J. T. Rhule, C. L. Hill, D. A. Judd and R. F. Schinazi, *Chem. Rev.* **1998**, *98*, 327-357.

[192] D. A. Judd, J. H. Nettles, N. Nevins, J. P. Snyder, D. C. Liotta, J. Tang, J. Ermolieff, R. F. Schinazi and C. L. Hill, *J. Am. Chem. Soc.* **2001**, *123*, 886-897.

[193] B. Hasenknopf, *Front. Biosci.* **2005**, *10*, 275-287.

[194] T. Yamase, *J. Mater. Chem.* **2005**, *15*, 4773-4782.

[195] D. L. Barnard, C. L. Hill, T. Gage, J. E. Matheson, J. H. Huffman, R. W. Sidwell, M. I. Otto and R. F. Schinazi, *Antiviral Res.* **1997**, *34*, 27-37.

[196] C. Ritchie, A. Ferguson, H. Nojiri, H. N. Miras, Y.-F. Song, D.-L. Long, E. Burkholder, M. Murrie, P. Kögerler, E. K. Brechin and L. Cronin, **2008**, *47*, 5609-5612.

[197] Y. V. Geletii, B. Botar, P. Kögerler, D. A. Hillesheim, D. G. Musaev and C. L. Hill, **2008**, *47*, 3896-3899.

[198] N. Fay, A. M. Bond, C. Baffert, J. F. Boas, J. R. Pilbrow, D.-L. Long and L. Cronin, *Inorg. Chem.* **2007**, *46*, 3502-3510.

[199] H. N. Miras, R. G. Raptis, N. Lalioti, M. P. Sigalas, P. Baran and T. A. Kabanos, *Chem. Eur. J.* **2005**, *11*, 2295-2306.

[200] F.-X. Liu, C. Marchal-Roch, D. Dambournet, A. Acker, J. Marrot and F. Sécheresse, *Eur. J. Inorg. Chem.* **2008**, *2008*, 2191-2198.

[201] N. Casan-Pastor, J. Bas-Serra, E. Coronado, G. Pourroy and L. C. W. Baker, *J. Am. Chem. Soc.* **1992**, *114*, 10380-10383.

[202] S. G. Mitchell, S. Khanra, H. N. Miras, T. Boyd, D.-L. Long and L. Cronin, *Chem. Commun.* **2009**, 2712-2714.

[203] T. Boyd, S. G. Mitchell, H. N. Miras, D.-L. Long and L. Cronin, *Dalton Trans.* **2010**, *39*, 6460-6465.

[204] C. du Peloux, A. Dolbecq, P. Mialane, J. Marrot, E. Rivière and F. Sécheresse, *Angew. Chem., Int. Ed.* **2001**, *40*, 2455-2457.

[205] M. J. Manos, H. N. Miras, V. Tangoulis, J. D. Woollins, A. M. Z. Slawin and T. A. Kabanos, *Angew. Chem., Int. Ed.* **2003**, *42*, 425-427.

[206] H. N. Miras, D. J. Stone, E. J. L. McInnes, R. G. Raptis, P. Baran, G. I. Chilas, M. P. Sigalas, T. A. Kabanos and L. Cronin, *Chem. Commun.* **2008**, 4703-4705.

[207] A. M. Todea, A. Merca, H. Bögge, T. Glaser, J. M. Pigga, M. L. K. Langston, T. Liu, R. Prozorov, M. Luban, C. Schröder, W. H. Casey and A. Müller, *Angew. Chem., Int. Ed.* **2010**, *122*, 524-529.

[208] Q. Yin, J. M. Tan, C. Besson, Y. V. Geletii, D. G. Musaev, A. E. Kuznetsov, Z. Luo, K. I. Hardcastle and C. L. Hill, *Science* **2010**, *328*, 342-345.

[209] U. Kortz, M. G. Savelieff, F. Y. A. Ghali, L. M. Khalil, S. A. Maalouf and D. I. Sinno, *Angew. Chem. Int. Ed.* **2002**, *41*, 4070-4073.

[210] S.-Y. Zhang, C.-L. Hu, C.-F. Sun and J.-G. Mao, *Inorg. Chem.* **2010**, *49*, 11627-11636.

[211] M. Delferro, C. Graiff, L. Elviri and G. Predieri, *Dalton Trans.* **2010**, *39*, 4479-4481.

[212] N. V. Izarova, M. H. Dickman, R. N. Biboum, B. Keita, L. Nadjo, V. Ramachandran, N. S. Dalal and U. Kortz, *Inorg. Chem.* **2009**, *48*, 7504-7506.

[213] F. A. Cotton, G. Wilkinson, C. A. Murillo and M. Bochmann, *Advanced Inorganic Chemistry*, Sixth Edition ed., Wiley-Interscience Publication, **1999**.

[214] R. Shannon, *Acta Crystallogr., Sect. A* **1976**, *32*, 751-767.

[215] H. T. Evans, B. M. Gatehouse and P. Leverett, *J. Chem. Soc., Dalton Trans.* **1975**, 505-514.

[216] K. Nakamoto and Editor, *Infrared and Raman Spectra of Inorganic and Coordination Compounds, Part A: Theory and Applications in Inorganic Chemistry, Sixth Edition*, John Wiley & Sons, Inc., **2009**.

[217] A. Müller, A. M. Todea, J. van Slageren, M. Dressel, H. Bögge, M. Schmidtmann, M. Luban, L. Engelhardt and M. Rusu, *Angew. Chem., Int. Ed.* **2005**, *44*, 3857-3861.

[218] B. Botar, P. Kogerler and C. L. Hill, *Chem. Commun.* **2005**, 3138-3140.

[219] A. Bjornberg, *Acta Cryst.* **1980**, *36*, 1530-1536.

[220] R. Canioni, C. Marchal-Roch, N. Leclerc-Laronze, M. Haouas, F. Taulelle, J. Marrot, S. Paul, C. Lamonier, J.-F. Paul, S. Loridant, J.-M. M. Millet and E. Cadot, *Chem. Commun.* **2011**, *47*, 6413-6415.

[221] C. Ritchie, K. G. Alley and C. Boskovic, *Dalton Trans.* **2010**, *39*, 8872-8874.

[222] Y.-K. Lu, J.-N. Xu, X.-B. Cui, J. Jin, S.-Y. Shi and J.-Q. Xu, *Inorg. Chem. Commun.* **2010**, *13*, 46-49.

[223] S. A. Malik and T. J. R. Weakley, *J. Chem. Soc. A* **1968**, 2647-2650.

[224] H. So and M. T. Pope, *Inorg. Chem.* **1972**, *11*, 1441-1443.

[225] K. Nomiya, M. Miwa, R. Kobayashi and M. Aiso, *Bull. Chem. Soc. Jpn.* **1981**, *54*, 2983-2987.

[226] H. Stratemeier, M. A. Hitchman, D. L. Kepert, B. W. Skelton, K. E. Sugars and A. H. White, *J. Chem. Soc., Dalton Trans.* **1992**, 3035-3039.

[227] G. Sheldrick, *Acta Crystallogr., Sect. A* **2008**, *64*, 112-122.

[228] R. C. Clark and J. S. Reid, *Acta Crystallogr., Sect. A* **1995**, *51*, 887-897.

[229] R. Blessing, *Acta Crystallogr., Sect. A* **1995**, *51*, 33-38.